

**Spectroscopic Studies of
Pharmaceutically and
Biologically Relevant Ions
using Laser Interfaced Mass
Spectrometry**

Uleanya Ogochukwu Kelechi

PhD

University of York

Chemistry

June 2021

Abstract

This thesis reports results obtained from laser induced photodissociation spectroscopy experiments performed on isolated biologically and pharmaceutically relevant molecules and cluster ions within a commercial adapted quadrupole ion-trap mass spectrometer.

Laser photodissociation spectroscopy has been used to measure the dissociative photochemistry of 2-thiouracil. This was the first study to investigate the effect of protonation/deprotonation, i.e pH at the molecular level on the photochemical and photophysical properties of thionucleobases. It is shown that the deprotonated and protonated forms decay by production of free radicals, with the major pathways being electron detachment and production of cationic specie, which is a product from direct excited state decay, respectively.

The effect of intra-cluster electron transfer and excited state modifications as a function of sulphur atom substitution on complexes of iodide with 2-thiouracil (2-TU), 4-thiouracil (4-TU) and 2,4-thiouracil (2,4-TU) were studied to better understand electron capture by thionucleobases, which are used in photo-radiation therapy. It was shown that electron detachment is the dominant decay pathway for all clusters with the respective stable valence molecular anions being formed for the 4-TU and 2,4-TU complexes. The 2-TU complex shows a near-threshold dipole-bound excited state, while the spectral profiles of the 4-TU and 2,4 TU complexes display strong chromophore excitations. Extending the phenomena of this work to the complex of a relatively large biological molecule, I⁻·RF where RF = riboflavin, the photochemistry strongly resembles that of the I⁻·4-TU and I⁻·2,4-TU complexes. We observed the formation of the RF⁻ anion, which is the first observation of the intact molecular anion for this important specie.

Finally, photodissociation spectroscopy has been used to study the effect of complexation on iron III metalloporphyrin (FeTPP⁺) and N-aromatic molecules (pyridine, quinoline and iso-quinoline), compared to the uncomplexed molecule. This is important because of MP's biological, pharmaceutical, and other scientific applications. The spectra revealed that their absorption strength is not reduced as a function of complexation, and both the ground-state and the excited-state properties are highly influenced by the intrinsic properties of the different ligand.

Contents

Abstract.....	ii
Contents.....	iii
List of Figures.....	ix
List of Tables.....	xix
Acknowledgements.....	xxii
Author's Declaration.....	xxiv

Chapter 1: Introduction to Spectroscopic Studies of Gaseous Biological and Pharmaceutical Ions.....1

1.1 Photodissociation Spectroscopy of Gaseous Biomolecules.....	1
1.2 Photodissociation Spectroscopy Overview.....	2
1.3 Ionization Sources in PD Spectroscopy.....	5
1.4 Other Gas-Phase Experiments.....	6
1.5 Instrumentation in PD Experiments.....	10
1.6 Thesis overview.....	15

Chapter 2: Photodissociation Methods and Theory.....16

2.1 Laser coupled - Mass Spectrometry Instrument Overview.....	16
2.2 The Laser-Coupled Bruker AmaZon Mass Spectrometer.....	17
2.2.1 The Modified Bruker AmaZon Mass Spectrometer.....	17
2.2.2 Electrospray Ionisation.....	18
2.2.3 Ion Optics.....	20
2.2.4 Quadrupole Ion Trap (QIT).....	20
2.2.5 Modifications to the Bruker AmaZon Quadrupole Ion Trap.....	24
2.3 Nd:YAG Pumped OPO laser.....	26
2.3.1 Nd:YAG pump laser.....	26
2.3.2 Optical Parametric Oscillator (Horizon) Laser.....	28
2.3.3 The optical pathway between the OPO laser and mass spectrometer.....	30
2.4 General Experimental Overview.....	33
2.4.1 Mass Spectrometry Methods.....	33
2.4.2 Gas-Phase Absorption Spectra.....	34

Contents

2.4.3 Gaseous Photofragmentation and Electron Detachment Spectra.....	36
2.4.4 Laser Power Measurement.....	38
2.5 The Orbitrap Mass Spectrometer.....	39
2.6 Computational Methods.....	40
2.6.1 Density functional theory (DFT) used within the thesis.....	41
2.6.2 Basis set superposition error.....	41
Chapter 3: Observation of Enhanced Dissociative Photochemistry in the Non-Native Nucleobase 2-Thiouracil.....	42
3.1 Abstract.....	42
3.2 Introduction.....	43
3.3 Experimental and Computational Method.....	45
3.3.1 Experimental method.....	45
3.3.2 Computational method.....	46
3.4 Results & Discussion.....	46
3.4.1 Geometric structures and TDDFT calculations [2-TU - H] ⁻ and [2-TU · H] ⁺	46
3.4.2 Photodepletion(absorption) spectrum of [2-TU-H] ⁻	51
3.4.3 Photofragmentation of [2-TU-H] ⁻	52
3.4.4 Photodepletion (absorption) spectrum of [2-TU · H] ⁺	55
3.4.5 Photofragmentation of [2-TU · H] ⁺	56
3.4.6 Comparison of Photofragmentation and HCD Fragmentation of [2-TU·H] ⁺	60
3.5 Further Discussion.....	60
3.5.1 More insight into the photofragmentation dynamics of [2-TU-H] ⁻	60
3.5.2 More insight into the photofragmentation dynamics of [2-TU · H] ⁺	62
3.6 Conclusion.....	62
3.7 Supplementary Information.....	64
3.7.1 Computational studies on [2-TU-H] ⁻ and [2-TU·H] ⁺	64
3.7.1.1 Time dependent density functional theory data of all tautomers of [2- TU-H] ⁻ and [2-TU·H] ⁺	64

Contents

3.7.1.2 Relative energies of fragments for each fragmentation pathway of [2-TU-H] ⁻ to parent ion energy.....	66
3.7.1.3 Relative energies of fragments for each fragmentation pathway of [2-TU · H] ⁺ to parent ion energy.....	67
3.7.1.4 Molecular orbital transitions in [2-TU-H] ⁻ and [2-TU·H] ⁺	70
3.7.2 Experimental studies on [2-TU-H] ⁻ and [2-TU·H] ⁺	
3.7.2.1 Higher energy collisional dissociation of [2-TU-H] ⁻ and [2-TU·H] ⁺	71
3.7.2.2 Electron detachment spectrum of [2-TU-H] ⁻	71
3.7.2.3 Comparison of photodepletion and solution phase absorption spectra of [2-TU-H] ⁻	72
3.7.2.4 Comparison of photodepletion and solution-phase absorption spectra of [2-TU · H] ⁺	74
3.7.2.5 Photofragmentation mass spectrum of [2-TU · H] ⁺	75
Chapter 4: Photodissociation Spectroscopy of Iodide Ion-Thiouracil Clusters: Mapping Chromophore Excitations on the Electron Detachment Spectrum.....	76
4.1 Abstract.....	76
4.2 Introduction.....	77
4.3 Experimental and Computational Method.....	79
4.3.1 Experimental method.....	79
4.3.2 Computational method.....	80
4.4 Results.....	80
4.4.1 Geometric structures and TDDFT of the I·TU clusters.....	80
4.4.2 Photodepletion spectra of the I·TU clusters.....	83
4.4.3 Photofragment mass spectra of the I·TU clusters.....	85
4.4.4 Photofragments production spectra of the I·TU clusters.....	87
4.5 Discussion.....	91
4.5.1 General overview of photodecay channels.....	91
4.5.2 Assignment of the observed excited states from the photodepletion spectra.....	91
4.5.3 Photofragment production.....	93

Contents

4.6 Further Discussion & Concluding Remarks.....	96
4.7 Supplementary Information.....	98
4.7.1 Computational studies on the I ⁻ ·TU clusters.....	98
4.7.1.1 DFT calculations on the tautomers of the I ⁻ ·TU clusters.....	98
4.7.1.2 Direction of the dipole moment the I ⁻ ·TU clusters.....	101
4.7.1.3 Time dependent density functional theory data of tautomers of the I ⁻ ·TU clusters.....	102
4.7.1.4 Equation of motion coupled-cluster singles and doubles (EOMCCSD) calculations of the I ⁻ ·2-TU cluster.....	106
4.7.1.5 Molecular orbitals involved in the TDDFT transitions of the I ⁻ ·TU clusters	108
4.7.2 Experimental studies on the I ⁻ ·TU clusters.....	117
4.6.2.1 Electron detachment spectra of the I ⁻ ·TU clusters.....	117
4.7.2.2 UV-VIS absorption spectra of the TU molecules.....	118
4.7.2.3 Higher-energy collisional dissociation of the I ⁻ ·TU clusters.....	120
Chapter 5: Exploring Riboflavin's Propensity to Capture Electrons through Direct or Dissociative Attachment: Laser Excitation of Iodide Ion Riboflavin Complex.....	121
5.1 Abstract.....	121
5.2 Introduction.....	121
5.3 Experimental and Computational Methods.....	124
5.3.1 Experimental Method.....	124
5.3.2 Computational Method.....	125
5.4 Results.....	126
5.4.1 Geometric structures and TDDFT calculations of the I ⁻ ·RF cluster.....	126
5.4.2 Higher-energy collisional dissociation of the I ⁻ ·RF cluster.....	130
5.4.3 Photodepletion Spectrum of the I ⁻ ·RF cluster.....	131
5.4.2 Photofragmentation of the I ⁻ ·RF cluster.....	132
5.4.2 Electron Detachment Yield Spectrum of the I ⁻ ·RF.....	135
5.5 Discussion.....	136
5.5.1 Overview of the I ⁻ ·RF Decay Channels.....	136

Contents

5.5.2 Assignment of the observed excited states from the photodepletion spectrum	137
5.5.3 Photofragment production	139
5.6 Further Discussion & Concluding Remarks	142
5.7 Supplementary Information	144
5.7.1 Computational studies on I ⁻ ·RF clusters	144
5.7.1.1 DFT calculations of grouped conformational isomers of the I ⁻ ·RF cluster	144
5.7.1.2 Direction of the dipole moment of the RF molecules in the I ⁻ ·RF Cluster	145
5.7.1.3 TDDFT calculations for individual selected conformational isomers of the I ⁻ ·RF clusters	146
5.7.1.4 Molecular orbitals involved in the TDDFT transitions of the lowest energy selected conformational isomer (structure a) of I ⁻ ·RF cluster	148
5.7.2 Experimental studies on I ⁻ ·RF clusters	153
5.6.2.1 Overlaid electron detachment and photodepletion spectra of I ⁻ ·RF clusters	153
Chapter 6: Collision-induced dissociation and laser photodissociation spectroscopy of N-aromatic metalloporphyrin complexes	154
6.1 Abstract	154
6.2 Introduction	155
6.3 Experimental and Computational Methods	158
6.3.1 Experimental methods	158
6.3.2 Computational methods	159
6.4 Results and Discussion	159
6.4.1 Low energy collisional induced dissociation of FeTTP ⁺ ·X clusters	159
6.4.2 Comparison of the fragmentation energies of the complexes	161
6.4.3 Geometric structures and time-dependent density functional theory calculations (TDDFT) on FeTTP ⁺ ·N clusters	165
6.4.4 Photodepletion spectrum of FeTTP ⁺ ·py cluster	171

Contents

6.4.5 Photodepletion spectrum of FeTTP ⁺ ·iQ cluster.....	172
6.4.6 Photodepletion spectrum of FeTTP ⁺ ·Q cluster.....	173
6.4.7 Photofragmentation spectra of the FeTTP ⁺ ·N-aromatics clusters.....	176
6.4.7.1 Photofragmentation spectra of the FeTTP ⁺ ·py cluster.....	176
6.4.7.2 Photofragmentation spectra of the FeTTP ⁺ ·iQ cluster.....	178
6.4.7.3 Photofragmentation spectra of the FeTTP ⁺ ·Q cluster.....	179
6.4.8 Laser power dependence of photofragments production of the FeTTP ⁺ ·N-aromatics clusters.....	182
6.5 Conclusion.....	186
6.6 Supplementary Information	
6.6.1 Experimental studies on FeTTP ⁺ ·N-aromatics clusters.....	188
6.6.1.1 Higher energy collisional dissociation of FeTTP ⁺ ·N-aromatics Clusters.....	188
6.6.1.2 Solution-phase spectrum of FeTTPCl in MeCN	189
6.6.1.3 Parent ion mass spectra of FeTTP ⁺ ·N-aromatics clusters.....	189
6.6.1.4 Photofragment mass spectra of FeTTP ⁺ ·N-aromatics clusters.....	191
6.6.1.5 Overlaid TDDFT and photodepletion spectra of the FeTTP ⁺ ·N-aromatics clusters.....	191
6.6.2 Computational Studies on FeTTP ⁺ ·N-aromatics clusters.....	194
6.6.2.1 Overlaid TDDFT spectra for N-ligated and π -stacking optimized structures of FeTTP ⁺ ·Q cluster.....	194
6.6.2.2 Molecular orbital (MO) predictions by TDDFT calculations for FeTTP ⁺ ·py cluster.....	194
Chapter 7: Summary and Outlook.....	202
References.....	206

List of Figures

Figure 1.1 Schematic diagram for the potential energy profile of a gaseous molecule representing electronic and vibrational excitation. The arrows define the magnitude of the different excitation energies.....	4
Figure 1.2 Schematic diagram for the ionization technique involved in one and two-colour REMPI experiments.....	7
Figure 2.1 The schematic diagram of laser the coupled-mass spectrometry experiment.....	16
Figure 2.1 The schematic diagram of laser the coupled-mass spectrometry experiment.....	17
Figure 2.3 Diagram of an electrospray ionisation (ESI) source. Positive and negative charges are included in the droplets to show that ESI can be used to produce gaseous cations or anions.....	19
Figure 2.4 Diagram of a quadrupole ion trap (QIT) mass spectrometer, adapted from the AmaZon Manual. 1 is the entrance end cap, 2 is the ring electrode, 3 is the exit end cap, and 4 is the ion cloud and buffer gas.....	21
Figure 2.5 Stability diagram for ions in a quadrupole ion trap. Image taken from the AmaZon Manual.....	22
Figure 2.6 Major scan segments for an MS scan, adapted from the AmaZon manual	23
Figure 2.7 Major scan segments for an MS(n) scan, adapted from the AmaZon manual.....	24
Figure 2.8 Labelled diagram of the modifications made to the QIT mass spectrometer to allow photodissociation experiments. (a) is a Nd:YAG pumped OPO tunable laser source; (b) is a 200 mm focal length UVFS lens (LE4467-UV, Thorlabs Inc.); (c) is an optical shutter (Model SH05, Thorlabs Inc.); (d) is a pair of flange mounted uncoated UVFS windows (WG41050, Thorlabs Inc.); (e) is a 2 mm hole drilled through the ring electrode of the ion trap to allow the passage of laser light; (f) is a pair of aluminium mirrors (PF05-03-F01, Thorlabs Inc.); (g) is a UV-Vis	

List of Figures

spectrometer (USB2000+ UV-VIS, Ocean Optics Inc); and (h) is the centre of the ion trap where photodissociation occurs.....25

Figure 2.9 Simplified diagram of the energy levels in Nd³⁺: Nd:YAG laser involved in the emission of 1064nm light.....27

Figure 2.10 Diagram of the Q-Switch used to produce laser pulses in the Surelite Nd:YAG laser. Image adapted from the Surelite manual.....27

Figure 2.11 Horizon OPO optical layout displaying the pathway of the OPO laser in producing different wavelengths.¹⁷² Image adapted from Horizon manual. Components 14 and 26 are optional optics and were not part of the Horizon laser used in this thesis.....29

Figure 2.12 Labelled pictures of the optical bench mounted on top of the AmaZon mass spectrometer with a) displaying the path of the UV (193 - 400 nm) and b) visible/NIR (400 - 2700 nm) light from the OPO laser to ion trap of the mass spectrometer. Pictures adapted from Ref. 152.....31

Figure 2.13 Labelled picture of the optical bench on top of the amaZon mass spectrometer, showing the region of the table containing the power measurement setup as well as the optical interface of the mass spectrometer. Picture adapted from Ref. 152.....32

Figure 2.14 Schematic diagram of potential energy surfaces of a gaseous molecule showing two fragmentation mechanisms in the electronic excited state and the vibrational electronic ground state..... 37

Figure 2.15 Schematic diagram of the Orbitrap Fusion Tribrid mass spectrometer. Image is adapted from the Orbitrap manual.....39

Figure 3.1 Schematic diagram of uracil (U) and 2-thiouracil (2-TU) with ring atom labels.....44

Figure 3.2 Low energy tautomers of [2-TU - H]⁻ obtained at the B3LYP/6- 311++G (2d, 2p) level of theory.....47

Figure 3.3 Low energy tautomers of [2-TU·H]⁺ obtained at the B3LYP/6- 311++G (2d, 2p) level of theory.....48

List of Figures

- Figure 3.4** Calculated TDDFT excitation energies (B3LYP/6-311++G(2d,2p)) for (a) the D1 tautomer of [2-TU-H]⁻, (b) the P1a tautomer of [2-TU·H]⁺, and (c) the P2 tautomer of [2-TU·H]⁺. Oscillator strengths (Osc.) of individual transitions ≥ 0.005 are shown by vertical bars, while the full line spectrum is a convolution of the calculated spectral transitions with a Gaussian function (0.25 eV HWHM).....50
- Figure 3.5** Gas-phase absorption (photodepletion) spectrum of [2-TU-H]⁻ measured over the range of 3.2 – 5.3 eV (234-390 nm). The arrow indicates the VDE of the D1 isomer. The solid line is a five-point adjacent average of data points.....51
- Figure 3.6** Photofragment difference (laseron – laseroff) mass spectrum of [2-TU - H]⁻, excited at 3.6 eV (344nm). *Represents parent ion signal with m/z 127.....52
- Figure 3.7** (a) Gas-phase absorption (photodepletion) spectrum of [2-TU-H]⁻, (b) photofragment action spectrum of SCN⁻ (m/z 58), and (c) photofragment production spectrum of m/z 93 from 3.2–5.3 eV (234–390 nm). The arrow included in (a) indicates the calculated VDE of the lowest-energy tautomer. The solid line is a five-point adjacent average of the data points.....54
- Figure 3.8** Gas-phase absorption (photodepletion) spectrum of [2-TU·H]⁺ across the range 3.6–5.8 eV (344–214 nm). The solid line is a five-point adjacent average of data points.....55
- Figure 3.9** (a) Photodepletion spectrum of [2-TU · H]⁺ ions and photofragment action spectra of (b) m/z 96, (c) m/z 128, (d) m/z 70 and (e) m/z 112 generated on photoexcitation across the range 3.6-5.7 eV (344 -214nm). The solid line is a five-point adjacent average of data points.....59
- Figure 3.10** Calculated TDDFT excitation energies (with the B3LYP/6-311++G (2d, 2p) functional and basis set) of D1, D2, D3a, D3b, D4a and D4b tautomers of [2-TU - H]⁻ geometric structures (Figure 3.2). The oscillator strengths (OSC.) on the y axis of individual transitions ≥ 0.005 within the experimental scan range are shown by vertical bars, while the full line spectrum is a convolution of the calculated spectrum with Gaussian function (0.25 eV HWHM).....64
- Figure 3.11** Calculated TDDFT excitation energies (with the B3LYP/6- 311++G (2d, 2p) functional and basis set) of P1a, P1b, P1c, P1d and P2 tautomer of [2-TU · H]⁺ geometric structures (Figure 3.3). The oscillator strengths (OSC.) on the y axis of individual transitions within the experimental scan range are shown by vertical

bars, while the full line spectrum is convolution the calculated spectrum with Gaussian function (0.25eV HWHM).....	65
Figure 3.12 Energy diagram for relative energies calculated at B3LYP/6-311++G (2d, 2p) (gas phase) for the fragmentation pathways of [2-TU - H] ⁻	67
Figure 3.13 Energy diagram for relative energies calculated at B3LYP/6-311++G (2d, 2p) (gas phase) for the major and the secondary fragmentation pathways of [2-TU · H] ⁺	68
Figure 3.14 Molecular orbital transitions predicted by TDDFT calculations at 3.75 and 4.73eV for [2-TU - H] ⁻	69
Figure 3.15 Molecular orbital transitions predicted by TDDFT calculations at 4.52 and 5.2eV for [2-TU · H] ⁺	70
Figure 3.16 Parent ion dissociation curve [2-TU - H] ⁻ alongside production curves of the 6 most intense fragments upon HCD between 0 and 50% energy. The data points fitted with the curved lines are viewing guides to show the profile for an individual fragment.....	71
Figure 3.17 Parent ion dissociation curve [2-TU · H] ⁺ alongside production curves of five most intense fragments upon HCD between 0 and 50% energy. The data points fitted with the curved lines are viewing guides to show the profile for an individual fragment.....	71
Figure 3.18 Electron detachment yield of mass selected [2-TU - H] ⁻ ions, across the range 3.2-5.2 eV (234-390nm). The solid line is a five-point adjacent average of data points.....	72
Figure 3.19 (a) Gas-phase photodepletion spectrum (absorption spectrum) of [2-TU - H] ⁻ across the range 3.2-5.3 eV (234-390nm). The solid line is a five-point adjacent average of data points. (b) Absorption spectrum (1×10^{-4} mol dm ⁻³ in MeOH) at a pH of 11.....	73
Figure 3.20 (a) Gas-phase photodepletion spectrum (absorption spectrum) of [2-TU · H] ⁺ across the range 3.6-5.7 eV (344 -214nm). The solid line is a five-point adjacent average of data points. (b) Absorption spectrum ($\sim 1 \times 10^{-4}$ mol dm ⁻³ in MeOH) at a pH of 3.7.	74

- Figure 3.21** Photofragment difference (laser_{on} – laser_{off}) mass spectrum of [2-TU · H]⁺ excited at 4.6 and 5.2eV (344nm). *Represents parent ion signal with *m/z* 127.....75
- Figure 4.1** Schematic diagram of uracil (U), 2-thiouracil (2-TU), 4-thiouracil (4-TU) and 2,4-Thiouracil (2,4-TU), illustrating how the C₂ - C₄ oxygens of uracil are replaced with sulphur.....78
- Figure 4.2** Global minima geometric structures of I·TU clusters optimised at the B3LYP/6-311++G(2d,2p) level of theory with SDD on I. TU = (a) 2,4-TU, (b) 2-TU and (c) 4-TU.....81
- Figure 4.3** TDDFT excitation spectra of a) I·2,4-TU, b) I·2-TU and c) I·4-TU clusters calculated at M062X/DEF2SVP. The oscillator strengths on the y axis of individual transitions ≥ 0.005 within the experimental scan range are shown by vertical bars while the full line spectrum is a convolution of the calculated spectrum with Gaussian function (0.25 eV HWHM). The red lines represent transitions from an iodide p-orbital and the green lines represent transitions from the thio-nucleobase (TU) π orbital.....83
- Figure 4.4** Photodepletion (gas-phase absorption) spectra of (a) I·2,4-TU, (b) I·2-TU and (c) I·4-TU across the range 3.1–5.7 eV. The solid line is a five-point adjacent average of the data points. Aqueous absorption spectrum of (d) 2,4-TU, (e) 2-TU and (f) 4-TU across the range 3.1–5.8 eV (400–213 nm).....84
- Figure 4.5** Photofragment difference (laser_{on} – laser_{off}) mass spectrum of I TU clusters excited at 3.5 eV (354 nm), 4.2 eV (295 nm) and 4.0 eV (310 nm) photodepletion band maxima of the individual I·TU clusters, respectively. *Represents the precursor cluster ion signal.....86
- Figure 4.6** (a) Gas phase photodepletion spectra of I·2,4-TU with the b) I, c) [2,4-TU-H]⁻, d) [2,4-TU]⁻ and e) SCN⁻, across the range 3.1-5.7 eV (400-218nm). The solid line is a five-point adjacent average of the data points, while the arrow represents the calculated VDE.....88
- Figure 4.7** a) Gas phase photodepletion spectrum of the I·2-TU cluster and b) the *m/z* 127 photofragment action spectrum, across the range 3.1-5.7 eV (400-218nm). The solid line is five-point adjacent average of data point while the arrow represents the calculated VDE.....89

- Figure 4.8** a) Gas phase photodepletion spectrum of the I·4-TU cluster and photofragment action spectra of b) m/z 127 and c) [4-TU]⁻ across the range 3.1-5.7 eV (400-218nm). The solid line is a five-point adjacent average of data point, while the arrow represents the calculated VDE.....90
- Figure 4.9** The vector direction of the axis of the dipole moment of the I·TU molecule, calculated for the neutral molecule at the geometry of the optimized ion-molecule complex.....101
- Figure 4.10** TDDFT excitation spectra of the lowest energy tautomers of a) I·2,4-TU, b) I·2-TU and c) I·4-TU clusters calculated at B3LYP/6-311++G(2d,2p) level and 6-311G(d,p)/SDD on I.....102
- Figure 4.11** TDDFT excitation spectra of the tautomers of I·2,4-TU clusters for the structures shown in Table 4.4. The oscillator strengths (OSC.) on the y axis of individual transitions ≥ 0.005 within the experimental scan range are shown by vertical bars, while the full line spectrum is a convolution of the calculated spectrum with Gaussian function (0.25 eV HWHM).....103
- Figure 4.12** TDDFT excitation spectra of the tautomers of I·2-TU clusters for the structures shown in Table 4.5. The oscillator strengths (OSC.) on the y axis of individual transitions ≥ 0.005 within the experimental scan range are shown by vertical bars, while the full line spectrum is a convolution of the calculated spectrum with Gaussian function (0.25 eV HWHM).....104
- Figure 4.13** TDDFT excitation spectra of the tautomers of I·4-TU clusters for the structures shown in Table 4.6. The oscillator strengths (OSC.) on the y axis of individual transitions ≥ 0.005 within the experimental scan range are shown by vertical bars, while the full line spectrum is a convolution of the calculated spectrum with Gaussian function (0.25 eV HWHM).....105
- Figure 4.14** Overlaid EOMCCSD, TDDFT of the lowest energy I·2-TU cluster and Photodepletion spectrum to explore the dipole bound state.....106
- Figure 4.15** Molecular orbital transitions I·2-TU involved in the dipole bound state predicted by EOMCCSD calculations between 3.87 – 4.21 eV. The excitation energies are offset by – 1.12 eV for comparison with the experimental data.....107

List of Figures

Figure 4.16 % Electron Detachment yield of I·2,4-TU, I·2-TU and I·4-TU clusters. The solid line is a five-point adjacent average of data point.....117

Figure 4.17 Aqueous absorption spectrum of (a) 2,4-TU, (b) 2-TU and (c) 4-TU across the range 3.1 – 5.8 eV (400 – 213 nm) in MECN/H₂O solvent at 10⁻⁴mol dm³.....118

Figure 4.18 Parent ion dissociation curve for I·2,4-TU, I·2-TU and I·4-TU alongside production curves of fragments upon HCD between 0 and 20% energy. The data points fitted with the curved lines are viewing guides to show the profile for an individual fragment.....119

Figure 5.1 Schematic diagram of (a) lumichrome and (b) riboflavin.....122

Figure 5.2 TDDFT (B3LYP/6-311++G(2d,2p) level, 6-311G(d,p)/SDD on I) excitation spectrum of the lowest energy isomer of I·RF cluster for the structure **a** shown in Table 1. The oscillator strengths (OSC.) on the y axis of individual transitions ≥ 0.005 are shown by vertical bars while the full line spectrum is a convolution of the calculated spectrum with Gaussian function (0.25 eV HWHM).....129

Figure 5.3 % Fragment ion yield from the dissociation of I·RF cluster upon HCD between 0 and 25% energy, illustrating fragmentation of the complex into iodide and riboflavin. The data points fitted with the curved lines are viewing guides to show the profile for an individual fragment.....130

Figure 5.4 Photodepletion spectrum of the I·RF cluster. The line is a five-point adjacent average of the data points. The arrow indicates the calculated VDE of 4.95 eV.....131

Figure 5.5 Photo-fragment mass spectrum (laser_{on}-laser_{off}) of the I·RF cluster excited at 4.37eV. * represents the parent ion mass spectra.....132

Figure 5.6 a) Gas phase photodepletion spectra of the I·RF cluster and photofragments spectra b) RF·, c) [LC-H]⁻, d) I⁻ and e) [m/z 198]⁻ generated on photoexcitation of mass selected I·RF cluster ions, across the range 2.4-5.6 eV (516-222 nm). The solid line is a five-point adjacent average of data points.....134

Figure 5.7 % Electron Detachment yield of I·RF cluster. The solid line is a five-point adjacent average of data points.136

Figure 5.8 The vector direction of the axis of the dipole moment of (a) RF monomer and (b) I·RF molecule, calculated for the neutral molecule at the geometry of their optimized ion-molecule respectively.....	145
Figure 5.9 TDDFT excitation spectra of the selected conformational isomers of I·RF clusters for the structures shown in Table 5.1. The oscillator strengths (OSC.) on the y axis of individual transitions ≥ 0.005 within the experimental scan range are shown by vertical bars while the full line spectrum is a convolution of the calculated spectrum with Gaussian function (0.25 eV HWHM). The arrow shows the position of the calculated VDE.....	146
Figure 5.10 Overlaid TDDFT excitation spectra of the selected conformational isomers and the experimental photodepletion spectrum of I·RF cluster.....	148
Figure 5.11 Overlaid % Electron Detachment yield (red) and % photodepletion intensity (green) of I·RF clusters. The solid line is a five-point adjacent average of data points.....	153
Figure 6.1 Schematic diagram of porphin which is the simplest form of porphyrin.....	155
Figure 6.2 Schematic diagram of a.) tetraphenyl porphyrin iron III cation (FeTTP^+) and b.) $\text{FeTTP}^+\cdot\text{X}$ complex where X = pyridine, quinoline and isoquinoline).....	157
Figure 6.3 Schematic diagram of pyridine, quinoline and isoquinoline.....	158
Figure 6.4 Parent ion dissociation curves for $\text{FeTTP}^+\cdot\text{iQ}$, $\text{FeTTP}^+\cdot\text{Q}$ and $\text{FeTTP}^+\cdot\text{py}$ alongside fragment production curves upon low-energy CID between 0 and 10% energy. Standard experimental errors obtained from repeat runs were $\pm 3\%$	160
Figure 6.5 Parent ion dissociation curves for $\text{FeTTP}^+\cdot\text{iQ}$, $\text{FeTTP}^+\cdot\text{Q}$ and $\text{FeTTP}^+\cdot\text{py}$ upon CID was between 0 and 10% energy. Standard experimental errors obtained from repeat runs were $\pm 3\%$	162
Figure. 6.6 TDDFT excitation spectra for the N-coordination structures of the (a) $\text{FeTTP}^+\cdot\text{py}$, (b) $\text{FeTTP}^+\cdot\text{iQ}$, (c) $\text{FeTTP}^+\cdot\text{Q}$ clusters and (d) FeTTP^+ monomer. The vertical bars represent the individual transitions of the oscillatory strength, and the full line spectrum gives a convolution of the calculated spectrum with a Gaussian function (0.15 eV HWHM).....	169

- Figure 6.7** Photodepletion (absorption) spectra of (a) FeTTP⁺·py and (b) FeTTP⁺ monomer across the range of 3.86 - 2.2 eV (322-564 nm). The solid lines are five-point adjacent averages of the data points.....171
- Figure. 6.8** Photodepletion (absorption) spectra of (a) FeTTP⁺·iQ and (b) FeTTP⁺ across the range of 3.86 – 2.2 eV (322-564 nm). The solid lines are five-point adjacent averages of the data points.....172
- Figure. 6.9** Photodepletion (absorption) spectra of (a) FeTTP⁺·Q and (b) FeTTP⁺ across the range of 3.86 – 2.2 eV (322-564 nm). The solid lines are five-point adjacent averages of the data points.....173
- Figure. 6.10** (a) *m/z* 668 (b) *m/z* 590 (c) *m/z* 514 and (d) *m/z* 512 photofragment production spectra for FeTTP⁺·py cluster across the range of 3.86 – 2.2 eV (322-564 nm). The solid lines are five-point adjacent averages of the data points.....177
- Figure. 6.11** (a) *m/z* 668 (b) *m/z* 590 (c) *m/z* 514 and (d) *m/z* 512 photofragment production spectra for FeTTP⁺·py cluster across the range of 3.86 – 2.2 eV (322-564 nm). The solid lines are five-point adjacent averages of the data points.....178
- Figure. 6.12** (a) *m/z* 668 (b) *m/z* 590 (c) *m/z* 514 and (d) *m/z* 512 photofragment production spectra for FeTTP⁺·Q cluster across the range of 3.86 – 2.2 eV (322-564 nm). The solid lines are five-point adjacent averages of the data points.....180
- Figure 6.13** Power studies comparing the production of the most intense photofragment *m/z* 668 = FeTTP⁺ with the laser pulse energy at 360 nm (3.44 eV) and 402nm (3.08 eV) (around the location of the maximum of the two bands in the Soret band region of the FeTTP⁺·py), respectively.....183
- Figure 6.14** Power studies comparing the production of the photofragment *m/z* 590 with the laser pulse energy at 360 nm (3.44 eV) and 402nm (3.08 eV) (around the location of the maximum of the two bands in the Soret band region of the FeTTP⁺·py), respectively.184
- Figure 6.15** Parent ion dissociation curve FeTTP⁺·N-aromatics clusters alongside production curves of fragments upon HCD between 0 and 17% energy. The data points fitted with the curved lines are viewing guides to show the profile for an individual fragment.....188
- Figure 6.16** Absorption spectrum of FeTPPCl at (1×10^{-6} mol dm⁻³) in MeCN....189

Figure 6.17 Parent ion mass spectrum of FeTTP ⁺ ·py cluster with m/z 749.....	189
Figure 6.18 Parent ion mass spectrum of FeTTP ⁺ ·iQ cluster. FeTTP ⁺ ·iQ and FeTTP ⁺ ·Q clusters have same mass-to-charge ratio (m/z 797).....	190
Figure 6.19 CID fragmentation mass spectrum of the FeTPP ⁺ monomer at 10% CID energy.....	190
Figure. 6.20 The photofragment mass spectra of a) FeTTP ⁺ ·iQ, b) FeTTP ⁺ ·iQ and c) FeTTP ⁺ ·Q clusters irradiated at 3.52 eV, 3.24 eV and 3.30 eV, respectively.....	191
Figure. 6.21 Overlaid experimental (red) and computational (blue) spectra for a) FeTPP ⁺ ·py and b) FeTPP ⁺ with -0.1 eV shift of the TDDFT spectrum of a and b towards lower energy. The features of both the experimental and computational spectra matched.....	192
Figure. 6.22 Overlaid experimental (red) and computational (blue) spectra for a) FeTPP ⁺ ·iQ and b) FeTPP ⁺ cluster with no shift in (a) and -0.1 eV shift in (b) to the TDDFT spectrum towards lower energy, respectively. The features of both the experimental and computational spectra matched.....	192
Figure. 6.23 Overlaid experimental (red) and computational (blue) spectra for a) FeTPP ⁺ ·Q and b) FeTPP ⁺ cluster with -0.1 eV shift to the TDDFT spectrum of a and b towards lower energy.....	193
Figure 6.24 a.) The photofragment production spectrum (red) of m/z 591 obtained from the photodepletion of the FeTPP ⁺ ·Q cluster and b.) the TDDFT calculated spectrum (blue) of the FeTPP ⁺ ·Q cluster with -0.05 eV shift towards lower energy.....	194
Figure 6.25 Overlaid TDDFT calculated spectra for N-ligated and π -stacking optimised structures of FeTTP ⁺ ·Q cluster.....	194

List of Tables

Table 3.1 Relative energies and % Boltzmann population of the lowest energy tautomers of $[2\text{-TU} - \text{H}]^-$ and $[2\text{-TU} \cdot \text{H}]^+$ calculated at B3LYP/6-311++G (2d, 2p) level of theory. Vertical detachment energy (VDE) and the vertical dipole moment (D) are also presented for the $[2\text{-TU} - \text{H}]^-$ anions.....	48
Table 3.2 Assignment of the fragmentation channels of $[2\text{-TU} - \text{H}]^-$ (m/z 127) observed upon, laser excitation at 3.2-5.2 eV. ^{a,b,c} and HCD collisional excitation...53	53
Table 3.3 Assignment of the fragmentation channels of $[2\text{-TU} \cdot \text{H}]^+$ (m/z 129) observed upon HCD collisional excitation, and laser excitation at 4.6 and 5.2 eV. ^{a,b}	57
Table 3.4 Relative energies calculated at B3LYP/6-311++G (2d, 2p) (gas phase) for the major fragmentation pathways of $[2\text{-TU} - \text{H}]^-$. All energies are zero point corrected.....	66
Table 3.5 Step 1: relative energies calculated at B3LYP/6-311++G (2d, 2p) (gas phase) for the major fragmentation pathways of $[2\text{-TU} \cdot \text{H}]^+$. All energies are zero point corrected.....	67
Table 3.6 Step 2: relative energies calculated at B3LYP/6-311++G (2d, 2p) (gas phase) for the possible fragments in the secondary fragmentation pathways of $[2\text{-TU} \cdot \text{H}]^+$ through the ionic fragments m/z 112(A) and m/z 70(B).....	68
Table 4.1 Calculated vertical detachment energies (VDE), cluster binding energies ^a and vertical dipole moment ^b using B3LYP/MP2 functional with 6-311++G (2d,2p)/SDD basis set.....	81
Table 4.2 Lists of photofragments with assignments observed at the Band I maxima of the I·TU clusters, shown with the HCD collision-induced dissociation fragments ^a	85
Table 4.3 Calculated structures and relative electronic energies of the tautomers 2,4-thiouracil iodide (I·2,4-TU) clusters. Structures were calculated at the B3LYP/6-311++G(2d,2p) level, 6-311G(d,p)/SDD on I (see main text for details).Energies are zero-point energy corrected.....	98

List of Tables

Table 4.4 Calculated structures and relative electronic energies of the tautomers 2-thiouracil iodide (I·2-TU) clusters. Structures were calculated at the B3LYP/6-311++G(2d,2p) level, 6-311G(d,p)/SDD on I (see main text for details). Energies are zero-point energy corrected.....	99
Table 4.5 Calculated structures and relative electronic energies of the tautomers 4-thiouracil iodide (I·4-TU) clusters. Structures were calculated at the B3LYP/6-311++G(2d,2p) level, 6-311G(d,p)/SDD on I (see main text for details). Energies are zero-point energy corrected.....	100
Table 4.6 Calculated TDDFT transition energies at the B3LYP/6-311++G(2d,2p)/SDD level of theory and oscillator strengths of the I·2,4-TU cluster. Only transitions below 5.7 eV with oscillator strength > 0.005.....	108
Table 4.7 Calculated TDDFT transition energies at the B3LYP/6-311++G(2d,2p)/SDD level of theory and oscillator strengths of the I·2,4-TU cluster. Only transitions below 5.6 eV with oscillator strength > 0.005.....	111
Table 4.8 Calculated TDDFT transition energies at the B3LYP/6-311++G(2d,2p)/SDD level of theory and oscillator strengths of the I·4-TU cluster. Only transitions below 5.7 eV with oscillator strength > 0.005.....	114
Table 5.1: Calculated structures and relative electronic energies of the selected ungrouped conformational isomers of Riboflavin iodide (I·RF) clusters. Structures were calculated at the B3LYP/6-311++G(2d,2p) level, 6-311G(d,p)/SDD on I. Energies are zero-point energy corrected.....	127
Table 5.2: Calculated bond lengths, ^a relative energies, % Boltzmann population, ^c vertical detachment energy (VDE) and vertical dipole moment (VDM) of the selected (I·RF) clusters structures calculated at B3LYP/6-311++G(2d,2p) level, 6-311G(d,p)/SDD on I.....	128
Table 5.3 Lists of photofragments with assignments observed at the Band I maxima of the I·RF clusters, shown with the HCD fragments. ^a	133
Table 5.4 Optimised I·RF clusters grouped conformers generated using Schrodinger's Macro-Model with mixed Monte Carlo torsional and low-mode sampling parameters minimised with OPLS3e force field. The structures were optimized at B3LYP/6-311++G(2d,2p) level of theory.....	144

List of Tables

Table 5.5 Calculated TDDFT transition energies at the B3LYP/6-311++G(2d,2p)/SDD level of theory and oscillator strengths of the I·RF cluster. Only transitions below 5.6 eV with oscillator strength > 0.005.....	149
Table 6.1 $E_{1/2}$ fragmentation energies, fragment ions and neutral fragments for FeTTP ⁺ ·N (N= pyridine(py), quinoline(Q) and isoquinoline (iQ)) complexes.....	161
Table 6.2 BSSE-corrected binding energies in (kJ mol ⁻¹) for the N-coordination structures of FeTTP ⁺ ·py, FeTTP ⁺ ·Q and FeTTP ⁺ ·iQ clusters.....	164
Table 6.3 BSSE-corrected binding energies in (kJ mol ⁻¹) for (π -stacking) structures of FeTTP ⁺ ·py, FeTTP ⁺ ·iQ and FeTTP ⁺ ·Q clusters.....	165
Table 6.4 Lowest obtained energy geometric structures of FeTTP ⁺ ·py, FeTTP ⁺ ·iQ and FeTTP ⁺ ·Q clusters for N-coordination ^a and π -stacking ^a obtained at (B3LYP/6-31G (d)) level of theory.....	166
Table 6.5 Band maxima at the Q and Soret band regions of the TDDFT calculated spectra for FeTTP ⁺ monomer, FeTTP ⁺ ·py, FeTTP ⁺ ·iQ and FeTTP ⁺ ·Q clusters and corresponding band shifts are listed.....	168
Table 6.6 TDDFT calculated transition energies (3.56-2.48 eV) and oscillator strengths of the FeTTP ⁺ ·py cluster, calculated at the B3LYP/6-31G (d) level.....	170
Table 6.7 Band maxima at the Q and Soret band regions of the experimentally acquired spectra of FeTTP ⁺ monomer, FeTTP ⁺ ·py, FeTTP ⁺ ·iQ and FeTTP ⁺ ·Q clusters and corresponding band shifts are listed.....	174
Table 6.8 Photofragments and HCD fragments observed for the FeTTP ⁺ ·iQ cluster, with assignments.....	181
Table 6.9 Calculated TDDFT transition energies at the B3LYP/6-31G(d) level of theory and oscillator strengths of the FeTTP ⁺ ·py cluster. MO transitions that contributed more than 20% to the excitations and with oscillator strength > 0.005.....	194

Acknowledgements

My foremost gratitude goes to Him who is able to do exceedingly abundantly above all I can ever think or ask or imagine, the love of my life and my saviour Jesus Christ for providing and being everything to me throughout this Ph.D journey.

I would also like to sincerely appreciate my dear supervisor, the indefatigable Prof. Caroline Dessent whose immeasurable support and motherly guidance made my journey which started tough, and challenge filled to be able to progress through thorns and thistle to this conclusive end. Thank you so much Ma. I could not have asked for anything better. I am honestly short of words to correctly communicate how much I have come to trust and appreciate your various most invaluable support, words of good counsel and motherly advice.

My big shout out also goes to the entire past and present members of Dessent group who did contributed in every way to making me come out a stronger person. I want to specially thank my friends Edward Matthews and Rosaria Cercola for their support and every effort to make me feel accepted and included. Ed those three parting words of yours stuck with me and remained the mainstay for my weathering through problems anytime they arise. I will ever always appreciate- it really did work. Rosaria, you have become not just a friend but a dear sister to me, I love you.

I also appreciate and thank the ever helpful and approachable staff of the chemistry Department for their enormous support especially the graduate office and for always being there for me.

To my family, what else would I have desired. I would like to thank my friend, confidant and husband Obi and our wonderful children, Chimdi and Kamso my awesome sons; you started the journey with me, I will forever appreciate you. Though young, you were a big support, always encouraging Mum to carry on at all times and showing very profound understanding when you could not get the maximum motherly attention from Mum who was totally consumed with work. My little baby girl Ngwugwungozi(my bundle of God's blessings) your most surprising entry into our family train did bring a sweet intrigue into the victorious climax of this most colourful Ph.D journey. I love you baby.

Acknowledgements

To the family of God, the Hope Centre Church, the cloud of his glory over us will never lift. Pastor Reuben Inwe, Mr Askew, Mr Crooks, my dear friend Joy and Bros Pee Ogbemudia, Paulette, Carol and all my dearest and most wonderful brethren, the Lord is the only reward for your labours of Love. Nothing I say can express how profoundly grateful I am for all your encouragements.

To the Almighty be all the glory forever and ever Amen.

Author's Declaration

I declare that the research presented in this thesis is my own and is original. This thesis has not previously been submitted for award at or any other institution.

All sources are acknowledged as References.

Chapter 3 has been published:

“Observation of Enhanced Dissociative Photochemistry in the Non-Native Nucleobase 2-Thiouracil”

K. O. Uleanya, R. Cercola, M. Nikolova, E. Matthews, N. G. K. Wong and C. E. H. Dessent, *Molecules* 2020, **25**(14),3157

<http://dx.doi.org/10.3390/molecules25143157>

Chapter 4 has been published:

“Photodissociation Spectroscopy of Iodide Ion-Thiouracil Clusters: Mapping Chromophore Excitations on the Electron Detachment Spectrum”

K.O Uleanya and C.E. Dessent, *Phys. Chem. Chem. Phys.*, 2021, **23**, 1021-1030 (PCCP HOT ARTICLE 2021)

<http://dx.doi.org/10.1039/D0CP05920J> (Paper)

Chapter 1

Introduction to Spectroscopic Studies of Gaseous Biological and Pharmaceutical Ions

1.1 Photodissociation Spectroscopy of Gaseous Biomolecules

The study of non-covalent interactions and their involvement in the photochemical processes of biological systems are of great importance. Weak interactions contribute to the different behaviour of biological systems.¹ For example, protein folding and self-assembly into their biologically active form², the binding of DNA to form the double helical structure³, interactions in multicellular networks¹, drug target interactions⁴ are all dependent on the non-covalent interactions between their different components. The use of photochemical processes by biological systems is evident in photosynthesis, which is dependent on the absorption properties of pigments like chlorophyll, carotenoids, and phycobilins.⁵ Vision, which occurs as a result of photoisomerism of retina in photoreceptor cells, is dependent on carotenoid-protein complexes.^{5,6} However, non-physiological photochemical processes can damage and destroy biological systems. An example is the absorption of ultraviolet (UV) light by the DNA nucleobases which can result in permanent damage to it.⁷ Photosensitized drugs and photo-radiation therapy are used in the treatment of disease conditions like cancer to decrease the complications encountered with whole body drug treatment.^{8,9}

Studies of isolated molecular systems in the gas phase are valuable, as they allow for the interrogation of a system without the interference of bulk-phase issues such as solvation effects. This provides a conducive environment for understanding the basic photochemistry of biologically important molecules. Studies on ionic systems are advantageous as mass selection can be employed, allowing the specific ion of interest to be identified. Although there are differences between the behaviour of gaseous and solution-phase molecules,^{10,11} much photochemical information can be obtained in the gas phase experiment. The absence of solvents makes gaseous environment

calculations easy, thus complex quantum calculations can be employed in the gas phase.

Spectroscopic studies of gaseous molecules can be done using different spectroscopic techniques to obtain the electronic absorption spectra. The choice of technique is determined by the charge state of the gaseous molecules being studied. The electronic structure of gaseous anions can be probed using photoelectron spectroscopy,¹² while electronic absorption spectra of neutral molecules and clusters can be obtained using ionization techniques like zero kinetic energy (ZEKE) spectroscopy and resonance-enhanced multiphoton ionisation (REMPI) spectroscopy.^{13,14} Ion photodissociation spectroscopy on the other hand is used to study gaseous cations and anions.¹⁵ These techniques do not measure the reduction in the laser intensity as it passes through the gaseous molecules or cluster. They track the intensity of the photofragment or photoelectron produced during an electronic excitation, via action spectroscopy.¹⁵

The use of laser photodissociation (PD) spectroscopy has been a powerful spectrometric tool for the study of the physical properties of gaseous ions since the late 1960's,¹⁶ thus the whole thesis will try to ascertain the structures and photochemistry of different native and non-native biological molecules and clusters in the gas-phase using a modified commercial quadrupole ion trap (QLT) mass spectrometer with focus on the electronic PD spectroscopy performed using UV and visible light sources.

1.2 Photodissociation Spectroscopy Overview

Since the first measurement of the photo detachment energies of hydroxide anions with an ICR spectrometer in 1969 by Brauman and Smyth,¹⁶ photodissociation (PD) spectroscopy has become a standard tool to explore the excited-state dynamics of gaseous ions,¹⁷ electronic absorption spectra,¹⁸ geometric structures,¹⁰ vibrational modes,¹⁹ and photofragmentation mechanisms.²⁰ PD spectroscopy involves the fragmentation of gaseous, isolated molecules through electron detachment or resonance excitation using adjustable lasers due to characteristics such as monochromatic light, collimation and power.²¹ The wide spread use of PD spectroscopy is demonstrated in its application in the studies ranging from small molecular ions (diatomic ions) to large molecular ions (proteins)^{16,22-24}. Information on the photochemistry and thermochemistry of these ions is acquired from their

fragmentation patterns.^{25,26} Other molecular species such as protonated or deprotonated organic molecules ($[X+H]^+$ or $[X-H]^-$),^{27,28} charged metal complexes ($[XLx]^{m-}$ nor $[XLx]^{m+}$),^{29,30} charged clusters ($Y \cdot Z^+$ or $Y \cdot Z^-$),^{20,31} and organic molecular ions (X^+ or X)³² etc are also studied using PD spectroscopy.

In many current PD spectroscopy experiments, the ions studied are generated in the mass spectrometer by electrospray. The generated gaseous ions are guided and trapped into an ion trap or storage ring. To certify the purity of trapped gaseous ions, they are mass isolated per charge ratio using quadrupole mass filters and resonant ejection methods. Packets of the isolated gaseous ion of $\sim 10^3$ - 10^6 molecules are explored by irradiating them with a monochromatic laser to induce photofragmentation on some of the trapped gaseous ions. The laser on and laser off mass spectra are recorded, ionic peaks seen only during the laser on window are regarded as the photofragments. The two major pathways to produce photofragments are electron detachment (for anions) and ionic fragmentation (Equations 1 and 2). The photofragments are identified from their mass-to-charge ratio.



The intramolecular dissociation mechanism is portrayed as a function of the wavelength, and the absorption coefficients are calculated from the intensities of depletion or photofragments production.^{16,33}

PD experiments in the gas phase supply additional information that is absent in the solution phase spectroscopy. Due to the absence of solvation effects, which results in the stabilization of both ground and excited-state orbitals, gas-phase studies simplify the interpretation and understanding of the photochemistry of isolated molecules. The PD experiment in the gas phase provides information on isolated molecules with spectral ambiguity and is therefore of great advantage. The unique characteristic of mass isolation also promotes understanding on the photophysics of various ionic clusters, which on the contrary may not be observed in solutions because the presence of varieties of different solvation and conformation motifs, therefore resulting in the production of a broad absorption profile³⁴. Mass isolation employed in the characterization of intact proteins produced from one ion source using liquid chromatography (LC) – ultraviolet photodissociation (UVPD) mass

spectrometry led to the identification of 46 peculiar sequences following fragmentation.³⁵

PD spectroscopic methods are common techniques employed in vibrational and electronic PD spectroscopic studies of gaseous ions. Electronic and vibrational PD spectroscopy share similar experimental techniques except for the difference in the tunable laser used in the dissociation of the ions. Although this thesis concentrates on electronic PD spectroscopy, it is important to briefly discuss vibrational PD spectroscopy because it can initiate the fragmentation of gaseous ions.³⁶ Tunable infrared (IR) lasers used in vibrational PD produce lower energy photons compared to the UV, thus multiple photons are required to effect dissociation. The technique of using multiple IR photon to initiate the fragmentation of gaseous ion is called infrared multiphoton dissociation (IRMPD) and has been employed in the study of many biologically important ions or clusters.³⁷⁻⁴⁰ Vibrational spectroscopy is of great importance because it is well known for identification of geometric structures especially when the structure of the ion present in solution phase is unknown, and for differentiating conformational and structural isomers.³⁸⁻⁴⁰

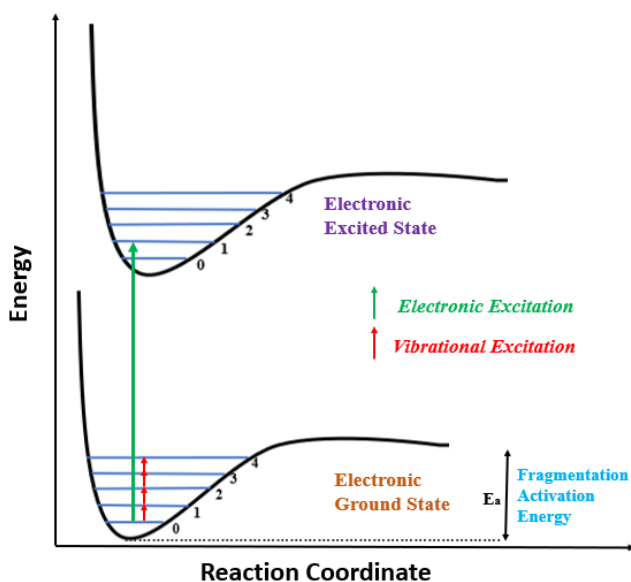


Figure 1.1 Schematic diagram for the potential energy profile of a gaseous molecule

representing electronic and vibrational excitation. The arrows define the magnitude of the different excitation energies.

Electronic PD spectroscopy is done using UV and visible light sources from tunable lasers, with single photon absorption typically leading to dissociation in the UV. The difference in the electronic and vibrational excitation energy of a gaseous specie is represented with a schematic diagram in Figure 1.1. Absorption spectra acquired from UV and visible photodissociation spectroscopy (UVPD) experiments can represent the absorption spectrum of the gaseous ion, if only one photon is absorbed, and no radiative relaxation pathways occur. UVPD experiments are performed on the ions and clusters discussed in this thesis, and the method is described in full in Chapter 2.

1.3 Ionization Sources in PD Spectroscopy

PD spectroscopy is conducted in a mass spectrometer, so that the range of systems studied is dependent on the ionization source used for the introduction of the ions into the mass spectrometer. Modifications and technological advancements in mass spectrometry to widen the range of molecules studied using this technique has also favoured PD spectroscopy, as numerous fragile biological molecules and clusters can now be studied.^{16,23} Hard ionization techniques, e.g. electron ionization (EI), which encourages optimal fragmentation of the sample ions is not suitable for generating ions of large biological molecules and clusters in the gas phase. This causes a significant limitation to PD spectroscopic studies of such molecules. In an earlier application of PD spectroscopic experiments, Brauman^{16,41} and Dunbar²³ generated gaseous ions using EI. Soft ionization sources e.g. Electrospray ionization (ESI) that is compatible with the production of fragile biomolecular and cluster ions was developed in the 1980's by Fenn.⁴² ESI is a soft ionization technique that involves preparing a solution of the compound of interest in a compatible ESI solvent (i.e. a polar solvent such as methanol, acetonitrile and water) and introducing the solution into the mass spectrometer. The prepared solution is passed through a charged needle into a nitrogen nebulising gas to generate gaseous ions which are subsequently trapped and analysed with minimal fragmentation.^{42,43} ESI is a suitable ionization source for producing gaseous ions of large biological molecules and clusters because its minimal fragmentation preserves the bonds within the molecules

or clusters from the solution phase to the gas phase.^{34,44} ESI has been widely used in current PD experiments because of its ability to generate varieties of ionic species for gas phase experiments.⁴⁵⁻⁵⁰ It is used in analytical studies of large polymeric biological molecules,⁵¹⁻⁵² and can produce ions clustered to solvent molecules by seeding the nitrogen nebulizing gas with the solvent of interest.⁵³

1.4 Other Gas-Phase Experiments

Experimental techniques employed in the interrogation of gas phase species are dependent on the nature of the system being explored. Electronic absorption spectra of gaseous ions are only widely obtained using UV PD spectroscopy, while other spectroscopic methods used to probe gaseous species include IRMPD, resonance enhanced multiphoton ionisation (REMPI) spectroscopy and photoelectron spectroscopy (PES). Mass spectrometric techniques, collision induced dissociation (CID) and ion mobility spectrometry (IMS) and other UV and IR analytical photodissociation methods can also be used to probe the structures of gaseous species.

1.4.1 Infrared Multiphoton Dissociation (IRMPD)

IRMPD, as briefly discussed earlier, is a type of PD experiment where gaseous ions are interrogated with multiple photons from IR tunable lasers to induce photofragmentation. Photofragmentation is caused by the resonance excitation of the vibrational modes in the gaseous ions, therefore making it highly dependent on structure and showing the molecular characteristic functional groups. IRMPD spectroscopy of ions in the gas phase has been widely studied for biomolecular and cluster ions in recent years.⁵⁴⁻⁵⁷ This method has been employed by several research groups in the study of the structure of magic clusters and has aided the understanding of their homochiral advantage and structures⁵⁸⁻⁶⁶. Johnson et al performed IR experiments on carboxylate-(H₂)_n clusters and acquired a vibrational high resolution absorption spectra of a cryogenically cooled 12-carbon dicarboxylate, due to the tagged molecule dissociation. The experiment was done by disintegrating the weakly bound clusters formed in a cold buffer gas, and it produced the gaseous clusters in a customized instrument at cryogenic temperatures. The result showed the existence of only one conformer.⁶⁷ Another application of IRMPD spectroscopy in the gas phase is in the study of metallated lumiflavin clusters (M⁺•LF) where M = (alkali = Li, Na, K, Cs and coinage = Cu, Ag) to probe the best binding sites for different

metals depending on their sizes.⁵⁵ Simulated vibrational absorption spectra acquired from quantum chemical calculations for the conformers of the different metal-lumiflavin clusters were used in assigning the gaseous structures for the experimentally recorded vibrational absorption spectra of the clusters.

1.4.2 Resonance Enhanced Multiphoton Ionisation (REMPI)

Resonance enhanced multiphoton ionization (REMPI) is a selective, sensitive and easy technique for detecting neutral gas-phase species and interrogating of atomic and molecular products generated from PD or crossed-beam experiments in the gas phase.⁶⁸⁻⁷¹ In a REMPI experiment, photoelectrons or molecular ions are produced from a supersonically expanded molecular beam overlapped with one or multiple lasers in a vacuum chamber.

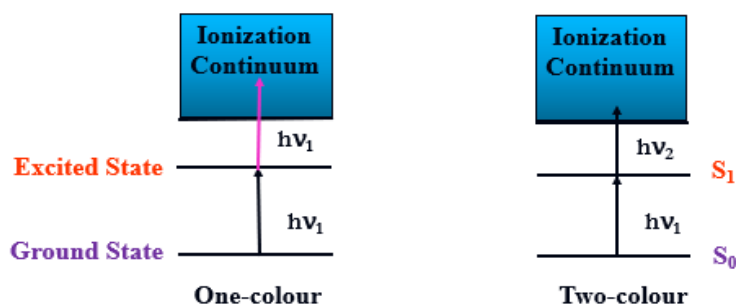


Figure 1.2 Schematic diagram for the ionization technique involved in one and two-colour REMPI experiments.

The effectiveness of supersonic expansion cooling of the neutral species supports high resolution spectroscopy experiments, and the generated photo ionic species can be detected. Nucleobase and base pairs were studied using REMPI spectroscopy by De Vries et al.⁷² Vibronic absorption spectra in the gas phase of the isolated molecules were acquired, and hole-burning spectroscopy was employed to separate the different tautomeric species present in the gas phase.⁷² Supersonic expansion cooling in the molecular beam made it possible for the hydrogen bonded nucleobase pair to be transferred to the gas phase, although for molecules to be introduced into the gas phase in a molecular beam, they require high vapour pressure because of heating. Due to this limitation, fewer biomolecules have been studied using Supersonic expansion cooling method compared to ESI source gas-phase

experiments which allows many biological molecules to be studied because of its soft ionization technique. Laser desorption provides an alternative method for forming gaseous species with low vapour pressure.

1.4.3 Photoelectron Spectroscopy (PES)

Photoelectron spectroscopy (PES) uses photoionization and subsequent energy measurement of the electrons emitted to determine the electronic structures of molecules, solids, and surfaces. It is also used in determining the electronic state of the surface region of solid samples.⁷³⁻⁷⁶ PES has been employed in exploring the photostability of nucleobases by investigating their photodynamic characteristics. The experimental techniques used for PES experiments can share some features with PD experiments, for example, ion sources. Verlet and co-workers used ESI and time-resolved photoelectron imaging (TRPEI) using ultrafast tunable lasers to investigate the photodynamic behaviours of deprotonated 2'-deoxy-adenosine-5'-monophosphate and its di- and trinucleotides. Comparison of the acquired result with the solution-phase transient-absorption spectra done by Stuhldreier et al show that the phosphate group is a spectator in the photo-relaxation pathway. Furthermore, the charge and the environment do not have any effect on the photo-relaxation dynamics in the gas phase.⁷⁷⁻⁷⁸ Verlet et al used the same approach to study the π -stacked anionic dimer and deduced that on an ultra-fast scale, the valence excited states above the electron detachment threshold experience internal conversion into a dipole-bound state.⁷⁹ PES has also been employed in investigating clusters. The electronic stability of deprotonated acids on hydrogen-bonded clustering was probed by Wang and Kass with a reduction in adiabatic detachment energy (ADE) being observed. This result was attributed to a hydrogen atom transfer rearrangement mechanism occurring upon photoionization on the neutral potential energy surface.⁸⁰

1.4.4 Collision Induced Dissociation (CID)

CID mass spectrometry has been widely used for the study of various sizes of molecular ions in the gas phase. These studies range from studying small molecular organic ions to large and complex proteins.⁸¹⁻⁸⁷ The mechanism behind energy transfer and the dissociation pathways for producing thermal fragments in CID has also been detailed over many years.⁸⁵⁻⁸⁷ In a CID experiment, the isolated gaseous ions have their kinetic energy increased by applying an electrical potential and allowing collisions with a buffer gas. The collisions cause some of the kinetic energy

of the gaseous ions to be converted to internal energy, which leads to rearrangements, bond breakage and fragmentation. A clear distinction can be made between low and higher energy collisional dissociation (HCD). Low energy CID involves low kinetic energy ions, and gentle heating through multiple very low energy ($\leq 1\text{keV}$) collisions with the buffer gas, which generally favours ion structural rearrangement and fragmentation through the pathway with the lowest activation energy. HCD involves increased ion kinetic energies to many kilovolts (1keV to 20 keV), which on collision with the buffer gas gives substantial fragmentation. HCD experiments have been used to deduce the fragmentation pathways of gaseous ions via their relative activation energies.⁸⁸⁻⁸⁹ It can also yield fragments that is not present in CID experiments.

1.4.5 Ion Mobility Spectrometry (IMS)

IMS is an analytical technique that is used in the gas phase to identify and separate gaseous ions based on their mobility under the effect of an electric field when passing through a buffer gas.⁹⁰ The method is used in the investigation of both small and large biological molecules.⁹¹ IMS instruments though of various sizes are very sensitive. They separate gaseous ions based on their sizes and shapes which determine their collision cross section. They are used in conjunction with mass spectrometry (IMS-MS), gas chromatography (IMS-GC), or high-performance liquid chromatography (IMS-HPLC). When coupled to a mass spectrometer, the IMS serves as a filter for the gaseous ions before mass spectrometric analysis of the ion is done.⁹² IMS has been used as a conformational filter for gaseous biomolecular ions produced by ESI, UVPD and IRMPD spectroscopy and with cryogenic cooling.⁹³⁻⁹⁷

1.4.4 Other Applications of photodissociation methods in Analytical Chemistry

Recent experiments have shown that the sequence and structures of large biological molecules can be conducted for analytical purposes using a photodissociation mass spectrometry technique.⁹⁴ This technique uses fixed output lasers (UV or IR) to fragment large biological ions in the gas phase. The amount of fragmentation is dependent on the power and time of exposure to the lasers.^{33,98} The degree of fragmentation of the parent ion helps provide more detailed information on the fragmentation pathways for large polymeric molecules and their secondary structures.⁹⁹⁻¹⁰² Brodbelt and co-workers have used the decay rate of the time-

domain transient signal from an orbit trap mass analyser to determine the collision cross-sections (CCSs) of protein ions. The results obtained for all charge states known to have single conformations in the gas-phase revealed that the CCSs measurement differ by $\sim 7\%$ compared to previous values published from similar study using IMS.¹⁰³

1.5 Instrumentation in PD Experiments.

Mass spectrometers used in PD experiments can be procured either commercial¹⁰⁴⁻¹⁰⁶ or custom-built.^{107,108} The two types of instruments have their pros and cons depending on the experiments of interest. Commercial mass spectrometers possess compact designs that make them reliable, robust, and easy to use by non-expert instrumentalists. They require minimal daily maintenance from the user, and for technical issues requiring manufacturers' assistance, engineers are available. The provision of commercial software aids the collection and processing of photofragment data and has added to the benefits of commercial mass spectrometers as it aids the understanding of photochemical reactions and the photodissociation pathways of gaseous ions. One of the disadvantages of these instruments is that because of their compactness there is little or no room for their modification to accommodate some experimental variations of interest. Custom-built mass spectrometers in contrast, allow modification to their components for desired PD experiments, although they are difficult to build, use and maintain. They also allow updates and upgrading of the set up to match new experimental and technological developments in the field.

1.5.1 Adapted Commercial Mass Spectrometers for UVPD

Commercial mass spectrometers which have been adapted for PD experiments have been in use for some decades. Both IRMPD and UVPD experiments have been performed using such adapted commercial mass spectrometers.

The Dugourd research group has used an ESI QIT mass spectrometer (LCQ Duo, ThermoElectron) set up to perform both analytical and PD spectroscopic analysis on small and large biomolecules.^{24,105, 109-113} Due to the importance of understanding the effect of the biological environment on the behaviour of biological molecules, they have studied protonated flavin mononucleotide and deprotonated tryptophan, and were able to acquire both CID and UVPD results using this configuration.^{109,110} The

effect of electron detachment on the stability of gaseous large biological molecular anions was also studied using this instrument set up.¹¹¹⁻¹¹³ It was deduced from the CID result obtained from electron detachment from DNA polyanion that electron detachment promotes extensive fragmentation. The set up was also used to explore protein ions and proffer desirable information on the relationship between the intrinsic properties of protein ions and their optical spectra.²⁴ Dugourd and co-workers have also used commercially adapted ion mobility mass spectrometry (IMMS) to probe the shape of the arrival time distribution signals for polylactide ions and the steps involved during a folding process in gaseous polymer ions. The results revealed the absence of folded or extended structure interconversion on the IM time scale and within the MS ions lifetime at room temperature, due to the distinct distribution observed. Also, the absence of folded and extended interconversion of the structures of the polylactide ions even on collisional activation reveal that during electrospray desolvation or ionization processes, they are frozen in their specific 3D structure.¹¹⁴

The Weinkauff group was among the first to use a modified commercial ESI quadrupole ion trap (QIT) mass spectrometer (Esquire 3000, Bruker Daltonics) for its studies.^{17,115-117} The group's earlier experiments around 2004 used the above QIT mass spectrometer coupled to an excimer-pumped ns dye laser to explore the effect of the presence of a proton on the electronic spectrum of tryptophan.¹¹⁶ The group later modified their set up by coupling the QIT with an ultrafast Ti:Sapphire laser to take time-resolved measurements of gaseous ions. This was a significant breakthrough in modified mass spectrometric experiments because of the paucity of such experiments, even within custom-built PD experiments at this time.^{109,118-120} The modified commercial ESI quadrupole ion trap (QIT) mass spectrometer coupled with an ultrafast Ti:Sapphire laser was used to explore the excited state dynamics of important biological molecules such as protonated peptide H₂N-Leu-Trp-COOH and protonated adenine.^{17,117}

The Jockush group modified an ESI-QIT mass spectrometer (Esquire 3000+, Bruker Daltonics) to enable them to conduct PD spectroscopic experiments on isolated gaseous ions.¹²¹⁻¹²⁶ This novel modified set up also allows them to keep record of fluorescence spectra. Experiments performed with this set up to characterise an ESI produced gaseous ion of rhodamine 560, generated a fluorescence spectrum that is blue shifted from the analogous solution phase spectrum.¹²¹ The recording of the

emission spectrum is made possible by the nanoscale lifetime of the fluorescence spectrometer coupled in the mass spectrometer [as the spectrometer hopefully lives longer](#). Experiments that probed variable experimental conditions such as ion-trap pressure, accumulation time etc were conducted in a straightforward way using the inbuilt software in the commercial mass spectrometer to adjust the relevant parameters.

Organometallic complexes have also been studied using modified commercial mass spectrometers by the Riehn group.^{120,127,128} This experiment is different from the traditionally known one colour PD experiments done with commercial mass spectrometers. Their experimental set up is a QIT-MS (Amazon Speed, Bruker Daltonics) mass spectrometer modified to perform pump probe spectroscopic experiments on organometallic complexes in the gas phase where the excited state lifetimes in these experiments are measured from pump-probe time-resolved measurements.^{120,127,128} Results obtained from the PD experiment to probe the ultrafast dynamics of a Ru^{II} based photocatalyst showed a metal centre to another metal centre charge transfer emanating from a metal-to-ligand charge-transfer excited state.¹²⁰

Many PD experiments have also been performed using commercial mass spectrometers interfaced with IR lasers.^{39,129-130} IRMPD experiments require absorption of multi-photons to induce fragmentation. Some groups have used a table top laser (Nd:YAG pumped OPO/OPA),¹⁰ while other research groups have used the tunable free electron laser (FEL) as a source for higher energy in IRMPD experiments. FEL was employed by the Free Electron Laser for Infrared experiments (FELIX) laboratory in their experimental set up with (Amazon Speed ETD, Bruker Daltonik) for IRMPD gaseous experiments.¹³¹⁻¹³²

Studies on the deprotonation sites of small peptides and complexation with metal ions due to many metal-ion complexation sites provided by peptides were conducted using FEL coupled in (Amazon Speed ETD, Bruker Daltonik) mass spectrometer by Oomens group. They investigated how water microsolvation can have an effect on the binding mode of the metal ions using the same type of experimental set up.¹³³⁻¹³⁴ Oomens research group also explored the reaction pathways of some important biological molecules, characterised their binding patterns, and investigated the

deamidation and dehydration reaction of protonated dipeptide using also the same experimental set up in recent time.^{37,135}

The Brodbelt group modified a Fusion Lumos Orbitrap mass spectrometer (Thermo Scientific Instruments, San Jose, CA) with 193 nm Coherent Existar excimer laser (Santa Cruz, CA) to perform UVPD experiments in the high-pressure linear ion trap.^{136,137} The ability of this method to determine subtle structural differences was confirmed with studies on the detailed structural characterization of intact rough-type lipopolysaccharides (R-LPS), where the results revealed successful discernment of E.coli R-LPS structures with isomeric core structures.¹³⁶ The group also explored extensively the characterization and identification of human proteins and proteoforms whilst comparing UVPD and HCD in the characterization of overlapping proteoforms. The results revealed that UVPD and HCD are complementary for the characterization of proteoform and extensive protein profiling.¹³⁷

IRMPD experiment have been conducted on protonated tryptophan gaseous ions trapped in the Penning trap of a Fourier transform ion cyclotron resonance (FTICR) (4.7 T Bruker FTICR) instrument and a custom-built Paul trap irradiated with a tunable OPO laser (Linus Photonics, Munich, Germany) by Polfer and co-workers.^{36,138} The result showed enhanced IRMPD yield in the Paul trap than in the Penning trap IRMPD spectrum. This is attributed to minimal subsection of the ion cloud to photon flux due to the shape of the ion cloud, which compromises the overlap between the ion cloud and the laser focus. A multiple pass approach of the photon flux is suggested to improve this limitation. The ICR cell of the FTICR at the FELIX facility has polished electrodes to encourage multi-pass exposure of the ion cloud to the photo flux.^{36,138}

1.5.2 Custom-built UV Photodissociation Mass Spectrometers

High-resolution spectroscopy experiments are best performed in instruments coupled with custom-built mass spectrometers specifically designed for PD spectroscopic experiments. Although cooling of gaseous ions promotes high-spectral resolution in PD experiments, not all custom-built experiments are done with cryogenically cooled ion traps. Nielsen and co-workers have performed custom-built experiments which do not include ion cooling to study charged fluorescent dyes to

determine the shift in their absorption spectra going from the solution to the gaseous phase.¹³⁹ They have also studied the influence of single water molecules on the electronic absorption spectra of ortho and para nitrophenolates, and probed if the spectral shift is red or blue.¹⁴⁰ Custom-built experiments have been used to study and acquire electronic absorption spectra for both organic and inorganic gaseous ions.^{49, 139-141}

Electronic spectroscopy of cryogenically cooled gaseous ion trapped in a Paul ion trap was performed on organic and organometallic ions to obtain high resolution absorption spectra and ascertain the gas phase structures of these molecules by Jouvét and co-workers. Their results provided reliable vertical transition energies and were supported with theoretical calculations.¹⁴²⁻¹⁴⁴ Wester's research group performed a UVPD experiment on cooled hydroxide ions trapped in a linear ion trap (LIT) and obtained a high-resolution absorption spectrum which showed the onset of electron detachment as the photon energy increases from the rotational states. The population of the ions at different rotational states was used to calculate the internal temperature of the ions.¹⁴⁵

Some home-built instruments have been designed to perform experiments with multiple lasers. High resolution UV-IR double resonance absorption spectra of some biologically relevant molecules have been obtained in PD experiments by Zwiér and Rizzo research groups.¹⁴⁶⁻¹⁴⁹ Zwiér and co-workers performed UV-photofragmentation spectroscopy and IR spectroscopy on cold gaseous ions of two prototypical guaiacyl complexed with metal ions. The double resonance spectroscopic results were used to determine the structural changes because of the complexation and also characterise the favourable binding sites for the metal cations.¹⁴⁷ Rizzo and co-workers used IR-UV hole-filling spectroscopy to study conformational isomerisation of a helical peptide.¹⁴⁸ After sufficient cooling of the trapped ions, UVPD was used to determine the individual conformer while the IR induced spectroscopy is used to identify the population of the four stable conformers. The high-resolution UVPD absorption spectrum of the helical peptide showed four separate well-resolved conformational isomer absorption bands.

1.6 Thesis Overview

The work discussed in this thesis was conducted in a laser interfaced commercial mass spectrometer (LIMS). UVPD experiments were performed on some gaseous biological relevant ions and clusters with an Nd:YAG pumped OPO laser coupled to an ESI quadrupole ion trap mass spectrometer over a wide scanning range of 213 to 600 nm. The experimental set up allows photofragmentation and photodepletion spectra to be acquired.

Chapter 2 describes the experimental protocol and the instrumental design used to perform both PD and thermal dissociation experiments. There is also a description of the computational calculation methods employed to help in the interpretation of the acquired data.

Chapter 3 describes the PD experiment to explore the intrinsic gas-phase photochemistry of 2-thiouracil (2-TU) with the aim of characterising the effect of protonation and deprotonation on the excited states and photoproducts of 2-TU by studying the isolated deprotonated ($[2\text{-TU-H}]^-$) and protonated ($[2\text{-TU-H}]^+$) ions. The photofragmentation pathways of the protonated and deprotonated ions are highly distinctive, with the deprotonated system producing just a few, very low intensity photofragments while the protonated system produces extensive photofragments.

Chapter 4 presents a study of the complexes of iodide with the non-native nucleobases, 2-thiouracil (2-TU), 4-thiouracil (4-TU) and 2,4-thiouracil (2,4-TU) to investigate the modifications on the excited state behaviour of a non-native nucleobase due to the presence of one or more sulphur atoms. The experiments allow the electron capture properties of these novel molecules to be probed. In chapter 5 we extended this type of study to very large biological molecule riboflavin (RF). The electronic PD study of I·RF cluster showed photophysical and photochemical behaviour that mirrors those of the iodide-thiouracil earlier studied in Chapter 4. The results obtained were therefore discussed in a similar arrangement.

Chapter 6 reports the PD spectroscopic experimental studies on the complexes of iron (III) metalloporphyrin (FeTPP^+) and N aromatic molecules (pyridine, quinoline and iso-quinoline) in the gas-phase to explore the effect of complexation on the photochemistry and spectroscopy compared with the uncomplexed free MP.

Chapter 2

Photodissociation Methods and Theory

2.1 Laser coupled - Mass Spectrometry Instrument Overview

The instrument used to acquire the data presented in this thesis is a modified Bruker AmaZon electrospray ionisation quadrupole ion-trap (ESI-QIT) mass spectrometer coupled to a 10 Hz Nd:YAG (Surelite, Continuum) pumped OPO (Horizon 1, Continuum) which can selectively produce wavelengths ranging between 193–2700 nm (6.42 – 0.46 eV). Figure 2.1 shows a simplified diagram of the experimental hardware set-up. The mass spectrometer has been modified by drilling two holes into the ring electrode thereby allowing the pulsed laser to pass through the ion trap which results in the dissociation of the ions. The laser beam is channelled by the optical guide into the mass spectrometer and a 200 mm plano-convex lens is used to focus the beam through the ion trap. The transmission of the laser beam into the mass spectrometer is controlled by a beam shutter (Model SH05, Thorlabs Inc.).

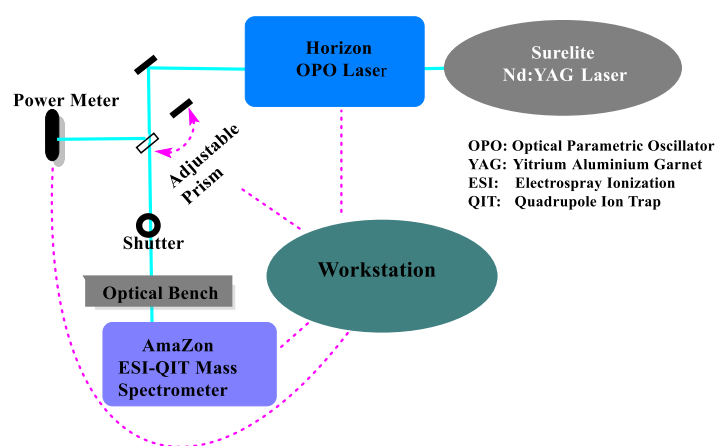


Figure 2.1 The schematic diagram of laser the coupled-mass spectrometry experiment.

A motorised flip mount (Model MFF001, Thorlabs Inc.) with a prism mounted on it is used to selectively direct the laser beam to the power meter (Power Detector UP19K-15S-VR, Monitor is a Gentec-EO Tuner) which takes a measurement of the power of the laser entering the ion trap. A workstation is used to control and monitor every part of the experimental setup thus allowing for the automation of the experimental process. The details of the different parts of the experimental setup are discussed below.

2.2 The Laser-Coupled Bruker AmaZon Mass Spectrometer

2.2.1 The Modified Bruker AmaZon Mass Spectrometer

The Bruker AmaZon mass spectrometer is a quadrupole ion trap (QIT) mass spectrometer with a nebulizer assisted electrospray ionisation (ESI) ion source and the source for generating the gaseous ions studied in the entire thesis. The QIT part of the mass spectrometer operates at a pressure 10^{-6} mbar which is $\sim 10^9$ less than the pressure required in the ESI region which requires atmospheric conditions.

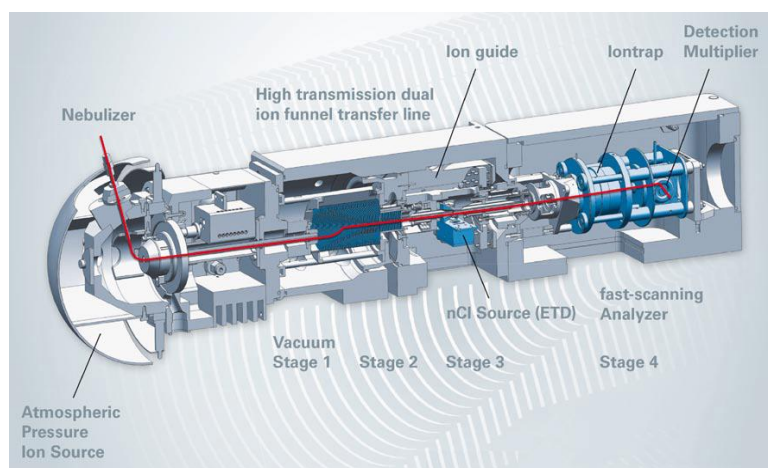


Figure 2.2 Diagram of the Bruker Daltonik AmaZon mass spectrometer. Image adapted from the AmaZon manual. Ref. 150

The ion trap can be used for tandem mass spectrometry experiments through helium buffer gas collision-induced dissociation of the trapped ions. The ESI source operates

under atmospheric conditions, whereas the QIT region of the mass spectrometer has an operational pressure in the region of 10^{-6} mbar. To achieve the $\sim 10^9$ decrease in pressure, four differentially pumped (rough and turbo pumps) vacuum stages are used in the mass spectrometer. The gaseous ions produced are guided by an electric field from the ESI source through an inlet capillary, which is heated to help the process of desolvation from the spray chamber to the vacuum system. The flow of heated drying gas around the entrance of the inlet capillary also aids the desolvation process. In the vacuum chamber, the ions are directed by an ion funnel, two multipole ion guides and two ion lenses to the QIT where the ions are collected, stored, mass isolated, fragmented and mass analysed. For collision-induced dissociation (CID) experiments, the trapped ions are collided with the helium gas, while in photodissociation experiments, the stored ions are probed with the laser. When the internal energy of the ions is increased sufficiently to induce dissociation, the ions are sequentially ejected from the QIT according to their mass-to-charge ratio, and detected by a Daly conversion detector, which is a dynode-based system. [The Daly detector is advantageous in this type of measurement because it reduces noise due to ion feedback.](#)

The workstation is used to control the amaZon mass spectrometer using the (trapControl version 7.2, Bruker Daltonik) commercial software. The TrapControl software is used to manage the conditions of the ionization settings (e.g. drying gas flow rate, the nebulizing gas pressure, the drying gas temperature and the voltage applied to the ESI needle), the voltages of the ion optics (multipole, ion funnel and lens voltages) and the trap conditions of the gaseous ions studied (eg. Amplitude, the mass isolation, fragmentation time and ion accumulation time). The trap control can be used to record and store mass spectra acquired over a controlled period of time during the laser experiments.

Further details on the principles governing the operations of the ESI, QIT and the mass spectrometry modifications to allow laser experiments will be explained in the subsequent sections.

2.2.2 Electrospray ionisation

The use of ESI as the source to produce gaseous ions in mass spectrometry is well established.^{6,10-15,35} The processes of electro spraying undergone by samples in the

spray chamber can be divided into the formation of the charged droplets, nebulisation, desolvation and ion evaporation. Figure 2.3 shows the main features of ESI.

The solution containing the analyte is put into a syringe and injected through a capillary at a set flow rate using a syringe driver, with the potential difference between the needle and the spray cap maintained at 2-6kV. The solution is transported to the charged needle where ions of similar charge are attracted to the charged needle while ions of opposite charges are repelled thus increasing the concentration of the repelled ions in the solution as it passes through the needle. Under the influence of the electrostatic field, the ejected solution at the tip of the needle is distorted, forming a Taylor cone.¹⁵¹ Coulombic repulsions within ions of similar polarity and the effect of the nitrogen nebulizing gas assist the ejected solution to break apart into small droplets and start evaporating.

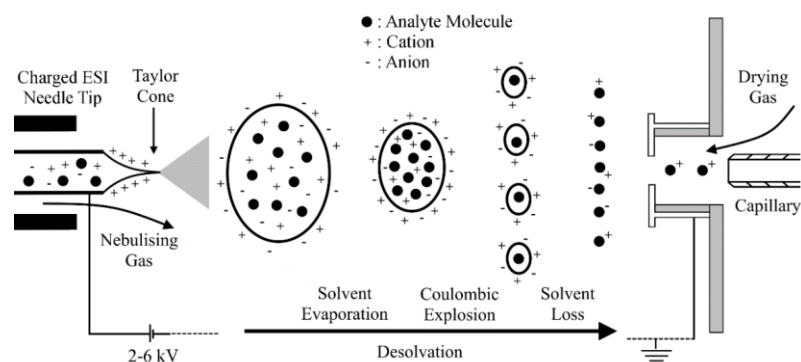


Figure 2.3 Diagram of an electrospray ionisation (ESI) source. Positive and negative charges are included in the droplets to show that ESI can be used to produce gaseous cations or anions.¹⁵²

The highly charged droplets which flow in the opposite direction to the drying gas (nitrogen) are heated up resulting in the evaporation of the solvent molecules from the droplets, therefore increasing the repulsion between the ions as they are forced closer together. The evaporation process continues until the repulsion between this ion of similar polarity becomes large enough to overcome the surface tension of the droplets (known as the “Rayleigh limit”), then coulombic explosion occurs giving

smaller droplets.¹⁵³ The process of evaporation and fission repeats until small analyte ions, assumed to be of nanometre diameters are created.^{154,155}

There are two models for the production of analyte ions which enter the quadrupole ion trap (QIT). The pathway for desolvation of analyte ions has been observed to be dependent on the analyte ion. Heavy globular species (e.g. folded proteins) are believed to enter the gas phase by the cycle of both solvent evaporation and coulombic explosion, until a droplet containing only a single ion evaporates. The solvent then leaves only the bare ion, which is known as the “charge residue model” (CRM).^{156,157} Low-mass analyte ions are believed to be transferred to the gas phase according to the ion evaporation model (IEM), which involves the droplets getting smaller with increased charge density until the repulsion becomes large enough to fully eject an ion from the droplet.^{158,159} The pathway and mechanisms for the effective production of analyte ions in the electrospray process are discussed widely in the literature.^{154,160-162} The molecular and cluster ions studied within this thesis are all $< 2000m/z$ -mass ions and clusters and thus are likely to be isolated by the IEM.

2.2.3 Ion Optics

The gas-phase ions can only be detected when they pass from the region of the atmospheric pressure ionisation chamber to a low-pressure ion trap region of the instrument. The use of a set of ion optics to transfer the ions between the different pumping regions helps this to be achieved. The ions will enter an octupole, which will direct them through a vacuum partition and into a second octupole. This octupole then directs the ions through a pair of electrostatic lenses, which focus the ions into the quadrupole ion trap.

2.2.4 Quadrupole Ion Trap (QIT)

The Paul and Steinwedel designed quadrupole ion trap (QIT) is a $\sim 1 \text{ cm}^3$ 3D mass analyser.¹⁶³ A schematic diagram of a QIT is shown in Figure 2.4, illustrating where the ions can be accumulated, selected, excited (*via* CID) and then ejected according to their mass-to-charge ratio. The trap consists of two end-cap electrodes (**1** and **3**) which are located on either side of a ring electrode (**2**) thus giving an internal surface

that has a profile which is almost hyperbolic. The end cap electrode (1) creates an inlet for the ions which are stored between the electrodes (4).

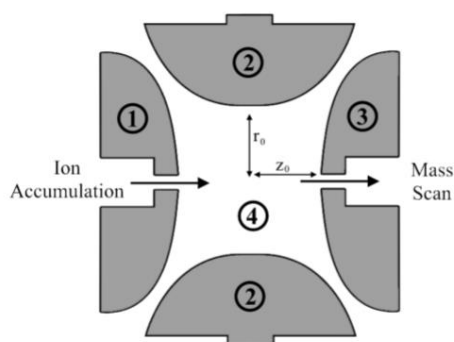


Figure 2.4 Diagram of a quadrupole ion trap (QIT) mass spectrometer, adapted from the AmaZon Manual.¹⁵⁰ 1 is the entrance end cap, 2 is the ring electrode, 3 is the exit end cap, and 4 is the ion cloud and buffer gas.

The incoming ions, though with very high kinetic energy, can be trapped because there is a continuous leak of helium gas into the trap, which acts as a buffer to the incoming ions. Collision of the ions with the helium atoms results in a reduction in the kinetic energy of the incoming ions, thus the ions can be trapped.

Ions that enter the (QIT) are made to operate under the influence of electric field created by the trapping positive potential(Φ_0) applied to the ring electrode in two ways, a constant direct potential, and an alternating potential. The movement of ions in the trap is dependent on these two potentials and on the mass-to-charge ratio of the trapped ion.¹⁶⁴ A negative potential is applied to the two end electrodes. The potential around the ring electrode is generated by high voltage while the end caps are maintained at oscillating alternating radio frequency voltage. The switching between positive and negative polarities for the applied voltage is in the radio frequency range. The influence of the electric field in the trap causes the charged ions to move towards the centre and edges of the trap in axial and radial directions. Due to the inhomogeneity of the field, a small average force is not cancelled for a while in the centre of the trap thus resulting in the formation of a pseudo-potential well which enables the storage of ions.¹⁶⁵ The presence of the helium buffer gas also aids the effective storage of the ions. The trajectories of these

trapped ions are best described by integrating their equations of motion in the form of the Mathieu equation, which has defined terms.^{166,167}

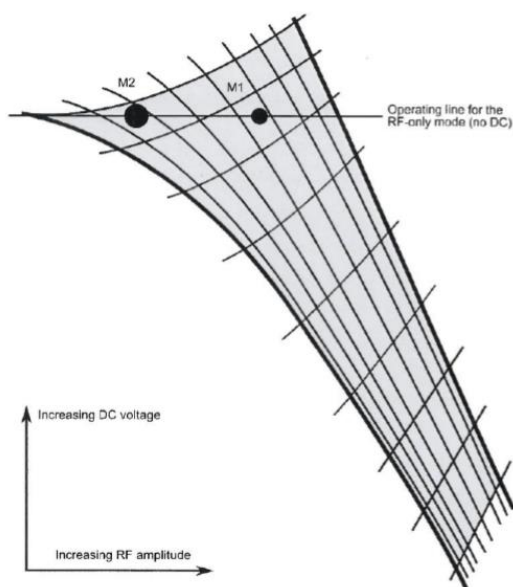


Figure 2.5 Stability diagram for ions in a quadrupole ion trap. Image taken from the Amazon Manual.¹⁵⁰

The stable trajectory of an ion with a particular m/z is obtained from the range of voltages (direct and alternate potential) taken from calculated ion trajectories.¹⁶⁸ This stability is defined as a trajectory where the ion position in the trap is not axial or radial at a point which exceeds the distance between the centre of the trap and the electrodes (r_0 and z_0 in Figure 2.4). Figure 2.5 shows a diagram of a typical example of the stability of ions in the QIT. Direct and alternating potentials with values that lie within M1 and M2 (an area of acceptable alternating voltages without any form of interjection from the direct potential) for an ion of a given m/z gives a stable trajectory. Thus, our QIT functions only with alternating voltages. The values of the alternating potential that generates a stable trajectory varies with changes in m/z . The highest voltage is inversely proportional to the m/z of the trapped ion. Therefore there is an m/z range where the QIT cannot trap stably, and this is known as “low-mass cut-off”.

Mass spectral acquisition during the experimental sequence in the QIT follows repeating steps, where each individual step is controlled using the trapControl software: in particular, Clear Trap, accumulate, and mass analyse.

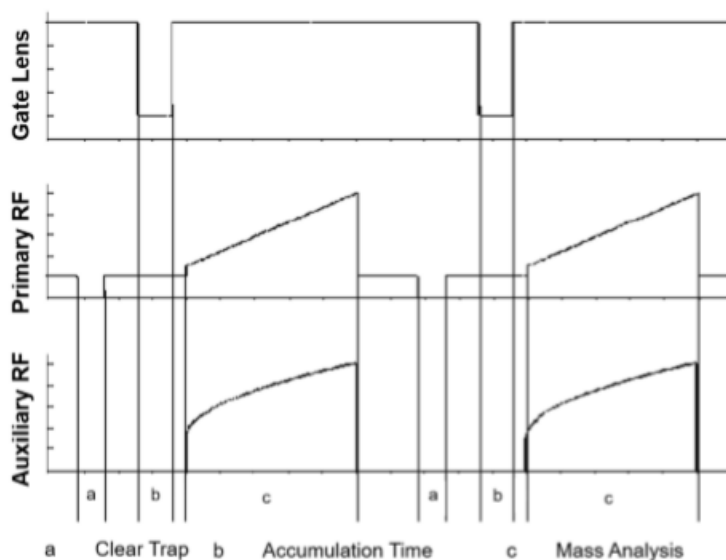


Figure 2.6 Major scan segments for an MS scan, adapted from the AmaZon manual.¹⁵⁰

Clear trap is the point when there are no ions in the trap. It is a step where the quadrupolar field is brought down to zero and thus empties the trap between two acquisitions. A blocking voltage is applied on the ion gate and the drop in voltage allows the flow of ions into the trap thus the accumulation starts. The accumulation time can be varied and the number of ions entering the trap monitored using the trapControl. A voltage is applied to the ion gate at the end of this segment, and the ions are cooled by their collisions with the buffer gas.

The isolation stage involves the excitation of the frequencies of the ions by applying a broadband alternating potential field to the QIT, thus causing the trajectories to be unstable. This alternating potential field possesses a narrow window which makes it possible for the frequency of a selected ion with m/z ratio not to be excited. These ions remain in the QIT.

Fragmentation of ions in the QIT is induced by applying a narrowband alternating potential field to the isolated ions to increase their kinetic energy, while maintaining

a stable trajectory. The collision of these ions with the buffer gas will result in the conversion of their kinetic energy to internal energy. At a point where the internal energy of these ions overcomes the activation energy of the reaction, fragmentation and rearrangement occurs, a process known as “collision-induced dissociation”.^{85,169}

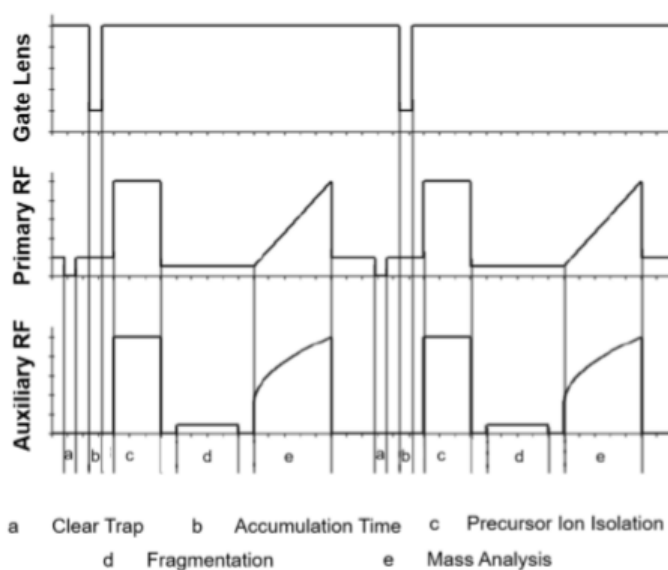


Figure 2.7 Major scan segments for an MS(n) scan, adapted from the AmaZon manual.¹⁵⁰

The amplitude of the alternating potential voltage and fragmentation time are controlled using the trapControl software. Fragments from parent ions can further be isolated and fragmented; this can be allowed up to 10 cycles by the trapControl software.

Ions present in the QIT are ejected according to their m/z ratio in a sequential manner and in fragmentation by gently increasing the amplitude of the alternating potential voltage.

2.2.5 Modifications to the Bruker AmaZon Quadrupole Ion Trap

All photodissociation experiments described in this thesis were done using the amaZon mass spectrometer modified to allow laser excitation of ions in the QIT. A

diagram of the laser-coupled QIT of the mass spectrometer displaying all the modifications made to the instrument is shown in Figure 2.8

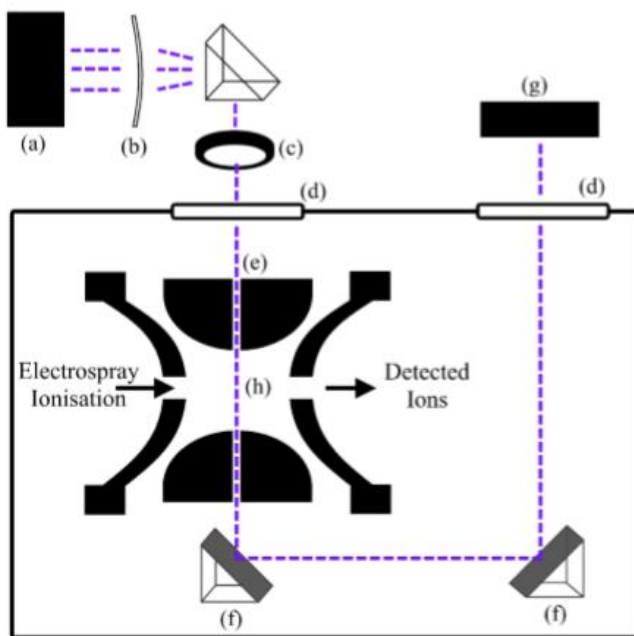


Figure 2.8 Labelled diagram of the modifications made to the QIT mass spectrometer to allow photodissociation experiments. (a) is a Nd:YAG pumped OPO tunable laser source; (b) is a 200 mm focal length UVFS lens (LE4467-UV, Thorlabs Inc.); (c) is an optical shutter (Model SH05, Thorlabs Inc.); (d) is a pair of flange mounted uncoated UVFS windows (WG41050, Thorlabs Inc.); (e) is a 2 mm hole drilled through the ring electrode of the ion trap to allow the passage of laser light; (f) is a pair of aluminium mirrors (PF05-03-F01, Thorlabs Inc.); (g) is a UV-Vis spectrometer (USB2000+ UV-VIS, Ocean Optics Inc); and (h) is the centre of the ion trap where photodissociation occurs. Image adapted from Ref. 20.

Two uncoated 5mm UV fused silica windows (d) are in the upper flange of the mass spectrometer. These windows are transparent to UV and visible light, thus a laser beam passes in and out of the vacuum chamber through them. Two holes are made into the upper vacuum flange of the mass spectrometer to fit a KF-16 centering ring, to accommodate the two uncoated UV fused silica (UVFS) windows. An O-ring is attached to the centering ring, which is designed to extend only downwards, which

allows the UVFS to be fitted on the O-ring. To maintain a suitable environment for our experiments, air is prevented from entering the high-vacuum chamber of the mass spectrometer through the seal that connects the UVFS windows, the vacuum flange, and the O-ring. QIT(e) is positioned directly under the first window and a hole drilled into it through the ring electrode to allow the laser to enter the trap. The drilled hole measures 6mm at the edge of the ring electrode and 2mm further into the centre of the QIT to reduce the loss of helium buffer gas from the trap.

Two 6mm aluminium mirrors are used to assist the alignment of the laser through the QIT. The QIT is positioned above the first aluminium mirror (f) which reflects across the range of 220nm-20 μ m. It reflects the laser to the second aluminium mirror (f), whose function is to reflect the laser beam out of the vacuum chamber through the second UVFS window.

To coordinate the operation of the laser beam between the OPO laser and the mass spectrometer, an optical bread board is fitted on top of the mass spectrometer to secure optical mounts that guide the laser beam.

2.3 Nd:YAG Pumped OPO laser

The laser used to produce photons in the photodissociation spectroscopy experiment is a Q-switched neodymium-doped yttrium aluminium garnet (Nd: YAG, Nd:Y₃Al₅O₁₂, Surelite, Continuum). This is used to pump the optical parametric oscillator (OPO, Horizon I, continuum).

2.3.1 Nd:YAG pump laser

The dopant present in the YAG rod is Nd³⁺ replacing circa 1% of the yttrium ions, and the lasing properties of YAG rod is dependent on it. The main transitions that occur in the laser activity are shown in figure 2.8. Flashlamps surrounding the YAG rod are used to generate light to electronically excite the Nd³⁺ ions present in the electronic ground state (⁴I_{9/2}) to (⁴F_{5/2}), which relaxes without emission into the excited state (⁴F_{3/2}). This excited state decays to another electronic state (⁴I_{11/2}) with the emission of a 1064 nm photon, before relaxing to the electronic ground state without any significant emission of radiation. Although the longest lifetime electronic excited state of Nd³⁺ is (⁴F_{3/2}), there is a condition in which most of the ions transit to a higher excited state (⁴F_{3/2}) than the lower (⁴I_{11/2}), known as

“population inversion” in the YAG rod. This is accompanied with radiative decay in this excited state, which is triggered by a photon at same energy.

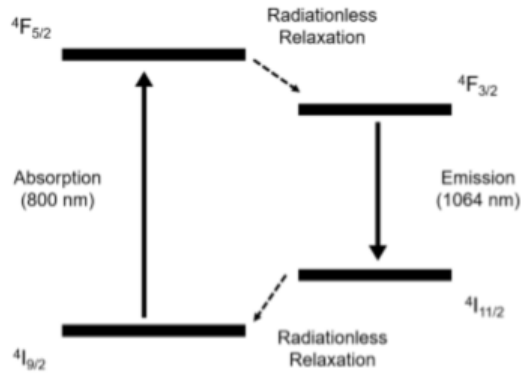


Figure 2.9 Simplified diagram of the energy levels in Nd^{3+} : Nd:YAG laser involved in the emission of 1064nm light.¹⁷⁰

This interaction forms the background for the lasing properties of the YAG rod. The YAG rod is irradiated repeatedly at a frequency of 10 Hz, thus population inversion and lasing of the YAG rod follow at the same frequency.

Figure 2.10 shows the use of the Q-switch in manipulating the laser pulses from the laser chamber.

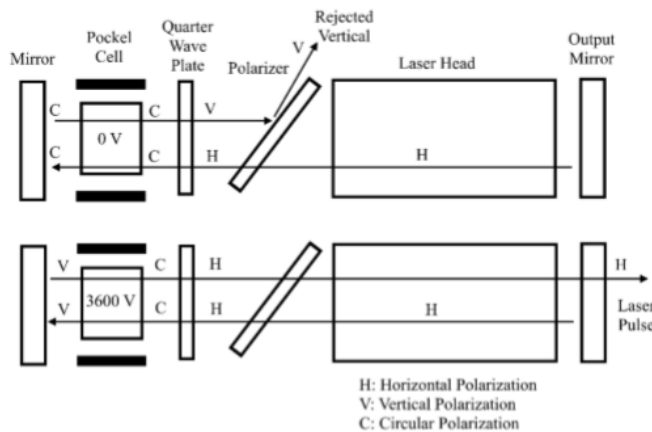


Figure 2.10 Diagram of the Q-Switch used to produce laser pulses in the Surelite Nd:YAG laser. Image adapted from the Surelite manual.¹⁷¹

The Q-switch holds the YAG rod and flash lamps that release the laser pulse, thus allowing the laser pulse only when the right voltage is applied to the Pockel cell enclosed in the laser chamber. Frequency doubling and sum frequency mixing of the fundamental and second harmonics are used to generate the second harmonics (532nm) and third harmonics (355nm) respectively from the fundamental laser output (1064 nm). The way this system operates is controlled using a manual knob that changes the direction of the crystals to support the production of the harmonic frequencies. The power of the third harmonics needed to pump the OPO is 1.8mJ.

2.3.2 Optical Parametric Oscillator (Horizon) Laser

The widely-adjustable and tunable photons used for the photodissociation experiments in this thesis is produced by an Nd:YAG pumped optical parametric oscillator (OPO) laser (Horizon, Continuum). An OPO system operation involves a single photon (the pump) being split into two low-energy photons that conserve the energy and momentum of the initial single photon. The higher energy photon of the two low-energy photons is called the “signal”, while the lower energy photon is known as the “idler”.

$$E_{\text{pump}} = E_{\text{signal}} + E_{\text{idler}} \quad \text{Equation 2.1}$$

$$K_{\text{pump}} = K_{\text{signal}} + K_{\text{idler}} \quad \text{Equation 2.2}$$

The equation above represents the conservation of energy(E) and conservation of momentum (K) by the two low-energy photons. Non-linear optics and β -barium borate (BBO, BaB_2O_4) crystals within the OPO are used in the processes of the OPO laser (Horizon). The angle the OPO axis of the BBO crystals makes with the pump beam determines the frequencies of the signal and the idler. Accurate rotation of the BBO crystals makes our laser a tunable laser source, which allows the assessing of far UV to near IR wavelengths used in our experiments.

Figure 2.11 displays the pathway of the OPO laser in producing different wavelengths. The visible wavelengths are generated by the splitting of the third harmonics of the Nd:YAG laser (355 nm) by the BBO crystals 10 and 11. A Pelin

Broca prism (16) is used to make sure that the idler and signal are emitted through the left exit port at exactly 90° of reflection.

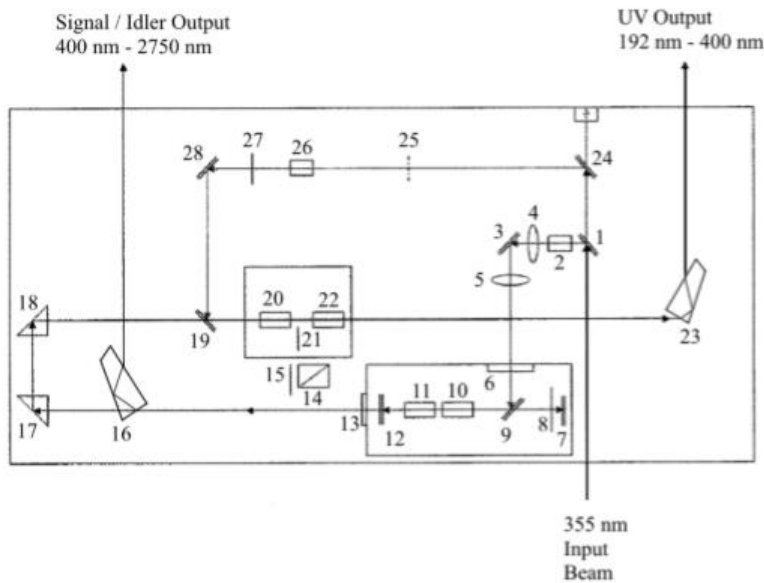


Figure 2.11 Horizon OPO optical layout displaying the pathway of the OPO laser in producing different wavelengths.¹⁷² Image adapted from Horizon manual. Components 14 and 26 are optional optics and were not part of the Horizon laser used in this thesis.

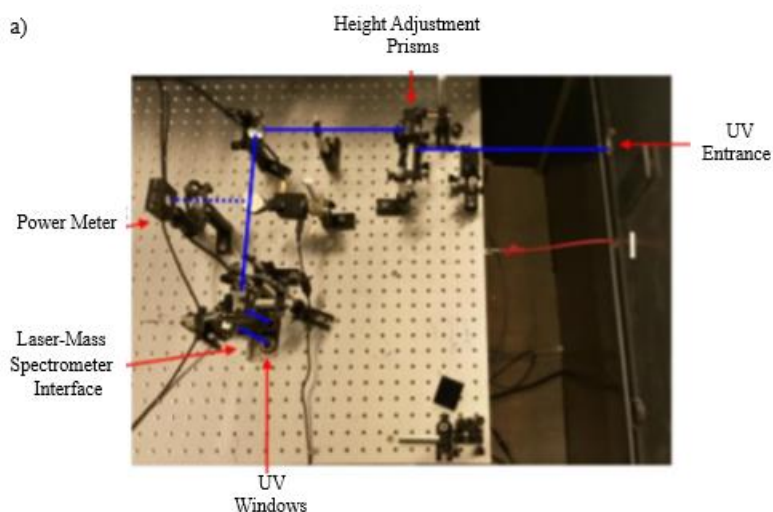
The scanning region associated with this is 400- 2750nm. The BBO crystals 20 and 22 are used to generate the UV photons. This is achieved by frequency doubling or sum-frequency generation of the idler/signal and fundamental wavelength (1064nm) of the Nd:YAG. The overlap between idler/signal and fundamental is achieved by reflecting the fundamental wavelength on the optics 24, 28 and 19. The exit of the UV photons generated with a range of 192 – 400nm requires another Pelin Broca prism (23), which also ensures that the emitted beams leave through the right exit port when reflected at a 90° angle. The adjustment of the positions of the optical elements 15, 21 and 25 enables the switching between the UV and visible regions. Other optical components of the Horizon OPO are enlisted: 355 nm Dichroic Mirror- 1, 3, Half Wave Plate- 2a, 8, 15, 27, Lens 4, 5, Mirror -12, 19, 24, 28, Polarizer -2b,

14, 26, 90 Degree Prism -17, 18, Window - 6, 13, Waveplate -21, Porro Prism-7, Beam Dump Assy-25 and Injection Pump Mirror -9.

The Horizon software is used to control the OPO laser from the workstation via a USB connection. The control of the orientation of the BBO crystals and the Pelin Broca prisms mounted on step-motors from the workstation is used to adjust the alignment, obtain different required working wavelengths and the power of the laser. The OPO generates approximately 1mJ average pulse energy for each wavelength between 650-220nm.

2.3.3 The optical pathway between the OPO laser and mass spectrometer

The experimental setup showing the pathway taken by the laser beam into the ion trap is displayed in Figures 2.12a and b. Figures 2.12a shows the pathway taken by the UV photons into the ion trap, while Figures 2.12b shows the pathway taken by the visible / near IR photons into the trap. The UV and the visible / near IR photons exit the OPO laser into the optical bench through two different black tubes. The height of the incoming UV beam is adjusted by ~ 8cm above the optical table using two right-angled UV-fused silica prisms. This which simplifies the adjustment of the photons into the ion trap. These UV fused prisms act as a periscope to achieve the desired height-adjusted beam. The adjusted beam is reflected by 90° towards the mass spectrometer by hitting a right-angled prism.



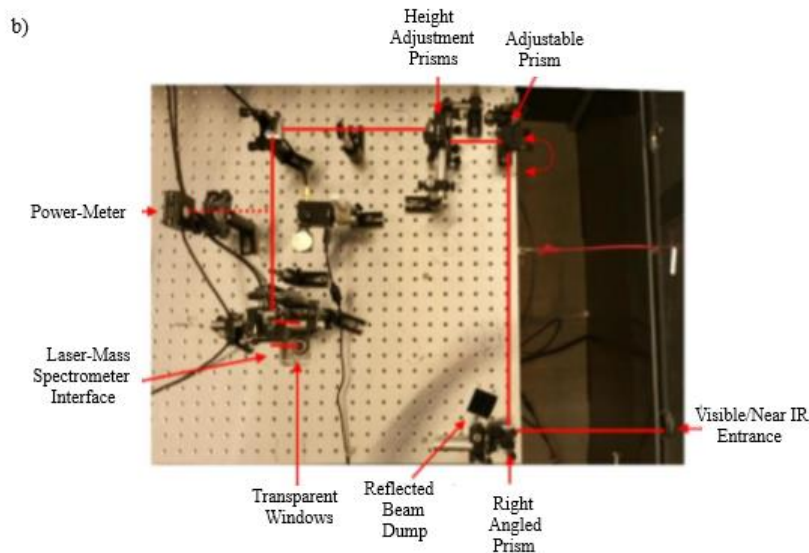


Figure 2.12 Labelled pictures of the optical bench mounted on top of the AmaZon mass spectrometer with a) displaying the path of the UV (193 - 400 nm) and b) visible/NIR (400 - 2700 nm) light from the OPO laser to ion trap of the mass spectrometer. Pictures adapted from Ref. 152

On the optical bench, a right-angled prism at the exit of the visible/near IR beam and the adjustable right-angled prism are used to overlap the UV and visible/near IR routes. The visible/near IR beam follows the same pathway as the UV beam after passing through the adjustable prism on the optical bench.

The zoomed picture of the optical pathway of the photons after passing through the height-adjustment prism is displayed in figure 2.12. From the height-adjustment prism, the beams pass through the iris (a) and hit a right-angled prism (j) which reflects the beam at 90° towards the mass spectrometer (e). In situations where the adjustable prism (b) is on the path of the laser, the beam is reflected towards the power meter (h) by passing through a lens (i) as shown in figure 2.12.

If the adjustable prism is not on the laser route, the beam will be reflected to the right-angled prism(d) passing through an iris (c) and lens (g). The right-angled prism (d) which is located on top of the QIT of the mass spectrometer reflects the beam downwards towards the QLT.

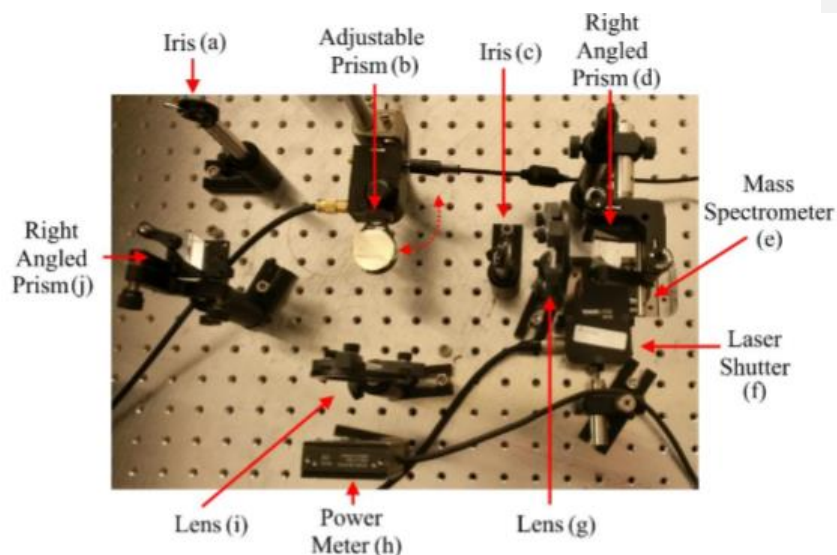


Figure 2.13 Labelled picture of the optical bench on top of the amaZon mass spectrometer, showing the region of the table containing the power measurement setup as well as the optical interface of the mass spectrometer. Picture adapted from Ref. 152.

The reflected beam passes through the optomechanical shutter (f) and a transparent window into the QIT of the mass spectrometer and leaves the QIT through a second transparent window as initially discussed.

A motorised flip mount (Model MFF001, Thorlabs Inc) which is attached to the adjustable prism is used to switch the orientation of the beam towards the power meter and out of the beam path. The switching in the orientation of the flip mount is powered by the receipt of a 5V transistor-transistor logic (TTL) signal and can be controlled through the workstation by using a home-written LabVIEW virtual instrument program which is used to trigger a data acquisition (DAQ) device (Model USB-6211, National Instruments) to send the 5V TTL signal.

2.4 General Experimental Overview

This section presents an overview of the data acquisition, processing, and extraction during gas phase photodissociation spectroscopy experiments used in this thesis. A detailed description of the experimental process is presented in Ref. 152.

2.4.1 Mass spectrometry methods

All isolated ions and clusters studied in this dissertation are generated via an ESI process discussed in Section 2.2.4. The sample solutions were prepared in ESI-compatible solvents (polar; water, methanol and aprotic; acetonitrile) at concentrations between 10^{-4} and 10^{-6} mol dm⁻³. (ESI conditions for each of the studied systems are given in detail in their different Chapters). Sample solutions were injected into the mass spectrometer using a 1cm³ syringe through a PEEK tubing connected to the ESI needle. The ESI experimental conditions for different experiments are controlled and adjusted using the trapControl software to maintain an intense and stable flow of the studied ions and cluster ions. The trapControl software is also used to optimise the QIT conditions and the applied voltages.

Full ion mass spectra of the ions generated through ESI are collected to identify the nature of the ions produced. The identity of the different analyte species was verified by comparing the isotopic distribution pattern of the analyte species from the acquired full ion mass spectra with the simulated isotopic pattern. These species are offset by +1 or -1 m/z unit from their neutral mass when they are protonated or deprotonated, except where the charge results from the oxidation state of a metal in metal complexes (eg. the tetraphenyl porphyrin iron III ion).

The confirmed analyte ion is isolated in the ion trap in one or two step isolation, and CID is employed to fragment it. The process of analysing the ion of interest with CID is performed by exciting secular frequencies of the isolated ions with an RF voltage whose amplitude can be changed between 0 to 2.5V. The change in the amplitude during a CID experiment is controlled using the trapControl software and the amplitude is increased until there is total fragmentation of the isolated parent ion. The thermal fragments are identified by determining the neutral fragments and the CID spectra were obtained by plotting the percentage of the ion production at each amplitude against the percentage amplitude.^{173,174} The generated CID fragmentation spectra are used to compare the binding energies of different clusters. There are three

scan modes (extended resolution, ultrascan and enhanced resolution) with different scan rates in which the QIT of our instrument can be operated. The resolution of the mass spectra is dependent on the operative scan mode of the QIT mass spectrometer. The enhanced resolution scan mode was used in the whole of this thesis to obtain high quality data.

2.4.2 Gas-phase absorption spectra

Solution-phase electronic absorption spectroscopy measures and records the changes in light intensity caused by the molecule or ion in a sample solution when light is passed through it, in line with the Beer–Lambert law. The number of molecules or ions present in a solution per mole is 6.02×10^{23} according to Avogadro's number thus the direct measurement of the absorption of molecules in solution is possible at a typical concentration. In the gas-phase photodissociation experiments, this is not possible because there is a relatively low number of ions that can be stored in the trap (10^3 - 10^6).³⁶ To address this challenge, action spectroscopy is employed to measure the gaseous absorption cross sections. This involves the quantification of absorption with the photo related chemical changes that gaseous ions undergo when light is passed through them. The absorption of light by gaseous ions will result in allowed photochemical changes (which are electron detachment or fragmentation), or there will be no depletion of the parent ion as a result of absorption in the absence of a radiative relaxation pathway.^{24,175,176}

The foremost equation derived from the Beer-Lambert law to define absorption cross-section in terms of a probability for photodetachment was first derived by Brauman and Smyth in their experiment to study the photodetachment of the hydroxide anion using a continuous-wave laser with wide spectral output.¹⁵⁷

$$I(t) = I_0 \exp(-tf \int \sigma(\lambda) \rho(\lambda) d\lambda) = I_0 \exp(-P) \quad \text{Equation 2.3}$$

Where I_0 and $I(t)$ are the intensity of an ion without irradiation and after being irradiated for duration t , respectively. f is the geometrical overlap factor between the light beam and the ions, $\sigma(\lambda)$ is the absorption cross section at wavelength λ , and $\rho(\lambda)$ is the photon flux. In our experiments, a 10 Hz pulsed laser is used which has a narrow spectral output and is tunable thus gives room for control over the irradiation time of the gaseous ions and the wavelength of the experiment. If the overlap

between the ion packet and laser pulse is assumed to be constant at every wavelength, and the irradiation of the ions is done by one laser pulse, we can rewrite the above equation to give the absorption coefficient.

$$\sigma(\lambda) = \ln(I_0/I) / \rho(\lambda) \quad \text{Equation 2.4}$$

Where I_0 is the intensity of a gaseous ion without irradiation, and I the intensity of a gaseous ion with irradiation. Assuming that the profile and duration of each laser pulse is the same, then we can approximate the photon flux $\rho(\lambda)$ by the average number of photons per pulse. The number of photons per pulse is estimated to be proportional to the product of the wavelength of the laser and the average laser pulse energy which is calculated from the laser power measurements. The approximate gaseous absorption coefficient represented in Equation 2.4 is also known as “photodepletion” and can be defined to be the same as gaseous absorbance when the laser power employed in the experiments is significantly low that only one photon is absorbed and each excitation as a result of the absorption of one photon causes the gaseous ion to deplete. Equation 2.4 can be simplified and rewritten as a definition for photodepletion (PD):

$$\text{PD} = \ln(I_0 / I) / P\lambda \quad \text{Equation 2.5}$$

The gas-phase absorption spectrum is acquired by collecting and comparing the Laser on and Laser off ion intensity. Laser on and Laser Off data in Chapters 3, 4 and 5 are recorded in separate files while in the data recorded in Chapter 6, the Laser on and Laser off data were collected using the same file, with the functionality of the amaZon mass spectrometer referred to as “Multiple Reaction Monitoring” (MRM).³⁴ It is a technique in mass spectrometry used to record the CID fragmentation of multiple (up to ten) mass-isolated parent ions. In a PD experiment, the MRM technique involves the isolation and fragmentation of up to five different ions in the QIT in a single acquisition, recording and storing the Laser on and Laser off mass spectra of the different ions in a successive manner within a chromatogram. The individual ion chromatogram can be deconvoluted from the single chromatogram acquired using the MRM method, which uses the Bruker Daltonik program known as “DataAnalysis”.

For all the experimental data presented in this work, the fragmentation time used to ensure the interaction of the ion packet with only one laser shot is 100 ms and the acquisition time for each ion mass spectrum at a particular wavelength is 60 seconds. The switching between laser on and laser off during the acquisition is controlled by the optomechanical shutter. This opens to allow the laser into the QIT once the fragmentation functionality is turned on and closes during laser off acquisition of the mass spectra.

The laser power is acquired for each wavelength to keep a record of the photon flux within the QIT, and the data collected are analysed and plotted against the photo energy (wavelength) to obtain the gas-phase photodepletion spectra. The automated operations employed in the collection and analysing of the data presented in this thesis are also explained in detail in Ref 152.

2.4.3 Gaseous photofragmentation and Electron detachment spectra

Photodepletion experiments involve the measurement of the depletion in ion intensity of a gaseous ion because of interaction with laser irradiation; this occurs through ionic fragmentation and electron detachment. The pathways by which gaseous fragmentation reactions occur in mass spectrometry are well characterized.^{168,177} In our experimental setup, we can measure the production of ionic photofragments with m/z greater than 50, which is the low mass cut-off in the amaZon mass spectrometer. Equation 2.5 shows the formula used in calculating the photofragment production spectra.

$$PF = (I_F / I_0) / P\lambda \quad \text{Equation 2. 6}$$

During electronic excitation, ionic fragmentation can happen through two main pathways, fragmentation through a directly dissociative excited state or through internal conversion and subsequent fragmentation on the electronic ground state. In electronic excitation, excited state fragmentation occurs when the potential energy surface of an excited state is repulsive in regard to the bond coordinates, and the lifetime for the dissociative excited state is longer or comparable to the time scale for the dissociation of the unimolecular system along the repulsive potential energy surface.¹⁷⁸

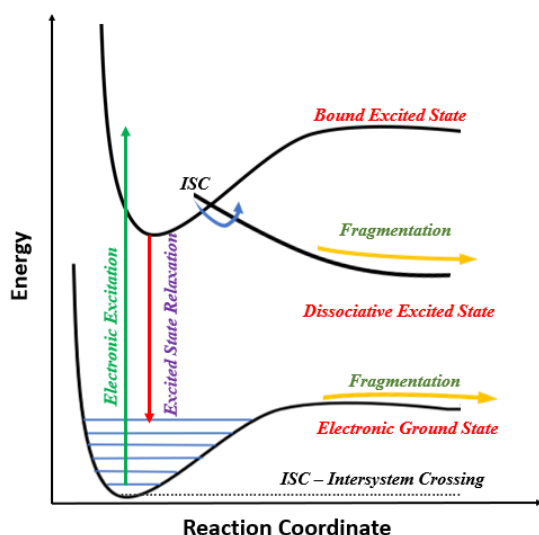


Figure 2.14 Schematic diagram of potential energy surfaces of a gaseous molecule showing two fragmentation mechanisms in the electronic excited state and the vibrational electronic ground state.

If an excited state is short lived and the pathway for relaxation into the electronic ground state is non-radiative, then ionic fragmentation can occur in the vibrationally excited electronic ground state.¹¹⁵ Vibrational relaxation is absent in the gas phase because the vibrational hot molecules dissipate their internal energy on the electronic ground state by ionic fragmentation. This is different from the pathway in solution, where hot molecules can decay by vibrational relaxation through collision with the solvent molecules. Ground state fragmentation mechanism can be verified by comparing the photofragments observed to those observed in CID.

In an anionic PD experiment, a mechanism or channel that results in the depletion of the parent ion population known as “Electron Detachment” (ED) is very important. Electron detachment occurs when the monoanionic ion is irradiated with a photon of higher energy than the binding energy of the excess electron present in the anionic species. The loss of an electron from a monoanionic species results in neutral species which is undetectable by the mass spectrometer thus the cross-section for electron detachment can be measured from the photodepletion.¹¹⁰ Electron detachment can be measured directly in multi charged anionic (MCA) species. However, for it to

occur, the photon energy must exceed the binding energy and overcome the repulsive-coulombic barrier of the excess electrons.^{179,180}

To calculate the ED yield from our experimental data we assume that any depletion that does not result in the production of a photofragment must have occurred from the loss of an electron. Therefore, we calculate electron detachment with the formula in Equation 2.7.

$$ED = [(PD_{IC} - \Sigma I_F)/I_{OFF}]/ P\lambda \quad \text{Equation 2. 7}$$

Where $PD_{IC} = I_{off} - I_{on}$.

2.4.4 Laser Power Measurement

Laser power measurement is done by collecting laser-mass spectrometry data at one or more wavelengths as we vary the power of the laser. The absorption maxima of the PD spectra provide the preferred choices for the data collection wavelengths. This study is important because it reveals the part multiphoton effects play on PD spectra. Equation 2.8 shows the relationship between photodepletion and the power series of different photon processes. The probability of n -photon absorption is proportional to the n -photon excitation cross-section [$\sigma(nPA)$] and the photon flux to the power n .¹⁸¹

$$\ln I_0/ I = \sigma(1PA,\lambda) \times \rho(\lambda) + \sigma(2PA,\lambda) \times \rho(\lambda)^2 + \sigma(3PA,\lambda) \times \rho(\lambda)^3 \dots \quad \text{Equation 2. 8}$$

Comparing the magnitude of [$\sigma(nPA)$] to those of multi-orders, it is evident that the magnitude for the one-photon transition is larger and therefore higher light intensity is required for it to be achieved.

For laser power studies, laser powers are chosen above and below the PD experimental scan laser power (~10mW), and PD data are acquired multiple times (3-5 times) for each laser power. The collected data are extracted, the logarithm of depletion of the ion signal, ($\ln I_0/ I$), is plotted against the laser power and a linear or polynomial function is used to fit the data points. A good fit to a linear function may be viewed as a confirmation of a one-photon process.²⁷

2.5 The Orbitrap Mass Spectrometer

Figure 2.15 displays an Orbitrap Fusion Tribrid mass spectrometer (Thermo Fisher Scientific), coupled with an ESI source, which is employed for the Higher-energy collisional dissociation (HCD) experiments. The instrumental analysis employed in the Orbitrap for HCD experiments is an MS/MS or MS² technique also known as “tandem mass spectroscopy”, and it is also applicable in triple quadrupole fragmentation.¹⁸² HCD experiments were used in this thesis to probe the ground state fragments and subsequent comparison with the photofragments acquired from the laser experiment to identify ground-state fragments.

The Orbitrap instrument possesses linear ion trap (LIT) and Orbitrap mass analysers, and two mass filters (LIT and quadrupole ion trap (QIT)). When performing a HCD analysis either of the mass filters can be used for mass selection and the ions are trapped in the C-trap which is a curved linear trap before being moved to the ion routing multipole (IRM) where they are fragmented by collision with a nitrogen buffer gas. The nitrogen gas gives the higher collisional energy used in the HCD experiment, compared to CID where the buffer gas is helium. The produced fragment in the IRM is transferred back to the particular mass analyser used (LIT or Orbitrap) for detection.

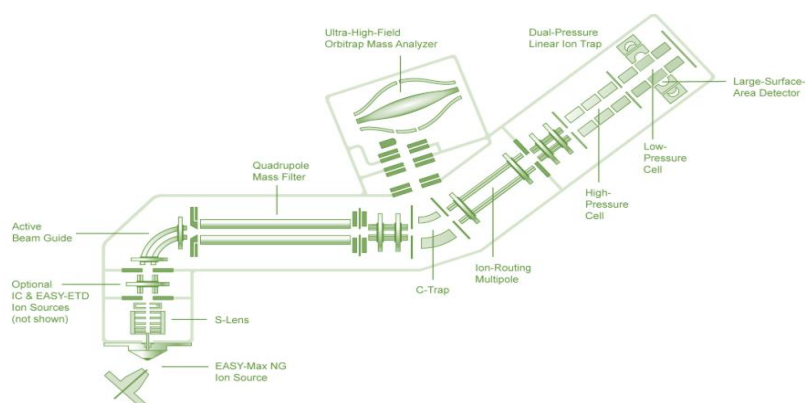


Figure 2.15 Schematic diagram of the Orbitrap Fusion Tribrid mass spectrometer. Image is adapted from the Orbitrap manual.¹⁸³

The potential difference between the C-trap lenses and the ion routing multipole is the normalised HCD collisional energy and is varied between 0 and 50% where 100% is ~100 V. This is the standard procedure for performing standard HCD experiments.^{184,185} The HCD collisional energy is increased until the parent ion fragments completely, and the ion intensity percentage is plotted against the HCD energy.

Equation 2.9 defines the relationship between the maximum amount of kinetic energy provided for conversion to internal energy during one collision (E_{CM}) and the dependence on the mass of the buffer gas.

$$E_{CM} = zRN / (m_p + N) \quad \text{Equation 2.9}$$

Where z represents the charge and R is related to the instrument settings. m_p and N are the mass of the precursor ion and the mass of the collision gas, respectively.¹⁸⁶

2.6 Computational Methods

All experimental results presented in this thesis were supported with quantum chemical calculations using Gaussian'09 (revision D.01, Gaussian, Inc.)¹⁸⁷ and a variety of functionals and basis sets. Density functional theory (DFT) was used in calculations involving ions in their electronic ground state to explore the following:

- identity of photofragments,
- conformer/isomer searching to obtain the lowest energy structure of a parent ion/cluster ion,
- calculating the vertical and adiabatic electron detachment energies of anionic species etc.

Time dependent density functional theory (TDDFT) was used to simulate the electronic spectra and predict the excited states of the ion of interest. Solution-phase properties were also calculated using implicit solvent models where needed. Frequency calculations were performed to ensure global minima for all optimised geometry. Specific calculations used for each system studied are outlined in detail in the different thesis Chapters.

Schrödinger's MacroModel with mixed Monte Carlo torsional and low-mode sampling parameters were employed to conduct conformational molecular dynamics

searches to generate possible conformers. The generate possible conformers rapid energy gradient were minimized with the OPLS3e force field.¹⁸⁸

2.6.1 Density functional theory (DFT) used within the thesis

Density functional theory is based on the idea that the physical properties of a molecule can be controlled by their electronic structures. It follows that once the electron density of a molecule is known, its physical properties can be calculated. In this thesis the B3LYP and MO6-2X functionals are the main functionals used in the computational calculations.

B3LYP uses the Lee-Yang-Parr (LYP) and Vosko-Wilk-Nusair (VWN) correlation functionals and Becke's three parameter (B3) exchange functionals. B3LYP also possess 20% the exact Hatree Fock exchange^{189,190} and is parametrised for the rare gases.

MO6-2X is a "Minnesota" functional developed by Yan Zhao and Donald G. Truhlar.^{191,192} It is a high non-locality functional with double the amount of non-local exchange (2X), and it is parameterized only for non-metals and thermochemistry. It uses 54% exact exchange to calculate exchange energy while the remaining exchange energy is calculated by a M05 co-relational functional.¹⁹³

2.6.2 Basis set superposition error

In computational analysis, it has been seen that the use of a finite basis set normally poses an error. This is because as the molecules interacting in a system comes close to each other, their basis sets overlap, with each of them trying to compensate the other by allowing each other to borrow functionals from themselves. This means that increasing their basis sets may produce a more liable result for calculated derived parameters such as energy. The mismatch between the energies of the mixed basis set system and the unmixed system brings about the error. This error is avoided using the counterpoise method of correction, which is an approximate method for estimating the size of the basis set superposition error (BSSE) in this thesis.¹⁹⁴⁻¹⁹⁶

Chapter 3

Observation of Enhanced Dissociative Photochemistry in the Non-Native Nucleobase 2-Thiouracil

This work has been published in the *Molecules*. All computational and part of the experimental data have been collected, formally analysed, and investigated by me. The initial draft of the manuscript was prepared by me and revised by Caroline Dessent.

Full Reference to the publication:

“Observation of Enhanced Dissociative Photochemistry in the Non-Native Nucleobase 2-Thiouracil”

*“DOI:<http://dx.doi.org/10.3390/molecules25143157>, *Molecules* **2020**, 25(14), 3157”*

3.1 Abstract

The first study to measure the dissociative photochemistry of 2-thiouracil (2-TU), an important nucleobase analogue with applications in molecular biology and pharmacology is presented. Laser photodissociation spectroscopy is applied to the deprotonated and protonated forms of 2-TU, which are produced in the gas-phase using electrospray ionization mass spectrometry. Our results show that the deprotonated form of 2-thiouracil ($[2\text{-TU-H}]^-$) decays predominantly by electron ejection and hence concomitant production of the $[2\text{-TU-H}]^\cdot$ free-radical species, following photoexcitation across the UVA-UVC region. Thiocyanate (SCN^-) and a m/z 93 fragment ion are also observed as photodecay products of $[2\text{-TU-H}]^-$ but at very low intensities. Photoexcitation of protonated 2-thiouracil ($[2\text{-TU-H}]^+$) across the same UVA-UVC spectral region produces the m/z 96 cationic fragment as the

major photofragment. This ion corresponds to ejection of an HS· radical from the precursor ion and is determined to be a product of direct excited state decay. Fragment ions associated with decay of the hot ground state (i.e. the ions we would expect to observe if 2-thiouracil was behaving like UV-dissipating uracil) are observed as much more minor products. This behaviour is consistent with enhanced intersystem crossing to triplet excited states compared to internal conversion back to the ground state. These are the first experiments to probe the effect of protonation/deprotonation on thionucleobase photochemistry, and hence explore the effect of pH at a molecular level on their photophysical properties.

3.2 Introduction

The canonical nucleobases of DNA and RNA are renowned for their ability to dissipate harmful UV, primarily via ultrafast excited-state relaxation to the ground state, either directly or indirectly through excited singlet states.^{197–202} Thiobases represent a class of structurally modified nucleobases where an oxygen atom of the carbonyl group is substituted by a sulphur atom. These molecules display dramatically different relaxation dynamics compared to their canonical nucleobase analogues.^{203–208} Molecules such as 4-thiothymine and 2-thioguanine possess excited states that evolve by intersystem crossing (ISC) on sub picosecond timescales, resulting in nearly unity triplet yields.^{203–207} The ensuing triplet state constitutes a highly reactive molecule, which by itself or by generating singlet oxygen^{205,207} can damage biomolecules within the cell.^{209,210} Hence these molecules are of considerable current interest in phototherapeutic applications.^{205,211–17}

Given the growing application of thionucleobases, there has been considerable interest in characterizing their fundamental photophysics. Time-resolved experiments using time-resolved photoionization techniques have provided complementary insight into the intrinsic decay dynamics,^{214–216} as well as a straightforward comparison against theoretically derived potential energy surfaces.^{215,222–227}

In this work, the intrinsic (i.e., gas-phase) photochemistry of 2-thiolated uracil (2-TU) (Figure 3.1) is explored. In particular, the aim is to characterise the effect of protonation and deprotonation on the excited states and photoproducts of 2-TU by

studying the isolated deprotonated ($[2\text{-TU-H}]^-$) and protonated ($[2\text{-TU}\cdot\text{H}]^+$) ions via laser-interfaced mass spectrometry (LIMS).^{27,228–230} These are the first experiments to directly measure the dissociative photochemistry of a thionucleobase. They are also the first to probe the effect of protonation/deprotonation on a thionucleobase photochemistry, and hence explore the effect of pH at a molecular level on 2-TU photophysical properties. The experiments are important in the context of the use of 2-TU both as a photodynamic therapy agent and biochemical labelling agent, since local biochemical environments can display variable pH.

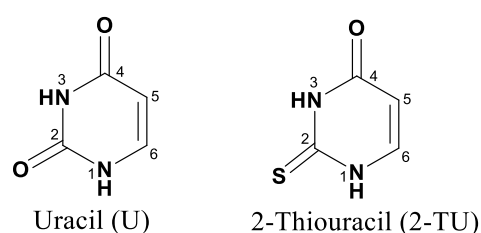


Figure 3.1 Schematic diagram of uracil (U) and 2-thiouracil (2-TU) with ring atom labels.

The electronic properties of neutral 2-thiouracil (2-TU) have been the subject of multiple theoretical and experimental studies.^{216,221,226,231–233} Crespo-Hernández and co-workers have applied femtosecond broadband transient absorption spectroscopy in aqueous and acetonitrile solutions,²³¹ while Ullrich and co-workers used time-resolved photoelectron spectroscopy to characterise the gaseous excited state dynamics.²³³ Complementary theoretical calculations have been conducted by Gonzalez and co-workers.^{225,226} The consensus to emerge from this work is that the main excited-state relaxation pathway following initial excitation to the S2 state is $S2 \rightarrow S1 \rightarrow T3 \rightarrow T1$, with $S2 \rightarrow S1 \rightarrow T1$ occurring as a minor pathway.²²⁶ Very recently, experimental and computational evidence has been published providing evidence for the existence of two minima within the T1 state.²²¹ Work has also been conducted on the negative ions of 2-TU.^{234,235} These studies are motivated by the fact that ionizing radiation can initiate DNA strand breaks via the formation of transient negative ions.^{236,237}

3.3 Experimental and Computational Method

3.3.1 Experimental method

The gaseous ion absorption and photofragment spectra of $[2\text{-TU} - \text{H}]^-$ and $[2\text{-TU} \cdot \text{H}]^+$ were recorded in vacuo using action spectroscopy. UV photodissociation experiments were conducted in an AmaZon quadrupole ion-trap mass spectrometer (Bruker, Billerica, MA, USA) modified for the laser experiments.^{20,48} UV photons were produced by an Nd:YAG (10 Hz, Surelite, Amplitude Laser Group, San Jose, CA, USA) pumped OPO (Horizon, Amplitude Laser Group, San Jose, CA, USA) laser, giving ~1 mJ across the range 390–234 nm (3.2–5.3 eV) and 214–344 nm (3.6–5.7 eV) for deprotonated and protonated 2-TU respectively, using a 2 nm laser step size.

2-thiouracil (99%) was purchased from Acros Organics and HPLC-grade MeOH was purchased from Fisher Scientific, Inc. (Pittsburg, PA, USA), both were used without further purification. The compound was dissolved in 100 ml methanol to a concentration of approximately $1 \times 10^{-6} \text{ mol dm}^{-3}$. Two separate solutions were used for protonated and deprotonated 2-thiouracil in the gas phase: with the addition of a drop of trifluoroacetic acid (TFA) or 2 ml of 30% ammonium hydroxide, respectively. The solutions were introduced into the mass spectrometer by electrospray ionisation (ESI) using a nebulizing gas pressure of 9 and 13 psi, an injection rate of 0.25 and 0.35 ml h⁻¹, a drying gas flow rate of 8 and 3l min⁻¹, and run in positive/negative ion mode at capillary temperatures of 110 °C and 140 °C respectively. Photofragmentation experiments were run with an ion accumulation of 100 ms with a fragmentation time of 100 ms, ensuring an average of one laser pulse per ion packet and thereby reducing the possibility of multiphoton occurrences. UV excited gaseous ion fragment upon relaxation and produce a gas-phase absorption spectrum by photodepletion^{24,48,238} at negligible fluorescence.²³⁹ The $[2\text{-TU} - \text{H}]^-$ and $[2\text{-TU} \cdot \text{H}]^+$ peaks were mass isolated using the multiple reaction monitoring (MRM) functionality of the mass spectrometer. The photodepletion intensity (PD) of the mass selected ions $[2\text{-TU} - \text{H}]^-$ and $[2\text{-TU} \cdot \text{H}]^+$ and the photofragment production (PF) were calculated using the methods described in Chapter 2.

Higher-energy collisional dissociation (HCD) experiments were performed in an Orbitrap Fusion Tribrid mass spectrometer (Thermo Fisher Scientific) to acquire a

wider fragmentation profile for the collisional excited ground electronic state of protonated and deprotonated 2-thiouracil.²⁴⁰⁻²⁴¹ The operating software's automatic tuning capabilities at a flow rate of $5 \mu\text{L min}^{-1}$ were used to obtain the following parameters in positive mode (negative mode values are the same unless as shown with the values in brackets): spray voltage: 3600 (-4000) V; sweep gas flow rate: 1 arb; sheath gas flow rate: 10 arb; aux gas flow rate: 5 arb; ion transfer tube temperature: 275 (325) °C; vaporizer temperature: 350 °C.

Solution-phase UV absorption spectra of $[2\text{-TU} - \text{H}]^-$ and $[2\text{-TU} \cdot \text{H}]^+$ ($1 \times 10^{-5} \text{ mol dm}^{-3}$) in MeOH were obtained using a UV-1800 UV-Visible spectrophotometer (Shimadzu, Kyoto, Japan) with a 1cm cuvette. To obtain a UV spectrum for $[2\text{-TU} - \text{H}]^-$ and $[2\text{-TU} \cdot \text{H}]^+$, the solution of 2-TU in MeOH were alkalified with NaOH (2.0 M) and acidified with HCl (3.0 M).

3.3.2 Computational method

All optimization and vertical detachment energy (VDE) calculations were done in the gas phase and implicit methanol solvent using density functional theory at the B3LYP/6-311++G (2d, 2p) level of theory as performed in Gaussian 09.¹⁸⁷ The vertical dipole moments of the tautomers were calculated using MP2/6-311++G(2d,2p). Frequency calculations were performed to ensure that all optimised structures correspond to true energy minima. Time-dependent density functional theory (TDDFT) calculations (50 states) were performed to calculate the gaseous excited state spectra, with implicit methanol solvent being used to obtain the corresponding solution-phase spectra.

3.4 Results & Discussion

3.4.1. Geometric structures and TDDFT calculations $[2\text{-TU} - \text{H}]^-$ and $[2\text{-TU} \cdot \text{H}]^+$

Figure 3.2 displays the low energy tautomers of $[2\text{-TU} - \text{H}]^-$ and $[2\text{-TU} \cdot \text{H}]^+$ gaseous structures calculated at B3LYP/6-311++G (2d, 2p) level. Relative energies for these tautomers are displayed in Table 3.1. Rotational isomers are grouped together, using small case alphabetical labels (e.g., D3a and D3b). The D1 tautomer corresponding to removal of the N1 proton lies substantially lower in energy than the higher-energy tautomers. It will therefore be the only tautomer produced following electrospray in

methanol solvent.⁴⁸ In solution, this pattern is repeated, so that the D1 tautomer is again predicted to dominate. Vertical detachment energies (VDEs) were calculated for the [2-TU-H]⁻ isomers, with the value for the D1 isomer predicted to be 3.82 eV. This value can be compared to the experimental value for deprotonated uracil of 2.5 eV.²⁴²

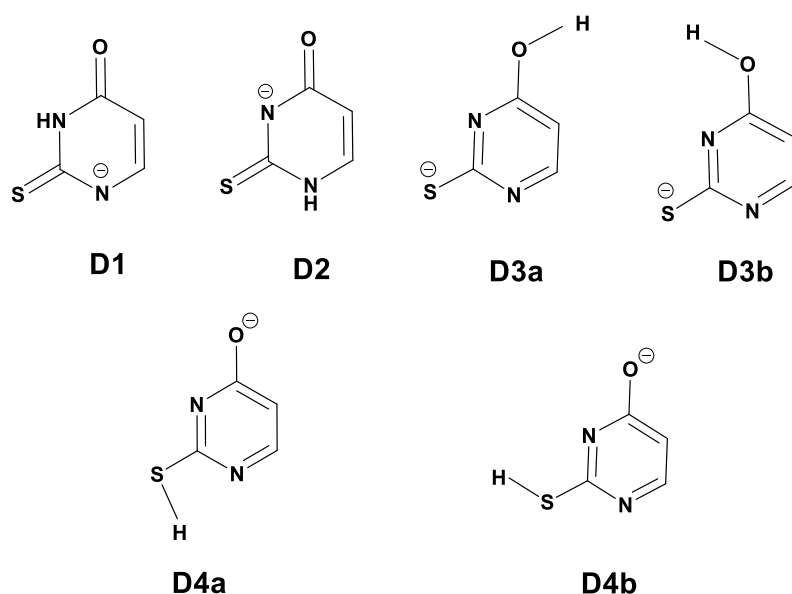


Figure 3.2 Low energy tautomers of [2-TU-H]⁻ obtained at the B3LYP/6-311++G(2d, 2p) level of theory.

Figure 3.3 displays the five lowest-energy calculated tautomers of [2-TU-H]⁺, which are in good agreement with the previous results of Nei et al.²⁴³ Rotational isomers are again grouped together, using small case alphabetical labels (i.e. P1a–P1d). The lowest-energy gaseous tautomers, P1a and P1b, correspond to a pair of cis and trans enol-enol rotamers, with other tautomers lying at significantly higher energy. The lowest-energy enol-keto tautomer, P2, is predicted to lie 20.25 kJ mol⁻¹ higher in energy than P1a. We therefore expect that P1a will dominate the experimental ion ensemble following electrospray, with some P1b also being present.

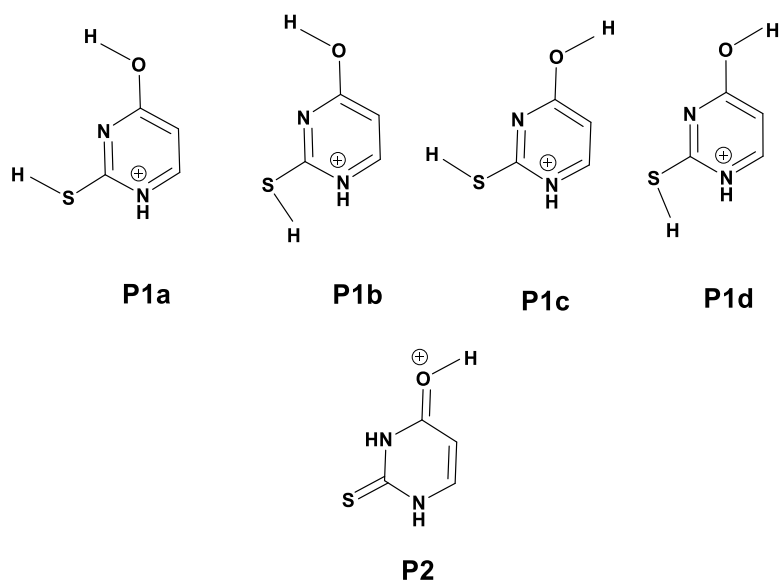


Figure 3.3 Low energy tautomers of $[2\text{-TU}\cdot\text{H}]^+$ obtained at the B3LYP/6-311++G (2d, 2p) level of theory.

Table 3.1 Relative energies and % Boltzmann population of the lowest energy tautomers of $[2\text{-TU} - \text{H}]^-$ and $[2\text{-TU} \cdot \text{H}]^+$ calculated at B3LYP/6-311++G (2d, 2p) level of theory. Vertical detachment energy (VDE) and the vertical dipole moment (D) are also presented for the $[2\text{-TU} - \text{H}]^-$ anions.

	Tautomer	Relative energy (kJmol⁻¹)^{a,b}	% Boltzmann Population^{b,c}	VDE	Dipole moment (D)
[2-TU-H]⁻	D1	0.0 (0.0)	99.999 (99.791)	3.82	3.50
	D2	45.95 (15.28)	0 (< 0.1)	3.66	8.61
	D3a	101.56 (58.94)	0 (< 0.1)	2.91	3.35
	D3b	74.58 (49.49)	0 (< 0.1)	3.00	0.71
	D4a	58.18 (51.69)	0 (< 0.1)	3.69	3.93

	D4b	56.49 (51.47)	0 (< 0.1)	3.69	2.54
	P1a	0.0(0.0)	93.880 (35.918)		
	P1b	6.81 (1.32)	0.077 (1.366)		
[2-TU·H] ⁺	P1c	17.61 (8.10)	0.003 (0.761)		
	P1d	26.18 (9.55)	6.010 (21.083)		
	P2	20.25(-0.32)	0.026 (40.871)		

a Zero-point corrected energies. b Values in parenthesis are calculated in methanol. c Determined at 293°K

TDDFT calculations were conducted to aid the assignment of the excited-state spectra presented below, with the calculated excitation spectra for the lowest-energy tautomers of [2-TU-H]⁻ (D1) and [2-TU·H]⁺ (P1a) displayed in Figure 3.1. The calculated TDDFT excitation spectra for all tautomers, transition energies, and assignments of the bright transitions (≥ 0.005 oscillator strength) are included in the Supplementary information (Figure 3.13 and Figure 3.14). For the sets of rotational isomers (e.g., P1a-P1d of [2-TU·H]⁺, and D3a and D3b of [2-TU-H]⁻), the TDDFT spectra are very similar, and would be indistinguishable at our experimental resolution.

The TDDFT calculations predict that the protonated and deprotonated forms of 2-TU will display dramatically different absorption profiles, with [2-TU-H]⁻ absorbing strongly through the UVA, with the primary absorption of [2-TU·H]⁺ occurring at significantly higher energies.

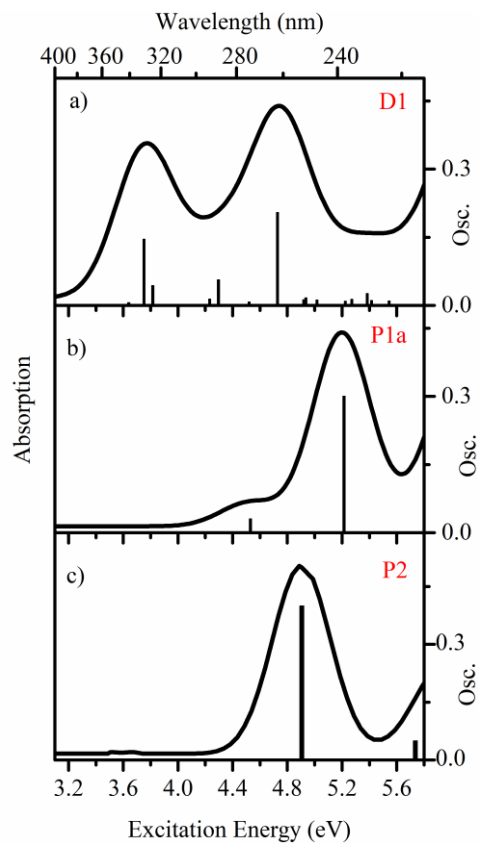


Figure 3.4 Calculated TDDFT excitation energies (B3LYP/6-311++G(2d,2p)) for (a) the D1 tautomer of $[2\text{-TU-H}]^-$, (b) the P1a tautomer of $[2\text{-TU-H}]^+$, and (c) the P2 tautomer of $[2\text{-TU-H}]^+$. Oscillator strengths (Osc.) of individual transitions ≥ 0.005 are shown by vertical bars, while the full line spectrum is a convolution of the calculated spectral transitions with a Gaussian function (0.25 eV HWHM).

We note that the TDDFT calculations may not accurately predict the spectra of the $[2\text{-TU-H}]^-$ negative ion well. Dipole-bound excited states, which are common in negative ion systems, are challenging in general for ab initio calculations, and their accurate calculation requires the use of diffuse functionals centred on the dipole-bound orbital.^{244–246} In addition, any electronic excitations that appear above the electron detachment threshold of an anionic species will correspond to resonance states.^{247,248} The accurate theoretical prediction of such states is beyond the scope of

the current work, however the TDDFT calculations presented here have been shown to provide a useful guide in interpreting similar experimental results.²⁴⁹⁻²⁵¹

3.4.2 Photodepletion(absorption) spectrum of [2-TU-H]⁻

Figure 3.5 displays the gas-phase absorption (photodepletion) spectrum of [2-TU-H]⁻ measured over the range 3.2–5.3 eV. The spectrum has an absorption onset at 3.2 eV with continuous absorption through to 5.2 eV. A high-intensity absorption band, labelled **I**, is evident between 3.2 to 4.2 eV, peaking at $\lambda_{\text{max}} = 3.7$ eV. This band lies just below the calculated VDE of the lowest-energy D1 tautomer (3.82 eV). From the relative energies presented in Table 1, only the D1 tautomer is expected to be present following electrospray in methanol. This feature is followed by a lower-intensity, broad absorption (**II**) from 4.2 to 5.2 eV. The overall profile of the [2-TU-H]⁻ gas-phase absorption spectrum is similar to that of other negatively charged molecules and clusters we studied previously. It can be primarily described as a near-threshold dipole-bound excited state (band **I**) followed by a higher-energy region where electron-detachment dominates (band **II**).⁴⁸ However, this picture can be complicated by the presence of electronic transitions of the chromophore, which may be evident superimposed on top of these electron detachment features.^{229,240}

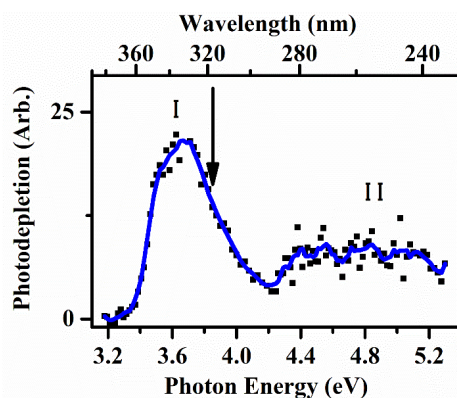


Figure 3.5 Gas-phase absorption (photodepletion) spectrum of [2-TU - H]⁻ measured over the range of 3.2 – 5.3 eV (234-390 nm). The arrow indicates the VDE of the D1 isomer. The solid line is a five-point adjacent average of data points.

The calculated TDDFT spectrum of [2-TU-H]⁻ (Figure 3.4a) predicts that [2-TU-H]⁻ has two main electronic transitions which peak at 3.8 and 4.8 eV. However, these

absorptions are not evident in our gaseous experimental spectrum presented in Figure 3.5, probably due to the dominance of electron detachment (Section 3.6.2.2). In the previous anionic systems we studied, these excited states have been more clearly visible in the photofragment production spectra.^{242,252,253} We therefore turn to inspecting the photofragmentation channels of $[2\text{-TU-H}]^-$ to further characterise the excited states and photochemistry.

3.4.3 Photofragmentation of $[2\text{-TU-H}]^-$

Figure 3.6 displays the photofragment difference (laser on – laser off) mass spectra of $[2\text{-TU-H}]^-$ irradiated at 3.6 eV close to the band I maximum (λ_{max}). $[2\text{-TU-H}]^-$ produces two photofragments, m/z 58 and 93, with the m/z 58 photofragment being more intense. These ionic photofragments have low intensities compared to the parent ion depletion. Both are produced weakly across band I of the photodepletion spectrum, and with negligible intensity across the band II region. This indicates that across the UV, $[2\text{-TU-H}]^-$ decays predominantly by electron detachment with associated production of the $[2\text{-TU-H}]^\cdot$ radical (Equation 1).

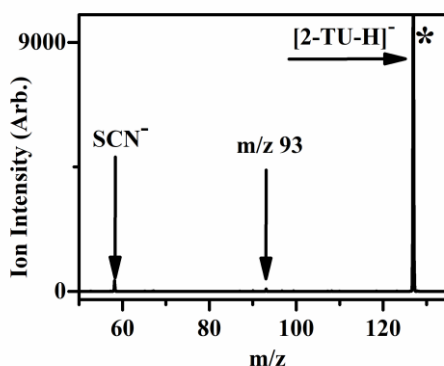


Figure 3.6 Photofragment difference (laser on – laser off) mass spectrum of $[2\text{-TU-H}]^-$, excited at 3.6 eV (344nm). *Represents parent ion signal with m/z 127.

The $m/z = 58$ photofragment (Equation 2) is assigned to thiocyanate (SCN^-). We note that this ion has been observed in low-energy dissociative electron attachment to 2-TU, as well as in collisional activated decomposition of 2-thiouridine.²³⁴ While SCN^- was observed in higher-energy collisional dissociation (HCD) of $[2\text{-TU-H}]^-$,

the $m/z = 93$ ion was not (Section 3.6.2.1). This indicates that the $m/z 93$ ion (Equation 3) is a solely photochemical product.

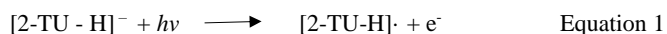
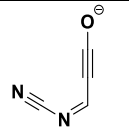


Table 2 lists the photofragments and corresponding neutral fragments of $[2\text{-TU-H}]^-$. We note that there are two possible structures of $\text{C}_3\text{H}_3\text{NO}$ (Section 3.6.1.2). One of these is acrylamide, a potent neurotoxin,²⁵⁴ while the other is a potentially harmful free radical species. Further computational results on the observed fragments are presented in (Section 3.6.1.2)

Table 3.2 Assignment of the fragmentation channels of $[2\text{-TU} - \text{H}]^-$ ($m/z 127$) observed upon, laser excitation at 3.2-5.2 eV.^{a,b,c} and HCD collisional excitation.

Photo fragment m/z	Proposed Structures	Neutral Radical loss or	HCD	3.6 eV
58	SCN^-	$\text{C}_3\text{H}_3\text{NO}$	✓	✓ (w)
93		H_2S	X	✓ (vw)

^avw is very weak. ^bw is very weak. ^cX is not present.

The photofragment production spectra are displayed in Figure 3.7 and are presented with the gas-phase absorption spectrum for comparison. While SCN^- is produced through band I, the full-width half maximum for this feature is 0.31 eV, which is narrower than that of the band I feature (0.43 eV).

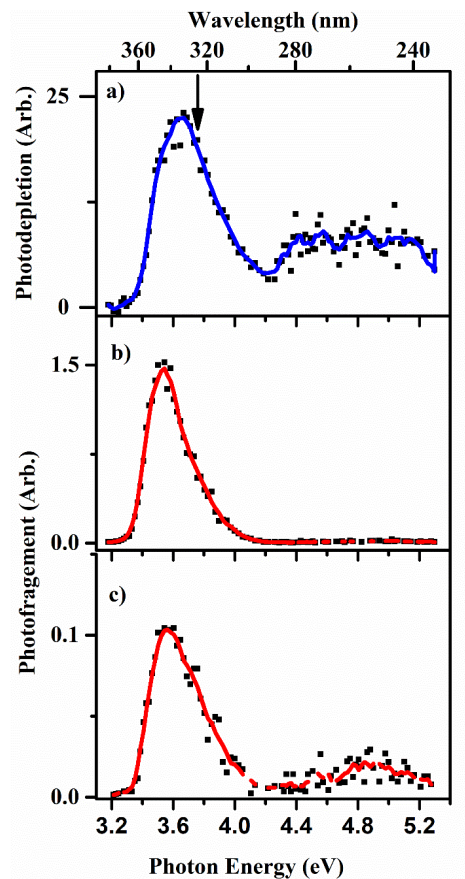


Figure 3.7 (a) Gas-phase absorption (photodepletion) spectrum of $[2\text{-TU-H}]^-$, (b) photofragment action spectrum of SCN^- (m/z 58), and (c) photofragment production spectrum of m/z 93 from 3.2–5.3 eV (234–390 nm). The arrow included in (a) indicates the calculated VDE of the lowest-energy tautomer. The solid line is a five-point adjacent average of the data points.

Indeed, comparison of the spectra presented in Figure 3.7 reveals that SCN^- is produced only through the lower energy region of band I. It is interesting to note that the SCN^- production spectrum appears to be broadened on the high-energy side of the peak, possibly due to unresolved vibrational features. This is reminiscent of near-threshold excitation of $\text{I}^- \cdot \text{CH}_3\text{I}$, where the I^- photofragment production spectrum contained a vibrational progression in the C-I stretch, originating in the intermediate transient negative ion.²⁵⁵

The production profile of the m/z 93 fragment is very similar to that of the m/z 58 fragment, although it is produced at ~ 10 times lower intensity. Some non-zero production of m/z 93 is visible in the region between 4.6–5.2 eV, the area where the second bright transition of $[2\text{-TU}\cdot\text{H}]^-$ is predicted to occur. Indeed, there is also very low-level production of m/z 58 in this region. The nature of the excited states and photofragmentation pathways of $[2\text{-TU}\cdot\text{H}]^-$ will further be discussed.

3.4.4 Photodepletion (absorption) spectrum of $[2\text{-TU}\cdot\text{H}]^+$

Figure 3.8 displays the gas-phase absorption (photodepletion) spectrum of $[2\text{-TU}\cdot\text{H}]^+$ across the UV region. The spectrum displays two resolved bands, which are labelled **I** and **II**, with λ_{max} at 4.68 and 5.3 eV, respectively.

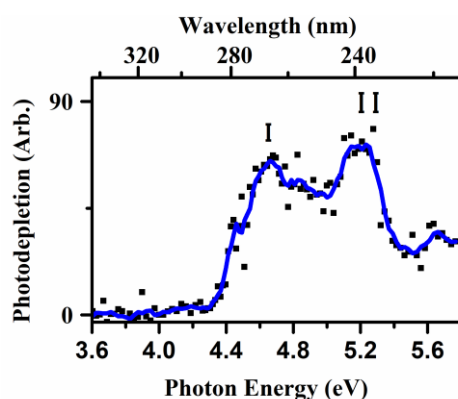


Figure 3.8 Gas-phase absorption (photodepletion) spectrum of $[2\text{-TU}\cdot\text{H}]^+$ across the range 3.6–5.8 eV (344–214 nm). The solid line is a five-point adjacent average of data points.

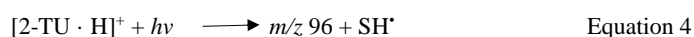
It is instructive to compare the gas-phase absorption spectrum of $[2\text{-TU}\cdot\text{H}]^+$ with that of protonated uracil, which has been studied at low resolution by Pedersen et al.,²⁵⁶ and at high resolution by Berdakin et al.²⁵⁷ In both studies, protonated uracil displayed a spectrum that consisted of two bands, a weaker intensity band between 260 and 317 nm and a stronger intensity band at higher energies from 227–256 nm. These bands were assigned to the presence of two isomers, an enol-keto tautomer for the weaker band and an enol-enol tautomer for the stronger band. This spectral

pattern is remarkably similar to the spectral profile of $[2\text{-TU}\cdot\text{H}]^+$ observed here, allowing us to assign band **I** to the P2 tautomer, and band **II** to P1 tautomers. Although our calculations did not predict that the P2 tautomer would be present in the gas-phase, it is known that relative tautomer energies for this type of system can be unreliable. Indeed, there is direct evidence from the IRMPD study of Nei et al on $[2\text{-TU}\cdot\text{H}]^+$ that an enol-keto tautomer such as P2 is present in the gas-phase following electrospray ionisation.²⁴³ It is also important to note that in previous studies where electrospray has been used to transfer similar molecular ions (e.g., protonated nicotinamide) from the solution into the gas-phase, higher-energy tautomers have been observed, possibly due to the kinetics of the electrospray process.²⁷ Similar effects may therefore occur for the 2-TU system.

We next turn to inspecting the photofragment action spectra to further probe the nature of the two bands evident in gas-phase absorption spectrum of $[2\text{-TU}\cdot\text{H}]^+$.

3.4.5 Photofragmentation of $[2\text{-TU}\cdot\text{H}]^+$

Photofragment mass spectra of $[2\text{-TU}\cdot\text{H}]^+$ were obtained at 4.6 and 5.2 eV close to the λ_{max} of bands **I** and **II** (Section 3.6.2.5). Table 3 provides a list of the most intense photofragments, along with proposed structures and accompanying neutral fragments. The m/z 96 photofragment, which corresponds to loss of an SH radical, is the most intense photofragment in both bands **I** and **II**.

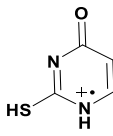
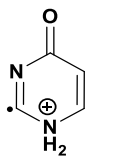
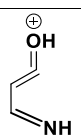


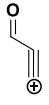
Other photofragments observed with significant intensities in both bands are m/z 128 (H atom loss), m/z 112 (NH_3 loss), and m/z 70 (HNCS loss). The m/z 68 and m/z 79 photofragments were not observed in the band **I** region (Figure 21a) but were seen in the higher-energy band **II** region (Figure 21b), although with very low intensities.

HCD (Higher-Energy Collisional Dissociation) was performed on $[2\text{-TU}\cdot\text{H}]^+$ to explore the thermal fragmentation pathways of the electronic ground state, with the results compiled in Table 3.2. HCD fragmentation of $[2\text{-TU}\cdot\text{H}]^+$ produces the m/z 112 (NH_3 loss) and m/z 70 (HSCN loss) ions as the dominant products at moderate collision energies which should correspond to internal ion energies close to the photon energies employed in this study.²⁴⁰ These product ions are in line with those

observed for CID of protonated uracil, where loss of NH_3 dominates, and loss of HNCO is seen as a more minor product ion.²⁵⁶⁻²⁵⁸ For protonated uracil, loss of H_2O is also observed although we do not observe the equivalent loss of H_2S for $[\text{2-TU}\cdot\text{H}]^+$. Notably, the major photofragment, m/z 96 (SH loss), was not seen in the HCD results (Section 3.6.2.1). Further computational results on the observed fragments are presented in (Section 3.6.1.3).

Table 3. Assignment of the fragmentation channels of $[\text{2-TU}\cdot\text{H}]^+$ (m/z 129) observed upon HCD collisional excitation, and laser excitation at 4.6 and 5.2 eV.^{a,b}

Photofragment m/z	Proposed Structure	Neutral or Radical loss	HCD	PF Intensity at 4.6 eV ^b	PF Intensity at 5.2 eV ^b
128		H^\bullet	✓	✓ (w)	✓ (m)
112	$\text{C}_4\text{H}_2\text{NO}^+$	NH_3	✓	✓ (w)	✓ (w)
96		SH^\bullet	X	✓ (vs)	✓ (vs)
79	C_4HNO^+	$\text{SH}^\bullet + \text{NH}_3$	X	X	✓ (vw)
70		HNCS	✓	✓ (m)	✓ (m)
68	$\text{C}_3\text{H}_4\text{N}_2^+$	$\text{SH}^\bullet + \text{CO}$	X	X	✓ (vw)

60	CNSH ₂ ⁺	NH ₃ + C ₃ O	✓	✓ (vw)	✓ (vw)
53		NH ₃ + HNCS	✓	✓ (vw)	✓ (vw)

^a vs is very strong, m is medium, w is weak and vw is very weak. ^bPF = Photofragment.

Note: m/z 84 had medium intensity at high HCD energy but is not present as a photofragment.

To gain more insight into the photofragments production dynamics of [2-TU · H]⁺ we consider the photofragment spectra acquired across the scan range presented in Figure 3.9 along with the gas-phase absorption spectrum for comparison.

Figure 3.9b shows the production spectrum for m/z 96 (SH loss), the most intense fragment across the entire scanned region, which displays a profile that is very similar to the gas-phase absorption spectrum (Figure 3.9a). The second most intense photofragment is m/z 128 (H loss), which displays the action spectrum displayed in Figure 3.9c. As for the m/z 96 photofragment, m/z 128 peaks strongly across the band II region ($\lambda_{\text{max}} = 5.3$ eV), although its intensity is significantly reduced across band I. Figure 3.9d presents the production spectrum for the m/z 70 photofragment (HNCS loss). This spectrum is very like that of m/z 96, although an additional region of production is also visible in the low-energy region between 3.8–4.2 eV. It is notable that the m/z difference between m/z 128 (Figure 3.9c) and m/z 70 (Figure 3.9d) is 58, which corresponds to the SCN unit. It may be that m/z 128 has a propensity to fragment into m/z 58 over the low-energy region. Indeed, m/z 128 is observed to fragment into lower mass channels at higher HCD energies.

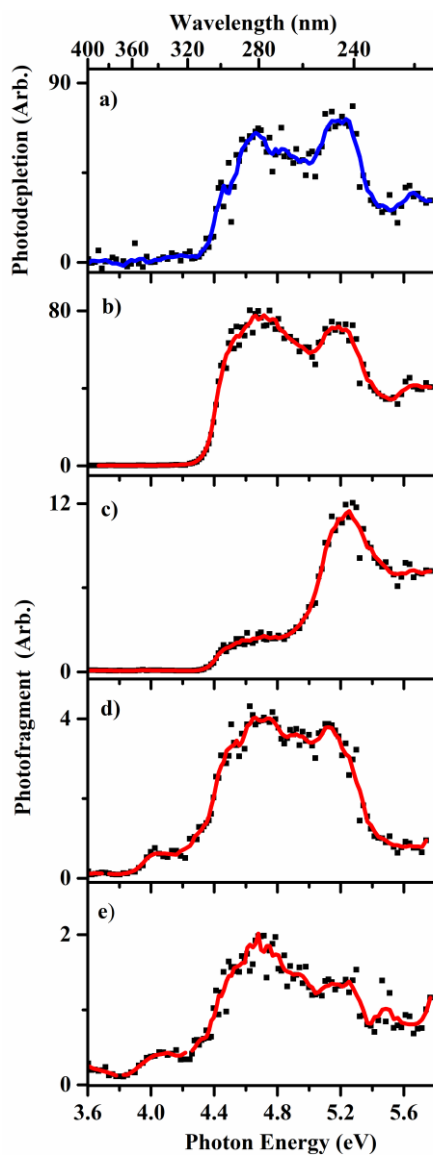


Figure 3.9 (a) Photodepletion spectrum of $[2\text{-TU} \cdot \text{H}]^+$ ions and photofragment action spectra of (b) m/z 96, (c) m/z 128, (d) m/z 70 and (e) m/z 112 generated on photoexcitation across the range 3.6-5.7 eV (344 -214nm). The solid line is a five-point adjacent average of data points.

Finally, the spectrum for the m/z 112 photofragment is shown in Figure 6e. This is similar to the m/z 70 fragment spectrum (Figure 6d), although the relatively lower

intensity of the fragment at higher energies may reflect the fact that it fragments more readily than the other fragments at higher internal energies.

3.4.6 Comparison of Photofragmentation and HCD Fragmentation of [2-TU-H]⁺

When the photofragments observed match the fragments obtained by thermal dissociation of the ground-electronic state as in HCD, the situation is described as “statistical decay”. In contrast, if dissociation occurs directly from the excited state without the involvement of a conical intersection to return the system to a near-starting point geometry, “non-statistical” decay occurs.²⁵⁹ In non-statistical decay, the photofragments obtained will be notably different in their identities and relative intensities from the ground electronic states fragments obtained from HCD thermal dissociation. Our measurements on [2-TU-H]⁺ show a striking difference in the relative intensities of the photofragments compared to the HCD fragments. In the region of band **I**, the photofragments display relative intensities of the order $m/z\ 70 > m/z\ 128 > m/z\ 112$, while in band **II** region, the order changes to $m/z\ 128 > m/z\ 70 > m/z\ 112$. These relative intensities compare to the HCD relative intensities of $m/z\ 112 > m/z\ 70 > m/z\ 128$ in the HCD fragments (Section 3.6.2.1). These differences in intensity, particularly given that $m/z\ 96$ (a purely photochemical fragment) is the major photofragment, indicate that non-statistical decay is dominant. The observation of such non-statistical decay for the isolated, gas-phase ion, is consistent with the photophysical behaviour of 2-TU in solution.²³¹

3.5 Further Discussion

3.5.1 More insight into the photofragmentation dynamics of [2-TU-H]⁻

As discussed above, the gas-phase absorption spectrum of [2-TU-H]⁻ is characterised by two regions which we labelled above as band **I** and band **II**. Band **I** was linked to the existence of a dipole-bound excited state, in the region of the electron detachment threshold. Dipole-bound excited states can decay with the formation of either intact dipole-bound anions, or valence-bound anions (either intact or the products of dissociative electron attachment).^{255,260} For [2-TU-H]⁻, SCN⁻ is produced as a photofragment primarily in the lower-energy part of band **I**. This fragment has been observed in low-energy electron impact studies on 2-thiouracil,²³⁴

suggesting that the initially formed dipole-bound excited state of $[2\text{-TU-H}]^-$ decays via formation of a temporary negative ion, which produces SCN^- as the end ionic fragment through a similar molecular process as 2-TU. The difference in the widths of the SCN^- production spectrum versus the width of band **I** in the photodepletion spectrum is intriguing. One explanation would be that the dipole-bound excited state lies just below an electronic transition of $[2\text{-TU-H}]^-$. This transition would then lie within the free-electron continuum as it is above the VDE (3.82 eV), and can therefore decay via electron detachment, leading to photo-detachment rather than photofragmentation. Indeed, the TDDFT calculations predict that $[2\text{-TU-H}]^-$ displays an electronic absorption at 3.8 eV, in line with this interpretation. Band **II** lies fully within the electron detachment continuum and is therefore expected to correspond largely to direct electron detachment. However, some absorption is likely to be associated with the $\pi\text{-}\pi^*$ transition predicted by the TDDFT calculations at 4.73 eV (Section 3.6.1.4). This excitation is clearly visible in the m/z 93 photofragment action spectrum shown in Figure 3.9c, indicating that the m/z 93 photofragment is produced through direct decay of the excited state accessed in this region. The pattern of photofragment action spectra observed here for the m/z 58 and m/z 93 photofragments is reminiscent of behaviour we observed recently in studies of iodide-nucleobase complexes.^{253,254,261} These complexes similarly display a dipole-bound excited state in the vicinity of the VDE, which decays with production of the respective valence anion produced upon low-energy electron attachment to the nucleobase. At higher energies, a nucleobase-localized electronic transition occurs, which decays primarily with production of a second photofragment. Although two distinctive photofragments would be expected to be produced by these two very different excited states, we observed that both photofragments are produced in the regions of both excited states. This phenomenon appears to be unique to negative ions, and likely reflects coupling of the two excited states via the electron detachment continuum.^{180,262} The dominance of electron detachment following photoexcitation of $[2\text{-TU-H}]^-$ across the UV and hence free radical production, leads to questions as to whether similar decay pathways occur in the condensed phase. Future work would be useful to explore this point directly.

3.5.2 More insight into the photofragmentation dynamics of $[2\text{-TU}\cdot\text{H}]^+$

While the gas-phase absorption spectrum of protonated 2-TU is very similar to that of protonated uracil, its photofragmentation pathways are dramatically different. $[\text{U}\cdot\text{H}]^+$ decays with production of the statistical fragments observed in thermal decay of the ground-state system, while $[2\text{-TU}\cdot\text{H}]^+$ photodecays primarily via ejection of an HS radical. This is true for both the band **I** and band **II** regions, corresponding to the enol-enol and enol-keto tautomers. Thus, it appears that the introduction of the S atom on moving from U to 2-TU perturbs the excited state surfaces of both 2-TU tautomers, so that access to conical intersections facilitating ultrafast decay to the respective electronic ground states is prohibited. This behaviour in the protonated system appears to closely mimic that of neutral thiouracil.²¹⁶ Inspection of the major bright transition for the P1a tautomer of $[2\text{-TU}\cdot\text{H}]^+$ at ~ 5.2 eV reveals that this $\pi \rightarrow \pi^*$ transition corresponds to a reduction of electron density around the sulphur atom (Section 3.6.1.4), promoting C-S photochemical bond fission. The appearance of m/z 128 (H atom loss) as a photochemical fragment is also notable, as photoinduced H loss is a common decay channel for gaseous nucleobases. A similar change in electron density for the band **I** transition is also predicted by the TDDFT calculations of the P2 tautomer (Figure 3.15).

3.6 Conclusion

Laser photodissociation spectroscopy of the deprotonated and protonated forms of the non-natural nucleobase, 2-TU, was performed in the gas-phase for the first time. The gas-phase absorption (photodepletion) spectra of $[2\text{-TU}\cdot\text{H}]^-$ and $[2\text{-TU}\cdot\text{H}]^+$ are highly distinctive. Whereas the gaseous absorption spectrum of $[2\text{-TU}\cdot\text{H}]^-$ displays features that can be attributed to the propensity of the negative ion to photodetach above its electron-detachment threshold, the corresponding spectrum of $[2\text{-TU}\cdot\text{H}]^+$ more closely resembles the ions' solution-phase absorption spectrum.²³¹ The photodecay pathways of the protonated and deprotonated ions are also highly distinctive, with the deprotonated system producing only a small number of very low intensity fragments whereas the protonated system decays with extensive fragmentation.

Previous studies on the photophysics of thiouracil compared to uracil have found that thiolation perturbs the ability of the nucleobase to dissipate harmful UV excitation. Theoretical studies have shown that this occurs due to the initially populated bright S₂ state decaying into the T₁ state.^{225,226} Similar photophysics appears to be present for protonated thiouracil, since the major photoproducts correspond to radical species that are indicative of dissociative triplet state decay. While the behaviour of protonated 2-TU mirrors that of neutral TU,²³¹ our study is the first where the dissociative photoproducts have been identified. Knowledge of the identity of these photoproducts is important for assessing the suitability of thiouracil as a biochemical probe, as well as understanding its mechanistic behaviour as a photopharmaceutical.

3.7 Supplementary Information

3.7.1 Computational studies on $[2\text{-TU-H}]^-$ and $[2\text{-TU-H}]^+$

3.7.1.1 Time dependent density functional theory data of all tautomers of $[2\text{-TU-H}]^-$ and $[2\text{-TU-H}]^+$

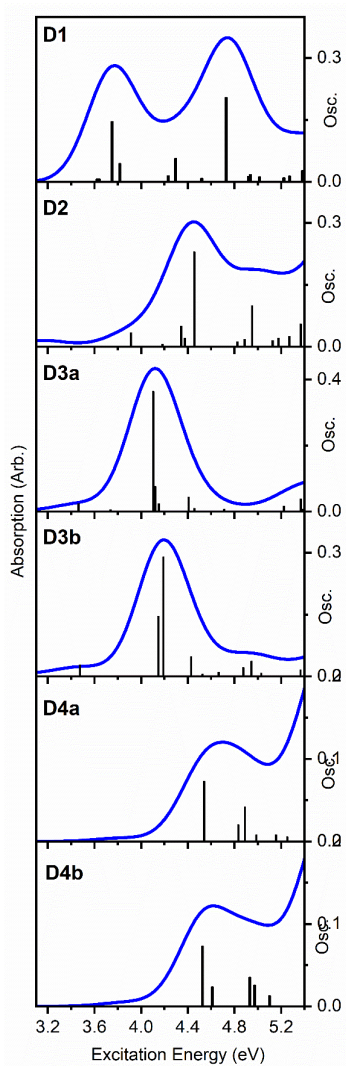


Figure 3.10 Calculated TDDFT excitation energies (with the B3LYP/6-311++G (2d, 2p) functional and basis set) of D1, D2, D3a, D3b, D4a and D4b tautomers of $[2\text{-TU-H}]^-$ geometric structures (Figure 3.2). The oscillator strengths (OSC.) on the

y axis of individual transitions ≥ 0.005 within the experimental scan range are shown by vertical bars, while the full line spectrum is a convolution of the calculated spectrum with Gaussian function (0.25 eV HWHM)

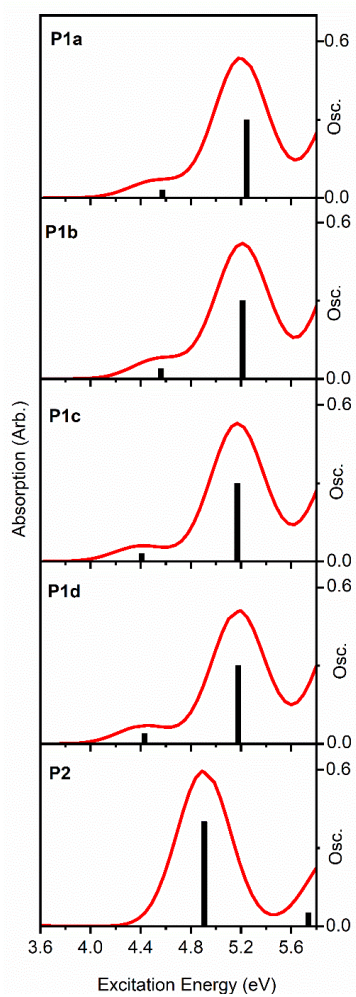


Figure 3.11 Calculated TDDFT excitation energies (with the B3LYP/6-311++G(2d, 2p) functional and basis set) of P1a, P1b, P1c, P1d and P2 tautomer of [2-TU · H]⁺ geometric structures (Figure 3.3). The oscillator strengths (OSC.) on the y axis of individual transitions within the experimental scan range are shown by vertical

bars, while the full line spectrum is convolution the calculated spectrum with Gaussian function (0.25eV HWHM).

3.7.1.2 Relative energies of fragments for each fragmentation pathway of [2-TU - H]⁺ to parent ion energy

The relative energies are calculated with a comparison of the sum of the zero-point energies of the ionic fragments and the neutral or radical fragments with the parent ion zero-point energy. In the secondary fragmentation pathway, the comparison is done with the energy of the ionic parent fragment. This is done with an assumption that the global minima energies of the fragments could give insight into their stability.

$$\text{Parent ion (E)} - (\text{Fragment A(E)} + \text{Fragment B (E)}) = \text{Relative energies}$$

Where E = zero- point energy, fragment A = ionic fragment and fragment B = neutral or radical fragment.

Table 3.4 Relative energies calculated at B3LYP/6-311++G (2d, 2p) (gas phase) for the major fragmentation pathways of [2-TU - H]⁺. All energies are zero point corrected.

	Rel. Energies (eV)
<i>D1 tautomer</i>	0.0
<i>Thiocyanate + Acrylamide</i>	-0.48
<i>Thiocyanate + 3-aminopropan-2-enal</i>	0.207

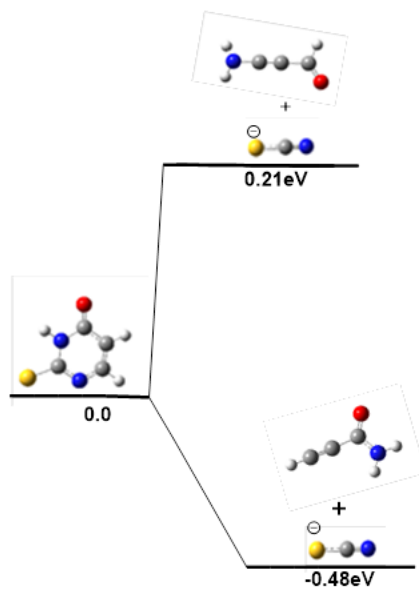


Figure 3.12 Energy diagram for relative energies calculated at B3LYP/6- 311++G (2d, 2p) (gas phase) for the fragmentation pathways of [2-TU - H]⁺.

3.7.1.3 Relative energies of fragments for each fragmentation pathway of [2-TU · H]⁺ to parent ion energy

Table 3.5 Step 1: relative energies calculated at B3LYP/6- 311++G (2d, 2p) (gas phase) for the major fragmentation pathways of [2-TU · H]⁺. All energies are zero point corrected.

	Rel. Energies (eV)
P1 tautomer	0.0
<i>m/z</i> 112 + NH ₃	0.21
<i>m/z</i> 70 + HNCS	0.1

Table 3.6 Step 2: relative energies calculated at B3LYP/6-311++G (2d, 2p) (gas phase) for the possible fragments in the secondary fragmentation pathways of [2-TU · H]⁺ through the ionic fragments m/z 112(A) and m/z 70(B).

A		B	
	Rel. Energies (eV)		Rel. Energies (eV)
m/z 112	0.00	m/z 70	0.00
CO + m/z 84	0.10	m/z 53 + NH ₃	0.29
m/z 52 + m/z 60	0.50		
m/z 59 + m/z 53	0.17		

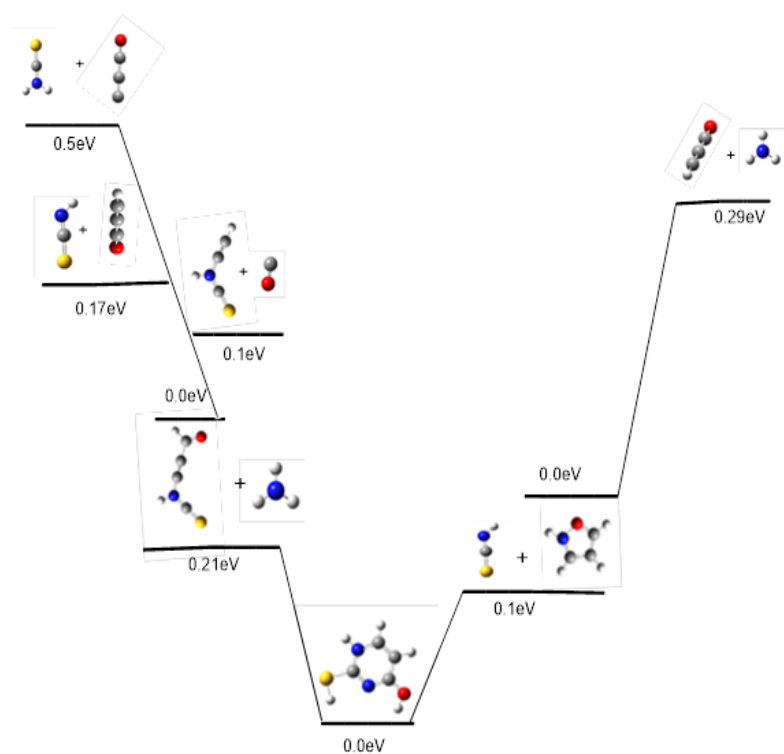


Figure 3.13 Energy diagram for relative energies calculated at B3LYP/6-311++G

(2d, 2p) (gas phase) for the major and the secondary fragmentation pathways of [2-TU · H]⁺

3.7.1.4 Molecular orbital transitions in [2-TU-H]⁻ and [2-TU-H]⁺

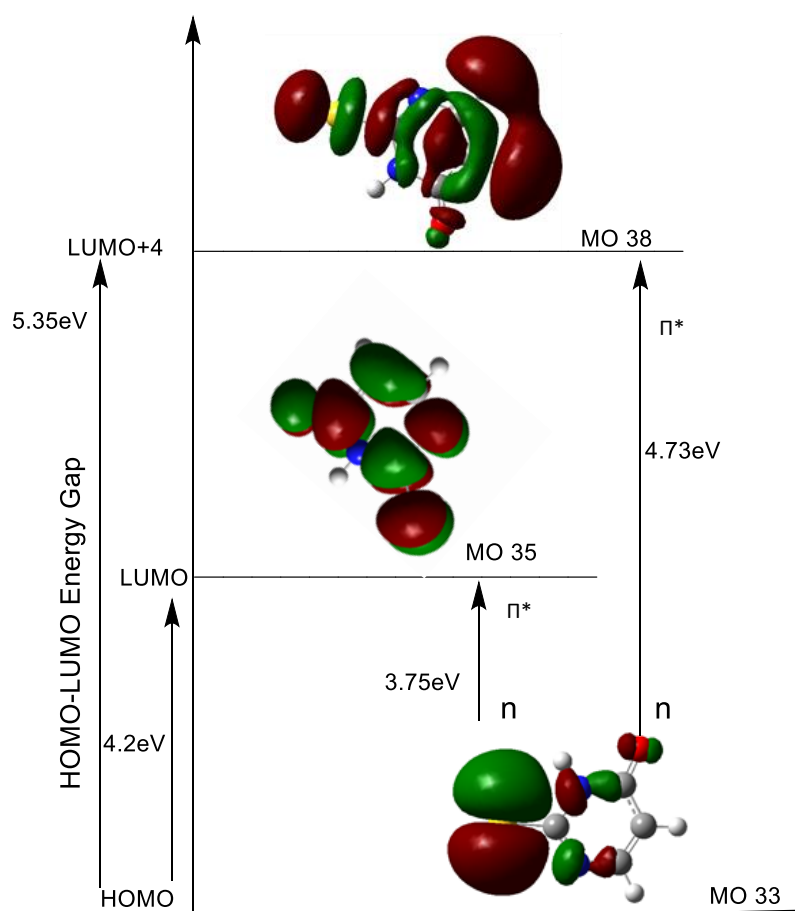


Figure 3.14 Molecular orbital transitions predicted by TDDFT calculations at 3.75 and 4.73 eV for [2-TU - H]⁻

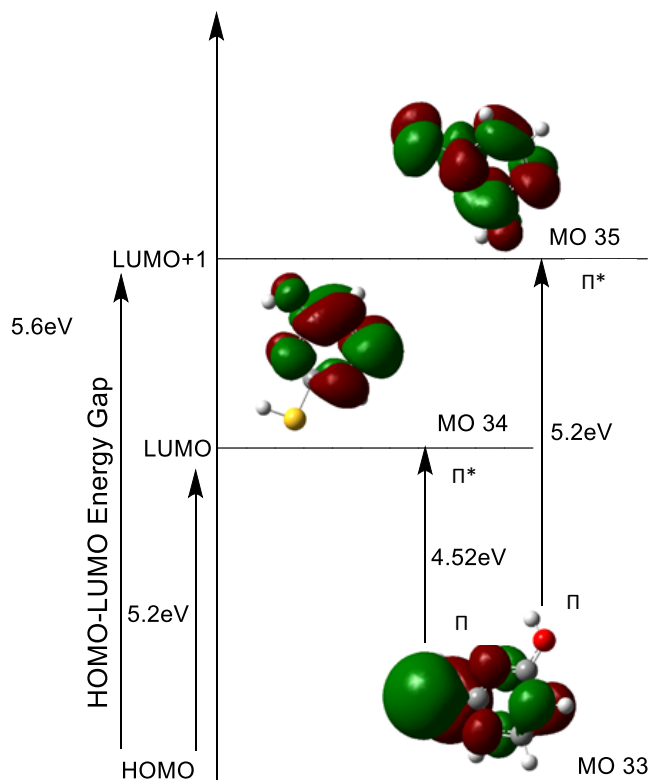


Figure 3.15 Molecular orbital transitions predicted by TDDFT calculations at 4.52 and 5.2 eV for [2-TU·H]⁺

3.7.2 Experimental studies on [2-TU-H]⁻ and [2-TU·H]⁺

3.7.2.1 Higher energy collisional dissociation of [2-TU-H]⁻ and [2-TU·H]⁺

Higher energy collisional dissociation (HCD) was performed on isolated deprotonated and protonated 2-thiouracil to determine the ground state thermal fragments. Fig. 3.10 and 3.11 display as a function of applied % HCD energy, the relative intensities of the deprotonated and protonated 2-thiouracil parent ion and fragments production intensities, respectively.

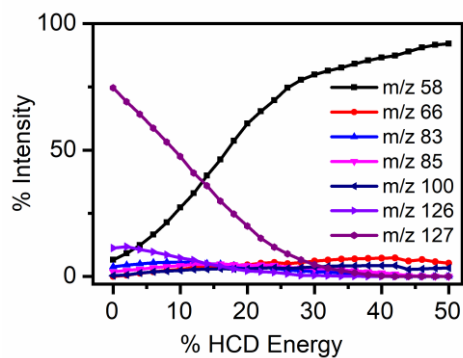


Figure 3.16 Parent ion dissociation curve $[2\text{-TU} - \text{H}]^-$ alongside production curves of the 6 most intense fragments upon HCD between 0 and 50% energy. The data points fitted with the curved lines are viewing guides to show the profile for an individual fragment.

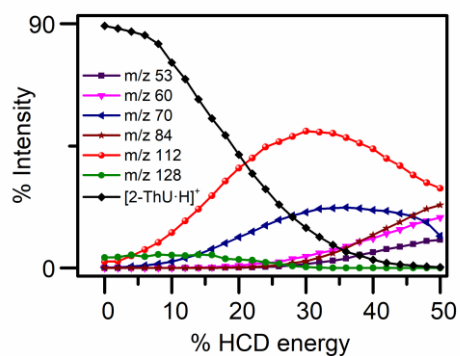


Figure 3.17 Parent ion dissociation curve $[2\text{-TU} \cdot \text{H}]^+$ alongside production curves of five most intense fragments upon HCD between 0 and 50% energy. The data points fitted with the curved lines are viewing guides to show the profile for an individual fragment.

3.7.2.2 Electron detachment spectrum of $[2\text{-TU} - \text{H}]^-$

Figure 3.18 displays electron detachment (ED) yield for $[2\text{-TU} - \text{H}]^-$ ion. We calculate electron loss by assuming that any photodepleted ions that are not detected

as ionic fragments are electron loss because it cannot be directly measured in our instrument. Our instrument cannot also detect ions with $> m/z$ 50

$$\% \text{ Electron Detachment} = [(Photodepletion \text{ ion count} - \sum Photofragment \text{ ion count}) / Int_{OFF}] / (\lambda * p)$$

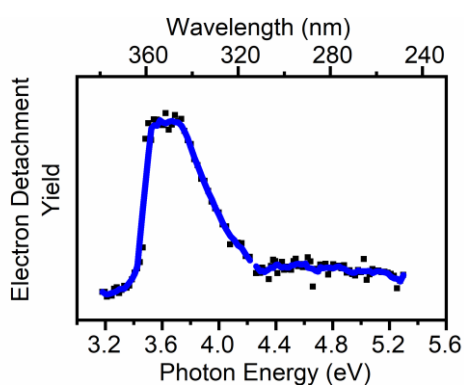


Figure 3.18 Electron detachment yield of mass selected $[2\text{-TU} - \text{H}]^-$ ions, across the range 3.2-5.2 eV (234-390nm). The solid line is a five-point adjacent average of data points.

3.7.2.3 Comparison of photodepletion and solution phase absorption spectra of $[2\text{-TU} - \text{H}]^-$

Figure 3.19 (a) displays the gas-phase photodepletion spectrum (absorption spectrum) and (b) solution phase absorption spectrum of $[2\text{-TU} - \text{H}]^-$ across the range 3.2-5.3 eV (234-390nm). The high intensity absorption band labelled (I) shows absorption from 3.2 to 4.2 eV which peaks at ($\lambda_{\text{max}} = 3.7$ eV). The lower intensity band with broad absorption band labelled (II) has an onset at 4.2 and absorption cross section from 4.2 to 5.2 eV.

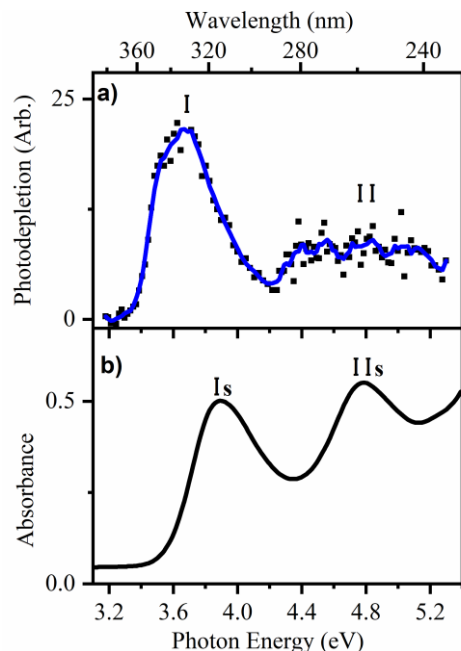


Figure 3.19 (a) Gas-phase photodepletion spectrum (absorption spectrum) of [2-TU - H] across the range 3.2-5.3 eV (234-390nm). The solid line is a five-point adjacent average of data points. (b) Absorption spectrum ($1 \times 10^{-4} \text{ mol dm}^{-3}$ in MeOH) at a pH of 11.

The solution-phase spectrum obtained under basic condition is displayed in Figure 3.19. This spectrum shows two resolved band maxima at **I_s** (3.9 eV) and **I_{Is}** (4.8 eV). The **I** and **II** labelling of the bands is to help in their identification, while the subscript **S** added in the solution-phase labelling is to differentiate the phases. The gas-phase and solution-phase spectra are quite similar round band I and the difference around band II may be attributed to the strong influence of electron detachment in this region in the gas phase. The calculated relative energies presented in Table 1 show that only D1 tautomer dominates in the gas phase while the solution-phase may have D2 present. This could explain the modification found in the solution phase spectra. The TDDFT spectrum of the optimized D1 structure calculated in the gas phase gave similar spectra to the solution-phase UV-VIS spectra generated because it is known to predict better chromophore centred transitions.

3.7.2.4 Comparison of photodepletion and solution-phase absorption spectra of $[2\text{-TU} \cdot \text{H}]^+$

Figure 3.20a displays the photodepletion spectra of $[2\text{-TU} \cdot \text{H}]^+$ acquired in the gas phase within the scan range of 3.6 – 5.8 eV. The spectrum has two resolved bands labelled **I** and **II** with λ_{max} at 4.68 eV and 5.3eV respectively. Band **I** is broad with a cross-section of 0.94 eV while band **II** is narrower with a width of $\sim 0.3\text{eV}$.

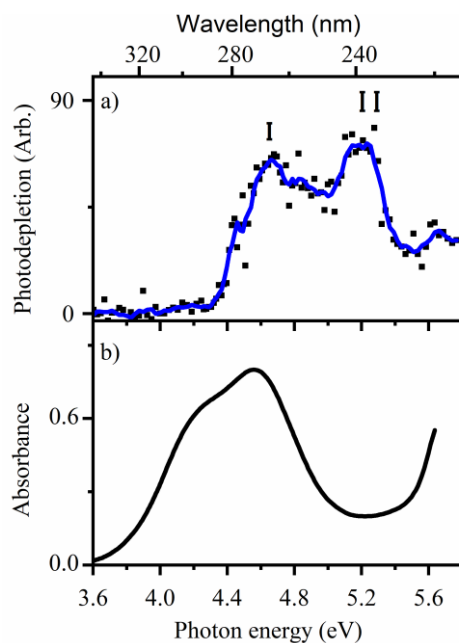


Figure 3.20 (a) Gas-phase photodepletion spectrum (absorption spectrum) of $[2\text{-TU} \cdot \text{H}]^+$ across the range 3.6-5.7 eV (344 -214nm). The solid line is a five-point adjacent average of data points. (b) Absorption spectrum ($\sim 1 \times 10^{-4} \text{mol dm}^{-3}$ in MeOH) at a pH of 3.7.

Figure 3.20b shows the solution-phase spectrum of protonated 2-thiouracil obtained under acidic conditions. This absorption spectrum is in good agreement with the spectrum obtained for 2-thiouracil in methanol as (Ref. 263). Two unresolved peaks can be discerned in the spectrum with a strong peak at 4.58 eV and a shoulder at 4.26 eV. It has been reported that the main peak and the shoulder become more resolved when the spectrum is measured in acetonitrile solvent and, in contrast, they merge into one broader peak in water. It has also been suggested that there are two electronic absorption origins sensitive to the polarity of solvent.²⁶³ It may be because

of the reduced perturbation of solvent environment in gas-phase experiments, that the two origins' absorptions become more distinct. The TDDFT obtained spectra for the tautomers showed similar spectra for P1a, P1b, P1c, P1d and a different absorption profile for P2 optimised structures. In the gas spectra, two tautomers appear to contribute to the absorption spectrum. The TDDFT obtained results for all the tautomers are presented in Figure 3.11.

3.7.2.5 Photofragmentation mass spectrum of $[2\text{-TU} \cdot \text{H}]^+$

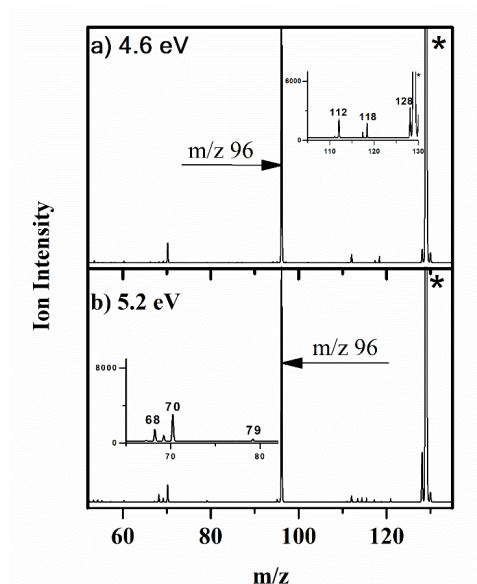


Figure 3.21 Photofragment difference (laseron – laseroff) mass spectrum of $[2\text{-TU} \cdot \text{H}]^+$ excited at 4.6 and 5.2eV (344nm). *Represents parent ion signal with m/z 127.

Chapter 4

Photodissociation Spectroscopy of Iodide Ion-Thiouracil Clusters: Mapping Chromophore Excitations on the Electron Detachment Spectrum

This work has been published in the journal *Physical Chemistry Chemical Physics*. All experimental and computational data has been collected, formally analysed, and investigated by me. The initial draft of the manuscript was prepared by me and revised by Caroline Dessent.

The electronic supplementary information included with the publication is attached to this chapter as Section 4.6.

Full Reference to the publication:

“Photodissociation Spectroscopy of Iodide Ion-Thiouracil Clusters: Mapping Chromophore Excitations on the Electron Detachment Spectrum”

“DOI: 10.1039/D0CP05920J (Paper) Phys. Chem. Chem. Phys., 2021, 23, 1021-1030” (PCCP HOT ARTICLE 2021)

4.1 Abstract

Laser photodissociation spectroscopy (3.1–5.7 eV) has been applied to iodide complexes of the non-native nucleobases, 2-thiouracil (2-TU), 4-thiouracil (4-TU) and 2,4-thiouracil (2,4-TU), to probe the excited states and intra-cluster electron transfer as a function of sulphur atom substitution. Photodepletion is strong for all clusters (I·2-TU, I·4-TU and I·2,4-TU) and is dominated by electron detachment processes. For I·4-TU and I·2,4-TU, photodecay is accompanied by the formation

of the respective molecular anions, 4-TU⁻ and 2,4-TU⁻, behaviour that is not found for other nucleobases. Notably, the I·2-TU complex does not fragment with formation of its molecular anion. We attribute the novel formation of 4-TU⁻ and 2,4-TU⁻ to the fact that these valence anions are significantly more stable than 2-TU⁻. We observe further similar behaviour for I·4-TU and I·2,4-TU relating to the general profile of their photodepletion spectra, since both strongly resemble the intrinsic absorption spectra of the respective uncomplexed thiouracil molecule. This indicates that the nucleobase chromophore excitations are determining the clusters' spectral profile. In contrast, the I·2-TU photodepletion spectrum is dominated by the electron detachment profile, with the near-threshold dipole-bound excited state being the only distinct spectral feature. We discuss these observations in the context of differences in the dipole moments of the thionucleobases, and their impact on the coupling of nucleobase-centred transitions onto the electron detachment spectrum.

4.2 Introduction

The production of low-energy secondary electrons when high-energy radiation passes through biological molecules is a well-known phenomenon.^{264,265} In biological systems, these low-energy electrons ($\leq 10\text{eV}$) can induce single and double-strand breaks in DNA, leading to mutations and genetic damage.^{106,266-269} Quantum chemistry calculations have revealed that the nucleobase may be the initial site of electron attachment in DNA, with the resulting transient negative ion (TNI) corresponding to either a valence-bound anion via attachment to the base's π orbital or a dipole-bound anion.²⁷⁰⁻²⁷³ Experiments probing dissociative electron attachment have shown that an initially formed dipole-bound state can act as a gateway to the valence-bound anion.²⁷⁴ Due to the importance of low-energy electron-nucleobase interactions, a wide range of experiments have been performed to characterise the molecular dynamics involved.²⁷⁵⁻²⁸¹ One such series of experiments have involved iodide ion-nucleobase clusters,^{252,253,261,282-287} Photoexcitation of such clusters can be accomplished in the gas-phase, providing a highly-controllable environment for probing low-energy electron-nucleobase coupling. The experimental approach is based on the concept that the iodide ion is photodetached to produce a 'spectator' iodine atom and a low-energy free electron with a well-defined kinetic energy that can be captured by the adjacent molecule.^{260,287} The resulting TNI dynamics can then

be monitored either via time-resolved photoelectron spectroscopy or photofragment action spectroscopy.

In this work, the first study of complexes of iodide with the non-native nucleobases, 2-thiouracil (2-TU), 4-thiouracil (4-TU) and 2,4-thiouracil (2,4-TU) which are illustrated in Figure 4.1 is presented. The aim is to probe how the cluster excited states are modified by the presence of one or more sulphur atoms in a non-native nucleobase. Thiolated nucleobases are synthetic analogues of native nucleobases that have been applied in radiation therapy and photodynamic therapies for some time,^{205,211-213} motivating theory and experiments to understand their fundamental photochemical and photophysical behaviour. Investigations have focused on understanding their photodynamics through comparison with native nucleobase excited-state potential energy surfaces and relaxation pathways.²¹⁴⁻²²⁷ Given that thionucleobases are employed in both radiation therapy and phototherapy, we aim here to obtain novel experimental information on how free electrons interact with thiolated nucleobases, both in the electronic ground and excited states.^{234,235}

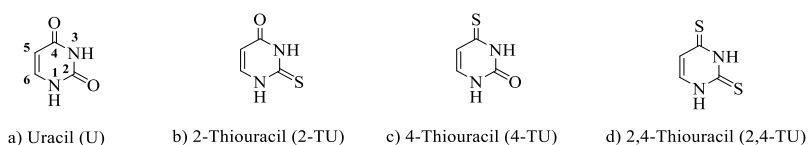


Figure 4.1 Schematic diagram of uracil (U), 2-thiouracil (2-TU), 4-thiouracil (4-TU) and 2,4-Thiouracil (2,4-TU), illustrating how the C₂ - C₄ oxygens of uracil are replaced with sulphur.

Low energy interactions with 2-thiouracil have been studied recently in a crossed-beam apparatus by Abdoul-Carime and co-workers.^{234,288} Electron-attachment was shown to produce three major anionic fragments, with deprotonated 2-thiouracil being the major product, followed by the thiocyanate anion and the sulphur anion. The loss of hydrogen to form the deprotonated anion was initially suggested to occur from a mixture of carbon or nitrogen sites,^{234,235} but was later found to arise from rupture of the N-H bond.^{288,289} It was also established that molecular dissociation resulted from the initial step of dissociative electron attachment occurring through

dipole-bound anion formation. Further experiments with 1-methyl-2-thiouracil gave fragments in line with this pattern of dissociative electron attachment, where significant loss of the methyl group from the N1 position was also seen.²⁸⁸ No work has been conducted to date to characterise the low energy electron scattering properties of 4-TU and 2,4-TU. It is noted that the electronic spectrum of the deprotonated form of 2-TU has been studied recently via laser photodissociation,²⁸ and photodetachment photoelectron spectroscopy has been employed to characterize the molecular anions, [4-TU]⁻ and [2,4-TU]⁻.^{290,291}

4.3 Experimental and Computational Method

4.3.1 Experimental method

The UV photodissociation experiment was conducted using a modified AmaZon (Bruker) ion-trap mass spectrometer that has been converted for laser experiments as has already been described in detail.^{20,238} The I⁻·2-TU, I⁻·4-TU and I⁻·2,4-TU clusters were generated by electrospraying solutions of thio-nucleobases and iodide in 98% acetonitrile (MeCN) and 2% deionized water (TUs solutions were made at 1×10^{-4} mol dm⁻³, mixed with cesium iodide solution (CsI) at 1×10^{-4} mol dm⁻³). 2-TU was purchased from Acros organics and 4-TU and 2,4-TU from Sigma while CsI was purchased from Avocado Research Chemicals Limited. All the chemicals were used without any further purification.

UV photons produced by an Nd:YAG (10 Hz, Surelite) pumped optical parametric oscillator (OPO) (Horizon) laser were used to irradiate mass isolated I⁻·TU clusters across the range 400–218nm (3.1–5.7eV). The solution was introduced into the mass spectrometer by electrospray ionisation (ESI) using a nebulizing gas pressure of 12 psi, an injection rate 0.35 ml h⁻¹, a drying gas flow rate of 10 ml min⁻¹ and run-in negative ion mode at capillary temperatures of 100°C. Photofragmentation experiments were run with an ion accumulation time of 100 ms with a fragmentation time of 100 ms, (one laser pulse per each ion packet) thereby limiting multiphoton processes. For systems where fluorescence is negligible,²³⁹ UV excited gaseous ions can fragment following excitation and produce a gas-phase absorption spectrum by photodepletion.^{24,28,48,238} These scans were conducted using a 2 nm step size increase, and the mass selected I⁻·TU clusters ion depletion intensities were taken as the gaseous absorption after irradiation. Photodepletion (PD) and photofragment

production (PF) were calculated as described in Chapter 2.

An Orbitrap Fusion Tribrid mass spectrometer (Thermo Fisher Scientific, Waltham, MA, USA) with an ESI source was employed to perform a higher-energy collision dissociation (HCD) to explore the ground-state fragmentation characteristics of I[•]-TU clusters and run-in negative ion mode. The HCD fragmentation technique using the Orbitrap mass spectrometer gives tandem mass spectrometry which is similar to triple quadrupole fragmentation.^{182,240,241} The instrument was operated with the following parameters: sweep gas flow rate, 0; sheath gas flow rate: 2.0; aux gas flow rate: 2.5; ion transfer tube temperature: 275 °C; vaporizer temperature: 30 °C; MS1 detector: Ion Trap; MS1 scan range: 80–300; MS1 maximum injection time 100 micros; MS2 detector: Ion trap; MS2 maximum injection time: 100 ms. HCD collisional energy was varied between 0% and 40%.

4.3.2 Computational method

Electronic structure calculations were conducted using Gaussian 09.¹⁸⁷ Cluster structures investigated were based on the six tautomers of the thiouracils. These were optimized at the B3LYP/6-311++G(2d,2p) level, with 6-311G(d,p)/SDD for I. The vertical dipole moment (i.e. the dipole moment of the neutral cluster at the ground-state geometry of the anionic cluster) of the clusters was calculated at the MP2/ 6-311++G(2d,2p) level, with 6-311G(d,p)/SDD for I. Global energy minima were confirmed for all optimized structures by performing frequency calculations. Time-dependent density functional theory (TDDFT) calculations were performed on the lowest-energy optimised tautomers of the I[•]-2-TU, I[•]-4-TU and I[•]-2,4-TU clusters to assign and describe the excited electronic state transitions. Several functionals were tested, with the calculations presented representing the best match to experiment. The equation of motion coupled cluster single and doubles (EOMCCSD) calculation was used to explore the dipole-bound excited state of I[•]-2-TU.

4.4 Results

4.4.1 Geometric structures and TDDFT of the I[•]-TU clusters

Figure 4.2 shows the lowest energy structures of the I[•]-2-TU, I[•]-4-TU and I[•]-2,4-TU clusters. (I[•]-TU will be used when we are discussing the group of clusters.) The

calculated structures are in good agreement with previous calculations of similar systems.^{252,253,261}

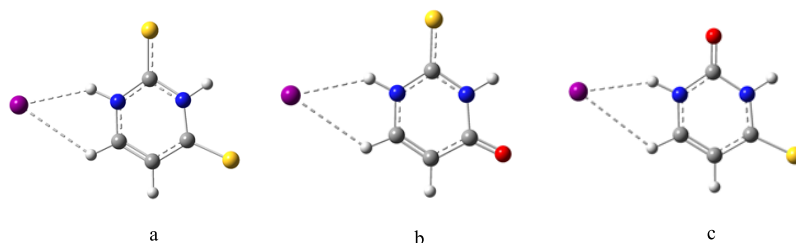


Figure 4.2 Global minima geometric structures of I·TU clusters optimised at the B3LYP/6-311++G(2d,2p) level of theory with SDD on I. TU = (a) 2,4-TU, (b) 2-TU and (c) 4-TU.

Additional calculations were conducted on other tautomers (Section 4.7.1.1), but the resulting cluster structures were found to have higher relative energies. In the lowest-energy structures (Figure 4.2), the iodide ion hydrogen bonds to the nucleobases in a planar geometry through the N1 H and the C6 H at a bond length of 2.661 Å and 3.018 Å for I·2,4-TU, I·2-TU and I·4-TU, respectively. At this location, the iodide ion is bound close to the axis of the permanent dipole moment of the thiouracil (Section 4.7.1, Figure 4.9).

Table 4.1 displays the calculated vertical detachment energies (VDEs), binding energies and the vertical dipole moments for the clusters.

Table 4.1 Calculated vertical detachment energies (VDE), cluster binding energies^a and vertical dipole moment^b using B3LYP/MP2 functional with 6-311++G(2d,2p)/SDD basis set.

Cluster	I·2,4-TU	I·2-TU	I·4-TU
VDE (eV)	4.31	4.30	4.26
Cluster BE (kJ mol ⁻¹)	105.90	96.99	103.47
Vertical dipole moment (D)	7.09	6.68	7.10
Monomer dipole moment ^c (D)	4.67	4.20	4.47

^aAll binding energies are BSSE corrected. ^bThe vertical dipole moment is calculated with MP2/6-311++G(2d,2p)/SDD level of theory. ^c Ref. 295.

We note that the calculated vertical dipole moments which is the dipole moment of the neutral cluster at the ground-state geometry of the anionic cluster indicates that all three clusters are sufficiently polar to support a dipole-bound state.²⁹²⁻²⁹⁴

The VDEs of the three clusters are similar to that of the native nucleobase cluster, I·U. As the experimentally measured VDE of I·U is 4.11 eV, while the calculated VDE is 4.30 eV,²⁶¹ we expect that the experimental values for the I·TU clusters are also likely to be around 4.1 eV. I·4-TU and I·2,4-TU are calculated to possess very similar vertical dipole moments and cluster binding energies, a result that is unsurprising given that 4-TU and 2,4-TU have similar dipole moments.²⁹⁵ In contrast, the dipole moment of 2-TU is much closer to that of uracil. Indeed, the dipole moment of uracil derivatives is known to increase significantly on thiolation at the C4 position.²⁹⁵

To gain further insight into the nature of the electronic transitions involved in the photoexcitation of I·TU clusters across the 3.1–5.8 eV range, TDDFT calculations were performed. The TDDFT calculated excitation spectra of I·TU clusters representing the best match to experiment for the lowest energy tautomers of the clusters are presented in Figure 4.3. (See Figure 4.10 for TDDFT calculated excitation spectra using B3LYP functional). Although TDDFT is known not to predict accurately the transitions of a dipole bound-excited state, within the scope of our work it gives a sufficient guide for interpreting the experimental results. Improved representation of dipole-bound excited state transition intensity could be acquired by using a tailored and diffused functional centred on the dipole bound orbital.²⁴⁴⁻²⁴⁶ The full TDDFT spectra of individual tautomers of the clusters, along with the oscillator strengths of the different transitions are presented in Section 4.7.1.

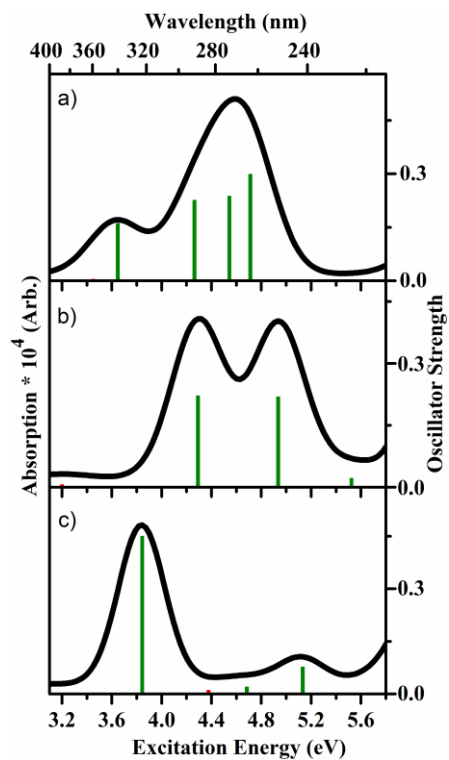


Figure 4.3 TDDFT excitation spectra of a) I·2,4-TU, b) I·2-TU and c) I·4-TU clusters calculated at M062X/DEF2SVP. The oscillator strengths on the y axis of individual transitions ≥ 0.005 within the experimental scan range are shown by vertical bars while the full line spectrum is a convolution of the calculated spectrum with Gaussian function (0.25 eV HWHM). The red lines represent transitions from an iodide p-orbital and the green lines represent transitions from the thio-nucleobase (TU) π orbital.

The TDDFT spectra will aid in assigning and interpretation of the experimental photo-excited state transitions within the I·TU clusters.

4.4.2 Photodepletion spectra of I·TU clusters

Figure 4.4 a-c shows the photodepletion spectra of the I·TU clusters collected across the range of 3.1-5.7 eV. The three spectra are strikingly different, which suggests that Sulphur atom substitution at different positions in a thio-nucleobase moiety contributes strongly to the electronic excited-state behaviour. Figure 4.4 d-f displays

the aqueous absorption spectra unclustered TU. The photodepletion and absorption spectra are presented together to aid comparison.

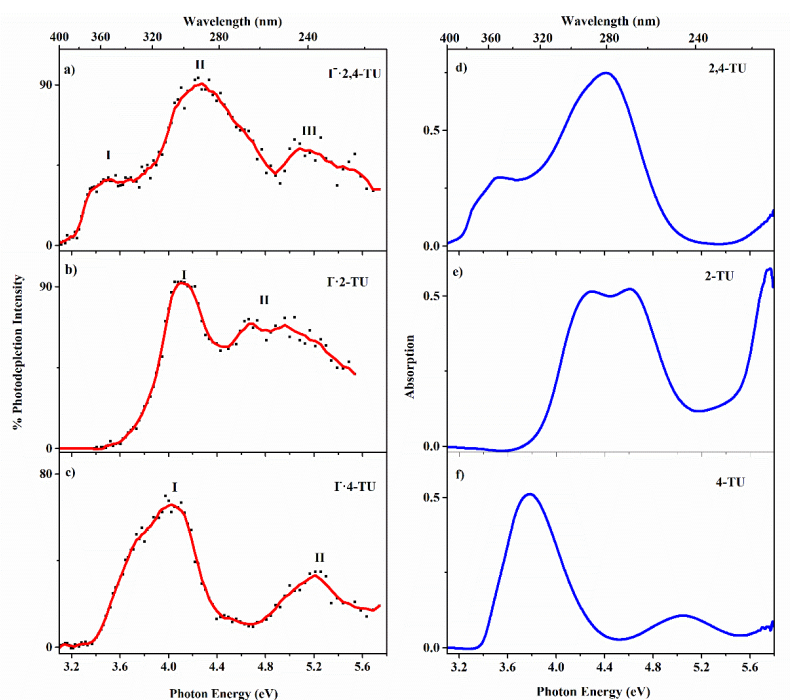


Figure 4.4 Photodepletion (gas-phase absorption) spectra of (a) I·2,4-TU, (b) I·2-TU and (c) I·4-TU across the range 3.1–5.7 eV. The solid line is a five-point adjacent average of the data points. Aqueous absorption spectrum of (d) 2,4-TU, (e) 2-TU and (f) 4-TU across the range 3.1–5.8 eV (400–213 nm).

The photodepletion spectrum of I·2,4-TU (Figure 4.4a) displays an onset at 3.2 eV and two band maxima (I and II) at 3.5 eV and 4.3 eV. A third broad band (III) is evident across the high energy region. Comparing the photodepletion spectrum of I·2,4-TU to the solution-phase absorption spectrum of 2,4-TU (Figure 4.4d),²⁹⁶ it is striking to observe that the solution-phase spectrum of the (unclustered) thiouracil is very similar to the gas-phase absorption spectrum of the cluster. The 2,4-TU solution-phase spectrum has two bands with energies and intensities close to bands I and II of the gaseous cluster spectrum.²⁹⁶ This indicates that the absorption spectrum of the 2,4-TU chromophore dominates the spectrum of its iodide cluster.

Band III of the photodepletion spectrum is absent from the solution-phase spectrum. The I·2-TU photodepletion spectrum has an onset at approximately 3.6 eV and displays a strong absorption band (I) between 3.6–4.3 eV with λ max at 4.2 eV, followed by a flatter, broad absorption region (II) between 4.6–5.6 eV. For this thionucleobase, the 2-TU monomer spectrum (Figure 4.4e) does not mirror the I·2-TU gaseous cluster spectrum since the monomer spectrum displays a broad region of absorption between 3.8–4.8 eV.²⁹⁶ Finally, Figure 4.4c shows the gas-phase photodepletion spectrum of I·4-TU, which displays an onset at 3.4 eV, with a first strong and broad absorption band (I) peaking at 4.02 eV. (A shoulder feature, centred close to 3.8 eV, is evident on the band's low-energy side.) A higher-lying absorption band (II) is evident from 4.76 to 5.56 eV. Intriguingly, the solution-phase spectrum of 4-TU (Figure 4.4f),²⁹⁶ and the I·4-TU cluster photodepletion spectrum are again very similar.

4.4.3 Photofragment mass spectra of the I·TU clusters

Figure 4.5 displays the photofragment mass spectra obtained when the I·TU clusters are excited at their absorption maxima, with Table 2 listing the photofragments observed and assignments. The most intense photofragment for all the clusters is the m/z 127 photofragment, with different minor photofragments being produced by the three clusters. It is notable that all of these photofragments are low intensity, indicating that the major channel for decay is through electron detachment.

Table 4.2 Lists of photofragments with assignments observed at the Band I maxima of the I·TU clusters, shown with the HCD collision-induced dissociation fragments^a.

	I·2,4-TU	I·2-TU	I·4 TU
Photofragments			
<i>m/z</i> 58	✓(SCN ⁻)	✓(SCN ⁻)	X
<i>m/z</i> 127	✓(I)	✓(I / [2-TU-H])	✓(I / [4-TU-H])
<i>m/z</i> 128	-	X	✓([4-TU-H])
<i>m/z</i> 143	✓([2,4-TU-H])	-	-
<i>m/z</i> 144	✓([2,4-TU])	-	-
HCD fragments			
<i>m/z</i> 126.90522	✓major (I)	✓major (I)	✓major (I)
<i>m/z</i> 126.99735	-	✓minor([2TU-H])	✓minor([4TUH])
<i>m/z</i> 142.97402	✓minor ([2,4-TU-H])	-	-

^aX = Not Seen

For $I\cdot 2,4\text{-TU}$, the m/z 127 photofragment can be straightforwardly assigned to $I\cdot$, however for $I\cdot 2\text{-TU}$ and $I\cdot 4\text{-TU}$, m/z 127 can correspond to either $I\cdot$ or the deprotonated anions of 2-TU and 4-TU at the resolution of the laser-interfaced mass spectrometer.^{20,238}

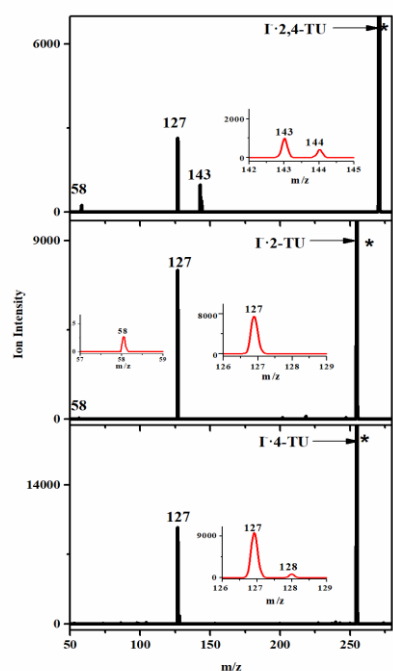


Figure 4.5 Photofragment difference (laser_{on} – laser_{off}) mass spectrum of $I\cdot$ TU clusters excited at 3.5 eV (354 nm), 4.2 eV (295 nm) and 4.0 eV (310 nm) photodepletion band maxima of the individual $I\cdot$ -TU clusters, respectively. * Represents the precursor cluster ion signal.

For other iodide–nucleobase clusters we have studied,^{252,253,261,286} we have observed both $I\cdot$ and the respective deprotonated nucleobase as photofragments, indicating that the m/z 127 peak present for $I\cdot 2\text{-TU}$ and $I\cdot 4\text{-TU}$ likely corresponds to a mixture of $I\cdot$ and $[2\text{-TU-H}]^-$ or $[4\text{-TU-H}]^-$.²⁹⁷ For $I\cdot 2,4\text{-TU}$, we do indeed observe the deprotonated anion $[2,4\text{-TU-H}]^-$ as a photofragment with m/z 143. Surprisingly, the molecular anion, i.e. TU, is observed as a photofragment from both $I\cdot 2,4\text{-TU}$ and $I\cdot 4\text{-TU}$, despite the fact that the corresponding nucleobase anions have not been observed as photofragments from other iodide–nucleobase complexes.^{252,253,261,286}

m/z 58 is the final photofragment observed. This ion corresponds to SCN^- , which is one of the major dissociative electron attachment product following electron attachment to 2-TU. We note that dissociative electron detachment to 2-TU also results in production of the $[\text{2TU-H}]^-$ and S^- anions.^{234,235,288} While $[\text{2TU-H}]^-$ appears to be produced in our experiment, S^- cannot be detected as its mass is below the cut-off of the ion trap.^{20,238} If S^- is being produced as an undetected photofragment in our experiment, its intensity should be comparable to that of SCN^- .^{234,235,288}

Finally, the ^{34}S isotope occurs with around 4.5% intensity, and studies of this cluster isotope could clarify the ambiguity in the identities of the photofragments for the $\text{I}\cdot\text{2-TU}$ and $\text{I}\cdot\text{4-TU}$ clusters. These experiments were not, however, possible here as even using the major ^{32}S isotope clusters, the $[\text{TU-H}]^-$ photofragments were close to the detection limits of our instrument.

4.4.4 Photofragments production spectra of $\text{I}\cdot\text{TU}$ clusters

Figure 4.6 displays the photofragment production spectra associated with $\text{I}\cdot\text{2,4-TU}$, shown with the photodepletion spectrum (Figure 4.6a) for comparison.

I^- (Figure 4.6b) is the most intense photofragment and is produced across the entire photodepletion spectrum with peaks in production through the band I and band II maxima. $[\text{2,4-TU-H}]^-$ is the second most intense fragment (Figure 4.6c). This photofragment's production is also maximised through the band I and II maxima, although its production drops sharply after the band II peak. The $[\text{2,4-TU}]^-$ fragment production profile (Figure 4.6d) is similar to that of $[\text{2,4-TU-H}]^-$ through the band II region, although its production through the band I region is somewhat lower. Finally, the production spectrum of the very low intensity photofragment, SCN^- , is shown in Figure 4.6e. This photofragment displays a distinctive production profile, with an onset at 3.65 eV, and production across a region that peaks just above the band II maximum.

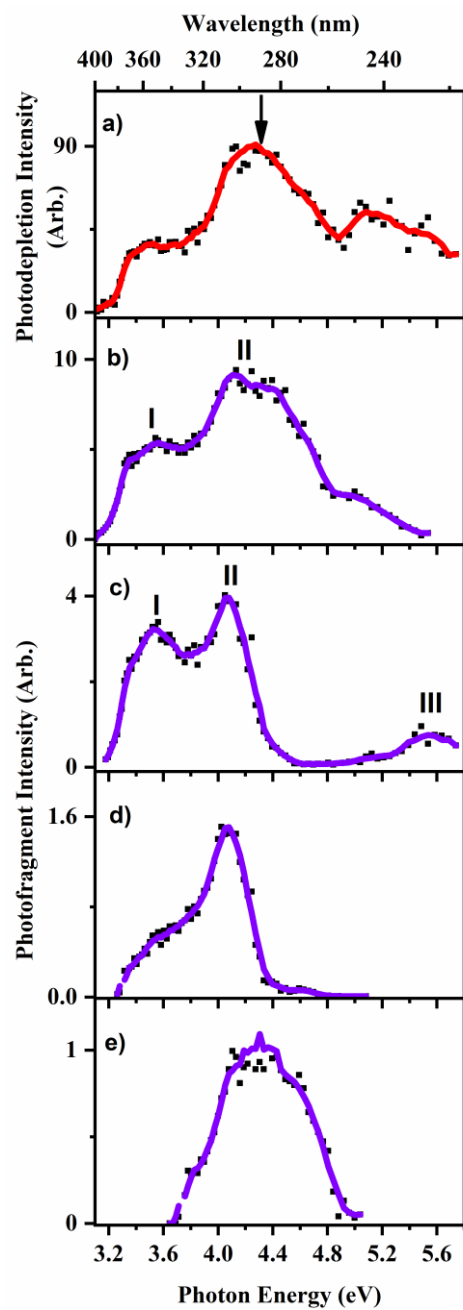


Figure 4.6 (a) Gas phase photodepletion spectra of I·2,4-TU with the b) I, c) [2,4-TU-H]⁻, d) [2,4-TU]⁻ and e) SCN⁻, across the range 3.1-5.7 eV (400-218nm). The

solid line is a five-point adjacent average of the data points, while the arrow represents the calculated VDE.

The m/z 127 (Γ and [2-TU-H] $^+$) photofragment action spectrum produced from Γ ·2-TU across the region 3.1–5.7 eV is presented with the photodepletion spectrum for comparison in Figure 4.7.

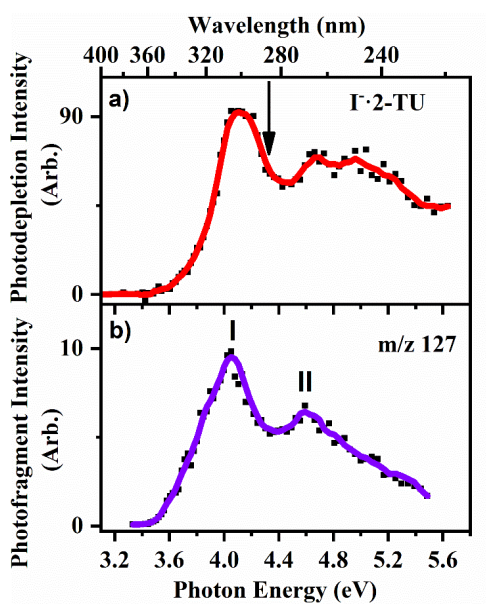


Figure 4.7 a) Gas phase photodepletion spectrum of the Γ ·2-TU cluster and b) the m/z 127 photofragment action spectrum, across the range 3.1–5.7 eV (400–218nm). The solid line is five-point adjacent average of data point while the arrow represents the calculated VDE.

The photofragment production spectrum peaks at ~ 4.04 eV (I) and ~ 4.6 eV (II), before tailing off to higher energies.

Figure 4.8 displays the photofragment production spectra for Γ ·4-TU, along with the photodepletion spectrum. The m/z 127 (Γ and [4-TU-H] $^+$) photofragment spectrum peaks at the band I maximum of 3.81 eV, and again with lower intensity (II) around 5.1 eV.

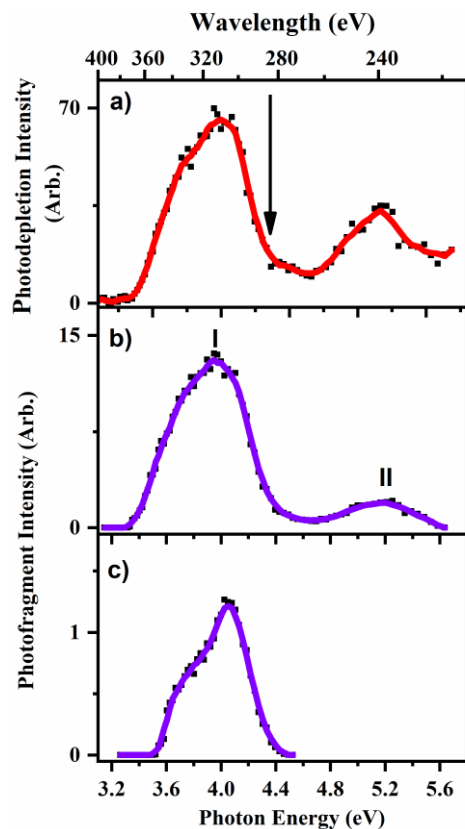


Figure 4.8 a) Gas phase photodepletion spectrum of the $\text{I}\cdot\text{4-TU}$ cluster and photofragment action spectra of b) m/z 127 and c) $[\text{4-TU}]^-$ across the range 3.1-5.7 eV (400-218nm). The solid line is a five-point adjacent average of data point, while the arrow represents the calculated VDE.

The m/z 128 molecular ion photofragment, $[\text{4-TU-H}]^-$ (Figure 4.8c), is produced only within the band I region, with an onset at 3.5 eV. Its production spectrum displays a shoulder at ~3.6 eV prior to a well resolved peak at 4.1 eV, with intensity that falls away sharply after the peak.

It is worthy to note that although the photofragment intensities are arbitrary, they can be directly compared for the photofragments from this cluster, providing a measure of branching ratio.

4.5 Discussion

4.6 4.5.1 General overview of photodecay channels

In the absence of fluorescence, photoexcited I·TU clusters can decay through several decay channels. The possible decay pathways for the I·TU clusters are given below.

The first group of fragmentation channels correspond to ionic fragmentation channels:

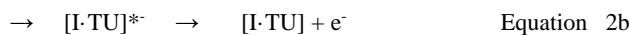


On the other hand, at energies above the electron detachment energy of the I·U clusters, excited-state decay is possible through direct electron detachment or indirect processes that are the result of different excited states of the cluster 2a-2b or through electron detachment from hot fragments 2c-2d:

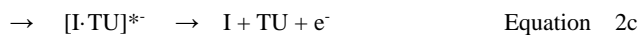
Electron detachment channels



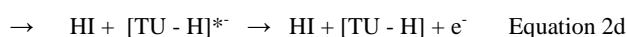
Direct detachment



Indirect detachment



“Hot” Photofragments



“Hot” Photofragments

Because of the low intensity of the ionic photofragments produced in our experiment, the dominant photodissociation channel is electron detachment (Figure 4.16). The electron detachment spectra of the I·TU clusters closely resemble the photodepletion spectra.

4.5.2 Assignment of the observed excited states from the photodepletion spectra

The solution-phase spectrum of 2,4-TU displays two peaks over the 3.2-5.7 eV spectral region, with λ_{max} at 3.45 eV and 4.55 eV.²⁹⁶ These peaks occur at similar

energies to bands I and II of the I·2,4-TU spectrum, indicating that the cluster excited states in these regions are associated with $\pi\text{-}\pi^*$ localized transitions of the 2,4-TU moiety. In other iodide-molecule clusters, dipole-bound excited states have been observed in the region of the VDE.^{252,253,261,286} We anticipate that the VDE of I·2,4-TU should occur around 4.1 eV, so a dipole-bound excited state is expected to occur for the cluster around this energy. The photodepletion spectrum does not display the sharp fall-off in photodepletion intensity that is typically observed at the high-energy edge of the dipole-bound excited state,^{229,298} so it is not possible to conclude that the dipole-bound excited state exists for I·2,4-TU from its photodepletion spectrum. This is a situation we have observed in previous studies of iodide-pyrimidine clusters,^{261,286} however, we will return to this point when we discuss the cluster's photofragment production spectra below. Band III of the photodepletion spectrum does not correlate with any prominent transitions of the 2,4-TU chromophore, and since this spectral region lies above the expected VDE of the cluster, it can be assigned to direct electron detachment (section 4.6.2, Figure 4.16).^{261,286}

In contrast to I·2,4-TU, the I·2-TU photodepletion spectrum does not display the same features as the solution-phase spectrum of 2-TU, which is characterised by a pair of partially resolved bands with λ_{max} of 4.2 and 4.7 eV.²⁹⁶ The I·2-TU spectrum displays a strong photodepletion onset around 3.6 eV, peaking at 4.1 eV, in the vicinity of the predicted VDE (band I). The near-threshold band is followed by a rather flat region of photodepletion between 4.6-5.6 eV. This spectral profile is typical of a number of iodide ion-polar molecule complexes,^{261,286} where the band I feature has been assigned to a dipole-bound excited state followed by a region of direct electron detachment.^{299,300} This leads us to assign band I to a near-threshold dipole-bound excited state of I·2-TU. There are no strong signatures of $\pi\text{-}\pi^*$ localized 2-TU excited states evident on the photodepletion spectrum, although two features are certainly seen at ~4.5 and 5 eV in the photodepletion spectrum which could correspond to the $\pi\text{-}\pi^*$ 2-TU excitations. However, they can tentatively not be described as prominent spectral features and are only just visible above the electron detachment background.

The solution-phase spectrum of 4-TU displays a very strong band with λ_{max} at ~3.8 eV, followed by a lower-intensity band with λ_{max} at ~5.0 eV.²⁹⁶ These features are associated with $\pi\text{-}\pi^*$ transitions of the 4-TU chromophore.²⁹⁶ The photodepletion

spectrum of I·4-TU displays a band peaking at ~4.1 eV (band I), followed by a lower-intensity band (II) at 5.2 eV. Band I could either be associated with a dipole-bound excited state or with excitation of the lower-energy strong 4-TU $\pi-\pi^*$ transition. It is probable that contributions from both of these very distinctive excited states are present in this excitation region, as will be discussed further below. Band II can be assigned to excitation of the higher-energy $\pi-\pi^*$ transition in the cluster.

Having performed a preliminary assignment of the excited states evident in the photodepletion spectra of the I·TU clusters, it is now useful to compare the experimental spectra to TDDFT generated spectra (Figure 4.3). The TDDFT calculations as was mentioned earlier, are expected to predict $\pi-\pi^*$ nucleobase-localized transitions reasonably well but are not expected to predict dipole-bound excited states accurately. Comparing the TDDFT calculated and experimental spectra, there is good agreement for I·2,4-TU and I·4-TU, while the I·2-TU calculated spectrum does not closely resemble the photodepletion spectrum. The good agreement observed for I·2,4-TU and I·4-TU reflects the fact that the experimental spectra for these complexes are dominated by the $\pi-\pi^*$ nucleobase-localized transitions.

Finally, it is of interest to consider whether the two spin-orbit states of the iodine atom in the photodetached clusters contribute to the photodepletion spectra. Although direct detachment to the upper $^2P_{1/2}$ neutral state around 5 eV has been observed for some iodide ion pyrimidine complexes (I·U and I·T) via photoelectron spectroscopy,^{261,286} photodepletion spectra did not clearly show the upper spin-orbit dipole-bound state.³⁰¹ The I·TU complexes behaviour appears to be in line with that of the previously studied iodide ion pyrimidine complexes (I·U and I·T), in that the upper spin orbit dipole-bound excited state is not clearly evident on the photodepletion spectra. (It would be expected to appear around 5.1 eV.) We conclude that the cross-section for excitation to the upper spin-orbit state is occurring with relatively low cross section.²⁶¹

4.5.3 Photofragment production

Two general mechanisms are associated with production of ionic photofragments in clusters such as the I·TU complexes studied here. The first group correspond to various intra cluster electron-transfer processes, including events that follow dipole-

bound excited state formation, ejection of a low energy electron from I⁻. This electron then undergoes electron scattering from the thionucleobase, or straightforward charge transfer from I⁻ to the thionucleobase valence orbitals.²⁸⁷ This group of processes is expected to result in production of either the dipole-bound anion of the thionucleobase through direct fragmentation of the dipole-bound excited state, or of the deprotonated thionucleobase, since this is the most intense fragment expected when the thionucleobase captures a free electron.

The second type of photofragmentation follows electronic excitation that is largely localized on the nucleobase chromophore. Native nucleobases are known for their propensity to decay back to the electronic ground state following UV excitation and then lose excess energy by thermal dissipation.³⁰² In an anion-nucleobase complex, when electronic relaxation of a nucleobase centred excited state results in a return to the electronic ground state, followed by thermal fragmentation, we expect to observe the same ionic fragments that would be produced upon low-energy CID.^{303,304} On conducting CID experiments for the I⁻·TU clusters, we observed production of the iodide ion and the respective deprotonated thionucleobase (Section 4.7.2, Figure 4.18). Simultaneous production of I⁻ and [TU-H]⁻ as photofragments could therefore be interpreted as arising from ultrafast decay of a thionucleobase-centred excited state. There are two important points however to note. Firstly, thionucleobases are known to exhibit much less efficient ultrafast decay than native nucleobases, potentially meaning that the I⁻·TU excited states could be significantly longer-lived than those of iodide-native nucleobases.^{216,217,221,224-227} Secondly, even in the iodide-native nucleobase clusters, excited states (both dipole-bound and nucleobase localized) have been observed to decay with long lifetimes, consistent with internal conversion to the ground electronic state followed by evaporation of I⁻ and the deprotonated nucleobase.^{261,286} Ultimately, analysis of the production profile of individual photofragments is crucial in assigning the nature of the excited state involved in generating specific photoproducts.

For I⁻·2-TU, the m/z 127 (I⁻ / [2-TU-H]⁻) photofragment profile is very like that of the comparable fragments for the iodide pyrimidine complexes,^{261,286} suggesting that similar photofragmentation mechanisms are present, *i.e.* intra cluster electron transfer dominates in the near threshold region, while 2-TU-centred excitations dominate close to the band II nucleobase localized π - π^* transition. In I⁻·4-TU, the m/z 127 (I⁻ / [4-TU-H]⁻) photofragment displays a similar profile to the m/z 127

photofragment of the I•2-TU cluster, indicating the presence of similar excited states and decay processes. However, there is a notable difference in the profile of the second photofragment - the molecular anion, [4-TU]⁻. Its production profile displays a very sharp falloff in intensity above the expected VDE, suggesting that this photofragment is formed directly from decay of a precursor dipole-bound excited state. Our experiment does not allow us to measure whether this anion is a dipole-bound or valence anion, although time-resolved photoelectron spectroscopy could be applied in future experiments to clarify this point.^{287,300}

I•2,4-TU provides the richest photofragmentation pattern. The I⁻ ion is produced across most of the scanned region with a profile that largely resembles that of photodepletion. (I⁻ production decreases > 5.0 eV, but this is consistent with electron detachment increasingly dominating at high excitation energies). The similar appearance of the I⁻ production and the photodepletion spectrum indicates that I⁻ is being produced from decay of all of the excited states present for the cluster, behaviour that again mirrors that seen for the iodide-pyrimidine complexes.^{261,286} As for the [4-TU]⁻ photofragment from I•4-TU, the [2,4-TU]⁻ molecular anion photofragment from I•2,4-TU displays a production profile indicative of production through a dipole-bound excited state in the region of the VDE, with a sharp fall in intensity around the expected VDE.²⁶⁰ Indeed, this photofragment's production profile can be directly associated with a dipole-bound excited state, and thus confirms that such a state is present in this region for I•2,4-TU.

The profile for production of [2,4-TU-H]⁻ is similar to that of the I⁻ photofragment in the lower energy region of the spectrum, again mirroring the behaviour of the iodide-pyrimidine complexes.^{261,286} However, its intensity drops sharply above 4.2 eV, on the high-energy edge of the dipole-bound excited state. This leads us to conclude that the dipole-bound excited state decays with production of both [2,4-TU]⁻ and [2,4-TU-H]⁻. (Low level production of the [2,4-TU-H]⁻ photofragment is observed in the region around 5.2 eV, possibly associated with decay of the upper spin-orbit excited state). It is noted that the [2,4-TU]⁻ photofragment is produced considerably less strongly through the lower energy band I region than [2,4-TU-H]⁻. Indeed, what is surprising is that [2,4-TU]⁻ is seen at all in this region, since band I corresponds to a thionucleobase localized excited state. The simplest explanation of the proximity of the thionucleobase band I excited state with the cluster dipole-bound excited state is the presence of strong coupling between these two very distinctive

excited states.

The SCN^- photofragment profile from $\text{I}\cdot\text{2,4-TU}$ is distinctive compared to the other photofragments, with production limited to the region between 3.6 eV-4.9 eV. It is notable that SCN^- production does not follow the dipole-bound excited state profile established by the $[\text{2,4-TU}]^-$ photofragment, allowing us to conclude that this fragment is not a biproduct of electron transfer onto 2,4-TU. This spectral region corresponds to the more intense $\pi\text{-}\pi^*$ localized transition of 2,4-TU. It is significant that $[\text{2,4-TU-H}]^-$ is not being produced though this region. This suggests that the chromophore-centred excited state accessed in this region does not decay directly back to the ground state with statistical evaporation of the primary fragment pair, but instead evolves to eject SCN^- as a dissociative photoproduct. This behaviour is in line with the known distinctive behaviour of thionucleobases compared to native nucleobases.²⁸

4.7 Further Discussion & Concluding Remarks

In most respects, the photophysics and photochemistry of the $\text{I}\cdot\text{TU}$ complexes closely resemble those of the iodide-pyrimidine complexes studied previously.^{262,287} Photoexcitation predominantly results in electron detachment, with ionic fragmentation representing only a minor decay pathway. However, two aspects of the results merit further discussion.

The first relates to the identities of the $[\text{4-TU}]^-$ and $[\text{2,4-TU}]^-$ anions produced following photoexcitation of $\text{I}\cdot\text{4-TU}$ and $\text{I}\cdot\text{2,4-TU}$, respectively. Photoelectron spectroscopy of $[\text{4-TU}]^-$ and $[\text{2,4-TU}]^-$ was conducted by Bowen and co-workers, with the results compared to the uracil molecular anion, U^- .²⁹⁰ While U^- was identified as a dipole-bound anion, both $[\text{4-TU}]^-$ and $[\text{2,4-TU}]^-$ were found to be valence anions. Accompanying theoretical calculations revealed that $[\text{4-TU}]^-$ and $[\text{2,4-TU}]^-$ are considerably more stable as valence anions than both $[\text{2-TU}]^-$ and U^- , with only $[\text{4-TU}]^-$ and $[\text{2,4-TU}]^-$ displaying positive vertical electron affinities.²⁹¹ The behaviour of uracil mirrors that of the other canonical nucleobases, since their valence anions have generally been elusive in the gas-phase (except in delicate Rydberg electron transfer experiments),³⁰⁵ likely due to their low electron affinities.²⁴⁶ Indeed, U^- was not observed as a photofragment in photoexcitation of $\text{I}\cdot\text{U}$,²⁸⁶ and it appears that the $\text{I}\cdot\text{2-TU}$ complex studied in this work is displaying very

similar behaviour, with 2-TU⁻ not being observed as a photofragment. Therefore, in our experiments on I[•]4-TU and I[•]2,4-TU, initial photoexcitation in the VDE region accesses a dipole-bound excited state, which decays with formation of [4-TU]⁻ and [2,4-TU]⁻ as stable valence molecular anions. For I[•]2-TU, photoexcitation in the near threshold region again accesses a dipole-bound excited state, but the ultimate photoproduct is [2-TU-H]⁻ as the valence-bound form of [2-TU]⁻ is not sufficiently stable, so that the dissociative electron attachment product is the end product.

In the context of the above discussion, it is notable that I[•]2-TU can also be considered to be the “odd man out” compared to I[•]4-TU and I[•]2,4-TU in relation to the general profile of the photodepletion (gas-phase absorption) spectra. The photodepletion spectra of I[•]4-TU and I[•]2,4-TU both strongly resemble the intrinsic absorption spectra of the uncomplexed nucleobases, i.e. the nucleobase localized π - π^* transitions dominate these spectra. Intriguingly, this is not the case for I[•]2-TU. Comparing the calculated properties of the clusters (Table 1) reveals that I[•]2-TU has a weaker cluster binding energy and vertical dipole moment than the other two clusters, due to the relatively lower dipole moment of 2-TU. An interesting possibility is that the stronger dipole moments of 4-TU and 2,4-TU are enhancing the coupling of the electron detachment continuum to nucleobase-centred transitions. Current understanding of the physics of how molecular excited states couple to the electron detachment continuum is an area of emerging interest,^{180,262,306,307} and further theoretical insight is urgently needed to better understand the photophysics and electron dynamics.³⁰⁷ The thionucleobases provide a useful series of molecules for extending the current studies given that the molecular dipole changes significantly with derivatization.

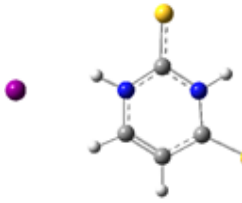
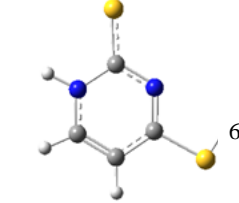
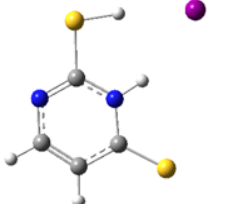
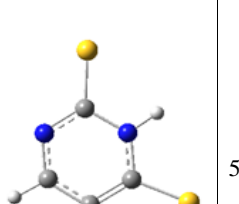
4.8 Supplementary Information

4.7.1 Computational studies on the I⁻·TU clusters

4.7.1.1 DFT calculations on the tautomers of the I⁻·TU clusters

The structures of the I⁻·TU clusters were optimised from multiple starting structures mainly from monomer tautomers obtained by Andrzej Les and Ludwik Adamowicz.³⁰⁸ The lowest energy structure of each thio-nucleobase-iodide cluster are presented in Tables 4.3, 4.4 and 4.5 respectively. For each thio-nucleobase-iodide cluster, the keto form was found to produce the lowest energy structure T1.

Table 4.3 Calculated structures and relative electronic energies of the tautomers 2,4-thiouracil iodide (I⁻·2,4-TU) clusters. Structures were calculated at the B3LYP/6-311++G(2d,2p) level, 6-311G(d,p)/SDD on I (see main text for details). Energies are zero-point energy corrected.

Tautomer	Energy (kJ/mol)	Tautomer	Energy (kJ/mol)
T1 	0.0	T4 	60.31
T2 	39.62	T5 	55.47

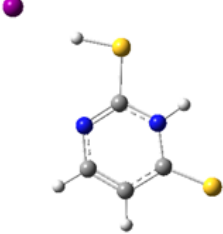
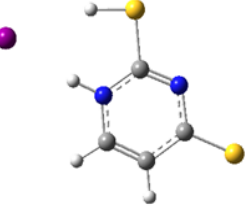
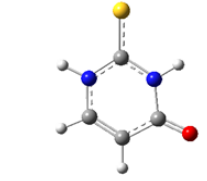
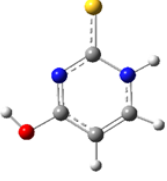
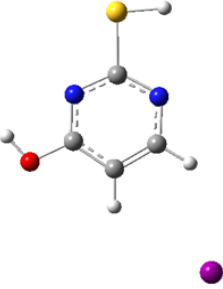
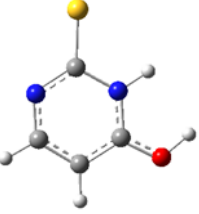
T3 	60.52	T6 	41.33
--	-------	--	-------

Table 4.4 Calculated structures and relative electronic energies of the tautomers 2-thiouracil iodide (I·2-TU) clusters. Structures were calculated at the B3LYP/6-311++G(2d,2p) level, 6-311G(d,p)/SDD on I (see main text for details). Energies are zero-point energy corrected

Tautomer	Energy (kJ/mol)	Tautomer	Energy (kJ/mol)
T1 	0.0	T4 	60.22
T2 	70.25	T5 	44.88

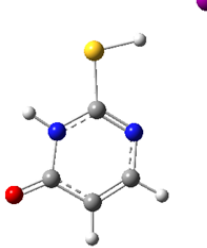
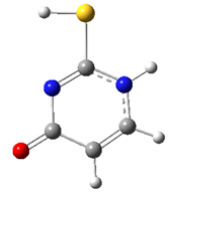
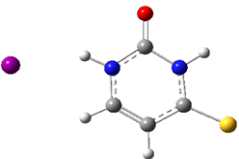


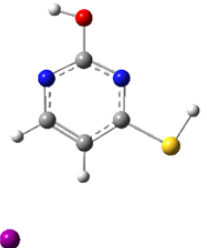
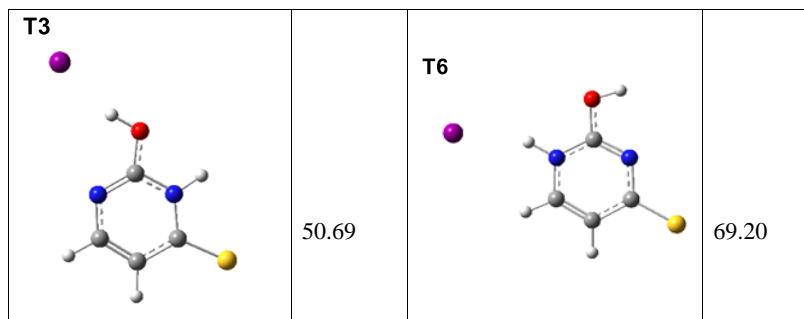
T3 	66.73	T6 	55.98
--	-------	--	-------

Table 4.5 Calculated structures and relative electronic energies of the tautomers 4-thiouracil iodide (I \cdot 4-TU) clusters. Structures were calculated at the B3LYP/6-311++G(2d,2p) level, 6-311G(d,p)/SDD on I (see main text for details). Energies are zero-point energy corrected

Tautomer	Energy (kJ/mol)	Tautomer	Energy (kJ/mol)
T1 	0.0	T4 	59.15
T2 	60.29	T5 	102.23



4.7.1.2 Direction of the dipole moment the I⁻TU clusters

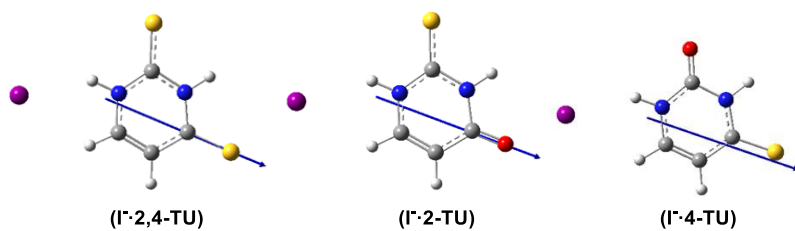


Figure 4.9 The vector direction of the axis of the dipole moment of the I⁻TU molecule, calculated for the neutral molecule at the geometry of the optimized ion-molecule complex.

4.7.1.3 Time dependent density functional theory data of tautomers of the I·TU clusters.

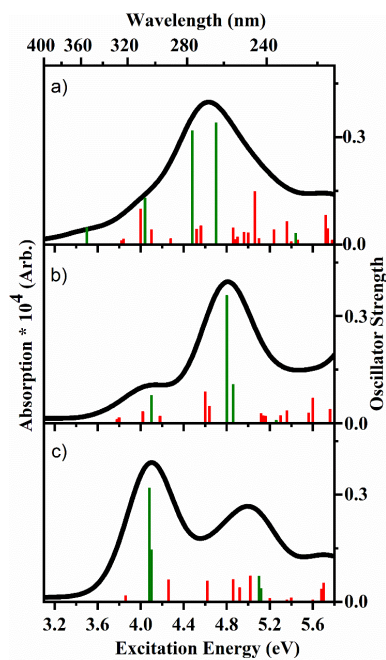


Figure 4.10 TDDFT excitation spectra of the lowest energy tautomers of a) I·2,4-TU, b) I·2-TU and c) I·4-TU clusters calculated at B3LYP/6-311++G(2d,2p) level and 6-311G(d,p)/SDD on I.

The oscillator strengths on the y axis of individual transitions ≥ 0.005 within the experimental scan range are shown by vertical bars, while the full line spectrum is a convolution of the calculated spectrum with Gaussian function (0.25 eV HWHM). The red lines represent transitions from an iodide p-orbital and the green lines represent transitions from the thio-nucleobase (TU) π orbital.

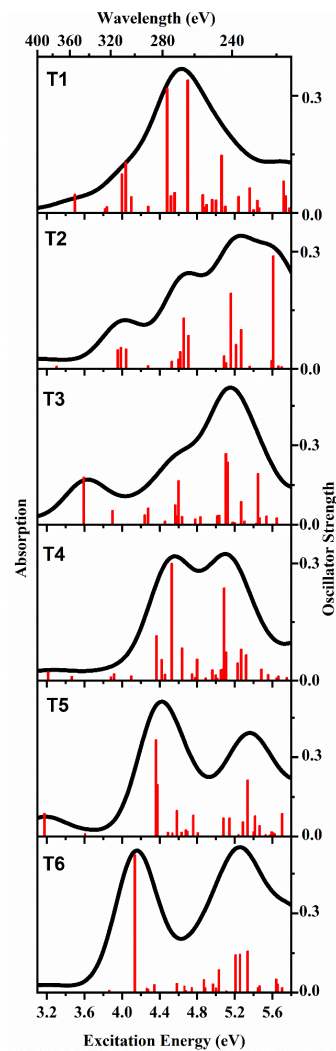


Figure 4.11 TDDFT excitation spectra of the tautomers of I·2,4-TU clusters for the structures shown in Table 4.4. The oscillator strengths (OSC.) on the y axis of individual transitions ≥ 0.005 within the experimental scan range are shown by vertical bars, while the full line spectrum is a convolution of the calculated spectrum with Gaussian function (0.25 eV HWHM).

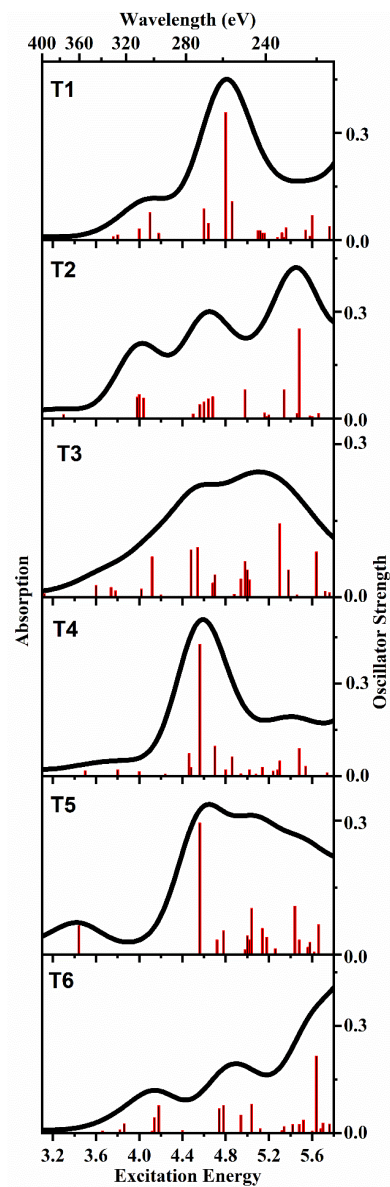


Figure 4.12 TDDFT excitation spectra of the tautomers of I·2-TU clusters for the structures shown in Table 4.5. The oscillator strengths (OSC.) on the y axis of individual transitions ≥ 0.005 within the experimental scan range are shown by vertical bars, while the full line spectrum is a convolution of the calculated spectrum with Gaussian function (0.25 eV HWHM).

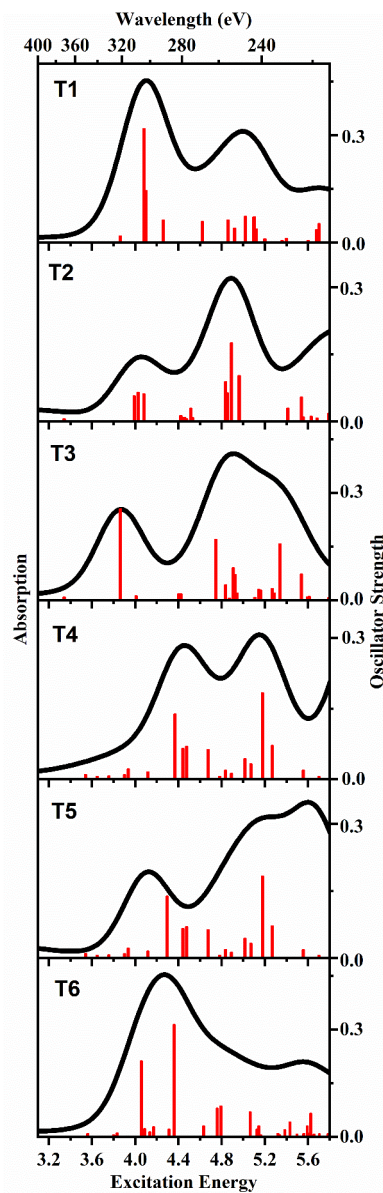


Figure 4.13 TDDFT excitation spectra of the tautomers of I·4-TU clusters for the structures shown in Table 4.6. The oscillator strengths (OSC.) on the y axis of individual transitions ≥ 0.005 within the experimental scan range are shown by vertical bars, while the full line spectrum is a convolution of the calculated spectrum with Gaussian function (0.25 eV HWHM).

4.7.1.4 Equation-of-motion coupled-cluster singles and doubles (EOMCCSD) calculations of the I-2-TU cluster

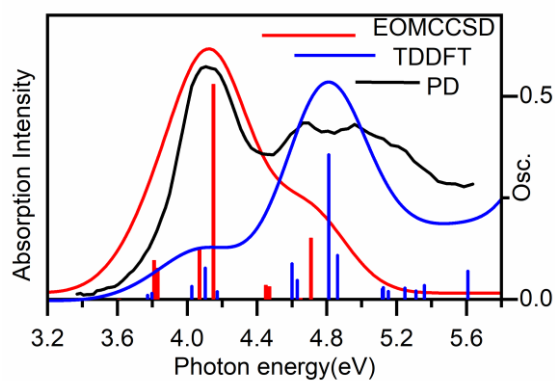


Figure 4.14 Overlaid EOMCCSD, TDDFT of the lowest energy I-2-TU cluster and Photodepletion spectrum to explore the dipole bound state.

The red lines represent transitions from iodide p-orbital obtained from EOMCCSD calculation displaying strongest transitions around band I of the photodepletion spectrum of I-2-TU cluster. The blue lines represent transitions from the TDDFT calculation which show weaker transitions around the band I of the PD. EOMCCSD calculation is centred on the dipole bound orbital.

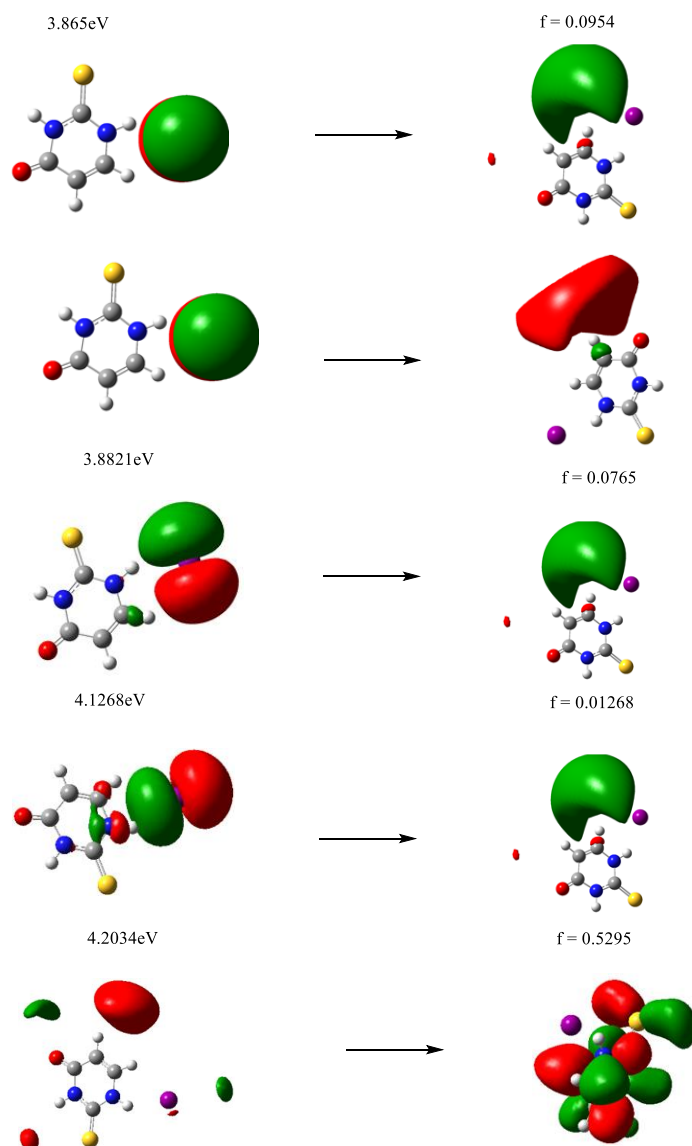


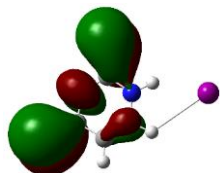
Figure 4.15 Molecular orbital transitions I-2-TU involved in the dipole bound state predicted by EOMCCSD calculations between 3.87 – 4.21 eV. The excitation energies are offset by -1.12 eV for comparison with the experimental data.

4.7.1.5 Molecular orbitals involved in the TDDFT transitions of the I-TU clusters

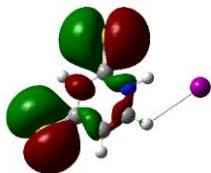
Table 4.6 Calculated TDDFT transition energies at the B3LYP/6-311++G(2d,2p)/SDD level of theory and oscillator strengths of the I-2,4-TU cluster. Only transitions below 5.7 eV with oscillator strength > 0.005

Orbital transitions	ΔE (eV)	f
(0.26)35(π) \rightarrow 42(π^*)	3.51	0.0470
(0.65)37(π) \rightarrow 42(π^*)		
(0.69)41(n) \rightarrow 44(σ^*)	3.81	0.0102
(0.69)40(n) \rightarrow 44(σ^*)	3.84	0.0151
(0.53)35(π) \rightarrow 42(π^*)	4.05	0.1301
(0.35)37(π) \rightarrow 43(π^*)		
(0.26)35(π) \rightarrow 43(π^*)		
(0.69)39(n) \rightarrow 44(σ^*)	4.09	0.0407
(0.69)40(n) \rightarrow 45(π^*)	4.29	0.0159
(0.34)35(π) \rightarrow 42(π^*)	4.47	0.3131
(0.36)35(π) \rightarrow 43(π^*)		
(0.35)37(π) \rightarrow 43(π^*)		
(0.22)39(n) \rightarrow 45(π^*)		
(0.20)37(π) \rightarrow 42(π^*)		
(0.66)39(n) \rightarrow 45(π^*)	4.52	0.0428
(0.63)41(n) \rightarrow 46(σ^*)	4.57	0.0518
(0.25)41(n) \rightarrow 48(σ^*)		
(0.46)35(π) \rightarrow 43(π^*)	4.71	0.3399
(0.43)37(π) \rightarrow 43(π^*)		
(0.22)40(n) \rightarrow 46(σ^*)		
(0.63)39(n) \rightarrow 46(σ^*)	4.85	0.0462
(0.24)39(n) \rightarrow 48(σ^*)		
(0.66)41(n) \rightarrow 47(σ^*)	4.87	0.0134
(0.67)40(n) \rightarrow 47(σ^*)	4.90	0.0207
(0.60)41(n) \rightarrow 48(σ^*)	4.96	0.0339
(0.24)41(n) \rightarrow 46(σ^*)		
(0.21)41(n) \rightarrow 47(σ^*)		

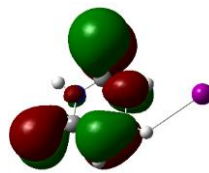
(0.61)40(n)→48(σ^*)	4.99	0.0321
(0.23)40(n)→46(σ^*)		
(0.65)38(n_s)→44(σ^*)	5.07	0.1476
(0.67)40(n)→50(σ^*)	5.16	0.0159
(0.61)39(n)→48(σ^*)	5.24	0.0413
(0.23)39(n)→47(σ^*)		
(0.22)39(n)→46(σ^*)		
(0.63)36(π)→44(σ^*)	5.35	0.0636
(0.21)38(n_s)→45(π^*)		
(0.64)41(n)→51(σ^*)	5.41	0.0075
(0.65)35(π)→44(σ^*)	5.45	0.0313
(0.60)40(n)→51(σ^*)	5.46	0.0123
(0.21)40(n)→53(σ^*)		
(0.61)41(n)→52(σ^*)	5.61	0.0068



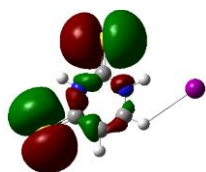
MO 35



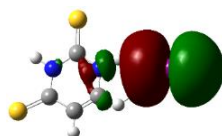
MO 36



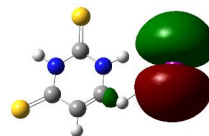
MO 37



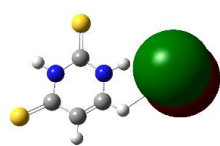
MO 38



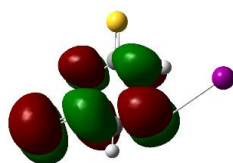
MO 39



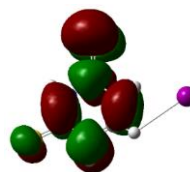
MO 40



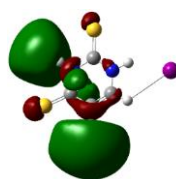
MO 41



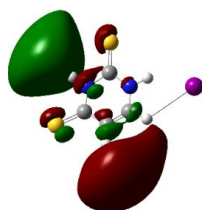
MO 42



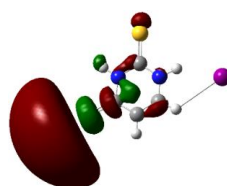
MO 43



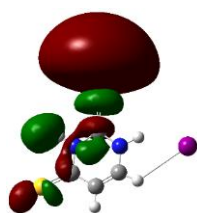
MO 44



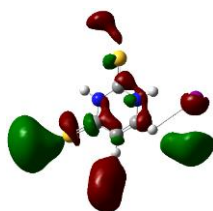
MO 45



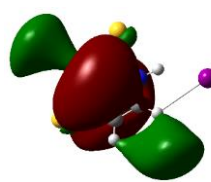
MO 46



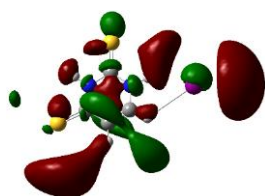
MO 47



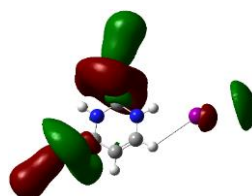
MO 48



MO 50



MO 51

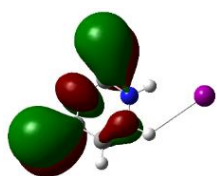


MO 53

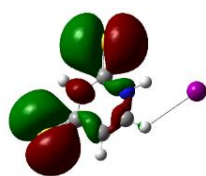
Table 4.7 Calculated TDDFT transition energies at the B3LYP/6-311++G(2d,2p)/SDD level of theory and oscillator strengths of the I-2,4-TU cluster. Only transitions below 5.6 eV with oscillator strength > 0.005

Orbital transitions	ΔE (eV)	f
(0.26)35(π) \rightarrow 42(π^*)	3.51	0.0470
(0.65)37(π) \rightarrow 42(π^*)		
(0.69)41(n) \rightarrow 44(σ^*)	3.81	0.0102
(0.69)40(n) \rightarrow 44(σ^*)	3.84	0.0151
(0.53)35(π) \rightarrow 42(π^*)	4.05	0.1301
(0.35)37(π) \rightarrow 43(π^*)		
(0.26)35(π) \rightarrow 43(π^*)		
(0.69)39(n) \rightarrow 44(σ^*)	4.09	0.0407
(0.69)40(n) \rightarrow 45(π^*)	4.29	0.0159
(0.34)35(π) \rightarrow 42(π^*)	4.47	0.3131
(0.36)35(π) \rightarrow 43(π^*)		
(0.35)37(π) \rightarrow 43(π^*)		
(0.22)39(n) \rightarrow 45(π^*)		
(0.20)37(π) \rightarrow 42(π^*)		
(0.66)39(n) \rightarrow 45(π^*)	4.52	0.0428
(0.63)41(n) \rightarrow 46(σ^*)	4.57	0.0518
(0.25)41(n) \rightarrow 48(σ^*)		
(0.46)35(π) \rightarrow 43(π^*)	4.71	0.3399
(0.43)37(π) \rightarrow 43(π^*)		
(0.22)40(n) \rightarrow 46(σ^*)		
(0.63)39(n) \rightarrow 46(σ^*)	4.85	0.0462
(0.24)39(n) \rightarrow 48(σ^*)		
(0.66)41(n) \rightarrow 47(σ^*)	4.87	0.0134
(0.67)40(n) \rightarrow 47(σ^*)	4.90	0.0207
(0.60)41(n) \rightarrow 48(σ^*)	4.96	0.0339
(0.24)41(n) \rightarrow 46(σ^*)		
(0.21)41(n) \rightarrow 47(σ^*)		

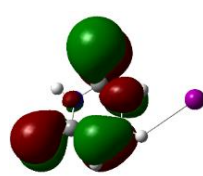
(0.61)40(n)→48(σ^*)	4.99	0.0321
(0.23)40(n)→46(σ^*)		
(0.65)38(n_s)→44(σ^*)	5.07	0.1476
(0.67)40(n)→50(σ^*)	5.16	0.0159
(0.61)39(n)→48(σ^*)	5.24	0.0413
(0.23)39(n)→47(σ^*)		
(0.22)39(n)→46(σ^*)		
(0.63)36(π)→44(σ^*)	5.35	0.0636
(0.21)38(n_s)→45(π^*)		
(0.64)41(n)→51(σ^*)	5.41	0.0075
(0.65)35(π)→44(σ^*)	5.45	0.0313
(0.60)40(n)→51(σ^*)	5.46	0.0123
(0.21)40(n)→53(σ^*)		
(0.61)41(n)→52(σ^*)	5.61	0.0068



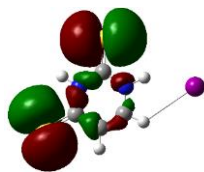
MO 35



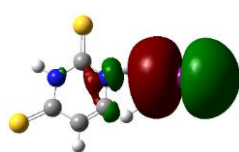
MO 36



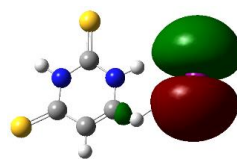
MO 37



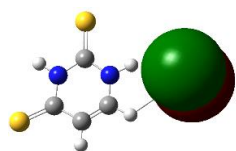
MO 38



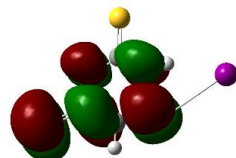
MO 39



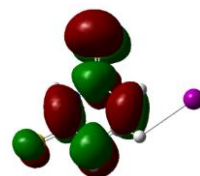
MO 40



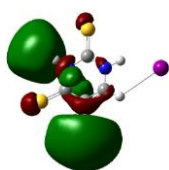
MO 41



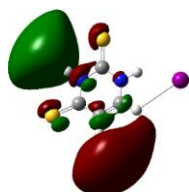
MO 42



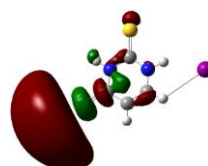
MO 43



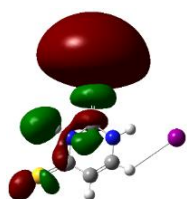
MO 44



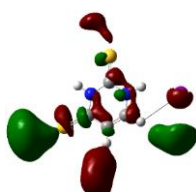
MO 45



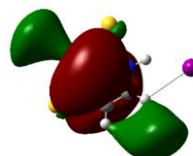
MO 46



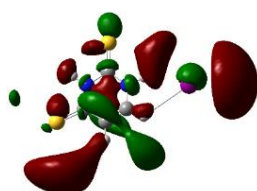
MO 47



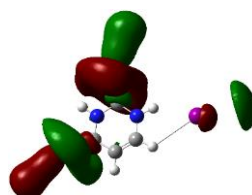
MO 48



MO 50



MO 51

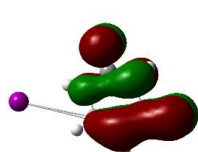


MO 53

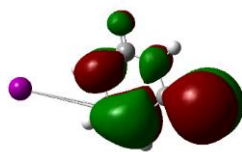
Table 4.8 Calculated TDDFT transition energies at the B3LYP/6-311++G(2d,2p)/SDD level of theory and oscillator strengths of the I-4-TU cluster. Only transitions below 5.7 eV with oscillator strength > 0.005

Orbital transitions	ΔE (eV)	f
(0.71)37(n) \rightarrow 39(π^*)	3.66	0.0067
(0.69)37(n) \rightarrow 40(σ^*)	3.82	0.0091
(0.69)36(n) \rightarrow 40(σ^*)	3.85	0.0177
(0.52)35(n) \rightarrow 40(σ^*)	4.09	0.3181
(0.44)33(π) \rightarrow 38(π^*)		
(0.52)33(π) \rightarrow 38(π^*)	4.11	0.1450
(0.46)35(n) \rightarrow 40(σ^*)		
(0.69)37(n) \rightarrow 41(π^*)	4.22	0.0059
(0.69)36(n) \rightarrow 42(σ^*)	4.26	0.0173
(0.62)37(n) \rightarrow 42(σ^*)	4.58	0.0618
(0.31)37(n) \rightarrow 43(σ^*)		
(0.62)36(π) \rightarrow 42(σ^*)	4.62	0.0583
(0.31)36(π) \rightarrow 43(σ^*)		
(0.62)35(n) \rightarrow 42(σ^*)	4.86	0.0626
(0.31)35(n) \rightarrow 43(σ^*)		
(0.61)37(n) \rightarrow 43(σ^*)	4.92	0.0395
(0.33)37(n) \rightarrow 42(σ^*)		
(0.61)36(n) \rightarrow 43(σ^*)	4.95	0.0309
(0.33)36(n) \rightarrow 42(σ^*)		
(0.68)34(n_s) \rightarrow 40(σ^*)	5.03	0.0727
(0.60)33(π) \rightarrow 39(π^*)	5.11	0.0716
(0.24)36(n) \rightarrow 45(σ^*)		
(0.20)37(n) \rightarrow 44(π^*)		
(0.43)36(n) \rightarrow 45(σ^*)	5.12	0.0376
(0.43)37(n) \rightarrow 44(π^*)		
(0.31)33(π) \rightarrow 39(π^*)		
(0.47)37(n) \rightarrow 44(π^*)	5.16	0.0200

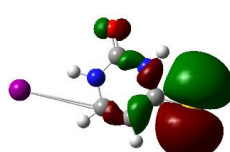
(0.45)36(n)→45(σ^*)		
(0.58)35(n)→43(σ^*)	5.19	0.0097
(0.30)35(n)→42(σ^*)		
(0.67)35(n)→45(σ^*)	5.36	0.0051
(0.53)37(n)→47(σ^*)	5.40	0.0112
(0.37)37(n)→46(σ^*)		
(0.58)36(n)→47(σ^*)	5.45	0.0079
(0.29)36(n)→46(σ^*)		
(0.70)33(n)→41(π^*)	5.61	0.0054
(0.63)34(n _s)→42(σ^*)	5.68	0.0354
(0.67)34(n _s)→43(σ^*)		
(0.45)35(n)→47(σ^*)	5.69	0.0526
(0.43)35(n)→46(σ^*)		



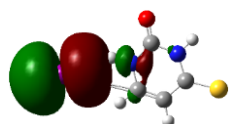
MO 32



MO 33



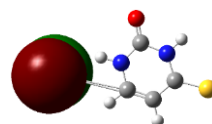
MO 34



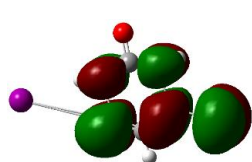
MO 35



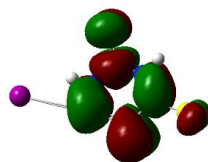
MO 36



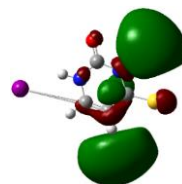
MO 37



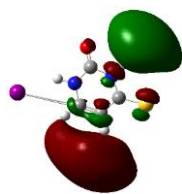
MO 38



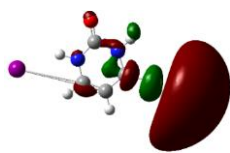
MO 39



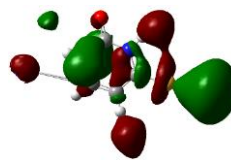
MO 40



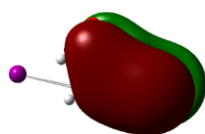
MO 41



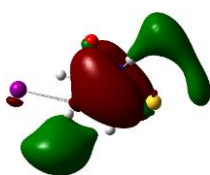
MO 42



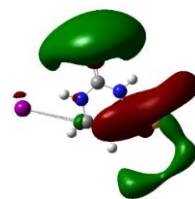
MO 43



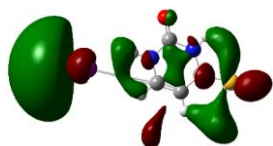
MO 44



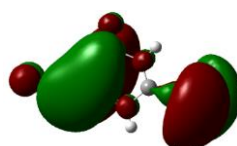
MO 45



MO 46



MO 47



MO 48

Note: The n_s are transitions from non-bonding orbital of the sulphur atom while n is the iodide n ($5p^6$)

4.7.2 Experimental studies on the I⁻·TU clusters

4.6.2.1 Electron detachment spectra of the I⁻·TU clusters

Electron detachment (ED) yield of I⁻·TU clusters is displayed in Figure 4.16. Although electron loss cannot be directly measured in our instrument, we calculate it by assuming that any photodepleted ions that are not detected as ionic fragments are electron loss.

Note that our instrument can only detect ions with $m/z > 50$

$$\% \text{ Electron Detachment} = [(Photodepletion \text{ ion-count} - \sum Photofragment \text{ ion-count}) / Int_{OFF}] / (\lambda * p)$$

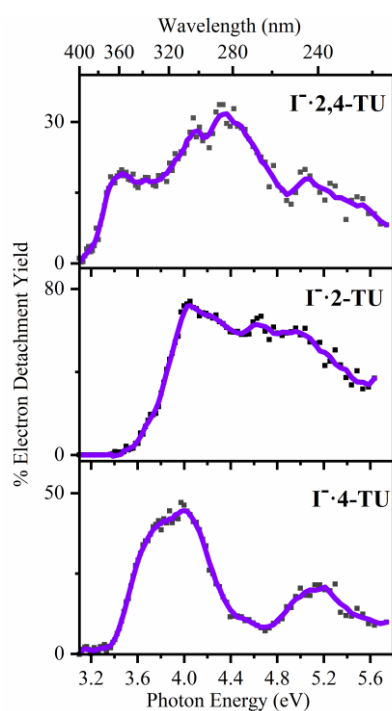


Figure 4.16 % Electron Detachment yield of I·2,4-TU, I·2-TU and I·4-TU clusters. The solid line is a five-point adjacent average of data point.

4.7.2.2 UV-VIS absorption spectra of the TU molecules

Figure 4.17 displays the solution-phase spectra for TU molecules. The acquired spectra will help in comparing and understanding the tautomer dominant in the solution and gas-phase of the individual TU molecule. The absorption spectrum for 2,4-TU in Figure 4.17a shows a low energy partially resolved band that peaks at 3.53 eV and well resolved broad peak at ~ 4.45 eV.

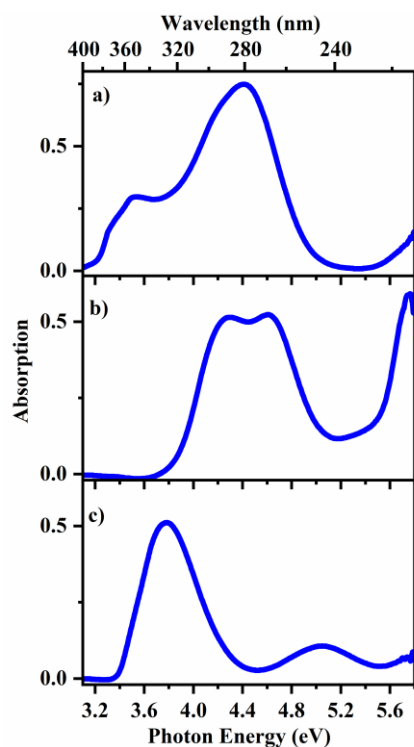


Figure 4.17 Aqueous absorption spectrum of (a) 2,4-TU, (b) 2-TU and (c) 4-TU across the range 3.1 – 5.8 eV (400 – 213 nm) in ME CN/H₂O solvent at 10^{-4} mol dm³.

Figure 4.17b is the solution phase spectrum for 2-TU with two very close unresolved bands at 4.23 eV and 4.62 eV. The spectrum for 4-TU is displayed in Figure 4.17c with two bands that peak at 3.8 eV and 4.92 eV.

The spectra aid in assigning and interpretation of the photo-excited state transitions within the I·TU clusters.

4.7.2.3 Higher-energy collisional dissociation of the I·TU clusters

Higher energy collisional dissociation (HCD) was performed on isolated I·TU clusters to determine the ground state thermal fragments. Figure 4.18 displays the relative intensities of the I·TU clusters parent ion and fragments production intensities, respectively as a function of applied % HCD energy,.

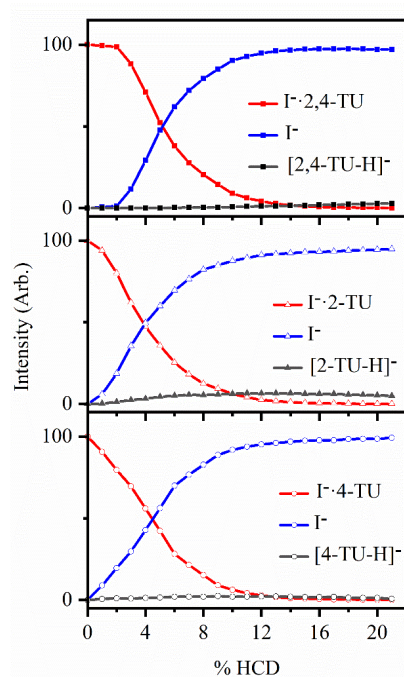


Figure 4.18 Parent ion dissociation curve for I·2,4-TU, I·2-TU and I·4-TU alongside production curves of fragments upon HCD between 0 and 20% energy. The data points fitted with the curved lines are viewing guides to show the profile for an individual fragment.

The HCD results obtained for the I·TU clusters show the fission of the cluster as the major pathway for thermal fragmentation. I ion is produced as a major fragment with very high intensity and a low ion intensity [TU-H]·- all through the HCD collision energy for the three clusters. The $E_{1/2}$ values which shows the % HCD energy for half the intensity of the parent ion to dissociate are 5.8, 4.0 and 4.3 for I

•2,4-TU, I•2-TU and I•4-TU clusters, respectively. This order is in good agreement with the calculated BSSE corrected binding energy of the clusters.

Chapter 5

Exploring Riboflavin's Propensity to Capture Electrons through Direct or Dissociative Attachment: Laser Excitation of Iodide Ion Riboflavin Complex

5.1 Abstract

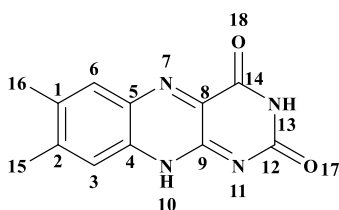
The excited states, intracluster electron transfer and accompanying photodegradation pathways of iodide riboflavin (I·RF) complex have been probed using anion photodissociation spectroscopy (2.4-5.7 eV). Electron detachment processes dominate the photodecay pathways followed by the formation of the molecular anion, RF⁻, a characteristic that is reported for the first time for the flavin family. The absence of the deprotonated riboflavin as a photofragment is unique to the (I·RF) cluster and differs from all the iodide complexes previously studied. This may be attributed to electron capture by RF not resulting in dissociative decay that support the production of the deprotonated RF at a rate that can competes with the production of smaller flavins (deprotonated lumichrome). We observed strong resemblance between the intrinsic absorption spectrum of the uncomplexed RF and the photodepletion spectrum of the cluster was observed, which demonstrates that the cluster's spectral profile is governed by chromophore excitations. The results are discussed to gain a better understanding of the coupling of the electron detachment continuum to RF-centred excitations.

5.2 Introduction

Flavins are of considerable biological importance because of their key roles in photoreceptors and enzymes found in plants and animals.^{229,230,309-312} They have received a fair degree of attention in the solution phase in a number of photochemical and photophysical studies because of their complex biochemical functions.³¹³⁻³¹⁵ The

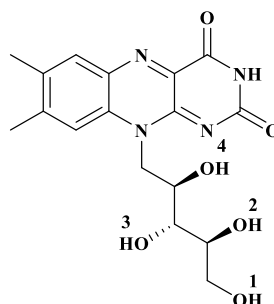
most well-known flavin derivatives: riboflavin (RF), flavin mononucleotide (FMN) and flavin adenine dinucleotide (FAD) differ in the substituent at the N-10 position of isoalloxazine, and are naturally found in foods like meat, eggs and cheese.^{316,317} The involvement of flavins in various redox and photochemical applications is attributed to the presence of the isoalloxazine ring structure.³¹⁸⁻³²⁰ Flavin mononucleotide (FMN) and flavin adenine dinucleotide (FAD) are the redox moieties and active chromophores found in photoreceptors and enzymes which are involved in important biological functions. Due to their versatile redox properties, they are involved in cellular metabolism, beta-oxidation of fatty acids and DNA repairs.³²¹⁻³²⁷

a.



Chemical Formula: $C_{12}H_{10}N_4O_2$
Exact Mass: 242.08

b.



Chemical Formula: $C_{17}H_{20}N_4O_6$
Exact Mass: 376.14

Figure 5.1 Schematic diagram of (a) lumichrome and (b) riboflavin

Riboflavin (vitamin B2) is a water-soluble vitamin which possesses fluorescence, photosensitizing and redox properties. Understanding the photophysical and photochemical behaviour of RF is very important because of its involvement in numerous photo-biological processes. It is known to undergo non-radiative intersystem crossing to an excited triplet-state on exposure to light,³²⁸ and may be employed in photodynamic therapy (PDT) therefore making the identification and understanding of the photoproducts important.^{310,329} Although there are several experimental studies supported by theoretical work on the flavins, there remains a paucity of studies on them as isolated molecules. This has been attributed to historical difficulties in the production of gaseous flavin molecules.^{230,330-334}

Photoexcitation of RF and its derivatives in solution are known to generate photofragments. The fundamental dissociation pathways for flavin derivatives in solution as proposed by Song and co-workers was the production of lumichrome and lumiflavin as fragments,³³⁵ while the complex processes involved in their photochemical behaviour were shown by Moore and Baylor.³³⁶ The photolysis studies performed by Vaid and co-workers on RF in aqueous solution identified lumichrome, lumiflavin and other photoproducts.³³⁷ Recently, photochemical and mass spectrometric studies done by Sikorski and co-workers on RF derivatives showed similarities between the photochemical decomposition and the EI MS results.³¹⁰ They indicated that the presence of the benzyl substituent gave stability to the isoalloxazine core of the 3-benzyl_RF, thus making it unyielding to both photolysis and EI-MS.³¹⁰

Recent studies have been carried out in our group using electrospray ionization and laser photodissociation spectroscopy on the alloxazine and lumichrome molecules. These are model chromophores and the building blocks of the biologically relevant flavins, and their study has led to a better understanding on the intrinsic photophysics and photochemistry of flavins.^{229,230} The evidence for the existence of protonated alloxazine as two protonation isomers in the gas phase was identified by their different electronic spectra and photofragmentation patterns. These suggested that the photofragmentation dynamics are dependent on the location of the proton in the ground state molecule.²³⁰

Studies of the deprotonated lumichrome [LC-H]⁻ molecules revealed the extent to which the methyl group in the chromophore moiety influences its intrinsic electronic behaviour. The results obtained suggest that the presence of the methyl group rotors in deprotonated lumichrome at the molecular dipole will block the existence of a transient negative ion that would facilitate valence electron capture and molecular dissociation.²²⁹

Deprotonated alloxazine [AL-H]⁻ was also studied because of theoretical interest in simpler flavin molecules.^{331,332} The results obtained revealed a long-lived resonance state which encouraged valence electron capture, and thus electronic dissociation.²²⁹ These studies have helped in providing a benchmark for gas phase electronic absorption characteristics for the simplest forms of the flavin chromophores.

Photochemical studies on more complex flavins have also received attention recently in the gas phase, with studies emphasising the challenges faced in assigning

protonation or deprotonation sites, and the importance of proton transfer in the excited state dynamics.^{109,317,338-342}

Investigation of the photochemistry of FAD dianions using tandem ion mobility spectrometry (IMS) compared with the action spectra and solution phase spectra of flavin monoanions FAD, FMN and RF, studied by Stockett and co-workers revealed that solvent effect blue shifts in the electronic absorption spectra of the isoalloxazine group. This strongly suggests charge transfer in deprotonated isoalloxazine group,³¹⁷ and confirms the strong charge transfer character observed in RF on the measurement of the photodissociation of deprotonated RF and the betaine zwitterion studied by Nielsen et al.³⁴³

Despite the different studies done on the flavin molecules in the gas phase, no work to the best of our knowledge has been done on investigating the photochemistry or photophysics behaviour of neutral flavin molecules. The study of low-energy electron flavin interactions using gas phase iodide ion-flavin complexes in which the photo-detachment of the iodine ion generate low energy free electrons is not well established. However, the iodide ion has previously been used as an initial electron donor in the study of low energy free electrons interactions in pyrimidines, thiouracil derivatives and other smaller iodide ion complexes.^{31,253,260,261,282-285,344,345} We therefore present the first gas phase studies on iodide ion – large molecule complex studies, using laser action spectroscopic studies of iodide-riboflavin ion(I⁻·RF) to explore the photodynamics of RF as transient negative ions in the presence of the spectator iodine atom, which acts as the initial electron donor. The photo detached electron from the iodide is captured by the RF moiety, thus resulting in fragmentation to smaller anionic and neutral species.

5.3 Experimental and Computational Methods

5.3.1 Experimental Method

The gaseous ion absorption and photofragment spectra of I⁻·RF were recorded in vacuo using laser interfaced mass spectrometry (LIMS). The LIMS experiments were conducted in a modified AmaZon quadrupole ion-trap mass spectrometer as described previously.^{20,238} UV photons were produced by an Nd:YAG (10 Hz, Surelite) pumped OPO (Horizon) laser, giving 0.3 mJ across the range 516 - 222nm (2.4-5.7 eV). using a 2 nm step size.

The clusters were generated by electrospraying a solution of riboflavin (1×10^{-4} mol dm^{-3}) mixed with droplets of caesium iodide (CsI) (1×10^{-4} mol dm^{-3}) solution in 98% acetonitrile (MeCN) and 2% deionized water. Riboflavin (99%) was purchased from Sigma-Aldrich and CsI was purchased from Avocado Research Chemicals Limited. All chemicals purchased were used without further purification. Typical operating conditions of our mass spectrometer provide mass resolution better than 0.3 amu. The solution was introduced into the mass spectrometer by electrospray ionisation (ESI) using a nebulizing gas pressure of 9 psi, an injection rate 0.35 ml h^{-1} , a drying gas flow rate of 8 ml min^{-1} and run-in negative ion mode at capillary temperatures of 110°C . Photofragmentation experiments were run with an ion accumulation time of 100 ms with a fragmentation time of 100 ms, (one laser pulse interacts with each ion packet) thereby limiting multiphoton processes. UV excited gaseous ions can fragment following excitation and produce a gas-phase absorption spectrum by photodepletion^{20,24,238} for systems where fluorescence is negligible.²³⁹ photodepletion (PD) and photofragment production (PF) were calculated as described in Chapter 2.

Higher-energy collisional dissociation (HCD) experiments were performed in an Orbitrap Fusion Tribrid mass spectrometer (Thermo Fisher Scientific) to acquire a wider fragmentation profile for the ground electronic states, as described previously.^{182,240,241} In these experiments, the following settings were employed: spray voltage: 3600V; sweep gas flow rate: 1 arb; sheath gas flow rate: 10 arb; aux gas flow rate: 5 arb; ion-transfer tube temperature: 275°C ; vaporizer temperature: 350°C .

5.3.2 Computational methods

Schrodinger's MacroModel with mixed Monte Carlo torsional and low-mode sampling parameters were employed to conduct conformational molecular dynamics searches, with a view to generating possible conformers of the I \cdot RF clusters. These possible conformers energy gradient were rapidly minimized with the OPLS3e force field.¹⁸⁸ 365 conformational isomers were generated. The generated conformers were arranged in cluster groups by average distance between all inter-cluster pairs linkage criteria. This is based on generating a structure (nearest to the centroid) per cluster normalised by applying the Kelley-Bryson penalty function technique for state-

constrained control problems.³⁴⁶ Each structure of the grouped isomers is the closest central structure representing a group of similar conformers. Out of the 26 grouped conformers, 12 optimised real structures (structures with no negative frequencies) were obtained. (Table 5.4, section 5.7.1.1)

The geometric structures of both the grouped and ungrouped I·RF clusters were further studied with Gaussian 09,¹⁸⁷ with optimisation at the B3LYP/6-311++G(2d,2p) level of theory on C, N, O, and H, and 6-311G(d,p) on I, with the iodine core electrons being described using the Stuttgart/Dresden (SDD) electron core pseudopotential.²⁵⁰ Frequency calculations were performed to ensure that the optimised structures correspond to true energy minima. To calculate the electronic excitations, time-dependent density functional theory (TDDFT) calculations (100 states) were performed on the lowest-energy I·RF optimised isomers and their spectra convolved with a Gaussian of HWHM 0.25 eV.

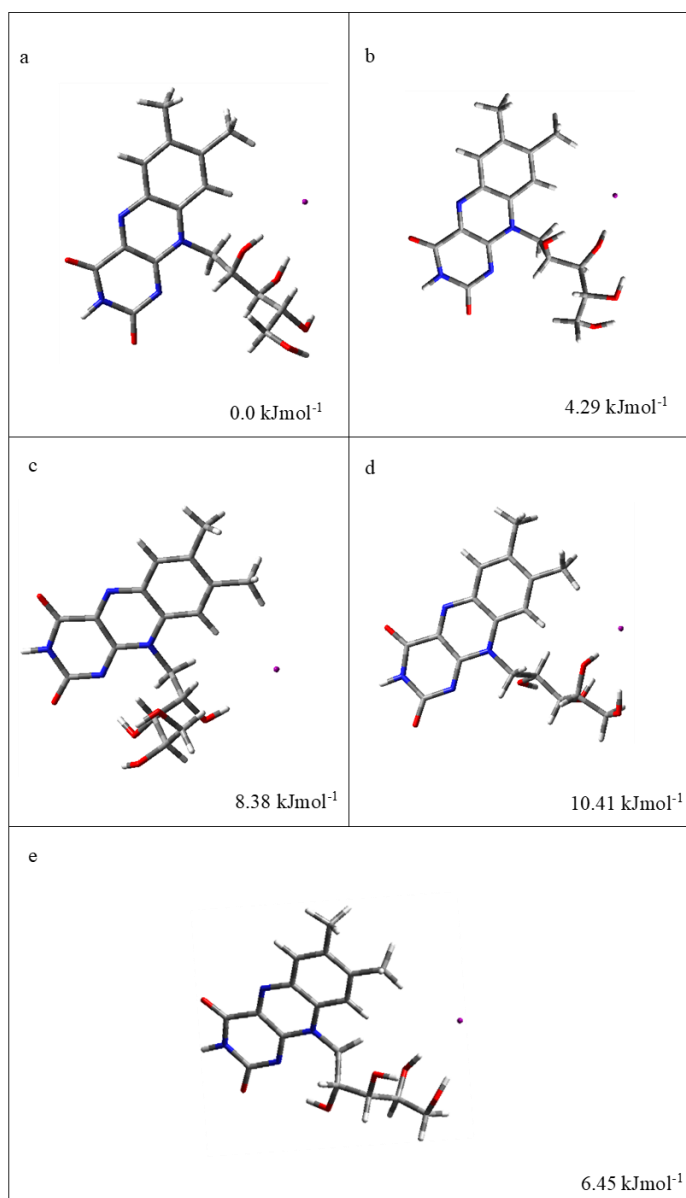
5.4 Results

5.4.1 Geometric structures and TDDFT calculations of the I·RF cluster

The lowest energy ungrouped conformational isomer and 4 randomly picked isomers with different binding motifs of relative energies within the range of 11 kJmol⁻¹ (range of significant Boltzmann population contributions) geometric structures of the I·RF cluster are displayed in Table 5.1. The generated I·RF cluster structures showed energy difference for any small rotation of the ribose group, which results in changes of its binding site and intramolecular average distances between all the inter-cluster bonds. The TDDFT spectra acquired provide the relevant information required to gain further insight into the nature of the electronic transitions involved in the photoexcitation of the I·RF clusters, and thus aid in the interpretation of experimental data. Table 5.1 shows structures of the selected isomers and their relative energies.

The structures displayed in Table 5.1 differ in their average binding distance of the hydrogen bond that exists between the iodide ion and the positions of the hydroxyl groups of the ribosyl group of the RF moiety.

Table 5.1: Calculated structures and relative electronic energies of the selected ungrouped conformational isomers of Riboflavin iodide ($I\cdot RF$) clusters. Structures were calculated at the B3LYP/6-311++G(2d,2p) level, 6-311G(d,p)/SDD on I. Energies are zero-point energy corrected.



Structures with bonding that are linked OH3 (see Figure 5.1b for labelling) gave more structures with lower relative energies.

Table 5.2 below shows the calculated bond lengths, the Boltzmann populations, vertical detachment energies (VDE) and vertical dipole moments (VDM). The calculated dipole moment of the neutral cluster at the ground-state geometry of the anionic cluster (VDM) is polar enough to support a dipole bound state,^{234,292-294} since it is greater than 2.5D.

The calculated VDE for the clusters appears to be greater than other iodide ion clusters,^{31,261} however this is not surprising because they possess high VDM.

Table 5.2: Calculated bond lengths,^a relative energies, % Boltzmann population,^c vertical detachment energy (VDE) and vertical dipole moment (VDM) of the selected (I·RF) clusters structures calculated at B3LYP/6-311++G(2d,2p) level, 6-311G(d,p)/SDD on I.

Structure	Bond Lengths (Å)				Relative Energies (kJmol ⁻¹)	% Boltzmann population	VDE (eV)	VDM (D)
	OH1→I	OH2→I	OH3→I	OH4→I				
a	X	X	2.56	2.61	0.0	73.32	4.96	9.27
b	2.55	2.65	X	X	4.29	15	4.78	7.77
c	X	2.52	2.62	X	8.38	3.3	4.86	7.73
d	X	X	2.45	X	10.41	1.48	4.77	8.72
e	X	X	X	2.56	6.45	6.9	4.70	9.22

^a Non-covalent Bond-lengths below 3Å. ^b X = Not applicable.

^c % Boltzmann populations calculated at 298 K.

These five conformational isomers are predicted to have significant Boltzmann populations at 298 K, which indicates that a number of isomers may be present in our gas phase experiment with (structure **a**) being the most populous. It is important to mention that between the lowest energy tautomer (structure **a**) to (structure **e**) which is the lowest randomly selected conformational isomer, there are 28 real structures with no negative frequency. We may conclude that many structures contribute to the spectra acquired in the gas phase, with (structure **a**) being the most populated. The TDDFT spectra of the isomers from Table 5.1 displayed in Figure

5.9 (section 5.7.1.3) show that the calculated electronic spectra are similar for each of these clusters. The TDDFT spectra (Figure 5.9) show no significant difference in the position of the Bands except for the ratio of their Band I and Band II intensity. This may be attributed to the excited state behaviour of riboflavin being determined mainly by the excitation of the lumichrome moiety which is the chromophore found in riboflavin. Figure 5.10 (section 5.7.2.1) presents an overlay of the calculated TDDFT spectra with the experimental photodepletion spectra, showing good agreement.

Figure 5.2 displays the TDDFT spectrum obtained for the lowest-energy isomer (structure **a**). The accurate prediction of dipole bound-excited states is challenging for TDDFT,²⁴⁴⁻²⁴⁶ but such calculations have been used in the interpretation of the electronic spectra of iodide clusters.^{31,250,251,261} It is notable that electronic excitations that occur above the electron detachment threshold of an anion will correspond to resonance states. Although the accurate theoretical prediction of such states is beyond the scope of this work, the theoretical calculations presented are expected to be useful for the interpretation of the experimental data.^{250,251}

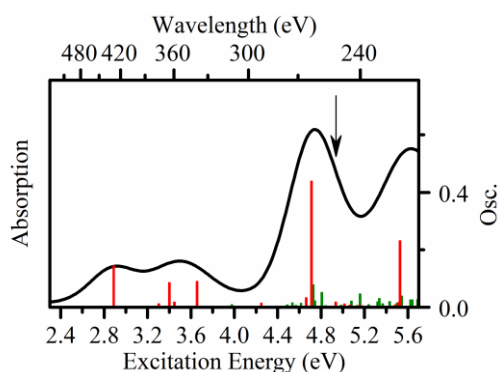


Figure 5.2 TDDFT (B3LYP/6-311++G(2d,2p) level, 6-311G(d,p)/SDD on I) excitation spectrum of the lowest energy isomer of I•RF cluster for the structure **a** shown in Table 1. The oscillator strengths (OSC.) on the y axis of individual transitions ≥ 0.005 are shown by vertical bars while the full line spectrum is a convolution of the calculated spectrum with Gaussian function (0.25 eV HWHM). The arrows represent the VDE. (The green line represents transitions from an iodide p-orbital and the red lines represent transitions from riboflavin π orbitals).

The TDDFT spectrum presented in Figure 5.2 above also showed the strong presence

of transitions from the iodide p-orbital(green) and riboflavin π orbitals(red) together at Band III. We will return to this in the discussion section.

5.4.2 Higher-energy collisional dissociation of the I·RF cluster

Higher-energy collisional dissociation (HCD) was performed on the isolated I·RF complex to determine the ground-state thermal fragments. Figure 5.3 displays the relative intensities of the I·RF complex ion decay and the corresponding fragment production as a function of applied % HCD energy. I is the only HCD fragment produced via cluster dissociation, with no significant break down of the RF molecule. It is notable that no deprotonated riboflavin is produced, although the deprotonated fragment ion has been observed in the HCD of some iodide molecule complexes.

The same pattern of thermal fragmentation wherein I is the sole ionic fragment was also observed in performing low-energy collision induced dissociation on iodide ion pyrimidine clusters. However, I and deprotonated thiouracil were observed in the HCD experiment of iodide ion thiouracil. The disparity in their behaviours could be attributed to the differences in the pKa of the monomers. Riboflavin and pyrimidines have close pKa (> 9) while thiouracil has a lower pKa of <8.

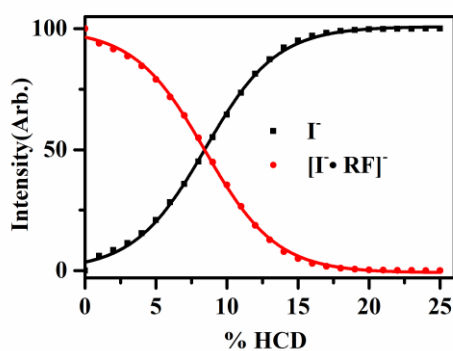


Figure 5.3 % Fragment ion yield from the dissociation of I·RF cluster upon HCD between 0 and 25% energy, illustrating fragmentation of the complex into iodide and riboflavin. The data points fitted with the curved lines are viewing guides to show the profile for an individual fragment.

A small amount of I⁻ is observed even at 0% HCD, revealing that the complex is slightly metastable. This is probably due to incomplete cooling of the relatively large I⁻·RF complex in the ion trap, rather than the complex being intrinsically unstable. Having established the thermal ground state behaviour, we now move to exploring the photoexcitation characteristics of the cluster.

5.4.3 Photodepletion Spectrum of the I⁻·RF cluster

The photodepletion spectrum of I⁻·RF across the range 516 – 222 nm (2.4-5.6 eV) is displayed in Figure 5.4. This spectrum corresponds to the gas-phase absorption spectrum of the complex in the limit where fluorescence decay of the excited state is negligible.²³⁹ It is important to note that as the system is anionic, for energies above the detachment energy, the photodepletion spectrum (PD) will reflect contributions from electron detachment, as well as intra-cluster electronic excitations.

The I⁻·RF photodepletion spectrum displays an area of low-intensity absorption in the range 2.6-3.0 eV, followed by three Bands with λ_{max} at ~3.13 (Band I), ~3.65 (Band II) and ~4.75 eV (Band III). Photodepletion rises strongly above 5.2 eV (IV). The photodepletion spectrum mirrors the solution phase spectrum with blue shifts of 0.35 and 0.33 eV for Bands I and II, respectively, in the photodepletion spectrum compared to the solution-phase spectrum.

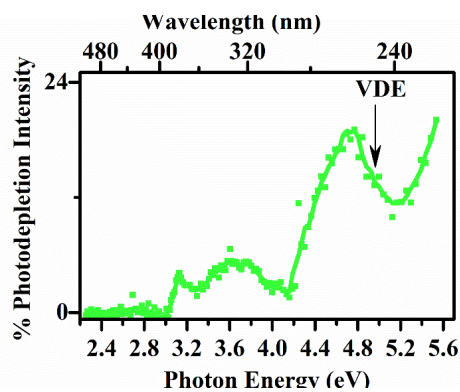


Figure 5.4 Photodepletion spectrum of the I⁻·RF cluster. The line is a five-point adjacent average of the data points. The arrow indicates the calculated VDE of 4.95 eV.

The observed shift is expected and can be attributed to solvent effects in the solution phase, although Band **III** seems not to be perturbed with just a Band shift < 0.09 eV. The photodepletion spectrum of gaseous deprotonated lumichrome displays three Bands that peak at 2.6 eV, 4.03 eV, 4.74 eV and a fourth at > 5.6 eV which mirror same pattern as seen in this experiment on I·RF cluster. Comparison of the solution phase spectrum of deprotonated lumichrome to its photodepletion spectrum revealed Band shifts at Bands **I** and **II**. These Band shifts are suggested to have resulted from the strong influence on electronic transition by solvent interaction.²²⁹ To further explore the nature of the excited states, we next turn to inspecting the action spectra for the photofragments that are produced across the same spectral region.

5.4.4 Photofragmentation of the I·RF cluster

Figure 5.5 displays the photofragment mass spectra obtained when I·RF is excited at 4.37 eV. At 4.37 eV, the most intense photofragment corresponds to m/z 376, the riboflavin anion. m/z 241, which corresponds to deprotonated lumichrome, [LC-H]⁻ and m/z 127 (the iodide ion) also appear as prominent photofragments along with m/z 198 as a more minor photofragment. Table 5.3 lists the photofragments along with assignments of the accompanying neutral fragments.

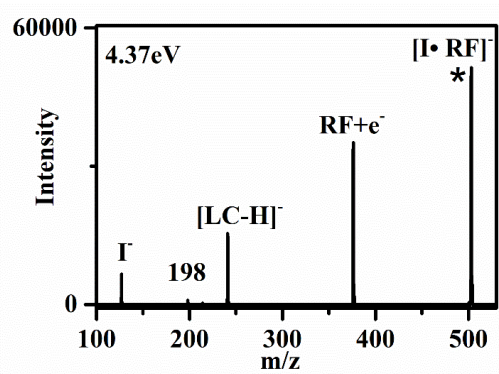


Figure 5.5 Photo-fragment mass spectrum (laser_{on}-laser_{off}) of the I·RF cluster excited at 4.37eV. * represents the parent ion mass spectra.

Table 5.3 Lists of photofragments with assignments observed at the Band I maxima of the I⁻·RF clusters, shown with the HCD fragments.^a

Fragments (m/z)	Photofragments	HCD fragments	Neutral fragments
376	✓ [RF] ⁻	X	I
241	✓ [LC-H] ⁻	X	I + C ₅ H ₁₂ O ₄
127	✓ (I)	✓ (I)	RF
198	✓	X	HNCO + ¹³ C ₅ H ₁₁ O ₄

^aX indicates fragment not observed in HCD.

To gain further insight into the production pathways for the photofragments from I⁻·RF cluster, it is useful to consider their production spectra. Figure 5.6 displays the spectra for RF, I, [LC-H]⁻ and *m/z* 198, which are presented with the photodepletion spectra for comparison. Overall, the production spectra profiles of the RF, [LC-H]⁻ and I photofragments are similar across the 2.4 – 5.6 eV range, with their photofragment production profiles largely mirroring the photodepletion spectrum in terms of the shapes and positions of the spectral features.

All the photofragments were produced across the whole region of the photodepletion spectrum, although with some modifications on the position of the Bands which can be attributed to the excited states decay pathway through which they are produced.

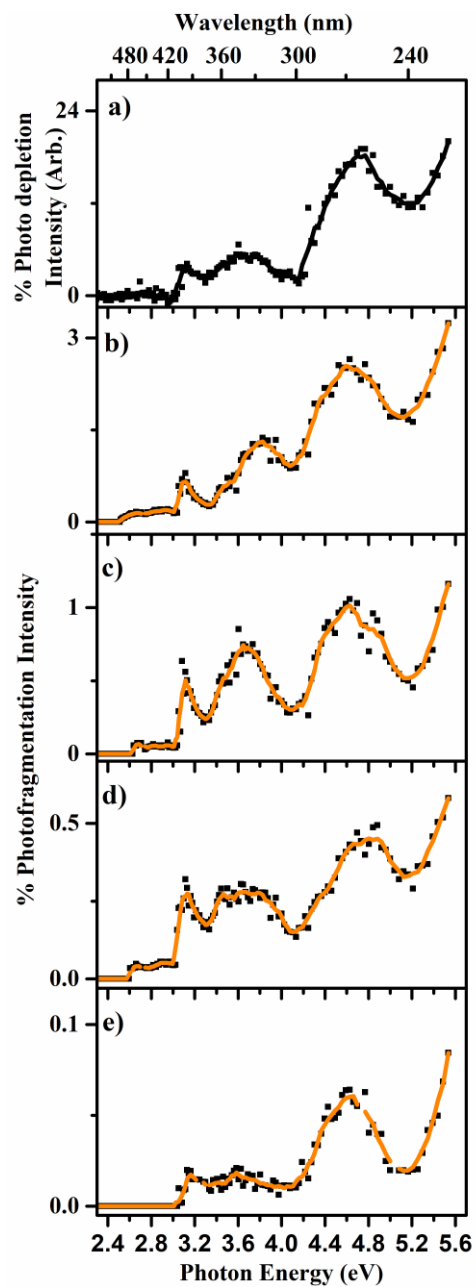


Figure 5.6 a) Gas phase photodepletion spectra of the I-RF cluster and photofragments spectra b) RF, c) [LC-H]⁺, d) I⁺ and e) [*m/z* 198]⁺ generated on

photoexcitation of mass selected $I\cdot RF$ cluster ions, across the range 2.4-5.6 eV (516-222 nm). The solid line is a five-point adjacent average of data points.

They display onset at about 2.4 eV except for m/z 198 that shows at a slightly higher energy onset at 2.9 eV. The position and features of the low intensity Band **I** in the photodepletion spectrum is the same for all the photofragments produced. Band **II** of the I ion showed a broad Band of width ~ 0.74 eV without any prominent peak, which is the same feature seen in the photodepletion spectrum. This may be attributed to their production by all the excited states involved in the photoexcitation of the $I\cdot RF$ cluster. The photofragment m/z 198 has a low production intensity that is like a flat extension of Band **I**, and which lies between 3.34 and 4.18 eV in the region of Band **II**. This behaviour is different from that seen in the production of the other photofragments, which have better enhanced intensity in this region. $[LC-H]^-$ (Figure 5.6c) has well resolved Band **II**, which lies across 3.34 and 4.18 eV at 3.62 eV. We note that the most intense photofragment RF^- (Figure 5.6b), although having a Band **II** that is within this same region, had its peak shifted to a slightly higher energy at 3.78 eV. Band **III** is the highest in intensity of the three Bands for all the photofragments and lies between 4.18 and 5.12 eV, which is in good agreement with the photodepletion spectrum. The photofragments production peaks at ~ 4.62 eV, except for the I ion, which shows an extended Band beyond the photodepletion peak at ~ 4.82 eV in this region.

However, the relative intensities of the photofragmentation spectral features below 4.2 eV compared to those above 4.2 eV, are higher than in the photodepletion spectrum. For example, if we compare the I production spectrum with the photodepletion spectrum, and consider the energies 3.64 eV and 4.74 eV, the relative spectral intensity for I is 0.62 ($\sim 0.28/0.45$), while it is 0.26 (5/19) for photodepletion. This effect is probably associated with enhanced electron detachment at higher energies. To explore this directly, we next turn to considering the electron yield detachment spectrum.

5.4.5 Electron Detachment Yield Spectrum of the $I\cdot RF$

The electron detachment yield spectrum for $I\cdot RF$ is shown in Figure 5.7. Figure 5.11(section 5.7.2) presents the electron detachment spectrum overlaid with the photodepletion yield (PD*) spectrum for comparison.

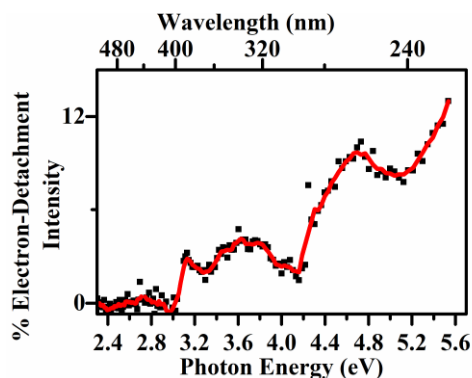


Figure 5.7 % Electron Detachment yield of I·RF cluster. The solid line is a five-point adjacent average of data points.

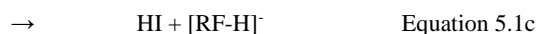
The electron detachment yield spectrum mirrors the photodepletion spectrum of the I·RF cluster and the electron detachment yield is of higher intensity than the photofragmentation yield. This indicates that ionic photofragmentation is a minor excited state decay pathway for the I·RF cluster at all the wavelengths scanned (2.3-5.6 eV). Here production of the RF⁻ photofragment is the most prominent ionic fragment (Figure 5.6a). The production of low intensity ionic photofragments compared to the photodepletion is similar to all the iodide ion clusters we have studied.^{31,261} Although the production of the monomer anion has been observed for some of the I·thiouracil clusters studied previously³¹, however the characteristics of RF⁻ being the most produced ionic photofragment with higher production intensity than the iodide ion appears to be unique to the I·RF cluster. The absence of the production of deprotonated RF is also peculiar to the I·RF cluster when compared to other iodide ion clusters studied.^{31,261}

5.5 Discussion

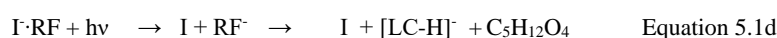
5.5.1 Overview of the I·RF Decay Channels

It is useful to review the possible decay pathways for I·RF, prior to discussing the photofragmentation dynamics. The first group of cluster decay channels result in

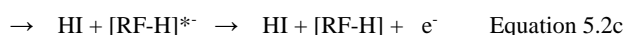
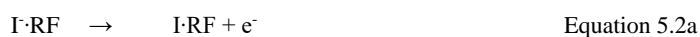
direct fragmentation of the precursor cluster. For I·RF this would correspond to pathways such as:



Secondary fragmentation can also occur through break up of hot primary photofragments (Equation 5.1d).



Alternatively, above the detachment threshold, electron detachment can occur, either via direct detachment (Equation 5.2a) or indirectly from an excited state of the cluster (Equation 5.2b). Electron detachment can also occur from hot photofragments, e. g. (Equation 5.2c) and (Equation 5.2d).



5.5.2 Assignment of the observed excited states from the photodepletion spectra

There are three Band peaks with λ_{max} at 2.78, 3.32 and 4.66 eV in the solution-phase spectrum of RF over our spectral scanned region. The photodepletion spectrum displayed a low intensity absorption within the visible region with its Bands **I**, **II** and **III** blue shifting in the UV region with peaks at 3.18 and ~4.74 eV for Bands **I** and **III** and a broad Band **II** centred around ~3.74 eV. The shift is attributed to solvent effects as mentioned earlier. These peaks occur at energies close to Bands in the solution-phase spectrum indicating that there are strong cluster excited states in these regions associated with $\pi\text{-}\pi^{\ast}$ localized transitions of the RF moiety. The extremely sharp onset at ~3.0 eV for Band **I** has been observed in the photoexcitation of deprotonated gaseous alloxazine and lumichrome although above 3.8 eV (Band **II**) in their photodepletion spectrum.²²⁹ Dipole-bound excited states have been seen to occur in the region of the measured VDE for iodide ion uracil and iodide ion thymine clusters. It is also worth noting that the calculated VDE is found around this region in other iodide molecules previously studied.^{31,253,261} Thus we expect any dipole-bound excited state to occur around the region of the calculated VDE of I·RF, i.e.

around 5 eV. The calculated VDEs are observed to shift by ~ 0.2 eV towards higher energy from the measured VDEs.^{31,253,261} The observation of dipole-bound excited states with our experimental method has been established with the signature of dipole-bound excited states observed upon near threshold excitation of iodide-pyrimidine clusters²⁶¹ and anionic salt clusters ($I \cdot MI$ where $M = Na, K, Cs$).²⁹⁸ Having established the relationship between the experimental and calculated VDE, we turn to assign the excited states of the $I \cdot RF$ clusters in the higher-energy region. The photodepletion spectrum does not really show the sharp fall-off in photodepletion intensity that is typically observed at the high-energy edge of the dipole-bound excited state,^{229,298} around Band **III** but the $I \cdot RF$ spectrum displays a strong photodepletion onset around 4.18 eV, peaking at 4.75 eV which is around the region of the predicted VDE (Band **III**). This near-threshold Band is followed by the rising edge of Band **IV** above 5.6 eV and within the vicinity of dominant electron detachment. This spectral behaviour is consistent with a dipole-bound excited state followed by a region of direct electron detachment,^{299,300} and has been observed in iodide ion-polar molecule clusters studied previously,^{261,286} so it is not possible to conclude that the dipole-bound excited state exists for $I \cdot RF$ from its photodepletion spectrum without exploring other aspects of the results.

The photodepletion spectrum of the $I \cdot RF$ cluster shows similar features to the solution-phase spectrum of RF, with λ_{\max} of 2.78, 3.32 and 4.66 eV for Bands **I**, **II** and **III**, respectively. There is strong agreement between the photodepletion spectrum and solution-phase spectrum within our scanned region except for the Band shifts which have earlier been addressed as coming from solvent effects. The features of the solution-phase spectrum are related to $\pi-\pi^*$ transitions of the RF chromophore. The lower-energy Bands (**I and II**) of the photodepletion spectrum of $I \cdot RF$ cluster are associated mainly with $\pi-\pi^*$ transitions but considering observations from other studied iodide ion clusters, the Band **III** region may also include a dipole-bound excited state as well as excitation of the higher-energy strong RF $\pi-\pi^*$ transition as was observed in the recent study of iodide ion thiouracil molecules,³¹ and will be discussed later.

TDDFT calculations predict $\pi-\pi^*$ localized transitions well but are less successful at predicting dipole-bound excited states. There is good agreement between the calculated TDDFT spectrum and our photodepletion spectrum except for a slight narrowing of ~ 0.05 eV in our experimental photodepletion spectrum for Band **III**.

This agreement seen for I•RF cluster shows that π - π^* RF-localized transitions dominate the experimental spectrum although the strong presence of transitions from iodide p-orbital around this Band are also present in the TDDFT spectrum. The explored molecular orbital models showed strong contributions from n- π^* and π - π^* in this region,

We next turn to discuss the I•RF cluster's photofragment production spectra below.

5.5.3 Photofragment production

Intra-cluster electron-transfer processes involve the trapping of the ejected low energy electron of the I in a diffuse orbital i.e. dipole-bound excited state formation or direct charge transfer from I to the RF valence orbitals. This is one of the mechanisms by which ionic photofragments can be produced.²⁸⁷ The mechanism is expected to generate through the decay of a dipole-bound excited state, a dipole-bound anion or the deprotonated form of the RF as observed for the iodide-thionucleobases studied previously.³¹

Another mechanism to produce photofragments is based on the electronic excitation of the RF chromophore. This excitation is expected to result in fragmentation into smaller flavins, as seen previously.^{109,347} When RF-localised transitions dominate in a photoexcitation, if the electronic relaxation to electronic ground state occurs by ultrafast decay, followed by thermal fragmentation, we would expect the same ionic fragments as those obtained upon low-energy collision induced dissociation.^{240,261} Higher energy collisional dissociation (HCD) was done on the I•RF clusters to identify the ground state thermal fragmentation ionic fragments. The result revealed I⁻ as the only ionic fragment which mirrors the behaviour of iodide-nucleobase complexes previously studied.^{252,253,261} Although the production of I⁻ as a photofragment could be explained as originating from the ultrafast decay of excitations within the RF moiety, the production of other photofragments suggest the photodissociation of I•RF clusters is non-statistical and its excited state does not decay solely by ultrafast internal conversion followed by loss of energy through thermal fragmentation on the ground-state surface.

Riboflavin is known to possess excited states that can decay to a long-lived triplet state via an intersystem-crossing transition from where non-radiative dissipation of energy to electronic ground state can occur. FMN (which shares the same tri-cyclic

iso-alloxazine chromophore with RF) has been suggested to decay by a non-radiative channel which includes electron detachment or inter-system crossing.³⁴⁸

Time-resolved photoelectron spectroscopy of iodide - native nucleobases dipole-bound, and nucleobase localized excited states reveal that both decay with long lifetimes.^{261,286} Thus there is a need to explore the photofragments production profile to help assign the nature of the excited states of these photofragments. The photofragment production spectra show that around Band **I**, all the photofragments reveal similar spectra features. They are thus likely to be produced by the decay of the same excited states, which could be assumed to be dominated by a riboflavin localized π - π^* transition. It has a similar profile to the photodepletion spectrum in this region. The intensity of the production of this Band compared to Band **II** differs for the individual photoproducts.

The Band **II** region showed features that are different for the individual photofragments. The I⁻ production spectrum shows a broader Band, with an onset from ~ 3.32 extending to ~ 4.12 eV. This band has no resolved peak, and the production is approximately the same intensity as Band **I**. The production of the m/z 198 photofragment appears as a flat extension from Band **I** in this region. The most intense photofragment is [LC-H]⁻ when compared with its Band **I**. This photofragment has a well resolved band that peaks at ~ 3.67 eV. The RF⁻ photofragment spectrum displays a band in this region with a peak at 3.8 eV. The band is blue shifted by ~ 0.13 eV from the peak of m/z 198 and [LC-H]⁻ although it is within the region of the photodepletion of the parent ion peak and the production of the I⁻ photofragment. Despite the differences in the spectra features, the excited state decay in this region may be attributed to the contributions of localized riboflavin π - π^* electronic transitions, from the TDDFT calculation.

Band **III** is the region that displays the highest photodepletion intensity. All the photofragments are also produced in their highest intensity in this region. The photofragments m/z 198, [LC-H]⁻ and RF⁻ possess well-resolved bands that peak at 4.62 eV. This is slightly below the energy of the peak for Band **III** in the photodepletion spectrum (4.75 eV), while the I⁻ photofragment has its peak in this region at 4.82 eV - a higher energy compared to the peak of the photodepletion spectrum. The presence of this near-threshold band just below the calculated VDE, could be association with the strong influence of a dipole-bound excited state of the cluster, although there was no evidence of a sharp fall in intensity around the

observed VDE for any of the photofragments. The cluster's calculated VDM above 2.5D, which indicates that it will support a dipole bound excited state. The spectral pattern in this region has also been observed in the iodide pyrimidines studied.²⁶¹ The TDDFT calculation suggests a strong π - π^* transition within the RF moiety in the region of this band too. The strong coupling of the two distinctive excited states has been identified earlier in the photoexcitation studies of iodide thiouracil complexes.³¹ Thus we assign the decay of the coupled excited states as the contributors in this region.

It is worth mentioning that electron detachment is very strong in all the band regions, and despite the observed spectra differences, all photofragments approach the baseline at the same energy before the onset of the next band.

With the observed differences in the spectral profile of the different photofragments, we can discuss, suggest, and assign transitions to the production of the individual photofragments.

The most intense photofragment RF^- was produced around the Band **I** and **II** regions which are associated to a riboflavin localized excited state. The production of an RF^- photofragment around this region is not surprising, because a similar profile has been observed for the photofragment production of 2,4 thiouracil anion [2,4-TU]⁻ in the studies of the iodide -2,4 thiouracil complex.³¹ This profile was simply explained as due to the proximity of the thionucleobase excited state with the cluster dipole-bound excited state, resulting in strong coupling of the two excited states. RF^- may be identified as a valence anion because it resulted in the production of other flavin photofragments. This is a known photo-property of large flavin molecules.³⁴⁷

The **I** photofragment produced across the scanned region has a profile that is like that of the photodepletion spectrum except, for further extension of its Band **III** by ~ 0.20 eV towards higher energy. The similarity suggests that **I** is produced by the decay of all the excited states existing in the excitation of the **I**·RF cluster. This behaviour has earlier been observed in studies of iodide pyrimidine and iodide thiouracil clusters.^{31,261} Although direct detachment to the upper $^2\text{P}_{1/2}$ neutral state has been identified around 5 eV has been identified using photoelectron spectroscopy for iodide-ion uracil and iodide-ion thymine complexes,^{261,286} the photodepletion spectrum does not clearly display an upper-spin orbit dipole-bound state,³⁰¹ The extension in the **I** Band **III** which occurred with a peak at 4.82 eV might be a

modification in the Band as a result of a contribution from the decay of the upper spin-orbit dipole-bound state coupled with other excited states (π - π^* localised transitions and dipole bound excited states of the cluster) identified in this region.

The m/z 198 photofragment spectrum to a large extent mirrors the production profile of $[\text{LC-H}]^-$ and has earlier been identified as a photofragment from the photoexcitation of $[\text{LC-H}]^-$.²²⁹ In that work, the m/z 198 photofragment is produced through the photodepletion of $[\text{LC-H}]^-$ but with a surprising lack of its production in the region of the second Band **II** (4.03 eV) of the photodepletion spectrum of the $[\text{LC-H}]^-$.²²⁹ In this region $[\text{LC-H}]^-$ photo depletes by electron loss.²²⁹ The spectral profile of the m/z 198 photofragment in the region of Band **II** in our work is in agreement with the features of the m/z 198 photofragment spectrum produced from the photodepletion of $[\text{LC-H}]^-$. The photodepletion of $[\text{LC-H}]^-$ by electron loss only in the Band **II** region accounts for the very low and almost flat profile observed in the m/z 198 photofragment production spectrum around the Band **II** ($\sim 3.38 - 4.1$ eV) region from the photodepletion of $\text{I}\cdot\text{RF}$ cluster. This is a significant difference in the spectra of the $[\text{LC-H}]^-$ and m/z 198 photofragments, thus confirming that m/z 198 is a secondary photofragment from $[\text{LC-H}]^-$. This behaviour in this Band **II** region has been identified as due to the electron capture by RF in this resonance region not resulting in dissociative decay at a rate that can compete with the electron auto detachment decay pathway.²²⁹

5.6 Further Discussion & Concluding Remarks

The formation of a dipole-bound state which is a doorway to valence-anion formation and hence molecular dissociation is an established fact.^{260,261,286,349} Using time-resolved anion photoelectron spectroscopy, Neumark and co-workers have presented work on dipole-bound states which may auto-detach or lead to the formation of a valence anion that eventually dissociates.^{286,349} The photophysics and photochemistry of the $\text{I}\cdot\text{RF}$ clusters mirrors those of the iodide-thiouracil earlier studied.³¹ Here electron detachment is the dominant pathway for photoexcitation decay, and production of ionic photofragments is a minor pathway. In the studies of $\text{I}\cdot 4\text{-TU}$ and $\text{I}\cdot 2,4\text{-TU}$ clusters, initial photoexcitation in the VDE region accesses a dipole-bound excited state that decays into stable valence $[4\text{-TU}]^-$ and $[2,4\text{-TU}]^-$ molecular anions.³¹ The presence of RF^- as a photofragment in the photoexcitation

of I•RF clusters most probably follows the same mechanism. The resemblance between the photodepletion spectrum and the absorption spectrum of the uncomplexed RF shows that the spectrum is dominated by RF localized π - π^* transitions. This is also in good agreement with what was seen in the studies of I•4-TU and I•2,4-TU clusters. Thus, there could be an improvement in the coupling of the electron detachment continuum to chromophore-centred transitions due to the intrinsic properties of the RF molecule and its large electric dipole moment.

In the absence of the deprotonated form of the RF present as an ionic photofragment, it is meaningful to attribute the production of the [LC-H]⁻ to secondary fragmentation occurring through the breakup of the hot primary photofragments RF⁻ (Equation 3d). This secondary fragment in turn photofragments through two different pathways. Production of m/z 198 around Band **I** and **III** and auto electron detachment in Band **II**. The production of m/z 198 has earlier been identified to be a photoproduct of the fast decay of the excited state, which is followed by thermal fragmentation on the electronic ground state surface.²²⁹ This pathway may be different in this study, because none of the photofragments were identified as fragments in the collision-induced dissociation of the I•RF cluster, (with the exception of the I) Thus RF⁻, [LC-H]⁻ and m/z 198 are assumed to be direct excited state photofragments.

In conclusion, it is important to mention that to the best of our knowledge, nothing has been reported on the existence of RF⁻ as a stable valence anion. Therefore the production of RF⁻ observed in our experiment is the first in this regard.

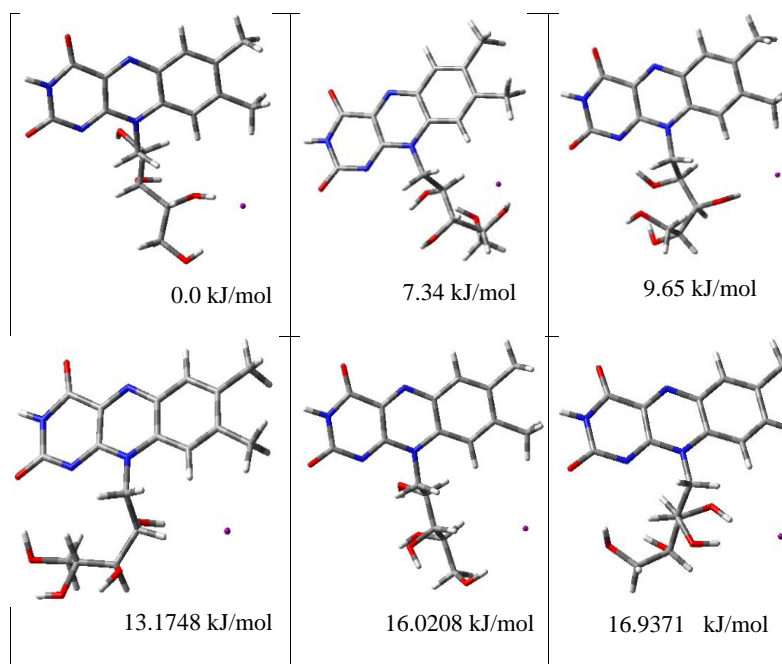
5.7 Supplementary Information

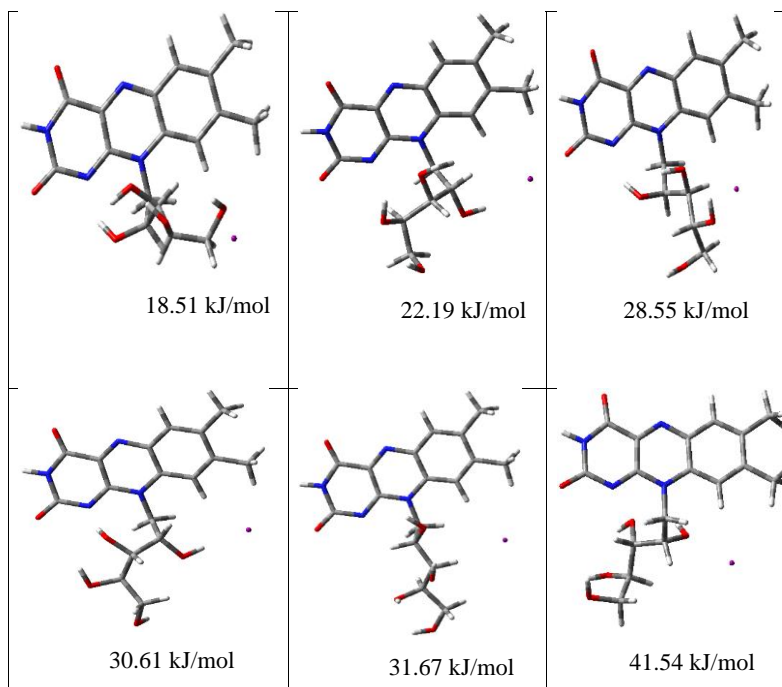
5.7.1 Computational studies on I·RF clusters

5.7.1.1 DFT calculations of grouped conformational isomers of the I·RF cluster

Conformational molecular dynamics search on I·RF clusters generated 26 cluster groups by average distance between all inter-cluster pairs linkage criteria. This is based on generating a structure (nearest to the centroid) per cluster normalised by applying the Kelley-Bryson penalty function technique for state-constrained control problems. 12 out of the 26 optimised conformers are real structures with no negative frequencies. (Table 5.4) The relative energies are in relation to the optimised lowest energy group conformer.

Table 5.4 Optimised I·RF clusters grouped conformers generated using Schrodinger's Macro-Model with mixed Monte Carlo torsional and low-mode sampling parameters minimised with OPLS3e force field. The structures were optimized at B3LYP/6-311++G(2d,2p) level of theory.





5.7.1.2 Direction of the dipole moment of the RF molecules in the $I \cdot RF$ cluster

The direction of the dipole moment shows the iodide ion is bound away from the direction of the dipole moment in the $I \cdot RF$ cluster but close to the direction of the dipole moment in the RF monomer.

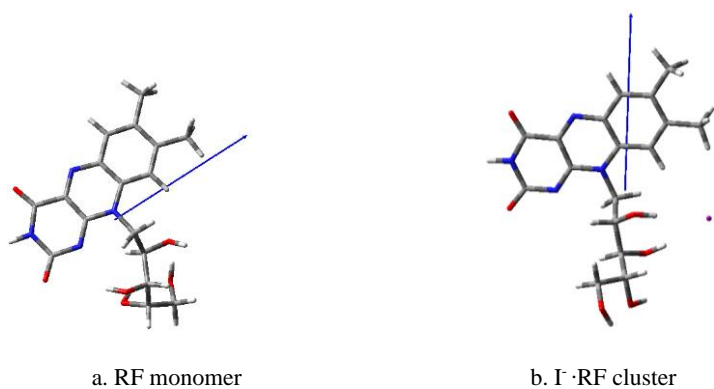


Figure 5.8 The vector direction of the axis of the dipole moment of (a) RF monomer

and (b) F⁻RF molecule, calculated for the neutral molecule at the geometry of their optimized ion-molecule respectively.

5.7.1.3 TDDFT calculations for individual selected conformational isomers of the F⁻RF clusters

TDDFT calculations were performed for the selected conformational isomer structures displayed in Table 5.1 as isolated gaseous ions. Their acquired excitation spectra are presented in Figure 5.9. The overlaid TDDFT excitation spectra selected conformational isomer and the experimental photodepletion spectrum for comparison are shown in Figure 5.10.

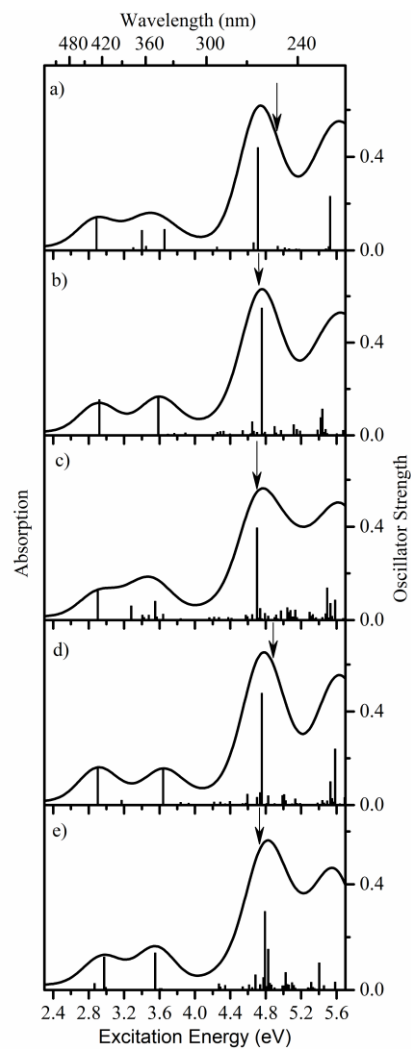


Figure 5.9 TDDFT excitation spectra of the selected conformational isomers of I·RF clusters for the structures shown in Table 5.1. The oscillator strengths (OSC.) on the y axis of individual transitions ≥ 0.005 within the experimental scan range are shown by vertical bars while the full line spectrum is a convolution of the calculated spectrum with Gaussian function (0.25 eV HWHM). The arrow shows the position of the calculated VDE.

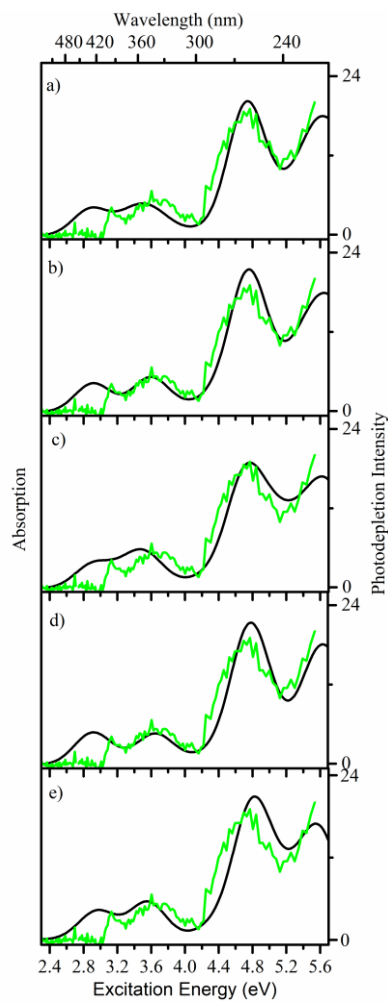


Figure 5.10 Overlaid TDDFT excitation spectra of the selected conformational isomers and the experimental photodepletion spectrum of I·RF cluster.

5.7.1.4 Molecular orbitals involved in the TDDFT transitions of the lowest energy selected conformational isomer (structure a) of I·RF cluster

Table 5.5 Calculated TDDFT transition energies at the B3LYP/6-

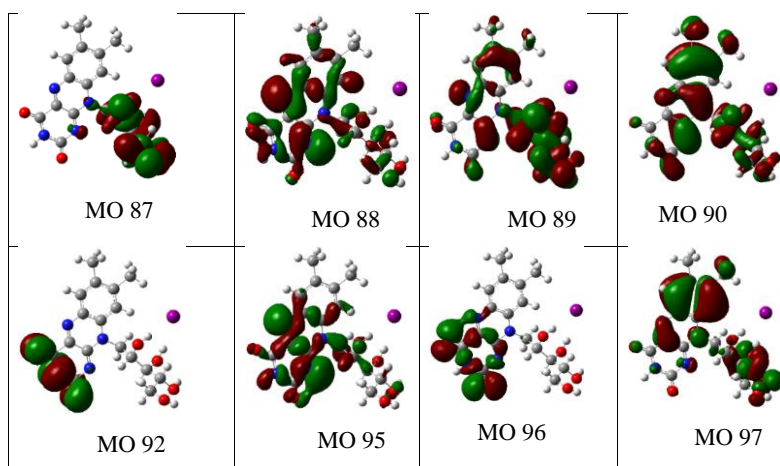
311++G(2d,2p)/SDD level of theory and oscillator strengths of the I-RF cluster.

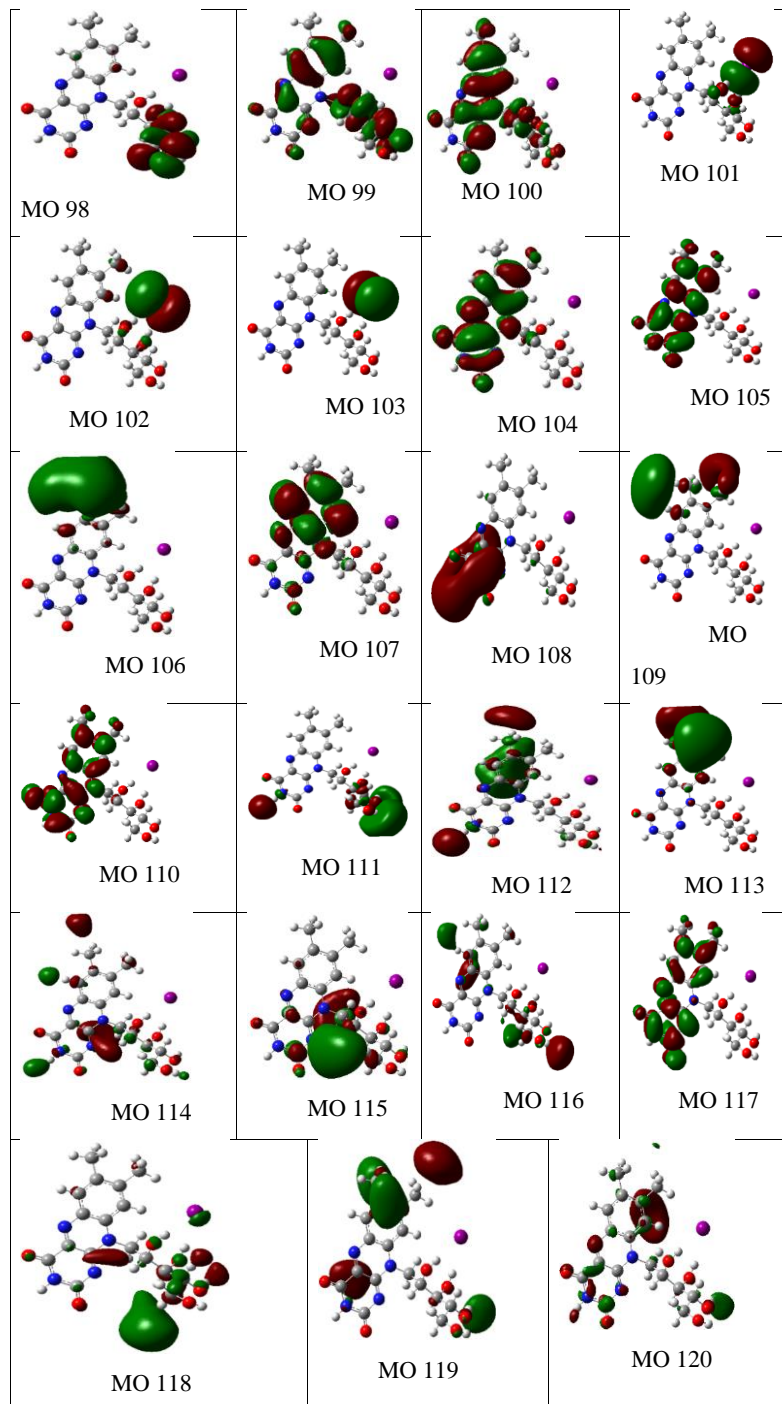
Only transitions below 5.6 eV with oscillator strength > 0.005

Orbital transitions	ΔE (eV)	f
(0.69)100(π) \rightarrow 104(π^*)	2.89	0.1440
(0.54)95(π) \rightarrow 104(π^*)	3.30	0.0120
(0.31)96(π) \rightarrow 104(π^*)		
(0.29)99(π) \rightarrow 104(π^*)		
(0.32)96(π) \rightarrow 104(π^*)	3.40	0.0849
(0.59)99(π) \rightarrow 104(π^*)		
(0.39)95(π) \rightarrow 104(π^*)	3.44	0.0172
(0.52)96(π) \rightarrow 104(π^*)		
(0.19)99(π) \rightarrow 104(π^*)		
(0.65)97(π) \rightarrow 104(π^*)	3.65	0.0893
(0.42)102(n) \rightarrow 106(σ^*)	3.98	0.0083
(0.55)102(n) \rightarrow 107(π^*)		
(0.65)92(π) \rightarrow 104(π^*)	4.26	0.0146
(0.20)100(π) \rightarrow 105(π^*)		
(0.63)103(n) \rightarrow 108(σ^*)	4.48	0.0077
(0.22)103(n) \rightarrow 109(π^*)		
(0.63)103(n) \rightarrow 109(π^*)	4.53	0.0148
(0.26)103(n) \rightarrow 108(σ^*)		
(0.63)102(n) \rightarrow 108(σ^*)	4.56	0.0055
(0.22)102(n) \rightarrow 109(π^*)		
(0.61)102(n) \rightarrow 109(π^*)	4.61	0.0136
(0.26)102(n) \rightarrow 108(σ^*)		
(0.54)88(π) \rightarrow 104(π^*)	4.66	0.0326
(0.30)89(π) \rightarrow 104(π^*)		
(0.21)90(π) \rightarrow 104(π^*)		
(0.56)100(π) \rightarrow 105(π^*)	4.72	0.4386
(0.22)103(n) \rightarrow 111(π^*)		
(0.24)100(π) \rightarrow 105(π^*)	4.73	0.0774
(0.25)103(n) \rightarrow 110(π^*)		
(0.54)103(n) \rightarrow 111(π^*)		

(0.64)101(n)→108(σ*)	4.74	0.0217
(0.63)101(n)→109(π*)	4.80	0.0510
(0.23)101(n)→108(σ*)		
(0.64)103(n)→112(π*)	4.83	0.0052
(0.22)97(π)→105(π*)	4.95	0.0179
(0.37)99(π)→105(π*)		
(0.46)100(π)→107(π*)		
(0.23)101(n)→110(π*)	4.98	0.0071
(0.60)101(n)→111(π*)		
(0.56)89(π)→104(π*)	5.02	0.0112
(0.24)100(π)→107(π*)		
(0.43)95(π)→105(π*)	5.07	0.0066
(0.21)97(π)→105(π*)		
(0.32)99(π)→105(π*)		
(0.31)100(π)→106(σ*)?		
(0.57)103(n)→114(π*)	5.08	0.0210
(0.26)103(n)→115(π*)		
(0.32)103(n)→114(π*)	5.12	0.0051
(0.61)103(n)→115(π*)		
(0.53)102(n)→114(π*)	5.16	0.0460
(0.25)102(n)→115(π*)		
(0.31)95(π)→105(π*)	5.17	0.0050
(0.21)96(π)→105(π*)		
(0.40)99(π)→105(π*)		
(0.59)103(n)→116(π*)	5.24	0.0086
(0.23)103(n)→118(π*)		
(0.59)102(n)→116(π*)	5.32	0.0182
(0.24)102(n)→118(π*)		
(0.56)101(n)→114(π*)	5.34	0.0301
(0.32)101(n)→115(π*)		
(0.23)101(n)→114(π*)	5.37	0.0118
(0.40)101(n)→115(π*)		
(0.21)103(n)→116(π*)		
(0.45)103(n)→118(π*)		

(0.29)102(n)→116(π^*)	5.44	0.0196
(0.59)102(n)→118(π^*)		
(0.61)103(n)→119(π^*)	5.49	0.0063
(0.27)103(n)→120(π^*)		
(0.26)97(π)→105(π^*)	5.50	0.0127
(0.23)100(π)→108(σ^*)		
(0.46)101(n)→116(π^*)		
(0.59)100(π)→108(σ^*)	5.51	0.0161
(0.30)101(n)→116(π^*)		
(0.35)97(π)→105(π^*)	5.52	0.2310
(0.25)99(π)→107(π^*)		
(0.23)100(π)→107(π^*)		
(0.23)100(π)→108(σ^*)?		
(0.28)101(n)→116(π^*)		
(0.25)103(n)→119(π^*)	5.54	0.0382
(0.57)103(n)→120(π^*)		
(0.23)101(n)→116(π^*)	5.62	0.0249
(0.56)101(n)→118(π^*)		
(0.22)102(n)→120(π^*)		





5.7.2 Experimental studies on I⁻·RF clusters

5.6.2.1 Overlaid electron detachment and photodepletion spectra of I⁻·RF clusters

Electron loss cannot be directly measured in our instrument. We calculate it by assuming that any photodepletion that is not detected as an ionic photofragment is caused by electron loss. This assumption is reasonable for the system studied, considering that both parent ions and fragment ions have close values of m/z .

N.B. Our instrument can only detect ions with $m/z > 50$.

$$\% \text{ Electron Detachment} = [(Photodepletion \text{ ion count} - \sum Photofragment \text{ ion count}) / Int_{OFF}] / (\lambda * p)$$

The electron detachment spectrum (red) at ~ 4.98 eV is in good agreement with our calculated VDE.

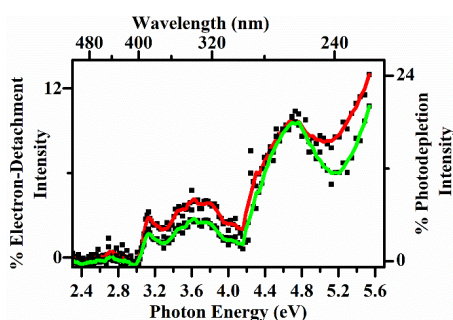


Figure 5.11 Overlaid % Electron Detachment yield (red) and % photodepletion intensity (green) of I⁻·RF clusters. The solid line is a five-point adjacent average of data points.

Chapter 6

Collision-induced dissociation and laser photodissociation spectroscopy of N-aromatic metalloporphyrin complexes

6.1 Abstract

Laser photodissociation spectroscopy is applied to iron centred metalloporphyrin complexing with N-aromatics (pyridine, quinoline, isoquinoline). The clusters ($\text{FeTPP}^+\cdot\text{py}$, $\text{FeTPP}^+\cdot\text{iQ}$ and $\text{FeTPP}^+\cdot\text{Q}$) are produced in the gas-phase using electrospray ionization mass spectrometry. Our results reveal that the photodepletion and higher-collisional dissociation (HCD) produced same fragments with m/z 668 = FeTPP^+ as the most intense fragment followed by sequential loss of the substituent groups of the FeTPP^+ moiety, respectively. Photodepletion spectra of the clusters show that the extinction coefficient of the metalloporphyrins studied does not reduce on ligation. The excited state of the clusters is suggested to decay by one and two photon absorption processes in the Soret band region and only one photon process in the Q-band region. The spectra difference between the photofragment m/z 668 and other photofragments in the Soret band region are attributed to contributions from the ultrafast decay of S_1 state through internal conversion followed by ergodic dissociation of the ground state cluster in the production of all the photofragments while intersystem crossing to a lower lying triplet state which is longer lived, decay results only in the production of m/z 668. Computational results have been used to assign the bands to our experimental results. The experimental results are hence discussed with regard to the contributions of ligation and the intrinsic properties of the N-aromatics to the binding preferences, binding energies and photochemistry of the clusters compared to the uncomplexed FeTPP^+ . These are the first experiments to characterise all the photofragments produced from the photodepletion of the clusters therefore giving a full picture of the effect of ligation on the photochemistry of iron centred metalloporphyrins.

6.2 Introduction

Porphyrins are heterocyclic macrocyclic tetra pyrrole organic compounds that are common in nature. They make up the red colour in blood (heme), the green colour in leaves (chlorophyll)³⁵⁰ and are found in a variety of enzymes, especially those involved in biological oxidation and reduction.³⁵⁰⁻³⁵⁶ Porphyrins play important roles in processes involving light absorption, charge transfer and emission. They also have complexing properties because of their highly conjugated ring structure and excited state characteristics,³⁵⁷ and have recently been applied in many areas.

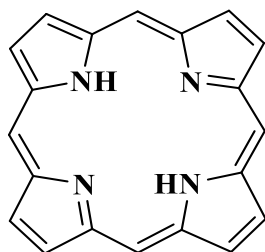


Figure 6.1 Schematic diagram of porphin which is the simplest form of porphyrin.

Metalloporphyrins (MPs) play important roles in a lot of biological and chemical processes, again because of their highly conjugated ring structure and its associated properties. MPs possess unique photochemical, photophysical, and photo-redox properties which are adjustable by structural modification.³⁵⁸ MPs have received a lot of attention in relation to understanding and characterizing their electronic structure and spectra. This is because of their multiple applications based on their novel excited state properties in many areas including photodynamic therapy, molecular electronic devices, nanoelectronics, petroleum and conversion of solar energy, biological imaging, nonlinear optics, drug design, magnetic resonance imaging, etc.³⁵⁷⁻³⁶⁵

The understanding of the binding of MPs with other directly complexed molecules has also become a current topical focus of research. Recently too, the desire for materials with low bandgaps in the field of nanoelectronics, has resulted in a lot of efforts being geared towards gaining a better understanding of the interactions between the spectroscopic and photophysical properties of MPs with other molecules. This can be explained by their robust coordination chemistry, optical oscillator strength and the polarisability of their complexes.^{366,367} Another area of

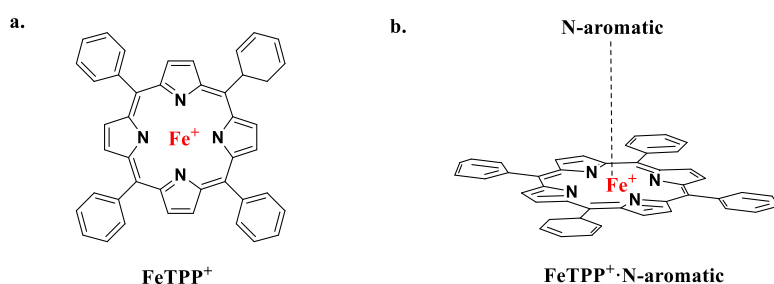
interest is the detection of MPs via UV-VIS spectroscopy in crude oil. This process is by no means an easy one because the MPs do not display their usual strong extinction coefficients in the crude oil, a phenomenon that has been attributed to complexation of the MPs with various composite molecules of the crude oil.³⁶⁵ With respect to antimalaria drug design, understanding the ligation of malaria chemotherapeutics with iron centre MPs has also gained significant attention.^{368,369}

To obtain a better understanding of the spectroscopy of porphyrins, a small number of experiments have been conducted on MPs and their complexes in the gas phase previously. Even and Jornter performed the first of such experiments by conducting laser-induced fluorescence spectroscopy on complexes in a supersonic jet expansion. Complexes of Zinc octaethylporphyrin with selected solvent molecules (water, methanol, acetonitrile, benzene, and pyridine) were studied to get information on spectral shifts.³⁷⁰ Performing these experiments was difficult because the porphyrin was first heated to vaporise it, an approach that generally will lead to the thermal decomposition of the porphyrin ring. More recently however, Nielsen and co-workers have performed spectroscopic experiments on porphyrins in which they have transferred them into the gas-phase by using electrospray ionization. This allowed the experimental characterisation of the excited-state behaviour of the porphyrins using an electrostatic ion storage ring to measure lifetimes of different excited states (10 -100 μ s) of isolated porphyrin ions in vacuo.³⁵⁶ They found that the initial singlet excited state decayed to the ground state more rapidly than the triplet state. They have also studied weakly bound complexes of Fe III heme cations with the NO ligand to ascertain the effect of ligation on the absorption spectrum using photo dissociation yield to measure absorption. In the experiment, they observed surprisingly a blue shift (to 357 nm) upon complexation of heme⁺ to NO for the Soret band, when compared to isolated heme⁺ with a band maximum at 380 nm.³⁷¹ The finding is surprising because a red shift is expected rather than a blue shift on NO ligation within a protein.³⁷¹ This observation contrasted to previous work done by van Eldik and co-workers in which they concluded that a red shift occurred on going from metamyoglobin to metamyoglobin ligated with NO in the Soret band and as large as 30nm in the Q band.³⁷² The Q band result for heme⁺-NO complex is in good agreement with that of metamyoglobin ligated with NO.³⁷³ Another work done by them on the isolated molecules of heme⁺ ligated to histidine showed that the Soret

band broadened to the blue and the Q band remained unchanged when compared with the Soret and Q bands of the heme⁺ cation.^{374, 375}

Theoretical approaches have also been employed in understanding the effect of complexation and dimerization on the optical and electrochemical properties of MPs.^{366, 376-378} Hobza and co-workers has recently reported a work on investigating the complexation of iron (II) phthalocyanine (FePc) and Fe (II)-porphyrazine (FePz) with carbenes [ImNH₂, ImN(CH₃)₂, ImN(CF₃)₂, and ImN(CCl₃)₂] using quantum chemical calculations to explore the possibility of stabilising both singlet and triplet spin states of the FePc/FePz-carbene complexes from an isolated quintet spin state of FePc/FePz, depending on the carbene selected.³⁶⁶ Previous work on iron (II) phthalocyanine (FePc) adsorbed on graphene and nitrogen-doped graphene has revealed that noncovalent interactions can be used to modify the spin state of the MP.³⁷⁸ They have also reported an expanded study on fused MP moieties by investigating their electronic behaviour using density functional theory (DFT). This work was based on previous reports of extensive modulation in the electronic properties of such complexes depending on the type of link between the MPs unit.³⁶⁶ They observed that an increase in electronic interaction between the MP's unit resulted in the lowering of the HOMO-LUMO gap which is a very important phenomena in obtaining higher electric conductivity.³⁷⁶

In this work, we report the formation of complexes of iron (III) metalloporphyrin with N-aromatic molecules (FeTPP⁺-N-aromatics, (N-aromatics = pyridine, quinoline and isoquinoline) in Figure 6.2b) in the gas-phase, exploring the effect of complexation on the photochemistry of these complexes compared with the uncomplexed free MP (FeTPP⁺, Figure 6.2a) using laser photodissociation spectroscopy.



Field Code Changed

Figure 6.2 Schematic diagram of a.) tetraphenyl porphyrin iron III cation ($FeTPP^+$) and b.) $FeTPP^+$ -*N*-aromatic complex where *N*-aromatics = pyridine, quinoline and isoquinoline).

A series of nitrogen-based aromatics were chosen to complex with the MPs, namely (pyridine(py), quinoline(Q) and isoquinoline (iQ), since these aromatics are ubiquitous in nature and have been postulated to be present in crude oil. They have been suggested as complexes which could mask the extinction coefficients of the MPs.³⁶⁵

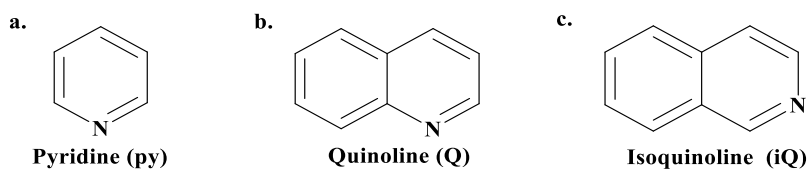


Figure 6.3 Schematic diagram of pyridine, quinoline and isoquinoline.

6.3 Experimental and Computational Methods

6.3.1 Experimental methods

All experiments were conducted in a modified Bruker AmaZon quadrupole ion trap and Orbitrap Fusion Tribrid mass spectrometers as described in chapter 2.

The CID graphs were typically recorded over 10-15 minutes with each voltage step given one minute and each individual data point being a 3 run average of its intensity. Initial samples of $FeTPP^+$ were prepared in 80% MeOH and 20% DCM which gave good solubility for the dye, but it was very difficult for clusters to be formed in this solvent system. This may be the result of the MeOH competing with the complexation molecule (i.e. the molecules we are trying to complex to the porphyrin) and forming $MP \cdot MeOH$ clusters instead. Enke and Mudring and co-workers have both discussed the differences for electrospraying MPs in methanol and acetonitrile.^{379,380} The use of acetonitrile as a solvent in studies where the aim is to form complexes via electrospray has also been recommended by McIndoe and co-workers.³⁸¹

Therefore, FeTTP⁺-N-aromatics clusters were prepared by electrospraying solutions of FeTTPCl at 1x10⁻⁶ M concentration and 20 μL of the N-aromatics at 1x10⁻³ M concentration in 100% acetonitrile (MeCN) with choice of MeCN based on the experiences of the supportive environment given to formation of clusters in our instrument. All the chemicals used were purchased from Sigma Aldrich and were used without further purification.

HCD experiments were performed using the operating software's automatic tuning capabilities at a flow rate of 5 μL min⁻¹ in the positive ion mode; spray voltage, 3500V; sweep gas flow rate, 1 arb; sheath gas flow rate, 10 arb; aux gas flow rate, 5 arb; ion transfer tube temperature, 250°C; vaporizer temperature, 300 °C.

Solution-phase UV absorption spectrum of FeTPP⁺ (1 x 10⁻⁶ mol dm⁻³) 100% acetonitrile (MeCN) was obtained using a UV-1800 UV-Visible spectrophotometer (Shimadzu, Kyoto, Japan) with a 1cm cuvette.

The UV photodissociation experiment was conducted as described in Chapter 2 using a 0.6 neutral density filter (NDF) fixed to the optics to reduce the intensity of light entering the mass spectrometer trap with fractional transmittance of 25%. This was important because of the high absorbance of our sample thus resulting in rapid photodepletion of the parent ion. The data was acquired at a laser power range of 0.03 -1mJ across different wavelengths. This was important because of the high absorbance of our sample thus resulting in rapid photodepletion of the parent ion.

6.3.2 Computational methods

Guassian 09 software was employed for all the DFT, BSSE and TDDFT calculations using the B3LYP functional with the 6-31G and 6-31G* polarised basis sets to support the experimental work. Harmonic frequencies were calculated to confirm global minima structures.¹⁸⁷ BSSE (basis set superposition error) corrected binding energies calculations were done to support the experimental binding energies ($E_{1/2}$) of the complexes and TDDFT to predict the electronic spectra.¹⁹⁴⁻¹⁹⁶ The relatively low level of theory was chosen for this study due to the size of the complexes.

6.4 Results and Discussion

6.4.1 Low energy collisional induced dissociation of $\text{FeTPP}^+ \cdot X$ clusters

Figure 6.4 displays the % CID fragmentation decay curves for $\text{FeTPP}^+ \cdot \text{py}$, $\text{FeTPP}^+ \cdot \text{iQ}$ and $\text{FeTPP}^+ \cdot \text{Q}$ clusters, with plots of onsets of the fragment obtained upon low-energy CID. The full ion mass spectra showed that the clusters were produced with strong ion signals, along with the uncomplexed FeTPP^+ monomer. (Section 3.6.1.3)



The low-energy CID conducted on these clusters showed similar fragmentation pathways as the clusters fragmented by simple fission of the cluster (Equations 6.1, 6.2 and 6.3). This reveals that the initial clusters were made up of intact molecular components of FeTPP^+ and the respective N-aromatics monomer units.

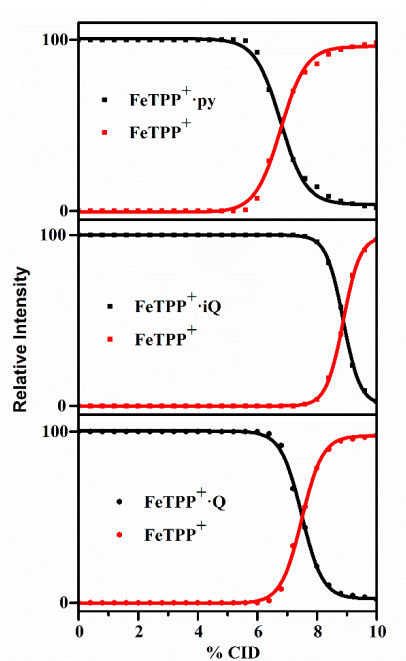


Figure 6.4 Parent ion dissociation curves for FeTTP⁺·iQ, FeTTP⁺·Q and FeTTP⁺·py alongside fragment production curves upon low-energy CID between 0 and 10% energy. Standard experimental errors obtained from repeat runs were ± 3%.

It is evident that no fragmentation pathways related to reactions between the FeTTP⁺ and the N-aromatics were observed for these clusters.

The % CID fragmentation curves for the three clusters displayed were obtained within the 0 -10 % CID range. It is worthy to note that the precursor cluster ions formed were stable molecular complexes and did not undergo metastable decay before the application of resonance excitation.^{173,174} The fragmentation curves show that the three clusters had high fragmentation onsets but at different % CID energies. This behaviour can be attributed to the different individual intrinsic properties of the N-aromatic binding strength to the MP. The results of the fragmentation experiments are summarised in the Table 6.1.

Table 6.1 E_{1/2} fragmentation energies, fragment ions and neutral fragments for FeTTP⁺·N (N = pyridine(py), quinoline(Q) and isoquinoline (iQ)) complexes

Complexes	E _{1/2}	Fragment ions	Neutral loss
FeTTP ⁺ ·iQ	8.95	FeTTP ⁺	iQ
FeTTP ⁺ ·Q	7.52	FeTTP ⁺	Q
FeTTP ⁺ ·py	6.91	FeTTP ⁺	py

^aE_{1/2} values are for 50% depletion of the precursor cluster.

In conclusion, measurements of low-energy CID of FeTTP⁺·N clusters give further evidence that the clusters studied are composed of intact moieties of FeTTP⁺ and N-aromatics. The binding energies of the clusters are different as seen by the E_{1/2} values, and thermal dissociation of ground-state potential energy complex, which gave the same cationic fragment (FeTTP⁺) for each of the clusters.

6.4.2 Comparison of the fragmentation energies of the complexes

The overlaid fragmentation curves for the FeTTP⁺·X clusters are shown in Figure 6.5 illustrating that the clusters decay at different fragmentation energies with E_{1/2} values of 6.91⁰, 7.52⁰ and 8.95 for FeTTP⁺·py, FeTTP⁺·Q and FeTTP⁺·iQ respectively. This indicates that FeTTP⁺·py has the lowest fragmentation barrier

height while $\text{FeTTP}^+\cdot\text{iQ}$ has the highest of the three complexes. The results shown in Figure 6.5 are in good agreement with the order $\text{iQ} > \text{Q} > \text{py}$ predicted by Kovalenko and co-workers from calculations which used an approximate global softness method to predict binding energies.³⁸²

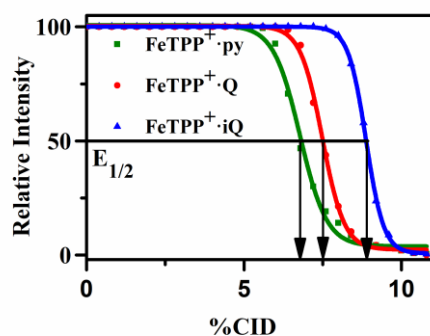


Figure 6.5 Parent ion dissociation curves for $\text{FeTTP}^+\cdot\text{iQ}$, $\text{FeTTP}^+\cdot\text{Q}$ and $\text{FeTTP}^+\cdot\text{py}$ upon CID was between 0 and 10% energy. Standard experimental errors obtained from repeat runs were $\pm 3\%$.

In the interpretation of fragmentation energy patterns, it is important to understand that fragmentation energies map the barrier height into the dissociation channel rather than providing the cluster binding energy (dissociation energy of the cluster).^{383,384} There is a correlation between the cluster binding energies and fragmentation energies for molecular systems dissociating by single inter or intra molecular bond breaking but not for those systems that disintegrate by multiple bond separation or rupture.^{385,386}

The BSSE-corrected binding energies at the B3LYP/6-31G* level for the $\text{FeTTP}^+\cdot\text{X}$ clusters calculated for the global minima structures in N-ligation are shown in Table 6.2, with structures shown in Figure 6.6. The results show that the calculated corrected binding energies for the $\text{FeTTP}^+\cdot\text{py}$ complex has the highest binding strength followed by $\text{FeTTP}^+\cdot\text{iQ}$ and then $\text{FeTTP}^+\cdot\text{Q}$ complexes. This did not match the experiment results, possibly due to the level of theory used in the calculation. Kovalenko and co-workers had earlier stated that the B3LYP functional did not perform well in estimating the threshold between the degrees of strength for axial

bound molecules. They also noted that steric effects were not accounted for in their calculations.³⁸² Durrant and co-workers have also reported that B3LYP functional and Lanl2DZ basis set is known to give a preliminary quantitative template for relative bond energies of some transition metal complexes. The information provided at this level of theory is sufficient in giving comparative relative bond energies for related complexes but does not predict quantitatively correct bond energies.³⁸⁷⁻³⁹⁰ There has been discussion of the ability of the B3LYP functional to predict the ground-state spin of Fe complexes especially for high-spin configurations of transition metal complexes. Hybrid exchange correction functionals eg. OPBE are known to perform better in this regard,^{391,392} however a combination of B3LYP functional with triple-zeta polarised basis set and solvent corrections have been reported by de Visser and co-workers to produce reliable bond energies for biologically important Fe complexes if the calculated data is normalised to experimental data.³⁹³

Iron III porphyrins have been identified to display different spin states, $S = 1/2$ (low spin), $S = 3/2$ (intermediate) and $S = 5/2$ (high spin), although when the energy gap between the intermediate and high spin are close to the spin coupling constant, a linear combination of the two spin state is formed.^{394,395} The presence of an axial ligand and the configuration of the porphyrin moiety, strongly contribute to determining the spin state. The spin state for a simple Fe (III) porphine is $S = 3/2$,³⁹⁶ but this can change depending on the effect of the axial coordination and the substituents group attached to the MP. A test run on different Fe (III) porphine complexes by Durrant with different functionals and basis sets revealed that the pyridine and quinoline complexes favoured a $3/2$ spin state,³⁶⁸ however complexes of two strong N ligand and electron-withdrawing substituents in the Fe (III) porphine are known to favour the low spin $S = 1/2$ state.^{394,397,398} In this our work, we have used the $S = 1/2$ spin state, based on the above knowledge however further computational work is desirable on other spin states in the future.

Although we used the double-zeta polarised basis set (6-31G(d)) in our calculation, the Fe-N bond length for N-coordination is in good agreement with that obtained by Durrant in his work on computational study of binding ligand affinities to iron III porphine (1.857-2.280Å) using B3LYP/6-311+G(d,p).³⁶⁸ Interestingly, they observed the same trend in which pyridine had a higher binding strength compared

to quinoline.³⁶⁸ This trend may be attributed to stronger steric effects in the quinoline. Durrant has also related the trend to the fact that quinoline has experimentally been noted to interact more favourably with iron (III) ferriprotoporphyrin IX (FePPIX) by π - π stacking rather than N-coordination.^{368,369} It is worthwhile noting that in the absence of a protic competing environment, most basic donor atoms form the strongest complexes with an Fe (III) center.³⁶⁹ Pyridine and isoquinoline are known to be more basic than quinoline. The proton affinities for the N-aromatics are 930 kJ/mol, 952 kJ/mol and 953 kJ/mol for pyridine, isoquinoline and quinolone respectively. This characteristic may be attributed to the fact that there is steric repulsion of the close ring that makes it difficult for the positive charge on the N atom of the quinoline moiety to solvate compared to the pyridine which has lesser steric hinderances.

399,400

399,400

Association through π -stacking are supported by increase in the number of π -electrons in the aromatic ring system, which actually indicates that the quinoline has a preference of interacting by π -stacking because it possesses higher number of π -electrons compared to pyridine (6 and 10 respectively). Therefore, the disparity in the trend for our experimental results obtained for the clusters compared to the computational results could possibly be because they are fragmenting over different barriers since different types of interaction have been noted for the three different clusters. The different types of interactions are identified to be dependent on the individual intrinsic properties of the N-aromatic compounds as mentioned above. Alternatively, the level of theory used in our calculations could also have contributed to the disparity in the results.

Table 6.2 BSSE-corrected binding energies in (kJ mol⁻¹) for the N-coordination structures of FeTTP⁺·py, FeTTP⁺·Q and FeTTP⁺·iQ clusters.

	FeTTP ⁺ ·py	FeTTP ⁺ ·Q	FeTTP ⁺ ·iQ
Binding Energy	84.68	78.79	81.76
E _{1/2}	6.91	7.52	8.95

^aResults obtained from calculations at B3LYP/6-31G* level of theory.

A repeat of the calculated BSSE binding energies for the three clusters with the interaction of the N-aromatics in the π -stacking position (Figure 6.6) showed a trend

that gave the highest dissociation energies for the FeTTP⁺·Q cluster, and FeTTP⁺·py displaying the lowest binding energy. (Table 6.3)

Table 6.3 BSSE-corrected binding energies in (kJ mol⁻¹) for (π -stacking) structures of FeTTP⁺·py, FeTTP⁺·iQ and FeTTP⁺·Q clusters.

	FeTTP ⁺ ·py	FeTTP ⁺ ·Q	FeTTP ⁺ ·iQ
Binding Energy	10.21	34.48	12.38
E _{1/2}	6.90	7.50	8.95

^aResults obtained from calculations at B3LYP/6-31G* level of theory.

Although the π -stacking structures were associated with the FeTTP⁺·Q cluster being the most strongly bonded by ligation, this result is still limited by the level of theory used. The FeTTP⁺·iQ cluster possesses a binding energy that is less than FeTTP⁺·Q but higher than that of FeTTP⁺·py might be attributed to the isoquinoline's intrinsic properties that support both N-coordination and π -stacking. Isoquinoline is more basic than quinoline and possesses a greater number of π -electron than pyridine that may have contributed to the trend in the results presented above. It is also worthy to mention that although the optimized structures displayed in Figure 6.6 all have no negative frequencies, the true structures for these complexes may be between two extremes (especially at room temperature) thus more advanced functionals that better account for dispersion interactions eg. MO6-2X are suggested for the re-optimization of the structures as future work.

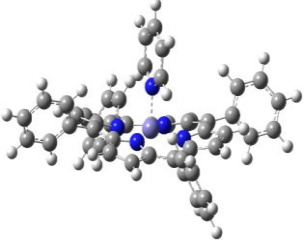
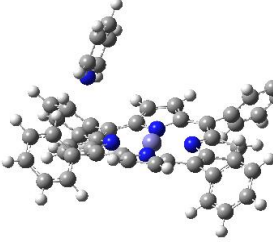
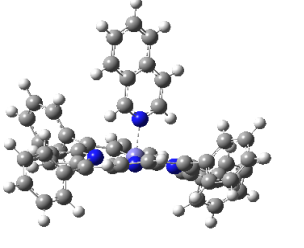
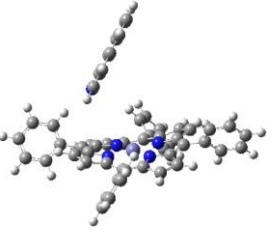
6.4.3 Geometric structures and time-dependent density functional theory calculations (TDDFT) on FeTTP⁺·N clusters

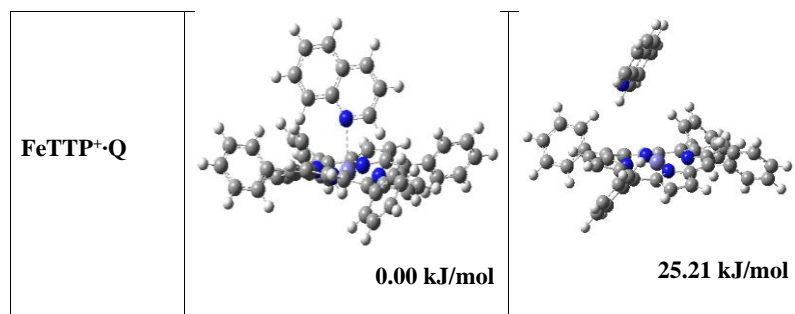
The DFT B3LYP/6-31G(d) calculated structures of the FeTTP⁺·N clusters (N = pyridine(py), quinoline(Q) and isoquinoline(iQ)) gave structures that are global minima without any negative frequencies for both N-coordination and π -stacking interactions. The different N-aromatics are in direct heteroatomic coordinated interaction with the Fe (III) centre and stable structures were obtained for these. For every one of the clusters the lowest energy geometry is presented with each of them being axially bound to the porphyrin moiety. The quinoline cluster showed the longest Fe-N bond length of (2.05 Å) while the isoquinoline and pyridine clusters had

very close bond lengths of (1.96Å and 1.97Å), respectively. The Fe-N bond lengths are within the range measured by Durrant for N donor ligands on axial coordination.³⁶⁸ The general structures correspond to the nitrogen atom of the N-aromatics interacting with the Fe-centre of the porphyrin. It is evident from other calculations conducted that those structures not axially bound to the porphyrin moiety are at higher energy.

Table 6.4 displays the lowest energy geometric structures obtained for the FeTTP⁺·py, FeTTP⁺·Q and FeTTP⁺·iQ clusters for N-coordination and π -stacking. The N-coordinate interactions with the Fe in the porphyrin centre are indicated with the dashed lines connecting to the Fe-center. In these structures, we note that opposite phenyl groups go in and out of plane on ligation at different angles with the highest distortion seen in the FeTTP⁺·Q. The cluster structures selected for the different interactions have no negative frequencies, and our calculations suggest that N-ligated structures should be present in our experiment.

Table 6.4 Lowest obtained energy geometric structures of FeTTP⁺·py, FeTTP⁺·iQ and FeTTP⁺·Q clusters for N-coordination^a and π -stacking^a obtained at (B3LYP/6-31G (d)) level of theory.

FeTTP ⁺ ·N-Aromatics	N-Coordination	π - Stacking
FeTTP ⁺ ·py	 <p>0.00 kJ/mol</p>	 <p>49.85 kJ/mol</p>
FeTTP ⁺ ·iQ	 <p>0.00 kJ/mol</p>	 <p>77.71 kJ/mol</p>



^aAtom colour: N = Blue, Fe = Purple, C = Grey and H = White

The energies are the relative zero-point corrected energies of the N-coordination structures to the π -stacking structures. The N-coordination structures have the lowest energy for the three different clusters. The bond lengths obtained for the N-coordination structure are 1.96 Å, 2.05 Å and 1.97 Å respectively as indicated by the connecting dashed line. The Fe atom lies out of the plane of the four nitrogen atoms in the porphyrin and is elevated towards the ligand at 0.78 Å, 0.48 Å and 0.42 Å respectively above the plane.

Figure. 6.6 displays a TD-DFT B3LYP/6-31G (d) calculated UV-VIS spectra of the three FeTTP⁺·N clusters and the different band maxima at the Q and Soret band regions as listed in Table 6.5. The associated assigned excitations are also listed in Table 6.6. The calculated spectra of the clusters and monomer each contain two band regions within the experimental region scanned (2.2 – 3.86 eV).

The FeTTP⁺ calculated spectrum displayed band maxima at 2.20 eV and 3.12 eV that can be assigned as the Q (labelled I) and Soret (labelled II) band regions, respectively. The calculated Q and Soret bands of the FeTTP⁺·py cluster (bands I and II) displayed maxima at 2.52 eV in band I region, two band maxima at 3.20 eV and 3.56 eV and a split at 3.40 eV in the region of band II, respectively. The Q band of the FeTTP⁺·iQ cluster has the same band maximum as the FeTTP⁺·py cluster, one band maximum at 3.20 eV and a shoulder with an onset at 3.40 eV which are the same energies as one of the peaks and the split displayed in the FeTTP⁺·py cluster spectra in the Soret band region.

Table 6.5 Band maxima at the Q and Soret band regions of the TDDFT calculated spectra for FeTTP⁺ monomer, FeTTP⁺·py, FeTTP⁺·iQ and FeTTP⁺·Q clusters and corresponding band shifts are listed.

	Q-Band Region (Maximum eV)	Band Shift	Soret-Band Region (Maximum eV)	Band Shift	Other Band Features (eV)
FeTTP⁺	2.20	—	3.12	—	—
FeTTP⁺·py	2.52	0.32 (B)	3.20 ^a 3.52 ^b	0.08(B) 0.40 (B)	3.40 (S)
FeTTP⁺·iQ	2.52	0.32 (B)	3.20	0.08 (B)	3.40 (SH)
FeTTP⁺·Q	2.20 2.74	X 0.46 (B)	3.20	0.08 (B)	3.64 (HEBM)

— = Not Applicable, X= Not seen, B = Blue Shift, S = Split, SH = Shoulder Onset, HEBM = Higher Energy Band Maximum

^aPeak before the split, ^b Peak after the split

The Q and Soret bands of the FeTTP⁺·iQ and FeTTP⁺·py are blue shifted by 0.32 eV and 0.08 eV (for the first peak in the FeTTP⁺·py cluster spectrum) respectively when compared to the FeTTP⁺ monomer. However, the first band in the Q band region of the FeTTP⁺·Q cluster is predicted not to be perturbed by the ligation with a maximum at 2.20 eV and the second blue shifted by 0.46 eV. The Soret band of the FeTTP⁺·Q cluster is also blue shifted by 0.08 eV and a low absorption band with band maximum at 3.64 eV was also observed. The splitting and the shoulder observed in the Soret bands of the FeTTP⁺·py and FeTTP⁺·iQ clusters respectively were absent in the FeTTP⁺·Q cluster spectrum. The spectra of the clusters displayed features of broadening towards the blue edge of the Soret bands while the Q bands remain unchanged in this regard. These results disagree with the predictions made by Kovalenko and co-workers on red band shifts because of axial coordination of N-aromatics to some metalloporphyrin in their Q and Soret band.³⁸²

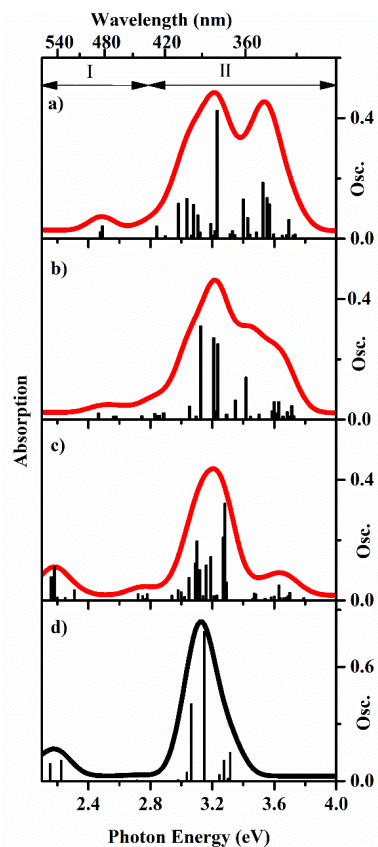


Figure 6.6 TDDFT excitation spectra for the N-coordination structures of the (a) $\text{FeTTP}^+\cdot\text{py}$, (b) $\text{FeTTP}^+\cdot\text{iQ}$, (c) $\text{FeTTP}^+\cdot\text{Q}$ clusters and (d) FeTTP^+ monomer. The vertical bars represent the individual transitions of the oscillatory strength, and the full line spectrum gives a convolution of the calculated spectrum with a Gaussian function (0.15 eV HWHM).

The splitting of the Soret band seen here for the $\text{FeTTP}^+\cdot\text{py}$ cluster has been predicted previously in the calculations of Kovalenko and co-workers,³⁸² and was also reported by Noro et al in their work on the axial coordination of pyridine to vanadium octaethyl porphyrin (VOOEP).^{398,400} Resonance Raman spectra of VOOEP in pyridine solvent displaying two $\text{V}=\text{O}$ bands in the Q-bands has also been reported.⁴⁰¹ This observation has been explained by El-Bayoumi and co-workers to be evidence of sufficiently strong transitions existing in the molecular aggregates' component molecules.⁴⁰²

Table 6.6 TDDFT calculated transition energies (3.56-2.48 eV) and oscillator strengths of the FeTTP⁺-py cluster, calculated at the B3LYP/6-31G (d) level.

Transition energies (eV)	Transitions	Oscillator strength
3.56	π - π^*	0.1145
3.55	π - π^*	0.1350
3.45	π - π^*	0.0690
3.33	π - π^*	0.0261
3.24	π - π^* , CT	0.4241
3.13	π - π^*	0.0207
3.11	π - π^*	0.0779
3.09	π - π^*	0.1123
3.06	π - π^*	0.0111
2.85	π - π^*	0.0414
2.50	π - π^*	0.4160
2.48	π - π^*	0.0218

CT= Charge Transfer

Investigation of the molecular orbitals of the FeTTP⁺-py clusters involved in the excitations with oscillator strength ≥ 0.005 within the experimental range show transitions from the ground state cluster where the orbitals are centred on the FeTTP⁺ moiety, or orbitals with their electron density on the porphyrin ring substituents, with minor delocalization of the FeTTP⁺ moiety. The excited states are localised either within the FeTTP⁺ unit or a pyridine π^* orbital. The most intense transition at 3.24 eV has been assigned to have a mixed character of π - π^* and charge transfer and has been noted by Lehnert and co-workers in their work on detailed assignment of transitions in UV-VIS spectra of high-spin FeTPPCl axially coordinated (with respect to the Cl) around this photon energy.⁴⁰³⁴ This assignment is in good agreement with the contour model of our molecular orbital and assignment of transitions as shown in Section 6.6.2.2.

To investigate the gas phase UV-VIS photophysics and photochemistry of the FeTTP⁺-N-aromatics clusters and the FeTTP⁺ monomer, their ions were photoexcited from 2.2 - 3.86 eV (564 -322 nm). The solution phase UV-VIS spectrum of FeTPPCl is included in Section 6.6.1.2 and TDDFT calculated spectra for the different systems studied experimentally are used as guides to assign the gas-phase absorption spectra.^{173,303} The photodepletion spectra of the FeTTP⁺-N-aromatics and FeTTP⁺

monomer are presented together to aid in comparing the band shifts, broadening of the Soret band and to assess any reduction in the absorption intensities of metalloporphyrin's because of complexation, as predicted by Kovalenko and co-workers.³⁸²

6.4.4 Photodepletion spectrum of FeTTP⁺·py cluster

The photodepletion spectra of FeTTP⁺·py and the FeTTP⁺ monomer, displayed in Figure 6.7, have absorption features over the range of 2.2 – 3.86 eV peaking at locations labelled I (Q band region) and II (Soret band region).

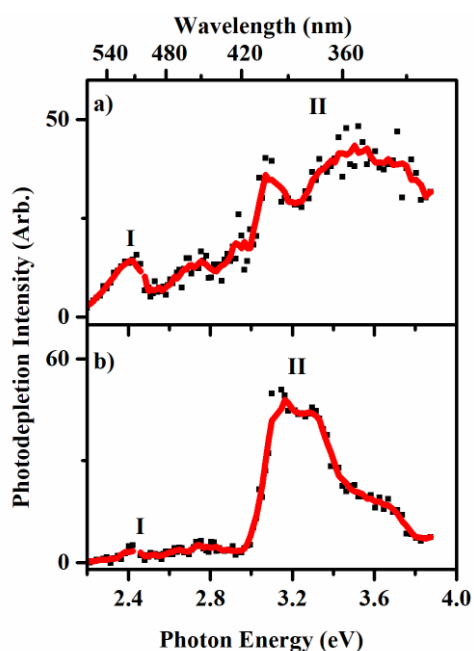


Figure 6.7 Photodepletion (absorption) spectra of (a) FeTTP⁺·py and (b) FeTTP⁺ monomer across the range of 3.86 - 2.2 eV (322-564 nm). The solid lines are five-point adjacent averages of the data points.

The FeTTP⁺·py photodepletion spectrum displays a peak maximum at 2.40 ± 0.01 eV, a second broad band centred at 2.70 ± 0.01 eV at in the band I region and a broad band II region from 3.0 - 3.86 eV. Band II show one local peak at 3.08 ± 0.02 eV, a drop at 3.22 ± 0.01 eV and a wide peak from 3.22 – 3.80 eV, centred at 3.54 ± 0.05 eV. The spectral absorption intensity increases gradually with increasing photon

energy. The FeTTP^+ monomer photodepletion spectrum (b) show a peak in band I region at 2.38 ± 0.01 eV and a wide peak that is centred at 3.18 ± 0.03 eV in band II region. It also displays a shoulder to higher energy with an onset at 3.41 ± 0.02 eV and centred at 3.6 ± 0.02 eV in the band II region.

6.4.5 Photodepletion spectrum of $\text{FeTTP}^+\text{-iQ}$ cluster

Figure. 6.8 displays the photodepletion spectra of the $\text{FeTTP}^+\text{-iQ}$ cluster and the FeTTP^+ monomer. The $\text{FeTTP}^+\text{-iQ}$ photodepletion spectrum also displayed absorption features from 2.2-3.86 eV peaking at features labelled I (Q band region) and II (Soret band region).

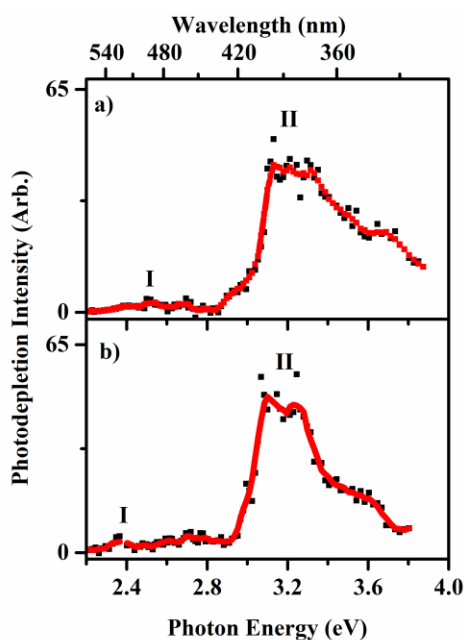


Figure. 6.8 Photodepletion (absorption) spectra of (a) $\text{FeTTP}^+\text{-iQ}$ and (b) FeTTP^+ across the range of 3.86 – 2.2 eV (322-564 nm). The solid lines are five-point adjacent averages of the data points.

Band I is only weakly visible, peak centred at 2.58 ± 0.03 eV and the band II displays a wide peak with band maximum intensity from 3.14 eV to 3.34 eV centred at 3.24 ± 0.03 eV. Band II again displays a shoulder to higher energy centred at 3.72 ± 0.02 eV.

6.4.6 Photodepletion spectrum of FeTTP⁺·Q cluster

The photodepletion spectra of FeTTP⁺·Q cluster and the FeTTP⁺ monomer is displayed in Figure 6.9. The spectra features are labelled I (Q band region) and II (Soret band region).

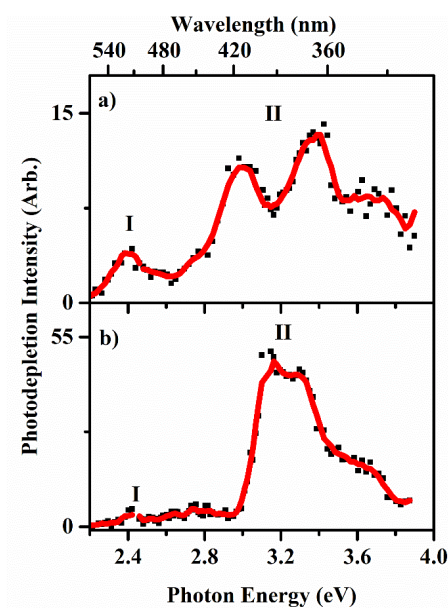


Figure 6.9 Photodepletion (absorption) spectra of (a) FeTTP⁺·Q and (b) FeTTP⁺ across the range of 3.86 – 2.2 eV (322-564 nm). The solid lines are five-point adjacent averages of the data points.

The FeTTP⁺·Q cluster photodepletion spectrum displays absorption all through the scanned region with a peak at 2.41 ± 0.01 eV labelled as band I in the region of the Q band. Band II consists of peaks at 3.01 ± 0.01 eV and 3.4 ± 0.01 eV, a drop in absorption at 3.18 ± 0.01 eV, and a higher-energy absorption feature centred at 3.72 ± 0.03 eV.

Summary of the Soret and Q bands features of FeTTP⁺·N aromatics cluster photodepletion spectra with corresponding band shifts when compared to FeTTP⁺ photodepletion spectrum are listed in Table 6.7.

Table 6.7 Band maxima at the Q and Soret band regions of the experimentally acquired spectra of FeTTP⁺ monomer, FeTTP⁺·py, FeTTP⁺·iQ and FeTTP⁺·Q clusters and corresponding band shifts are listed.

	Q-Band Region (Maximum eV)	Band Shift	Soret-Band Region (Maximum eV)	Band Shift	Other Band Features (eV)
FeTTP⁺	2.38 ± 0.01	—	3.18 ± 0.03	—	3.41(SH) ± 0.02
FeTTP⁺·py	2.41 ± 0.01 2.70 ± 0.01	0.03(B) 0.32(B)	3.08 ^a ± 0.02 3.54 ^b ± 0.05	0.10 (R), 0.36 (B)	3.20(S) ± 0.01
FeTTP⁺·iQ	2.58 ± 0.03	0.20(B)	3.24 ± 0.03	0.06 (B)	3.62(SH) ± 0.02
FeTTP⁺·Q	2.41 ± 0.01	0.03(B)	3.01 ^a ± 0.01 3.40 ^b ± 0.01	0.17(R) 0.22(B)	3.18(S) ± 0.01 3.72(HEBM) ± 0.03

— = Not Applicable, B = Blue Shift, R= Red Shift, S = Split, SH = Shoulder Onset, HEBM = Higher Energy Band Maximum

^aPeak before the split, ^bPeak after the split

The absorption profile of the experimental photodepletion spectra of the FeTTP⁺·py (Figure. 6.7 a) and FeTTP⁺·iQ (Figure. 6.8 a) clusters, mirror that of their respective TDDFT calculated spectra (see Figure 6.21 and Figure 6.22 for overlaid spectra). The TDDFT calculated spectrum of the FeTTP⁺·py cluster showed some weak transitions that matched with the position of the second partially resolved band seen around the assigned Q band region of the FeTTP⁺·py spectrum when shifted by –0.1 eV towards lower energy (see Figure 6.21). The features of the TDDFT spectrum for the FeTTP⁺·iQ cluster matched the photodepletion spectrum without any form of band shift. The agreement between the TDDFT and photodepletion spectra for the FeTTP⁺·py and FeTTP⁺·iQ cluster might indicate that the N-coordinated optimized structures are their real global minimum structures and thus the same structures of the molecular ions populate our experiments. The spectral features of the photodepletion spectrum of the FeTTP⁺·Q cluster (Figure 6.9 a) is different in the Soret band region except for the higher energy absorption feature that was also displayed in the TDDFT spectrum (see Figure 6.23). This disparity may be an indication that the N-coordinated optimised structure used in the TDDFT calculation is different from the structure present in our experiment. It has been mentioned

earlier that quinoline prefers to complex through π - π stacking.^{370,371} An extensive theoretical study on the π - π stacking interaction of the FeTTP⁺·Q cluster will be important in the future to unravel this disparity.

The FeTTP⁺·Q cluster photodepletion spectra surprisingly mirrors the photodepletion spectra of FeTTP⁺·py cluster except for minimal band shifts around band II and absorption feature on the higher energy side of the band. FeTTP⁺·py and FeTTP⁺·Q spectra both displayed minimal blue shift of ~ 0.03 eV in their Q bands region although the FeTTP⁺·py spectrum showed a second band that is blue shifted by ~ 0.32 eV in this region too. The FeTTP⁺·py and FeTTP⁺·Q spectra showed red shifts by ~ 0.1 eV and ~ 0.17 eV respectively in their Soret bands region when comparing their band before the split and the band of the Soret band of the FeTTP⁺ monomer, respectively. Blue shifts of ~ 0.36 eV and ~ 0.22 eV are also observed when the band after the split in the Soret band region spectra of the FeTTP⁺·py and FeTTP⁺·Q clusters are compared with the peak of the Soret band of the FeTTP⁺ monomer, respectively. Latos-grazynski and co-workers stated that the presence of covalent linker improves the fusion of coplanar chromophores which results in the split of the Soret and red-shifted Q-bands.⁴⁰⁴ There is no covalent linker in our clusters studied, however we observed a split of the Soret band but no red shift in our Q-band. The red-shift of the first peak in the Soret band region of both clusters within ± 0.01 eV error in our band maxima agrees with the red-shift observed by van Eldik and co-workers in their studies of metamyoglobin and metamyoglobin ligated to NO but not in the Q-band because they observed a red shift.³⁷² Again, the result agrees with the predictions made by Kovalenko and co-workers on red band shifts because of axial coordination of N-aromatics to some MPs in their Soret and Q band.³⁸² This result does not agree with our result for the Q-band as we observed a minimal blue shift (0.03 eV ± 0.01 eV error).

A contrasting result is seen with the FeTTP⁺·iQ cluster when compared with the FeTTP⁺ monomer as it is blue shifted by 0.2 eV and 0.07 eV in the Q band and Soret band, respectively. The blue shift in the Soret agrees with the result reported on comparing the Soret band of heme⁺ and ligation of heme⁺ to NO by Brondsted Nielsens and co-workers. However, the shift on the Q-band of the FeTTP⁺·iQ cluster is in contrast as their result reported that the Q-band was red shifted.³⁷¹ Blue shifts are also observed for the second peaks after the split in our FeTTP⁺·py and FeTTP⁺·Q spectra.

The broad absorption Soret bands displayed by the three clusters are in good agreement with the prediction of Kovalenko and co-workers,³⁸² and in line with the spectra of the MP complexes recorded by Brondsted Nielsens and co-workers.³⁷⁵ The shoulder seen on the higher energy side of the Soret band of the FeTTP⁺ monomer, FeTTP⁺·iQ and FeTTP⁺·Q clusters has been identified to be likely due to ligand-metal charge transfer.³⁷⁵

A comparison of the photodepletion intensities of the clusters and the FeTTP⁺ monomer reveal that the intensity of the Soret band does not decrease upon ligation. This result firmly contradicts the suggestion by Kovalenko and co-workers that complexation reduces the intensity of the Soret band of MPs, which was put forward to explain the fact that MPs cannot be observed by UV-VIS in samples of crude oils.³⁸²

6.4.7 Photofragmentation spectra of the FeTTP⁺·N-aromatics clusters

6.4.7.1 Photofragmentation spectra of the FeTTP⁺·py cluster

Figure 6.10 displays the photofragmentation production spectra pattern associated with the FeTTP⁺·py cluster. The photofragment spectrum for the FeTTP⁺·py cluster shows m/z 668 as the most intense photofragment. The m/z 668 photofragment spectrum displayed similar features in the Q and the Soret band as the photodepletion spectrum. It also clearly reveals some features that were only partially visible in the photodepletion spectrum. This is not surprising because the photodepletion spectrum has been noted in some of the systems we have studied previously not to clearly capture all the excited state features of the studied molecule.^{31,261} The m/z 668 photofragment spectrum showed visible bands that peak at 2.41 ± 0.01 eV and 2.70 ± 0.01 eV in the Q band and a split at 3.20 ± 0.01 eV, a resolved peak at 3.08 ± 0.02 eV and a second broad band in the Soret band region that increases in intensity as photon energy increases. This infers that it is produced throughout the entire region for the photodepletion of the cluster. The other photofragments (m/z 590, m/z 514 and m/z 512) display two visible low intensity peaks in Q band region and different features as the m/z 668 in the Soret band region.

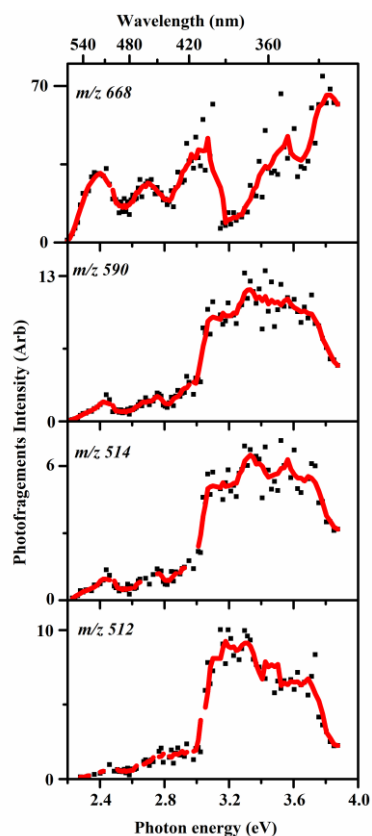


Figure 6.10 (a) m/z 668 (b) m/z 590 (c) m/z 514 and (d) m/z 512 photofragment production spectra for $\text{FeTTP}^+\cdot\text{py}$ cluster across the range of 3.86 – 2.2 eV (322–564 nm). The solid lines are five-point adjacent averages of the data points. *Note: m/z 591 is also present with very low intensity (see Section 6.6.1.4, Figure 6.18).*

They show a single broad band with an onset at ~ 3.0 eV to 3.86 eV centred at 3.41 ± 0.03 eV with no features of the first peak and split present in the Soret band region as was observed in the photofragment m/z 668 and photodepletion spectrum. The intensity of this broad band drops at higher photon energies. The change in the Soret band spectral features of the photofragments (m/z 590, m/z 514 and m/z 512) may be because they are photoproducted by the decay of a different excited state.

6.4.7.2 Photofragmentation spectra of the $\text{FeTTP}^+\text{-iQ}$ cluster

Figure 6.11 displays the photofragmentation production spectra for the $\text{FeTTP}^+\text{-iQ}$ clusters. The photofragment production spectrum of m/z 668 has similar spectral features as the photodepletion although it is produced in the Soret band with higher intensity as photon energy increases. The other photofragments (m/z 590, m/z 514 and m/z 512) are produced with low intensity and their spectral features display similar features as the m/z 668 in the Q band region. The spectra show broad low intensity absorption features with two partially resolved bands. Again, they show different spectral features to the spectrum of the m/z 668 and the photodepletion spectrum in the Soret band.

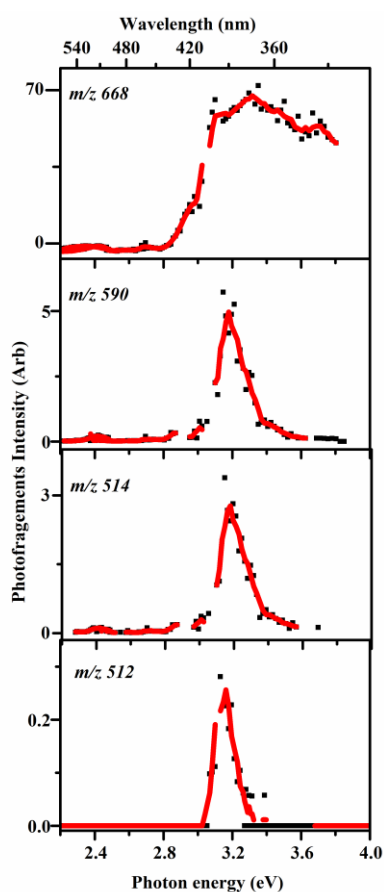


Figure 6.11 (a) m/z 668 (b) m/z 590 (c) m/z 514 and (d) m/z 512 photofragment production spectra for $\text{FeTTP}^+\text{-py}$ cluster across the range of 3.86 – 2.2 eV (322–564

nm). The solid lines are five-point adjacent averages of the data points. *Note: m/z 591 is also present with very low intensity (see Section 6.6.1.4, Figure 6.18).*

The Soret band displays a well resolved narrow band with a band width of 0.34 ± 0.03 eV that peaks at $3.2 \text{ eV} \pm 0.01 \text{ eV}$. The band sharply drops down at higher energy edge.

6.4.7.3 Photofragmentation spectra of the $\text{FeTTP}^+\text{-Q}$ cluster

The photofragment production spectra of the photofragments m/z 668, m/z 590, m/z 514 and m/z 512 of $\text{FeTTP}^+\text{-Q}$ clusters are displayed in Figure. 6.12. The photofragment m/z 668 spectrum shows strong resemblance to the photodepletion spectral profile except for the second broad absorption band observed in the Q band region. The band has an onset at 2.61 ± 0.02 eV to 3.0 ± 0.01 eV.

The photofragments, m/z 591, m/z 590, m/z 514 and m/z 512 display spectral profile that are different from that of m/z 668 and the photodepletion spectrum in the Soret band region. Although there is the presence of a very low intensity second absorption feature in their Q band region, it is shifted to lower energy compared to the onset of the second band in the Q band region of the m/z 668 spectrum. Their spectra show a low intensity band that peaks at 2.39 ± 0.02 eV, an unresolved low intensity absorption feature with onset at 2.48 ± 0.01 eV to 2.63 ± 0.02 eV, a well resolved high intensity band with band width of 0.58 ± 0.02 eV which peaks at 3.1 ± 0.01 eV and a low intensity band with onset at 3.21 ± 0.01 eV to 3.6 ± 0.01 eV.

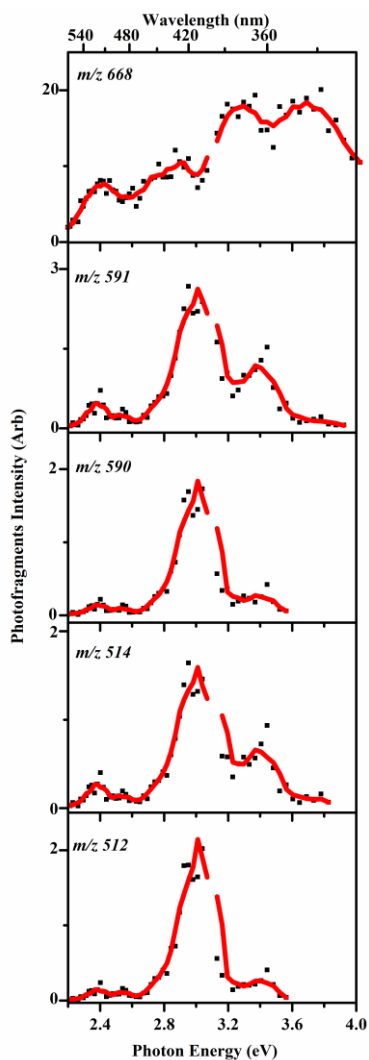


Figure 6.12 (a) m/z 668 (b) m/z 590 (c) m/z 514 and (d) m/z 512 photofragment production spectra for FeTTP⁺·Q cluster across the range of 3.86 – 2.2 eV (322-564 nm). The solid lines are five-point adjacent averages of the data points.

The spectral features for these photofragments match those observed in the TDDFT calculated spectrum for N-ligated optimised structure of FeTTP⁺·Q cluster (see Figure 6.24).

The m/z 668 = FeTTP⁺ is the most intense photofragment and no protonated form of the N-aromatics was seen as a photofragment for all the three clusters studied. Higher-energy collisional dissociation (HCD) experiment was conducted on the clusters and the % HCD spectra acquired to gain information on the ground state thermal fragments. (see % HCD spectra in Section 6.6.1.1). The HCD experiment was performed as described in Chapter 2. Table 6.6 lists the photofragments and HCD fragments observed and their assignments. The photofragments (m/z 591, m/z 590, m/z 514 and m/z 512) are the same fragments produced from the CID fragmentation of FeTTP⁺ (Figure 6.15).

Table 6.8 Photofragments and HCD fragments observed for the FeTTP⁺:iQ cluster, with assignments.

<i>m/z</i>	<i>Assigned Fragment</i>	<i>Photofragment</i>	<i>HCD</i>
668	FeTTP ⁺	✓	✓
591	FeTTP ⁺ - C ₆ H ₅ [•]	✓	✓
590	FeTTP ⁺ - C ₆ H ₆	✓	✓
514	FeTTP ⁺ - 2C ₆ H ₅ [•]	✓	✓
512	FeTTP ⁺ - 2C ₆ H ₆	✓	✓

The HCD fragmentation pathway with the production of the monomer and sequential loss of the porphyrin substituent groups has earlier been observed by Nielsen and co-worker.³⁷¹ The photofragments m/z 590, m/z 514 and m/z 512 were reported by Bohme and co-workers on the collision induced dissociation of FeTTPCL.⁴⁰⁵ The absence of m/z 591 as one of the reported fragments may be attributed to the limitations of their instrument resolution, although a closer look at their reported fragmentation mass spectrum showed a very low intensity peak at the position of m/z 591. The loss of the substituent groups from the FeTTP⁺ moiety during collisional excitation experiments has been attributed to a known reaction which involves the peripheral substituent groups of the porphyrin undergoing β -cleavage reaction.⁴⁰⁶⁻⁴¹⁰

The nature of the photofragmentation spectra of the clusters illustrates the complexity of the system and may be attributed to complicated excited state behaviour of the clusters. The broad absorption bands observed in the photodepletion

spectra of these clusters support ultrafast decay to the electronic ground state as has been identified by von Helden and co-workers.⁴¹¹

6.4.8 Laser power dependence of photofragments production of the $FeTTP^+ \cdot N$ -aromatics clusters

6.4.8.1 Laser power dependence of photofragments production of the $FeTTP^+ \cdot py$ cluster

Power studies was conducted on the $FeTTP^+ \cdot py$ cluster at 360 nm (3.44 eV) and 402 nm (~ 3.08 eV) which is around the maximum for the two bands in its Soret band region to probe the laser power dependence of the production of m/z 668 = $FeTPP^+$ and m/z 590 from the photodepletion of $FeTTP^+ \cdot py$ cluster (Figure 6.13 and Figure 6.14).

Figure 6.13a shows that the production of the m/z 668 = $FeTPP^+$ increases linearly with the pulse energy of the laser in the Soret band region with band maximum around 360 nm (~ 3.44 eV) which indicates that only one-photon processes occurred in this region during our experiment. Surprisingly, the production of the m/z 668 = $FeTPP^+$ displays an exponential increase with the pulse energy of the laser in the Soret band region with band maximum around 402 nm (~ 3.08 eV) (Figure 6.13b) which suggests that one and two photon processes are involved in this region. This non-linearity in the Soret band region has earlier been reported by Nielsen and co-workers in their spectroscopic study of heme⁺·NO complexes. They suggested two pathways that resulted in the one and two photon absorption processes observed. When ions are electronically excited to S_2 excited state, they quickly go through internal conversion (IC) to the S_1 excited state. In the S_1 excited state, some of the ions undergo internal conversion and ultrafast decay to the electronic ground state followed by rapid thermal dissociation of the ground state cluster. They associated this with a one-photon contribution while the remaining ions go from the S_1 excited state through intersystem crossing (ISC) to a lower-lying triplet state that is longer lived. They made this suggestion since ions in the S_1 excited state possesses enough internal energy to conquer any barrier from S_1 to T_1 potential energy surface. The ions in the T_1 excited state do not possess enough energy to dissociate thus there is a need for a second photon to be able to obtain a considerable degree of dissociation of the ions therefore accounting for the two-photon contribution to their fragment.

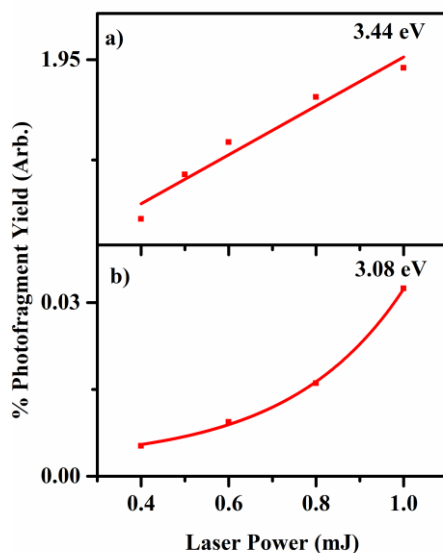


Figure 6.13 Power studies comparing the production of the most intense photofragment m/z 668 = FeTTP⁺ with the laser pulse energy at 360 nm (3.44 eV) and 402nm (3.08 eV) (around the location of the maximum of the two bands in the Soret band region of the FeTTP⁺·py), respectively.

Our experimental power studies for the photofragmentation production of m/z 668 show that there are two electronic excited states decay that led to its production in the Soret band region. We can therefore explain that the linear relationship displayed in Figure 6.13a for the photofragment production yield of m/z 668 shows that one photon absorption process is involved in its production within the second broad band in the Soret band region that increases in intensity as photon energy increases. This means that it is produced from the ultrafast decay of the S1 electronic excited state to the electronic ground state followed by thermal dissociation. Figure 6.13b shows that the production of the m/z 668 at the first band in the Soret band region that peaks at 3.08 ± 0.02 eV is from the contributions of one and two photon absorption processes thus it is produced in this region from the decay of the lower lying triplet state.

Figure 6.14 show linear relationship in both bands of the Soret band region for the probe of the laser power dependence of the production of m/z 590.

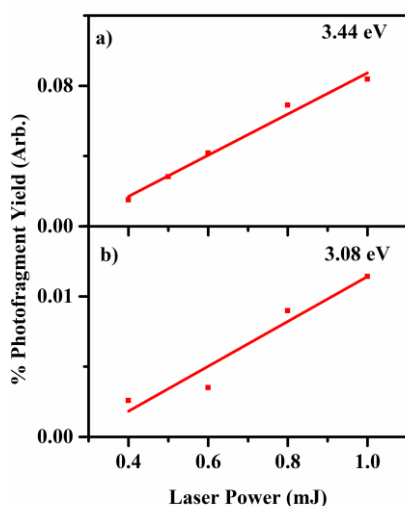


Figure 6.14 Power studies comparing the production of the photofragment m/z 590 with the laser pulse energy at 360 nm (3.44 eV) and 402nm (3.08 eV) (around the location of the maximum of the two bands in the Soret band region of the $\text{FeTTP}^+\text{-py}$), respectively.

The linear relationship signifies that m/z 590 is only produced from ultrafast decay of the S1 state to electronic ground state followed by ergodic decay of the electronic ground state cluster. This is a one-photon process. The photofragments m/z 514 and m/z 512 are also assumed to be produced from the same pathway because they have same spectral features as the m/z 590 photofragment. The absence of the first band that peak at 3.08 ± 0.02 eV in the Soret band region of these photofragments but present in the spectral profile of the photofragment m/z 668, this may be attributed to the T_1 excited state decay.

This electronic excited state does not possess enough energy to result in both the fission of the cluster and the dissociation of the m/z 668 moiety. It is worthy to mention that the photofragments m/z 591, m/z 590, m/z 514 and m/z 512 are also fragments produced from the ground state collision induced dissociation of the $\text{FeTTP}^+ = m/z$ 668 ion (Section 6.6.1.3, Figure 6.19).

This trend of disparity in the spectral features between the m/z 668 photofragment and the other photofragments in the Soret band region is also seen in the

photofragments production spectra for the FeTTP⁺·iQ and FeTTP⁺·Q clusters. In the FeTTP⁺·iQ photofragment production spectra for the *m/z* 590, *m/z* 514 and *m/z* 512 photofragments, they displayed a single narrow peak and band. This behaviour is also associated with their production from the decay of only the S₁ electronic excited state to the electronic ground state which is followed by thermal dissociation at the electronic ground state. The photofragments production spectra of *m/z* 591, *m/z* 590, *m/z* 514 and *m/z* 512 for the FeTTP⁺·Q cluster also showed disparity in the Soret band region from the *m/z* 668 spectrum. The *m/z* 591, *m/z* 590, *m/z* 514 and *m/z* 512 spectra also exhibited unique behaviour in that their spectra profile matched that of the TDDFT calculated spectrum for the N-ligated structure of the FeTTP⁺·Q cluster. This might indicate that although they are produced from the decay of the S₁ electronic state, there might be the contributions of different structures for the FeTTP⁺·Q cluster in our experiment. The TDDFT calculated spectrum for the π -stacking optimised structure for the FeTTP⁺·Q cluster presented in Table 6.4 mirrors that of the spectrum obtained for the N-coordinated structure (Section 6.6.2.1, Figure 6.25). This is not surprising because B3LYP is known not to account properly for dispersion interactions as was mentioned earlier or it might indicate that the real structure of the cluster present in our experiment is between two extremes (The cluster may also fluctuate between the two different structures at the ambient temperature of the experiment.). There is therefore a need for future computational work to establish the real structure of FeTTP⁺·Q cluster using a more advanced functional (eg. M06-2X) that better accounts for the dispersion interactions.

All the photofragments of different FeTTP⁺·N-aromatic clusters have similar features at the Q band region which can be attributed to their production from one-photon absorption process. This is because when the ions are excited directly to the S₁ excited state, they do not possess sufficient internal energy that can cause geometry change, therefore they cannot undergo ISC to the T₁ excited state. The pathway of relaxation in this region is by IC to the electronic ground state which is also followed by ergodic decay electronic ground state cluster.^{20,173}

The presence of the photofragments produced through IC and ultrafast decay to the electronic ground state as fragments in our HCD experiment both in terms of identity and relative intensity suggests statistical fragmentation. Statistical fragmentation has been reported for an IC decay pathway for Heme⁺ and Heme⁺·Histidine by Nielsen and co-workers.⁴⁰⁷

6.5 Conclusion

Isolated clusters of MP complex cations bound to individual N-aromatics were prepared using an electrospray ionization mass spectrometer. Ground-state collision induced dissociation was used to first confirm the intrinsic stability of the individual molecules and complexes, and then investigated to establish the ground-state thermal fragments. CID dissociation energy trends for the clusters ($\text{FeTTP}^+\cdot\text{iQ} > \text{FeTTP}^+\cdot\text{Q} > \text{FeTTP}^+\cdot\text{py}$) are in good agreement with predictions of preferential binding strength of the N-aromatics.³⁸² The disparity between the experimental and the calculated binding energies could be attributed to the differences in individual intrinsic properties of the N-aromatics which contributes to their preferred type of ligation and the limitations of the level of theory used. TDDFT calculated spectra for the N-ligated structures of the $\text{FeTTP}^+\cdot\text{py}$ and $\text{FeTTP}^+\cdot\text{iQ}$ clusters matched our photodepletion spectra thus suggesting that their N-coordinated structures are good descriptions of their geometric structures and that our experiments are populated by these structures. The photodepletion and TDDFT spectrum features for $\text{FeTTP}^+\cdot\text{Q}$ clusters do not match, but the spectra of its photofragments m/z 591, m/z 590, m/z 514 and m/z 512 do match the TDDFT calculated spectrum for the N-coordinated structure which suggests there might be the presence of two structures in our experiment. Alternatively, it may be that the resolution of the TDDFT simulated spectrum (i.e. the line width chosen for the electronic excitations) did not account for the features represented by the transitions in the TDDFT spectrum properly. This is unique to $\text{FeTTP}^+\cdot\text{Q}$ cluster. This disparity might also be attributed to the unique quinoline preferential ligation through π -stacking and the B3LYP functional not accounting for dispersion interactions properly, so that the real structure might be between two extreme possible structures.

The differences between the spectral features of the photofragment m/z 668 from the other photofragments m/z 591, m/z 590, m/z 514 and m/z 512 indicate that there is an additional decay of an excited state that contributed to its production. The m/z 668 photofragment of the clusters have been assigned to be produced from the combination of the ultrafast decay of the S_1 excited state, a lower lying T_1 electronic excited state in the Soret band region and the solo decay of the S_1 in the Q-band region, while the other photofragments m/z 591, m/z 590, m/z 514 and m/z 512 are

produced by the decay of only the S_1 electronic excited state in both the Soret and Q band regions. One and two-photon absorption processes have been identified to be involved in the decay of S_1 and T_1 electronic excited states in the Soret band region of the clusters, respectively. The ergodic decay of the electronic ground state cluster from the ultrafast decay of the S_1 state through IC has also been noted to result in statistical fragmentation. The photofragments corresponds to the HCD fragments which also supports the proposed statistical fragmentation.

The band shifts in the Soret and Q bands are different for the three clusters and the extinction coefficient of the MP studied does not reduce on ligation as was initially predicted.³⁸² This work has contributed to the better understanding of the UV-VIS photo absorption properties of iron centred metalloporphyrin and the effect of ligation on their photochemistry. This is essential because of its applications across various fields of endeavour, therefore making its various complexations with such molecules very topical. Future work is desirable to fine tune the preliminary spectra and theoretical work reported using functionals that describes the dispersion interactions better.

6.6 Supplementary Information

6.6.1 Experimental studies on FeTTP^+ ·*N*-aromatics clusters

6.6.1.1 Higher energy collisional dissociation of FeTTP^+ ·*N*-aromatics clusters

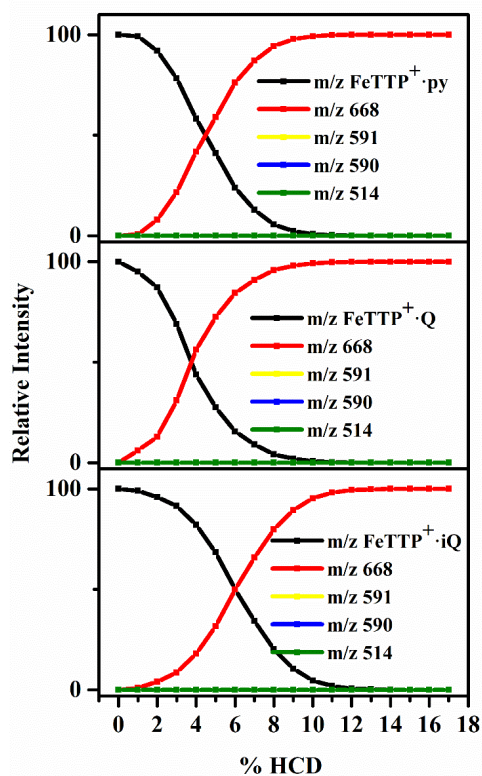


Figure 6.15 Parent ion dissociation curve FeTTP^+ ·*N*-aromatics clusters alongside production curves of fragments upon HCD between 0 and 17% energy. The data points fitted with the curved lines are viewing guides to show the profile for an individual fragment.

6.6.1.2 Solution-phase spectrum of FeTTPCl in MeCN

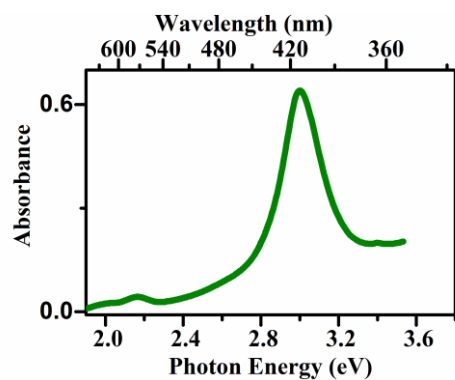


Figure 6.16 Absorption spectrum of FeTTPCl at ($1 \times 10^{-6} \text{ mol dm}^{-3}$) in MeCN.

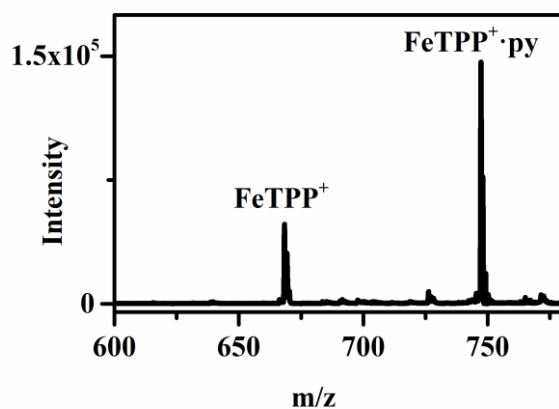
6.6.1.3 Parent ion mass spectra of FeTTP⁺ · N-aromatics clusters

Figure 6.17 Parent ion mass spectrum of FeTTP⁺ · py cluster with m/z 749.

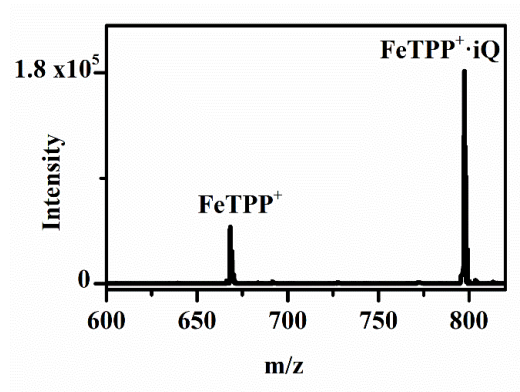


Figure 6.18 Parent ion mass spectrum of FeTTP⁺·iQ cluster. FeTTP⁺·iQ and FeTTP⁺·Q clusters have same mass-to-charge ratio (m/z 797).

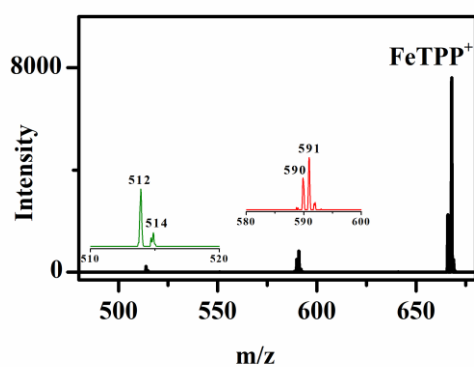


Figure 6.19 CID fragmentation mass spectrum of the FeTTP⁺ monomer at 10% CID energy.

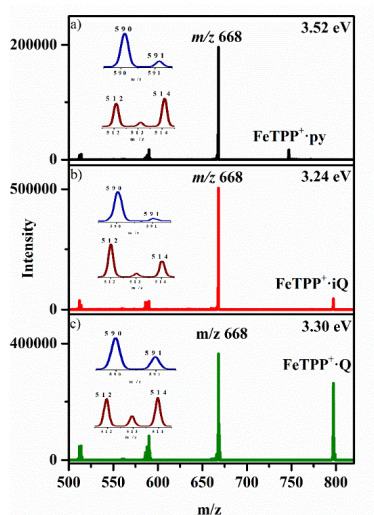
6.6.1.4 Photofragment mass spectra of $\text{FeTTP}^+ \cdot \text{N-aromatics}$ clusters

Figure. 6.20 The photofragment mass spectra of a) $\text{FeTTP}^+ \cdot \text{iQ}$, b) $\text{FeTTP}^+ \cdot \text{iQ}$ and c) $\text{FeTTP}^+ \cdot \text{Q}$ clusters irradiated at 3.52 eV, 3.24 eV and 3.30 eV, respectively.

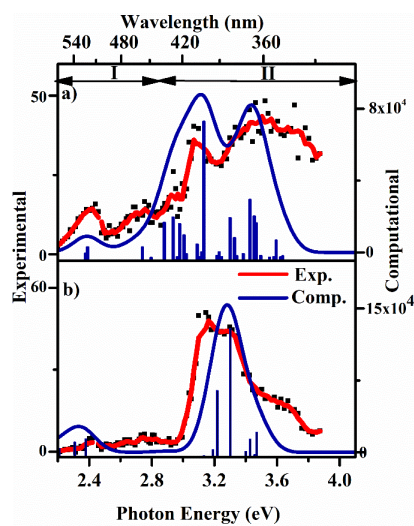
6.6.1.5 Overlaid TDDFT and photodepletion spectra of the $\text{FeTTP}^+ \cdot \text{N-aromatics}$ clusters.

Figure. 6.21 Overlaid experimental (red) and computational (blue) spectra for a)

FeTPP⁺:py and b) FeTPP⁺ with -0.1 eV shift of the TDDFT spectrum of a and b towards lower energy. The features of both the experimental and computational spectra matched.

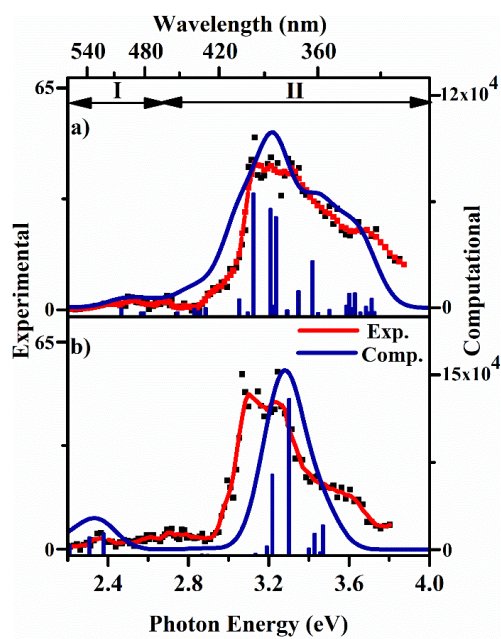


Figure 6.22 Overlaid experimental (red) and computational (blue) spectra for a) FeTPP⁺:iQ and b) FeTPP⁺ cluster with no shift in (a) and -0.1 eV shift in (b) to the TDDFT spectrum towards lower energy, respectively. The features of both the experimental and computational spectra matched.

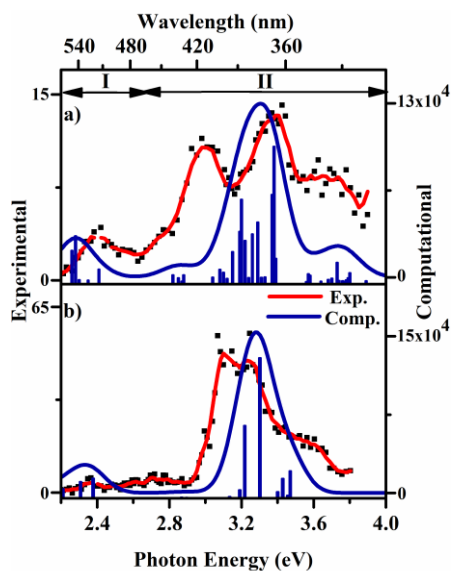


Figure 6.23 Overlaid experimental (red) and computational (blue) spectra for a) FeTPP⁺·Q and b) FeTPP⁺ cluster with -0.1 eV shift to the TDDFT spectrum of a and b towards lower energy. The features of both the experimental and computational spectra did not match.

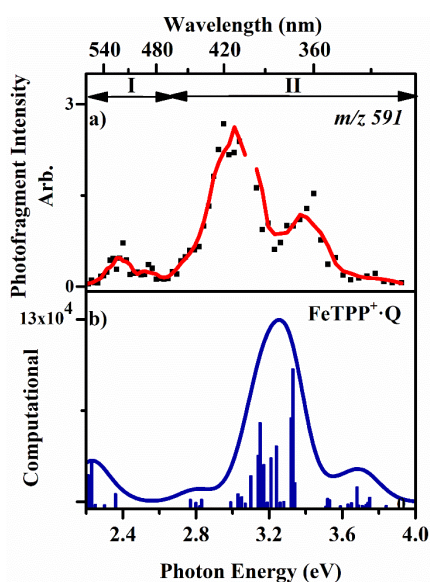


Figure 6.24 a.) The photofragment production spectrum (red) of m/z 591 obtained

from the photodepletion of the FeTTP⁺·Q cluster and b.) the TDDFT calculated spectrum (blue) of the FeTTP⁺·Q cluster with -0.05 eV shift towards lower energy.

6.6.2 Computational studies on FeTTP⁺·N-aromatics clusters

6.6.2.1 Overlaid TDDFT spectra for N-ligated and π -stacking optimised structures of FeTTP⁺·Q cluster.

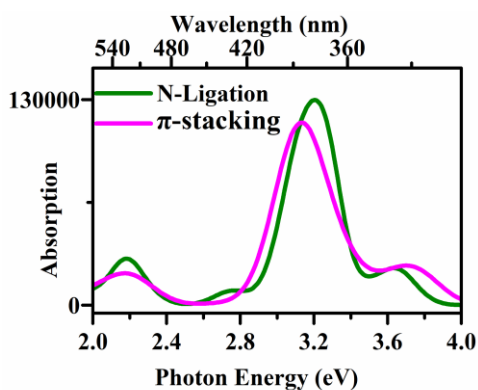
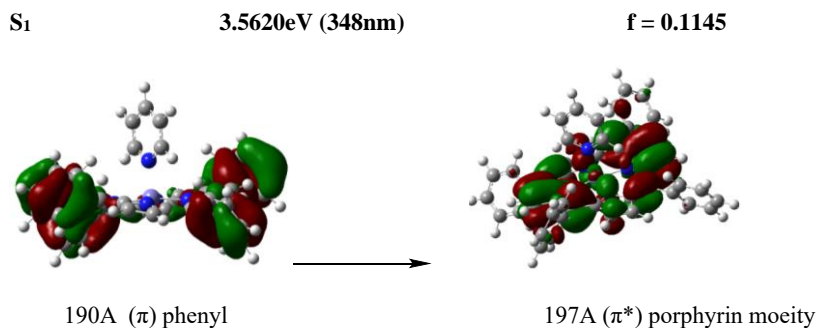
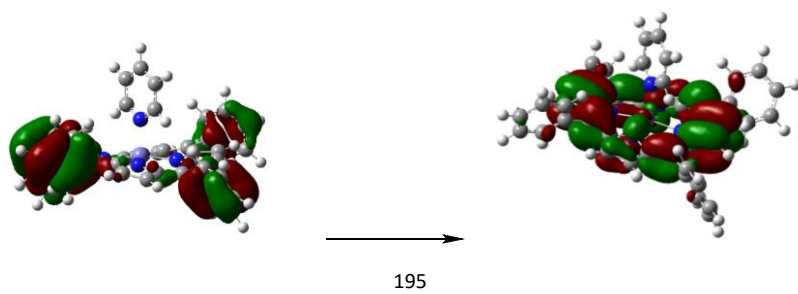
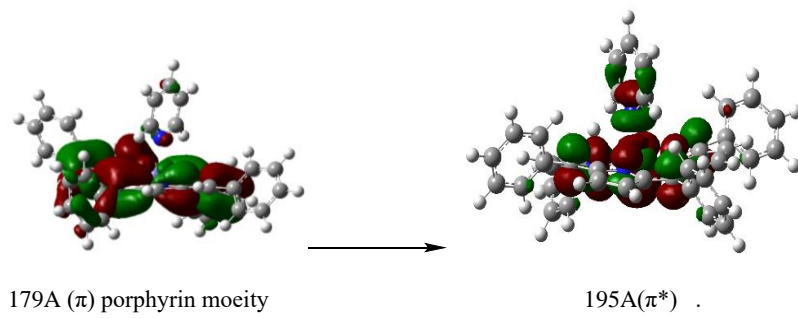
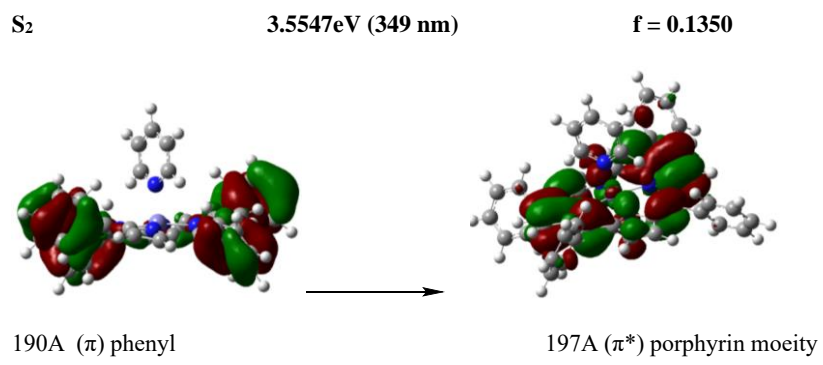
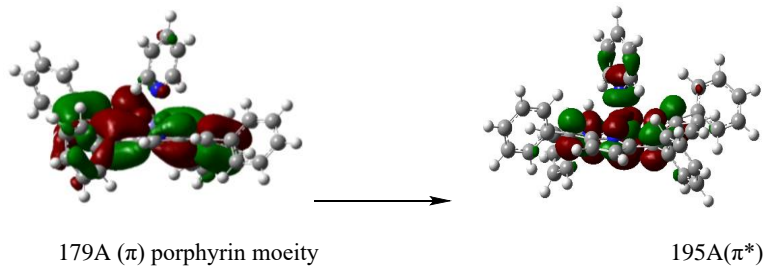


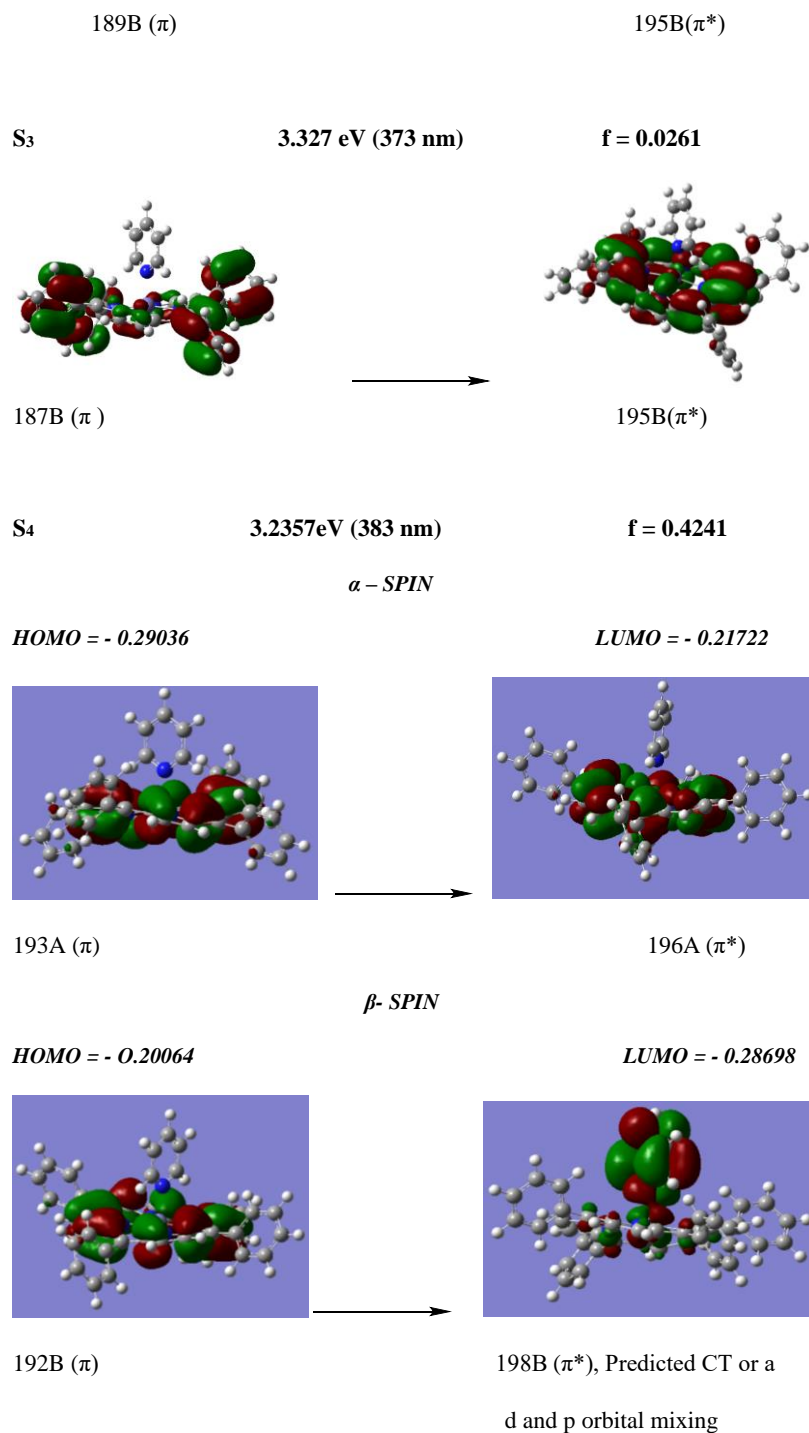
Figure 6.25 Overlaid TDDFT calculated spectra for N-ligated and π -stacking optimised structures of FeTTP⁺·Q cluster.

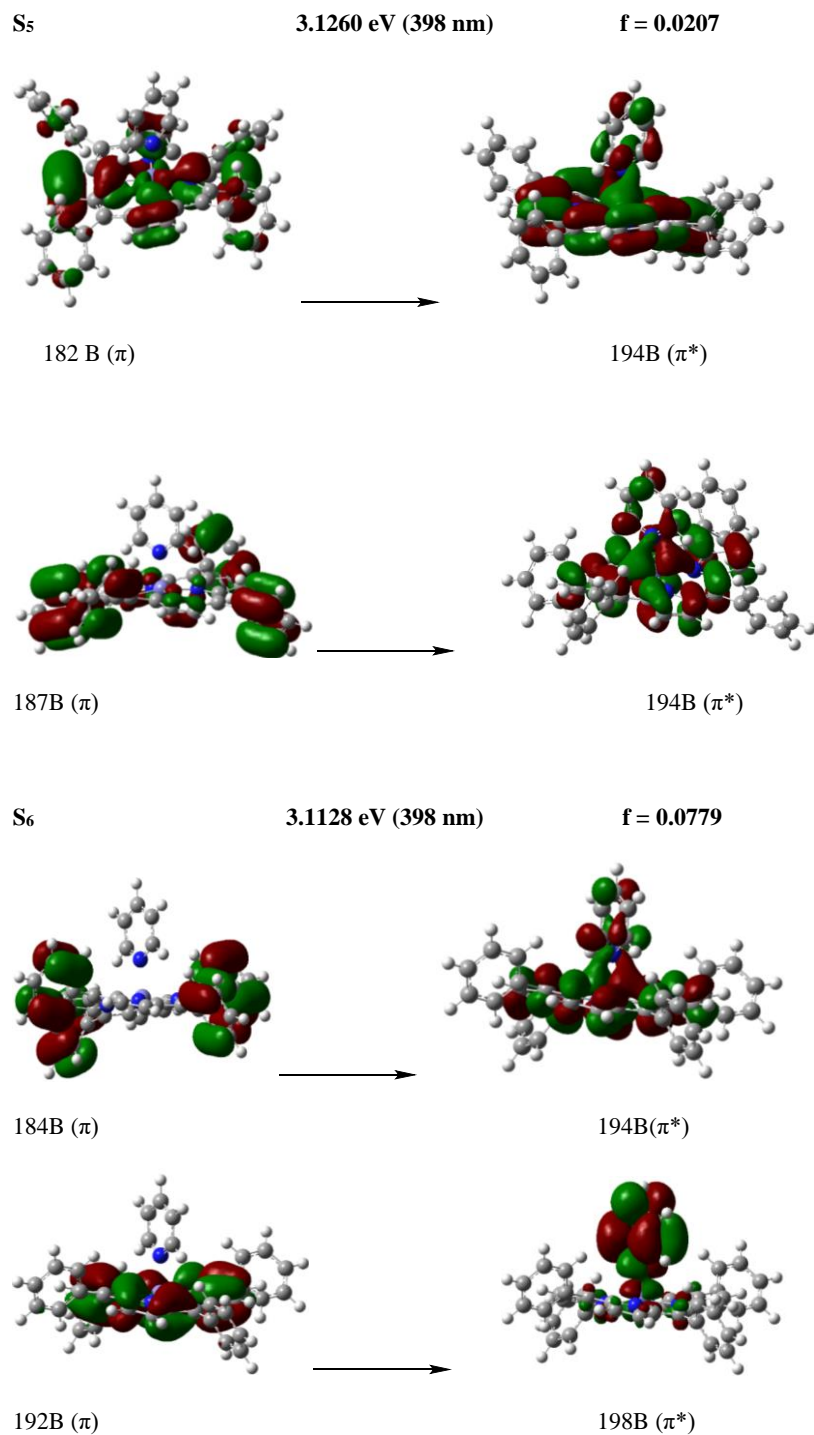
6.6.2.2 Molecular orbital (MO) predictions by TDDFT calculations for FeTTP⁺·py cluster.

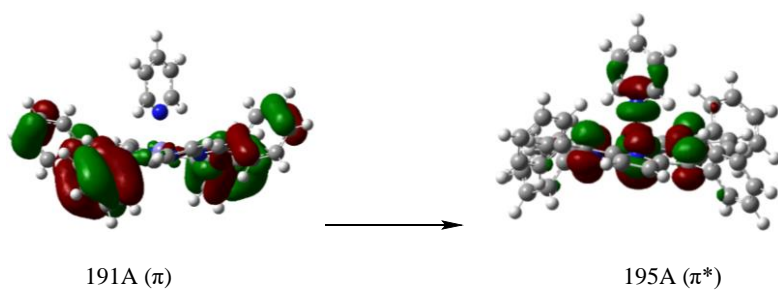
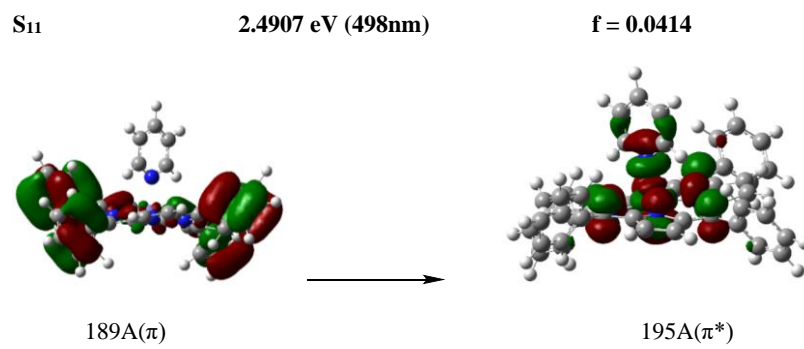
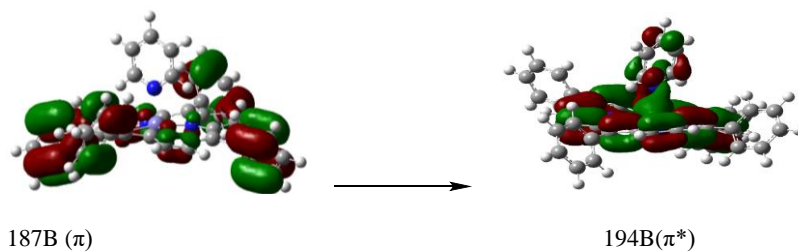
Table 6.9 Calculated TDDFT transition energies at the B3LYP/6-31G(d) level of theory and oscillator strengths of the FeTTP⁺·py cluster. MO transitions that contributed more than 20% to the excitations and with oscillator strength > 0.005 .

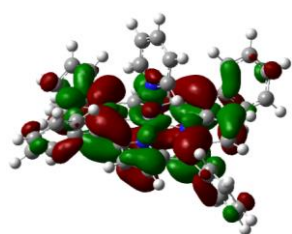




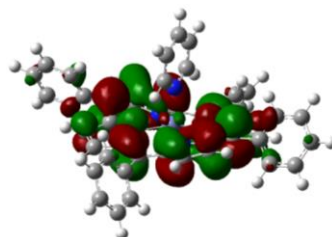




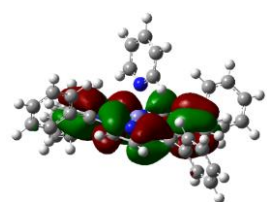




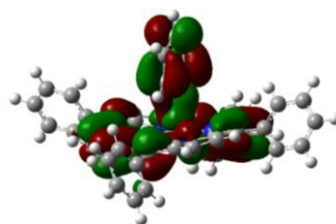
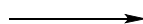
194A (π)



197A (π^*)



192B (π)

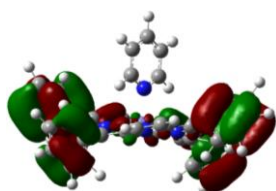


197B (π^*)

S₁₂

2.4830 eV (499nm)

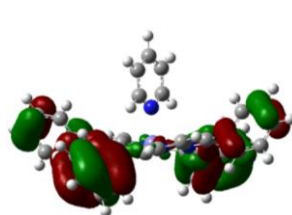
f = 0.0218



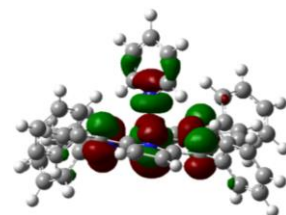
189A (π)



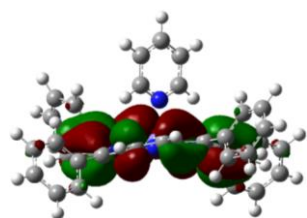
195A (π^*)



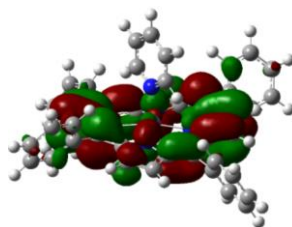
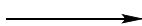
191A (π)



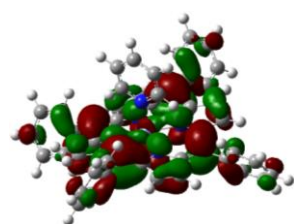
195A (π^*)



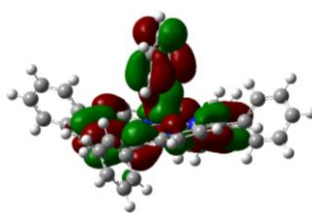
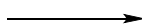
193A (π)



197A (π^*)



193B (π)



197B(π^*).

Chapter 7

Summary and Outlook

This thesis has presented the results of gas-phase photodissociation spectroscopy experiments of pharmaceutically and biologically relevant molecular and cluster ions performed within a laser-interfaced commercial mass spectrometer (LIMS). The aim of these studies has been to understand the fundamental photophysics and photochemistry of these biomolecular and cluster ions and to ascertain their fragmentation pathways on electronic photoexcitation. The studies also gave attention to the ability of the LIMS instrument to permit the detection and acquisition of all the photofragment ions produced at different wavelengths with masses above the mass cut-off of the mass spectrometer. All through this thesis, analytical information has been produced for the various molecular systems studied.

In Chapter 3, gas phase laser photodissociation spectroscopy is performed on the deprotonated and protonated forms of 2-thiouracil (2-TU), produced using electrospray ionization mass spectrometry across the UVA-UVC regions. This experiment was conducted to explore the effect of protonation and deprotonation on thionucleobase photochemistry, and therefore to probe the effect of pH on their photophysical properties at the molecular level. Our results show that the deprotonated form of 2-thiouracil ($[2\text{-TU-H}]^-$) decays predominantly by electron detachment and resulting in the production of free-radical species. Other anionic photofragments at very low intensities were also observed. Photoexcitation of protonated 2-thiouracil ($[2\text{-TU-H}]^+$) produces a cationic fragment which corresponds to ejection of an $\cdot\text{HS}$ radical from the precursor ion as the major photofragment. This ion was identified to be a product of direct excited state decay. Fragment ions related with decay of the hot ground state (i.e., the ions we would expect to observe if 2-thiouracil was behaving like UV-dissipating uracil) are observed as more minor products. This behaviour is consistent with enhanced intersystem crossing to triplet excited states compared to internal conversion back to the ground state. Two tautomers have been identified as present in our gas-phase absorption spectra for the protonated 2-TU. Although our calculation did not predict the presence of the second tautomer at the temperature of our experiments, higher-energy tautomers have previously been observed as present in our gas phase experiments.²⁷ The results for

the dissociative photochemistry of 2-TU and identification of the photoproducts are significant, given that it is an important nucleobase analogue with applications in molecular biology and pharmacology.²²⁶ The fact that electron detachment is the dominant decay pathway on photoexcitation of $([2\text{-TU-H}]^-)$ across the UV, followed by free radical production, leads to questions as to whether such decay pathways occur in the condensed phase. Future work to explore this directly will be useful in understanding this point, possibly using electron paramagnetic resonance (EPR) spectroscopy to detect the free radical species.⁴¹² Again, ion mobility mass spectrometry could be combined with our laser interfaced mass spectrometer (LIMS) to separate the protonated tautomers, hence providing structurally pure gaseous ions from the solution phase for the experiment. Hole-burning experiments would also be useful to confirm the presence of the tautomers.

In Chapter 4 we explored iodide complexes of non-nucleobases, 2-thiouracil (2-TU), 4-thiouracil (4-TU) and 2,4-thiouracil (2,4-TU) using laser photodissociation spectroscopy. This technique made it possible to probe the thionucleobase electron capture properties and the modifications on the excited state behaviour of these novel molecules due to the presence of one or more sulphur atoms. Photodecay of the clusters is dominated by electron detachment for the three complexes. The respective molecular anions were photoproducts for $\text{I}\cdot 4\text{-TU}$ and $\text{I}\cdot 2,4\text{-TU}$ clusters, but were not seen in the photodecay of $\text{I}\cdot 2\text{-TU}$ cluster. The $\text{I}\cdot 4\text{-TU}$ and $\text{I}\cdot 2,4\text{-TU}$ clusters also displayed similar general photodepletion spectra showing strong resemblance to the intrinsic absorption spectra of the respective uncomplexed thiouracil molecule. This indicates that these clusters' spectral profiles are determined by nucleobase chromophore excitations. This contrasts with the $\text{I}\cdot 2\text{-TU}$ photodepletion spectrum profile, where the near-threshold dipole-bound excited state is the only distinct spectral feature. This profile is attributed to the fact that the $\text{I}\cdot 2\text{-TU}$ cluster has a weaker cluster binding energy and vertical dipole moment than $\text{I}\cdot 4\text{-TU}$ and $\text{I}\cdot 2,4\text{-TU}$ clusters, due to the relatively lower dipole moment of 2-TU. The possibility that the stronger dipole moments of 4-TU and 2,4-TU are enhancing the coupling of the electron detachment continuum to nucleobase-centred transitions has been suggested as a conclusion of this work. Future experimental and theoretical works are required to aid in understanding the photophysics of how molecular excited states couple to the electron detachment continuum given that it is an area of emerging interest.

Furthermore, probing other thionucleobases derivatives may be useful in this regard given that derivatization creates significant changes to the molecular dipole.

The technique of probing the electron capture properties of biological relevant molecules is extended to the study of a larger biological molecule in Chapter 5. Photodissociation spectroscopy is conducted on the iodide riboflavin (I⁻RF) complex to understand further the photophysics and photochemistry of the riboflavin (RF) molecule, because of its involvement in many photo-biological processes. The study reveals that the I⁻RF cluster's behaviour mirrors that of the iodide thiouracil clusters. Electron detachment is the dominant pathway for photoexcitation decay, and the production of ionic photofragments a minor decay pathway. The strong resemblance between the photodepletion spectrum and the absorption spectrum of the uncomplexed RF shows strong coupling of the electron detachment continuum to the chromophore-centred transitions again. This can be attributed to the intrinsic properties of the RF molecule, primarily its large electric dipole moment. The production of riboflavin molecular anion (RF⁻) photofragment around the region associated to a riboflavin localized excited state is simply attributed to the proximity of the riboflavin excited state to the cluster dipole-bound excited state which results in strong coupling of the two distinct excited states. All photofragments observed for the RF molecule are assigned as direct excited state fragments because of their absence as thermal ground state fragments in collision-induced dissociation (CID) investigation of the ground state I⁻RF cluster. In the absence of the deprotonated form of the RF as an ionic photofragment, the production of the deprotonated lumichrome [LC-H]⁻ is attributed to secondary fragmentation occurring through breakup of the hot primary photofragment, RF⁻. This is the first time RF⁻ has been seen as a stable molecular anion. Time-resolved photoelectron spectroscopy experiments and high-quality theoretical calculations on the non-valence states of the RF⁻ are required to establish the nature of RF anion (i.e. valence or dipole bound anion).⁴¹³ Further work to explore the electron capture properties of flavins would be useful for other large flavin molecules because of their involvement in numerous biochemical processes. This work will also help us to understand the photophysics of how molecular excited states couple further to the electron detachment continuum. In Chapter 6, laser photodissociation spectroscopy is performed on the complexes of iron III metalloporphyrins (FeTPP⁺) and N aromatic molecules (pyridine, quinoline and iso-quinoline) and compared with the uncomplexed free metalloporphyrin

(MP). The objective is to probe the effect of ligation and photo-absorption properties of iron-centred metalloporphyrins. This molecule is relevant to a wide range of applications such as photodynamic therapy, drug design, biological imaging, magnetic resonance imaging etc. CID measurements revealed different fragmentation onsets for the complexes, in the order $iQ > Q > py$ which reflects the different binding strengths for each of the complexes. The disparity between the experimental and the calculated binding energies is attributed to the individual intrinsic properties of the N-aromatics, their preference for different ligation interactions, and steric effects which are presumed to be inadequate in the theoretical calculations performed. Photoexcitation of the complexes produced the same photofragments, with the excited state relaxation pathways presumed to follow very quick relaxation of the cluster to the electronic ground state. This is accompanied by redistribution of the vibrational energies resulting in cluster fragmentation, which is in line with collisional excitation of the ground electronic state. The band shifts and broadening of the Soret and Q bands are cluster-dependent, hence it is inferred that both the ground state and excited state properties are highly influenced by the intrinsic properties of the N-aromatics. Complexation did not reduce the absorption strength of the MP. Future work is desirable to refine the preliminary spectra presented in this thesis, alongside the necessary theoretical work. It would also be useful to explore extending these measurements further to other iron-centred metalloporphyrin complexes of pharmaceutical importance.

In this thesis, laser interfaced mass spectrometry within a commercially adapted ion trap along with computational chemistry has effectively been used to study a variety of gaseous ions, spanning small organic molecules and iodide-molecule complexes, where the molecule is biologically relevant to metalloporphyrin complexes. The acquisition of mass spectra and the recording and processing of the production of multiple photofragments as a function of wavelength using the commercial software has confirmed the reliability of the use of this type of instrumentation in photodepletion and photofragmentation experiments. Although several advances have been made using similar instruments to conduct spectroscopic experiments for over a decade, the experiments presented in this thesis are among the first to make contributions to such instruments as confirmed tools for photochemical analysis, electron detachment measurements alongside photofragmentation for the anions, and to establish the identification and stability of molecular anions in its experiment.

References

1. L.Gwennolkert and M. Conrad, *J. theor. Biol.*, (1998) **193**, 287-306.
2. Y. Zang and P.S. Cremer, *Current Opinion in Chemical Biology*, 2006,**10**, 658-663
3. A. H. J. Wang, G. J. Quigley, F. J. Kolpak, J. L. Crawford, J. H. van Boom, G. van der Marel and A. Rich, *Nature*, 1979, **282**, 680-686.
4. J.A. Hinson and D.W. Roberts, *Annual Review of Pharmacology and Toxicology*, 1992, **32**, 471-510.
5. J. D. Spikes, *Annu. Rev. Phys. Chem.*, 1967,**18**, 409-436.
6. O. P. Ernst, D. T. Lodowski, M. Elstner, P. Hegemann, L. S. Brown and H. Kandori, *Chem. Rev.*, 2014, **114**, 126-163.
7. R. P. Sinha and D. P. Hader, *Photochem. Photobiol. Sci.*, 2002, **1**, 225-236.
8. C. Li, Z. Li, E. Sletten, F. Arnesano, M. Losacco, G. Natile and Y. Liu, *Angew. Chem.* 2009, **121**, 8649–8652
9. N. J. Farrer, J. A. Woods, L. Salassa, Y. Zhao, K. S. Robinson, G. Clarkson, F. S. Mackay and P. J. Sadler, *Angew. Chem. Int. Ed.*, 2010, **49**, 8905-8908.
10. J. Schmidt, M. M. Meyer, I. Spector and S. R. Kass, *J. Phys. Chem. A*, 2011, **115**, 7625-7632.
11. Z. X. Tian, X. B. Wang, L. S. Wang and S. R. Kass, *J. Am. Chem. Soc.*, 2009,**131**, 1174-1181.
12. J. R. R. Verlet, D. A. Horke and A. S. Chatterley, *Phys. Chem. Chem. Phys.*, 2014, **16**, 15043-15052.
13. E. Nir, M. Muller, L. I. Grace and M. S. de Vries, *Chem. Phys. Lett.*, 2002, **355**, 59-64.
14. K. MullerDethlefs, *J. Electron. Spectrosc. Relat. Phenom.*, 1995, **75**, 35-46.
15. T. Baer and R. C. Dunbar, *J. Am. Soc. Mass. Spectrom.*, 2010, **21**, 681-693.
16. J. I. Brauman and K. C. Smyth, *J. Am. Chem. Soc.*, 1969, **91**, 7778-7780.
17. . D. Nolting, R. Weinkauff, I.V. Hertel and T.Schultz, *Chem. Phys. Chem.*, 2007, **8**, 751-755.
18. O.V. Boyarkin, S.R. Mercier, A. Kamariotis and T.R. Rizzo, *J. Am. Chem. Soc.*, 2006, **128**, 2816-2817

References

19. M. Z. Kamrath, E. Garand, P. A. Jordan, C. M. Leavitt, A. B. Wolk, M. J. Van Stipdonk, S. J. Miller and M. A. Johnson, *J. Am. Chem. Soc.*, 2011, **133**, 6440-6448.
20. E. Matthews, A. Sen, N. Yoshikawa, E. Bergstrom and C. E. H. Dessent, *Phys. Chem. Chem. Phys.*, 2016, **18**, 15143-15152.
21. H.H. Telle, A.G. Ureña and R.J. Donovan, *Laser Chemistry: spectroscopy, dynamics and application*, John Wiley & Sons, LTD, 2007, p 3.
22. J. Laskin and J. H. Futrell, *Mass Spectrom. Rev.*, 2005, **24**, 135-167
23. R. C. Dunbar, *J. Am. Chem. Soc.*, 1971, **93**, 4354-4358.
24. R. Antoine and P. Dugourd, *Phys. Chem. Chem. Phys.*, 2011, **13**, 16494-16509.
25. J. P. Reilly, *Mass Spectrom. Rev.*, 2009, **28**, 425-447.
26. D. M. Wetzel and J. I. Brauman, *Chem. Rev.*, 1987, **87**, 607-622.
27. E. Matthews and C. E. H. Dessent, *J. Phys. Chem. A*, 2016, **120**, 9209-9216.
28. K. O. Uleanya, R. Cercola, M. Nikolova, E. Matthews, N. G. K. Wong and C. E. H. Dessent, *Molecules*, 2020, **25**, 3157.
29. S. H. Kaufman, J. M. Weber and M. Pernpointner, *J. Chem. Phys.*, 2013, **139**, 194310.
30. R. Cercola, K. C. Fischer, S. L. Sherman, E. Garand, N. G. K. Wong, L. A. Hammerback, JM. Lynam, I. J. S. Fairlamb and C. E. H. Dessent, *Chem. Eur. J.* . 2020, **26** , 1 0297 – 1 0306
31. K.O. Uleanya and C.E. Dessent, *Phys. Chem. Chem. Phys.*, 2021,**23**, 1021-1030.
32. J. Oomens, D. T. Moore, G. Meijer and G. von Helden, *Phys. Chem. Chem. Phys.*, 2004, **6**, 710-718.
33. M. A. Halim, M. Girod, L. MacAleese, J. Lemoine, R. Antoine and P. Dugourd, *J. Am. Soc. Mass. Spectrom.*, 2016, **27**, 1435-1442.
34. A. J. A. Harvey, A. Sen, N. Yoshikawa and C. E. H. Dessent, *Chem. Phys. Lett.*, 2015, **634**, 216-220.
35. J. R. Cannon, M. B. Carnmarata, S. A. Robotham, V. C. Cotham, J. B. Shaw, R. T. Fellers, B. P. Early, P. M. Thomas, N. L. Kelleher and J. S. Brodbelt, *Anal. Chem.*, 2014, **86**, 2185-2192.
36. N. C. Polfer, *Chem. Soc. Rev.*, 2011, **40**, 2211-2221.
37. L. J. M. Kempkes, J. Martens, G. Berden and J. Oomens, *Int. J. Mass spectrom.*, 2018, **429**, 90-100.
38. J. Martens, J. Grzetic, G. Berden and J. Oomens, *Nat. Commun.*, 2016, **7**, 11754

References

39. K. S. Lancaster, H. J. An, B. S. Li and C. B. Lebrilla, *Anal. Chem.*, 2006, **78**, 4990-4997.
40. A. F. Cruz-Ortiz, M. Rossa, F. Berthias, M. Berdakin, P. Maitre and G. A. Pino, *J. Phys. Chem. Lett.*, 2017, **8**, 5501-5506.
41. K. C. Smyth, R. T. Mciver, J. I. Brauman and R. W. Wallace, *J. Chem. Phys.*, 1971, **54**, 2758-2759.
42. M. Yamashita and J. B. Fenn, *J. Phys. Chem.*, 1984, **88**, 4451-4459.
43. M. Yamashita and J. B. Fenn, *J. Phys. Chem.*, 1984, **88**, 4671-4675
44. Y. Inokuchi, T. Ebata and T. R. Rizzo, *J. Phys. Chem. A*, 2015, **119**, 11113-11118.
45. L. Voronina and T. R. Rizzo, *Phys. Chem. Chem. Phys.*, 2015, **17**, 2582825836.
46. F. Rosu, V. Gabelica, E. De Pauw, R. Antoine, M. Broyer and P. Dugourd, *J. Phys. Chem. A*, 2012, **116**, 5383-5391.
47. N. L. Burke, A. F. DeBlase, J. G. Redwine, J. R. Hopkins, S. A. McLuckey and T. S. Zwier, *J. Am. Chem. Soc.*, 2016, **138**, 2849-2857.
48. E. Matthews and C. E. H. Dessent, *Phys. Chem. Chem. Phys.*, 2017, **19**, 17434-17440.
49. C. S. Byskov, J. M. Weber and S. B. Nielsen, *Phys. Chem. Chem. Phys.*, 2015, **17**, 5561-5564.
50. S. H. Kaufman and J. M. Weber, *J. Phys. Chem. A*, 2014, **118**, 9687-9691
51. S. Banerjee and S. Mazumdar, *Int. J. Anal. Chem.*, 2012, **2012**, 282574.
52. C. S. Ho, C. W. K. Lam, M. H. M. Chan, R. C. K. Cheung, L. K. Law, L. C. W. Lit, K. F. Ng, M. W. M. Suen and H. L. Tai, *Clin. Biochem. Rev.*, 2003, **24**, 3-12.
53. C. T. Wolke, J. A. Fournier, E. Miliordos, S. M. Kathmann, S. S. Xantheas and M. A. Johnson, *J. Chem. Phys.*, 2016, **144**, 074305
54. R. C. Dunbar, J. Oomens, G. Berden, J. K. C. Lau, U. H. Verkerk, A. C. Hopkinson and K. W. M. Siu, *J. Phys. Chem. A*, 2013, **117**, 5335-5343.
55. P. Nieto, A. Gunther, G. Berden, J. Oomens and O. Dopfer, *J. Phys. Chem. A*, 2016, **120**, 8297-8308.
56. S. Warnke, J. Seo, J. Boschmans, F. Sobott, J. H. Scrivens, C. Bleiholder, M. T. Bowers, S. Gewinner, W. Schollkopf, K. Pagel and G. von Helden, *J. Am. Chem. Soc.*, 2015, **137**, 4236-4242.

References

57. I. Alata, M. Broquier, C. Dedonder-Lardeux, C. Jouvet, M. Kim, W. Y. Sohn, S. S. Kim, H. Kang, M. Schutz, A. Patzer and O. Dopfer, *J. Chem. Phys.*, 2011, **134**, 074307.
58. Y. Shi, M. Du, J. Ren, K. Zhang, Y. Xu and X. Kong, *Molecules* 2020, **25**, 5152
59. H. Oh, K. Breuker, S.K. Sze, Y. Ge, B.K. Carpenter and F.W. McLafferty, *Proc. Natl. Acad. Sci. USA*, 2002, **99**, 15863–15868.
60. Z. Takats, S.C. Nanita, R.G. Cooks, *Angew. Chem. Int. Ed.*, 2010, **42**, 3521–3523.
61. J. Ren, S. Bian, Y. Wang, and X. Kong, *Prog. Chem.* 2018, **30**, 383–397.
62. X. Kong, I.A. Tsai, S. Sabu, C.C. Han, Y.T. Lee, H.C. Chang, S.Y. Tu, A.H. Kung and C.C. Wu, *Angew. Chem. Int. Ed.* 2006, **45**, 4130–4134.
63. X. Kong, C. Lin, G. Infusini, H.B. Oh, H. Jiang, K. Breuker, C.C. Wu, O.P. Charkin, H.C. Chang and F.W. McLafferty, *Chem. Phys. Chem.* 2009, **10**, 2603–2606.
64. J. Seo, S. Warnke, K. Pagel, M.T. Bowers and G. von Helden, *Nat. Chem.* 2017, **9**, 1263–1268.
65. V. Scutelnic, M.A.S. Perez, M. Marianski, S. Warnke, A. Gregor, U. Rothlisberger, M.T. Bowers, C. Baldauf, G. von Helden, and T.R. Rizzo, *J. Am. Chem. Soc.* 2018, **140**, 7554–7560.
66. F.X. Sunahori, G. Yang, E.N. Kitova, J.S. Klassen and Y.J. Xu, *Phys. Chem. Chem. Phys.* 2013, **15**, 1873–1886.
67. M. Z. Kamrath, R. A. Relph, T. L. Guasco, C. M. Leavitt and M. A. Johnson, *Int. J. Mass spectrom.*, 2011, **300**, 91-98.
68. M.N.R. Ashfold and C.M. Western, in *Encyclopedia of Spectroscopy and Spectrometry*, 1999, 2nd Ed.
69. J. D. Rodriguez, M. G. Gonzalez, L. Rubio-Lago and L. Banares, *Phys. Chem. Chem. Phys.*, 2014, **16**, 406-413.
70. H. W. Li, Y. Fang, N. M. Kidwell, J. M. Beames and M. I. Lester, *J. Phys. Chem. A*, 2015, **119**, 8328-8337.
71. B. W. Toulson, J. P. Alaniz, J. G. Hill and C. Murray, *Phys. Chem. Chem. Phys.*, 2016, **18**, 11091-11103.
72. E. Nir, C. Plutzer, K. Kleinermanns and M. de Vries, *Eur. Phys. J. D*, 2002, **20**, 317-329

References

73. S. Hüfner, S. Schmidt and F. Reinert, *Nuclear Instruments and Methods in Physics Research A*, 2005, **547**, 8–239.
74. A. S. Chatterley, C. W. West, V. G. Stavros and J. R. R. Verlet, *Chem. Sci.*, 2014, **5**, 3963-3975.
75. A. B. Stephansen, S. B. King, Y. Yokoi, Y. Minoshima, W. L. Li, A. Kunin, T. Takayanagi and D. M. Neumark, *J. Chem. Phys.*, 2015, **143**, 104308(1-14).
76. E. V. Beletskiy, X. B. Wang and S. R. Kass, *J. Phys. Chem. A*, 2016, **120**, 8309-8316.
77. A.S. Chatterley, C.W. West, G.M. Roberts, V.G. Stavros and J.R.R. Verlet, *J. Phys. Chem. Lett.*, 2014, **5**, 843-848.
78. M.C. Stuhldreier and F. Temps, *Faraday Discuss.*, 2013, **163**, 173-188.
79. J. N. Bull, C. W. West, and J. R. R. Verlet, *Chem. Sci.*, 2016, **7**, 5352-5361
80. X. B. Wang and S. R. Kass, *J. Am. Chem. Soc.*, 2014, **136**, 17332-17336.
81. R.G Cooks, *J. Am. Soc. Mass. Spectrom.*, 1995, **30**, 197-206
82. F.W. McLafferty, *Tandem mass spectrometry*, 1983, Wiley, New York
83. D. Ortiz, P. Martin-Gagoc, A. Rierac, K. Song, J.Y. Salpina, R. Spezia, *Int. J. Mass Spectrom.*, 2013, **335**, 33–44.
84. F. W. McLafferty, P. F. Bente, R. Kornfeld, S. C. Tsai and I. Howe, *J. Am. Chem. Soc.*, 1973, **95**, 2120-2129.
85. J. M. Wells and S. A. McLuckey, *Biol. Mass Spectrom.*, 2005, 402, 148-185.
86. F. W. McLafferty, *Anal. Chem.*, 1959, **31**, 82-87.
87. A.K. Shukla and J.H. Futrell, *J. Am. Soc. Mass. Spectrom.*, 2000, **35**, 1069-1090
88. C. Singh, C.G. Zampronio, A. J. Creese and H.J Cooper, *J. Proteome Res.* 2012, **11**, 4517-25
89. Y. H. Ho and P. Kebarle, *Int. J. Mass spectrom.*, 1997, **165**, 433-455.
90. R. Cumeras, E. Figueras, C. E. Davis, J. I. Baumbach and I. Gracia, *Analyst*, 2015, **140**, 1376-1390.
91. F. Lanucara, S.W. Holman, C.J. Gray, and C.E. Eyers, *Nature Chemistry*, 2014, **6**, 281-294
92. R. Cumeras, E. Figueras, C. E. Davis, J. I. Baumbach and I. Gracia, *Analyst*, 2015, **140**, 1391-1410.
93. M.Z. Kamrath and T.R. Rizzo, *Acc. Chem. Res.* 2018, 51, **6**, 1487-1495
94. J. N. Bull, N. J. A. Coughlan, and E. J. Bieske, *J. Phys. Chem. A*, 2017, **121**, 6021-6027.

References

95. C. Masellis, N. Khanal, M. Z. Kamrath, D. E. Clemmer and T. R. Rizzo, *J. Am. Soc. Mass. Spectrom.*, 2017, **28**, 2217-2222.
96. J. Seo, S. Warnke, S. Gewinner, W. Schollkopf, M. T. Bowers, K. Pagel and G. von Helden, *Phys. Chem. Chem. Phys.*, 2016, **18**, 25474-25482.
97. J.C. Pouilly, G. Gregoire, R. Ballivian, P. Dugourd and J.P. Schermann, *Vib. Spectrosc.*, 2011, **56**, 105-109.
98. J. S. Brodbelt, *Chem. Soc. Rev.*, 2014, **43**, 2757-2783.
99. T. Doussineau, R. Antoine, M. Santacreu and P. Dugourd, *J. Phys. Chem. Lett.*, 2012, **3**, 2141-2145.
100. B. J. Ko and J. S. Brodbelt, *Anal. Chem.*, 2011, **83**, 8192-8200.
101. J. A. Madsen, T. W. Cullen, M. S. Trent and J. S. Brodbelt, *Anal. Chem.*, 2011, **83**, 5107-5113.
102. J. S. Brodbelt, *J. Am. Soc. Mass. Spectrom.*, 2011, **22**, 197-206
103. J. D. Sanders, D. Grinfeld K. Aizikov, A. Makarov, D. D. Holden, and J. S. Brodbelt, *Anal. Chem.* 2018, **90**, 5896-5902
104. V. Gabelica, F. Rosu, T. Tabarin, C. Kinet, R. Antoine, M. Broyer, E. De Pauw and P. Dugourd, *J. Am. Chem. Soc.*, 2007, **129**, 4706-4713.
105. B. Bellina, I. Compagnon, L. Joly, F. Albrieux, A.R. Allouche, F. Bertorelle, J. Lemoine, R. Antoine and P. Dugourd, *Int. J. Mass. Spectrom.*, 2010, **297**, 36-40.
106. L. Sanche, *Eur. Phys. J. D*, 2005, **35**, 367-390.
107. J.A. Stearns, S. Mercier, C. Seaiby, M. Guidi, O.V. Boyarkin, and T.R. Rizzo, *J. Am. Chem. Soc.*, 2007, **129**, 11814-11820.
108. M. Guidi, U.J. Lorenz, G. Papadopoulos, O.V. Boyarkin and T.R. Rizzo, *J. Phys. Chem. A*, 2009, **113**, 797-799.
109. L. Guyon, T. Tabarin, B. Thuillier, R. Antoine, M. Broyer, V. Boutou, J. P. Wolf and P. Dugourd, *J. Chem. Phys.*, 2008, **128**, 075103.
110. I. Compagnon, A. R. Allouche, F. Bertorelle, R. Antoine and P. Dugourd, *Phys. Chem. Chem. Phys.*, 2010, **12**, 3399-3403.
111. V. Gabelica, F. Rosu, E. De Pauw, R. Antoine, T. Tabarin, M. Broyer and P. Dugourd, *J. Am. Soc. Mass. Spectrom.*, 2007, **18**, 1990-2000.
112. V. Gabelica, T. Tabarin, R. Antoine, F. Rosu, I. Compagnon, M. Broyer, E. De Pauw and P. Dugourd, *Anal. Chem.*, 2006, **78**, 6564-6572.

References

113. C. Brunet, R. Antoine, J. Lemoine and P. Dugourd, *J. Phys. Chem. Lett.*, 2012, **3**, 698-702.
114. Q. Duez, T. Josse, V. Lemaire, F. Chiroz, C. M. Choi, P. Dubois, P. Dugourd, J. Cornil, P. Gerbaux, J. De Winter, *J Mass Spectrom.*, 2017, **52**, 133-138.
115. C. Marian, D. Nolting and R. Weinkauff, *Phys. Chem. Chem. Phys.*, 2005, **7**, 3306-3316.
116. D. Nolting, C. Marian and R. Weinkauff, *Phys. Chem. Chem. Phys.*, 2004, **6**, 2633-2640.
117. D. Nolting, T. Schultz, I. V. Hertel and R. Weinkauff, *Phys. Chem. Chem. Phys.*, 2006, **8**, 5247-5254.
118. H. Kang, C. Dedonder-Lardeux, C. Jouvot, G. Gregoire, C. Desfrancois, J. P. Schermann, M. Barat and J. A. Fayeton, *J. Phys. Chem. A*, 2005, **109**, 2417-2420.
119. H. Kang, C. Jouvot, C. Dedonder-Lardeux, S. Martrenchard, C. Charriere, G. Gregoire, C. Desfrancois, J. P. Schermann, M. Barat and J. A. Fayeton, *J. Chem. Phys.*, 2005, **122**, 084307.
120. D. Imanbaew, J. Lang, M. F. Gelin, S. Kaufhold, M. G. Pfeffer, S. Rau and C. Riehn, *Angew. Chem. Int. Ed.*, 2017, **56**, 5471-5474.
121. Q. Z. Bian, M. W. Forbes, F. O. Talbot and R. A. Jockusch, *Phys. Chem. Chem. Phys.*, 2010, **12**, 2590-2598.
122. H. Yao and R. A. Jockusch, *J. Phys. Chem. A*, 2013, **117**, 1351-1359.
123. M. W. Forbes and R. A. Jockusch, *J. Am. Chem. Soc.*, 2009, **131**, 17038-17039.
124. M. W. Forbes, A. M. Nagy and R. A. Jockusch, *Int. J. Mass spectrom.*, 2011, **308**, 155-166.
125. A. M. Nagy, F. O. Talbot, M. F. Czar and R. A. Jockusch, *J. Photochem. Photobiol. A*, 2012, **244**, 47-53.
126. M. W. Forbes and R. A. Jockusch, *J. Am. Soc. Mass. Spectrom.*, 2011, **22**, 93-109.
127. S. V. Kruppa, F. Bappler, W. Klopper, S. P. Walg, W. R. Thiel, R. Diller and C. Riehn, *Phys. Chem. Chem. Phys.*, 2017, **19**, 22785-22800.
128. Y. Nosenko, C. Riehn and W. Klopper, *Chem. Phys. Lett.*, 2016, **659**, 55-60.

References

129. E. Bodo, A. Ciavardini, A. Giardini, A. Paladini, S. Piccirillo, F. Rondino and D. Scuderi, *Chem. Phys.*, 2012, **398**, 124-128.
130. V. Gabelica, F. Rosu, E. De Pauw, J. Lemaire, J. C. Gillet, J. C. Pouilly, F. Lecomte, G. Gregoire, J. P. Schermann and C. Desfrancois, *J. Am. Chem. Soc.*, 2008, **130**, 1810-1811.
131. H. Elferink, M. E. Severijnen, J. Martens, R. A. Mensink, G. Berden, J. Oomens, F. P. J. T. Rutjes, A. M. Rijs and T. J. Boltje, *J. Am. Chem. Soc.*, 2018, **140**, 6034-6038.
132. J. A. Bendo, J. Martens, G. Berden, J. Oomens and T. H. Morton, *Int. J. Mass spectrom.*, 2018, **429**, 206-211.
133. R.C. Dunbar, J. Martens, G. Berden and J. Oomens, *Phys. Chem. Chem. Phys.*, 2016, **18**, 26923-26932.
134. R.C. Dunbar, J. Martens, G. Berden and J. Oomens, *J. Phys. Chem. Lett.*, 2017, **8**, 2634-2638.
135. L. J. M. Kempkes, G. C. Boles, J. Martens, G. Berden, P. B. Armentrout and J. Oomens, *J. Phys. Chem. A*, 2018, **122**, 2424-2436.
136. D.R. Klein, D.D. Holden, and J.S. Brodbelt, *Anal. Chem.*, 2016, **88**, 1044-1051
137. T.P. Cleland, C.J. DeHart, R.T. Fellers, A.J. VanNispen. J.B. Greer, R.D. LeDuc, W.R. Parker, P.M. Thomas, N.L. Kelleher and J.S. Brodbelt. *J. Proteome Res.*, 2017, **16**, 2072-2079.
138. W.K. Mino, Jr. K. Gulyuz, D.Wang, C.N. Stedwell and N.C. Polfer, *J. Phys. Chem. Lett.*, 2011, **2**, 4, 299-304
139. M. H. Stockett, C. Kjaer, M. K. Linder, M. R. Detty and S. B. Nielsen, *Photochem. Photobiol. Sci.*, 2017, **16**, 779-784.
140. J. Houmoller, M. Wanko, A. Rubio and S. B. Nielsen, *J. Phys. Chem. A*, 2015, **119**, 11498-11503.
141. M. B. S. Kirketerp and S. B. Nielsen, *Int. J. Mass spectrom.*, 2010, **297**, 6366.
142. G. Feraud, C. Dedonder-Lardeux, C. Jouvét and E. Marceca, *J. Phys. Chem. A*, 2016, **120**, 3897-3905.
143. G. Feraud, N. Esteves-Lopez, C. Dedonder-Lardeux and C. Jouvét, *Phys. Chem. Chem. Phys.*, 2015, **17**, 25755-25760.
144. M. I. Taccone, G. Feraud, M. Berdakin, C. Dedonder-Lardeux, C. Jouvét and G. A. Pino, *J. Chem. Phys.*, 2015, **143**, 041103.

References

145. R. Otto, A. von Zastrow, T. Best and R. Wester, *Phys. Chem. Chem. Phys.*, 2013, **15**, 612-618.
146. J. C. Dean, N. L. Burke, J. R. Hopkins, J. G. Redwine, P. V. Ramachandran, S. A. McLuckey and T. S. Zwier, *J. Phys. Chem. A*, 2015, **119**, 1917-1932.
147. N. L. Burke, J. G. Redwine, J. C. Dean, S. A. McLuckey and T. S. Zwier, *Int. J. Mass spectrom.*, 2015, **378**, 196-205.
148. T. K. Roy, V. Kopysov, N. S. Nagornova, T. R. Rizzo, O. V. Boyarkin and R. B. Gerber, *Chemphyschem*, 2015, **16**, 1374-1378.
149. C. Seaiby, A. V. Zabuga, A. Svendsen and T. R. Rizzo, *J. Chem. Phys.*, 2016, **144**, 014304.
150. AmaZon Mass Spectrometer User Manual, Bruker Daltonik..
151. Taylor. G, *Proceedings of the Royal Society of London. Series A. Mathematical and Physical Sciences*, 1964, **280**, 383.
152. E. Matthews, PhD Thesis, University of York, UK, 2018.
153. L. Rayleigh, *Philos. Mag.*, 1882, **14**, 184-186
154. L. Konermann, E. Ahadi, A. D. Rodriguez and S. Vahidi, *Anal. Chem.*, 2013, **85**, 2-9
155. N. B. Cech and C. G. Enke, *Mass Spectrom. Rev.*, 2001, **20**, 362-387.
156. M. Dole, L. L. Mack and R. L. Hines, *J. Chem. Phys.*, 1968, **49**, 2240-2249.
157. L. L. Mack, P. Kralik, A. Rheude and M. Dole, *J. Chem. Phys.*, 1970, **52**, 4977-4986.
158. B. A. Thomson and J. V. Iribarne, *J. Chem. Phys.*, 1979, **71**, 4451-4463.
159. J. V. Iribarne and B. A. Thomson, *J. Chem. Phys.*, 1976, **64**, 2287-2294.
160. H. D. Dewald, *J. Chem. Educ.*, 1999, **76**, 33.
161. R. B. Cole, *Electrospray and MALDI mass spectrometry: fundamentals, instrumentation, practicalities, and biological applications*, Wiley, Hoboken, N.J., 2010.
162. P. Kebarle and U. H. Verkerk, *Mass Spectrom. Rev.*, 2009, **28**, 898-917
163. W. Paul and H. Steinwedel, *U.S. Pat.*, 2,939,952, 7 June 1960.
164. R. E. March and J. F. J. Todd, *Quadrupole ion trap mass spectrometry*, Wiley, Hoboken, N.J., 2005.
165. W. Paul, *Rev. Mod. Phys.*, 1990, **62**, 531-540.
166. É. Mathieu, *J. Math. Pures Appl.*, 1868, **13**, 137-203.
167. V. I. Baranov, *J. Am. Soc. Mass. Spectrom.*, 2003, **14**, 818-824.

References

168. M. Barber, D. B. Gordon and M. D. Woods, *Rapid Commun. Mass Spectrom.*, 1990, **4**, 442-446.
169. A. R. Johnson and E. E. Carlson, *Anal. Chem.*, 2015, **87**, 10668-10678.
170. O. Svelto, *Principle of Lasers* (fifth Edition), Springer Science, Business Media, 2010, 380-381.
171. Operation and Maintenance Manual for Surelite™ Lasers, Revision W, 2014, Continuum Electro Optics, Inc.
172. Horizon I and II OPO Operation and Maintenance Manual Revision C, 2014, Continuum.
173. W.E. Boxford, J.K. Pearce, C.E.H. Dessent, *Chem. Phys. Lett.*, 2004, **399**, 465-470.
174. M.P. Ince, B.A. Perera and M.J. Van Stipdonk, *Int. J. Mass Spectrom.*, 2001, **207**, 41-55.
175. M.H. Stockett and S.B. Nielsen, *Phys. Chem. Chem. Phys.*, 2016, **18**, 6996-7000.
176. S.M.J. Wellman and R.A. Jockusch, *J. Phys. Chem. A*, 2015, **119**, 6333-6338.
177. M. M. Campbell and O. Runquist, *J. Chem. Educ.*, 1972, **49**, 104-108.
178. G. Gregoire, H. Kang, C. Dedonder-Lardeux, C. Jouvet, C. Desfrancois, D. Onidas, V. Lepere and J. A. Fayeton, *Phys. Chem. Chem. Phys.*, 2006, **8**, 122-128.
179. S.H. Kaufman, J.M. Weber and M. Pernpointner, *J. Chem. Phys.*, 2013, **139**, 194310.
180. A. Sen, G.L. Hou, X.B. Wang and C.E.H. Dessent, *J. Phys. Chem. B*, 2015, **119**, 11626-11631.
181. W. Kaiser and C.G.B. Garrett, *Phys. Rev. Lett.*, 1961, **7**, 229-232.
182. J.V. Olsen, B. Macek, O. Lange, A. Makarov, S. Horning and M. Mann, *Nat. Methods*, 2007, **9**, 709-712.
183. Orbitrap Tribrid Series, Hardware Manual, Revision A, 2018, Thermo Fisher Scientific Inc.
184. Y. Zhang, S.B. Ficarro, S. Li and J.A. Marto, *J. Am. Soc. Mass Spectrom.*, 2009, **20**, 1425-1434.
185. J.K. Diedrich, A.F.M. Pinto and J.R. Yates, *J. Am. Soc. Mass Spectrom.*, 2013, **24**, 1690-1699.

References

186. D.J. Douglas, *J. Am. Soc. Mass Spectrom.*, 1998, **9**, 101–113.
187. M. J. Frisch, G. W. Trucks, H. B. Schlegel, G. E. Scuseria, M. A. Robb, J. R. Cheeseman, G. Scalmani, V. Barone, B. Mennucci, G. A. Petersson, H. Nakatsuji, M. Caricato, X. Li, H. P. Hratchian, A. F. Izmaylov, J. Bloino, G. Zheng, J. L. Sonnenberg, M. Hada, M. Ehara, K. Toyota, R. Fukuda, J. Hasegawa, M. Ishida, T. Nakajima, Y. Honda, O. Kitao, H. Nakai, T. Vreven, J. A. Montgomery Jr., J. E. Peralta, F. Ogliaro, M. J. Bearpark, J. Heyd, E. N. Brothers, K. N. Kudin, V. N. Staroverov, R. Kobayashi, J. Normand, K. Raghavachari, A. P. Rendell, J. C. Burant, S. S. Iyengar, J. Tomasi, M. Cossi, N. Rega, N. J. Millam, M. Klene, J. E. Knox, J. B. Cross, V. Bakken, C. Adamo, J. Jaramillo, R. Gomperts, R. E. Stratmann, O. M. Yazyev, A. J. Austin, R. Cammi, C. Pomelli, J. W. Ochterski, R. L. Martin, K. Morokuma, V. G. Zakrzewski, G. A. Voth, P. Salvador, J. J. Dannenberg, S. Dapprich, A. D. Daniels, O. Farkas, J. B. Foresman, J. V. Ortiz, J. Cioslowski and D. J. Fox, *Gaussian 09, Revision D.01*, Gaussian, Inc., Wallingford, CT, 2009.
188. Schrödinger, *Journal*, 2019.
189. C. T. Lee, W. T. Yang and R. G. Parr, *Phys. Rev. B*, 1988, **37**, 785-789.
190. A. D. Becke, *J. Chem. Phys.*, 1993, **98**, 5648-5652
191. Y. Zhao and D. G. Truhlar, *Theor. Chem. Acc.*, 2008, **120**, 215-241
192. R. Peverati and D. G. Truhlar, *Phys. Chem. Chem. Phys.*, 2012, **14**, 16187-16191.
193. Y. Zhao, N. E. Schultz and D. G. Truhlar, *J. Chem. Phys.*, 2005, **123**, 161103
194. R. M. Balabin, *J. Chem. Phys.*, 2008, **129**, 164101.
195. K. R. Liedl, *J. Chem. Phys.*, 1998, **108**, 3199–3204.
196. E. Miliordos and S. S. Xantheas, *J. Chem. Phys.*, 2015, **142**, 094311
197. A.L. Sobolewski and W. Domcke, *Europhys. News* 2006, **37**, 20–23.
198. C.T. Middleton, K. de La Harpe, C. Su, Y.K. Law, C.E. Crespo-Hernández and B. Kohler, *Annu. Rev. Phys. Chem.* 2009, **60**, 217–239.
199. M. Barbatti, A.J.A Aquino, J.J Szymczak, D. Nachtigallova, P. Hobza and H. Lischka, *Proc. Natl. Acad. Sci. USA* 2010, **107**, 21453–21458.
200. K. Kleineremanns, D. Nachtigallova and M.S. de Vries, *Int. Rev. Phys. Chem.* 2013, **32**, 308–342.
201. V.A. Spata, W. Lee and S. Matsika, *J. Phys. Chem. Lett.* 2016, **7**, 976–984.

References

202. R. Improta, F. Santoro and L. Blancafort, L. Chem. Rev. 2016, **116**, 3540–3593.
203. C. Reichardt and C.E. Crespo-Hernández, J. Phys. Chem. Lett. 2010, **1**, 2239–2243.
204. Y. Harada, C. Okabe, T. Kobayashi, T. Suzuki, T. Ichimura, N. Nishi, Y.-Z. Xu, J. Phys. Chem. Lett. 2010, **1**, 480–484.
205. M. Pollum, S. Jockusch and C.E. Crespo-Hernández, J. Am. Chem. Soc. 2014, **136**, 17930–17933.
206. S. Mai, M. Pollum, L. Martínez-Fernández, N. Dunn, P. Marquetand, I. Corral, C.E. Crespo-Hernández and L. González, Nat. Commun. 2016, **7**, 13077.
207. B. Ashwood, S. Jockusch and C.E. Crespo-Hernández, Molecules 2017, **22**, 379.
208. B. Ashwood, M. Pollum and C.E. Crespo-Hernández, Photochem. Photobiol. 2019, **95**, 33–58.
209. P. Karran and N. Attard, Nat. Rev. Cancer 2008, **8**, 24–36.
210. V.-N. Nguyen, S. Qi, S. Kim, N. Kwon, G. Kim, Y. Yim, S. Park and J. Yoon, J. Am. Chem. Soc. 2019, **141**, 16243–16248.
211. O. Reelfs, P. Karran and A.R. Young, Photochem. Photobiol. Sci. 2012, **11**, 148–154.
212. G. Trigiante and Y.Z. Xu, Photodynamic Therapy: Fundamentals, Applications and Health Outcomes; Hugo, A.G., Ed.; Nova Science Publishers: Hauppauge, NJ, USA, 2015.
213. K.M. Farrell, M.M. Brister, M. Pittelkow, T.I. Sølling and C.E. Crespo-Hernández, J. Am. Chem. Soc. 2018, **140**, 11214–11218.
214. R. Borrego-Varillas, D.C. Teles-Ferreira, A. Nenov, I. Conti, L. Ganzer, C. Manzoni, M. Garavelli, A. Maria de Paula and G. Cerullo, J. Am. Chem. Soc. 2018, **140**, 16087–16093.
215. H. Yu, J.A. Sanchez-Rodriguez, M. Pollum, C.E. Crespo-Hernández, S. Mai, P. Marquetand, L. González, S. Ullrich, Phys. Chem. Chem. Phys. 2016, **18**, 20168–20176.
216. J.A. Sánchez-Rodríguez, A. Mohamadzade, S. Mai, B. Ashwood, M. Pollum, P. Marquetand, L. González, C.E. Crespo-Hernández and S. Ullrich, Phys. Chem. Chem. Phys., 2017, **19**, 19756–19766.

References

217. M. Pollum, S. Jockusch and C.E. Crespo-Hernández, *Phys. Chem. Chem. Phys.* 2015, **17**, 27851–27861.
218. V. Vendrell-Criado, J.A. Sáez, V. Lhiaubet-Vallet, M.C. Cuquerella and M.A. Miranda, *Photochem. Photobiol. Sci.* 2013, **12**, 1460.
219. Y. Harada, T. Suzuki, T. Ichimura and Y. -Z. Xu, *J. Phys. Chem. B* 2007, **111**, 5518–5524.
220. L. Martínez-Fernández, G. Granucci, M. Pollum, C.E. Crespo-Hernández, M. Persico and I. Corral, *Chem. A Eur. J.* 2017, **23**, 2619–2627.
221. D. Koyama, M.J. Milner and A.J. Orr-Ewing, *J. Phys. Chem. B* 2017, **121**, 9274–9280.
222. L. Martínez-Fernández, L. González and I. Corral, *Chem. Commun.* 2012, **48**, 2134–2136.
223. G. Cui and W. Fang, *J. Chem. Phys.* 2013, **138**, 044315.
224. J.P. Gobbo and A.C. Borin, *Comput. Theor. Chem.*, 2014, 1040–1041, 195–201.
225. S. Mai, P. Marquetand and L.A. González, *J. Phys. Chem. A* 2015, **119**, 9524–9533
226. S. Mai, P. Marquetand and L.A. González, *J. Phys. Chem. Lett.* 2016, **7**, 1978–1983.
227. D.C. Teles-Ferreira, I. Conti, R. Borrego-Varillas, A. Nenov, I.H.M. Van Stokkum, L. Ganzer, C. Manzoni, A.M. Paula, G. Cerullo and M.A. Garavelli, *Chem. A Eur. J.* 2020, **26**, 336–343.
228. N.G.K. Wong, J.A. Berenbeim, M. Hawkrige, E. Matthews and C.E.H. Dessent, *C.E.H. Phys. Chem. Chem. Phys.* 2019, **21**, 14311–14321.
229. E. Matthews and C.E.H. Dessent, *J. Phys. Chem. Lett.* 2018, **9**, 6124–6130.
230. E. Matthews, R. Cercola and C.E.H. Dessent, *Molecules* 2018, **23**, 2036.
231. M. Pollum and C.E. Crespo-Hernández, *Communication, J. Chem. Phys.* 2014, **140**, 071101.
232. L. Martinez-Fernandez, T. Fahleson, P. Norman, F. Santoro, S. Coriani and R. Improta, *Photochem. Photobiol. Sci.* 2017, **16**, 1415–1423.
233. S. Mai, A. Mohamadzade, P. Marquetand, L. González and S. Ullrich, *Molecules*, 2018, **23**, 2836.
234. J. Kopyra, H. Abdoul-Carime, F. Kossoski and M.T. do N. Varella, *Phys. Chem. Chem. Phys.*, 2014, **16**, 25054–25061.

References

235. J. Kopyra and H. Abdoul-Carime, *J. Chem. Phys.* 2016, **144**, 034306.
236. Y. Zheng and Sanche, *Int. J. Mol. Sci.* 2015, **20**, 3749.
237. E. Alizadeh, T.M. Orlando and L. Sanche, *Annu. Rev. Phys. Chem.* 2015, **66**, 379–398.
238. A. Sen, T. F. Luxford, N. Yoshikawa and C. E. Dessent, *Phys. Chem. Chem. Phys.*, 2014, **16**, 15490–15500.
239. S. M. Wellman and R. A. Jockusch, *J. Phys. Chem. A*, 2015, **119**, 6333–6338
240. R. Cercola, E. Matthews and C.E.H Dessent, *J. Phys. Chem. B* 2017, **121**, 5553–5561.
241. M. P. Jedrychowski, E. L. Huttlin, W. Haas, M. E. Sowa, R. Rad and S. P. Gygi, *Mol. Cell. Proteomics*, 2011, **10**, M111.009910.
242. W.-L. Li, A. Kunin, E. Matthews, N. Yoshikawa, C.E.H. Dessent and D.M. Neumark, *J. Chem. Phys.* 2016, **145**, 044319.
243. Y. -W. Nei, T.E. Akinyemi, J.D. Steill, J. Oomens and M.T. Rodgers, *Int. J. Mass Spectrom.* 2010, **297**, 139–151.
244. W.J. Morgan and R.C Fortenberry, *Theor. Chem. Acc.*, 2015, **134**, 47.
245. M. Gutowski, K.D. Jordan and P. Skurski, *J. Phys. Chem. A*, 1998, **102**, 2624–2633.
246. P. Skurski, M. Gutowski and J. Simons, *J. Int. J. Quantum Chem.* 2000, **80**, 1024–1038.
247. J. Simons, *Annu. Rev. Phys. Chem.* 2011, **62**, 107–128.
248. J. Simons, *J. Phys. Chem. A* 2008, **112**, 6401–6511.
249. T. Stein, L. Kronik, and R.J. Baer, *Am. Chem. Soc.*, 2009, **131**, 2818–2820.
250. Y. Noguchi, M. Hiyama, H. Akiyama, and N.J. Koga, *J. Chem. Phys.*, 2014, **141**, 044309.
251. K. Støchkel, B.F. Milne and S.B. Nielsen, *J. Phys. Chem. A*, 2011, **115**, 2155–2159.
252. R. Cercola, E. Matthews and C.E.H. Dessent, *Mol. Phys.*, 2019, **117**, 3001–3010.
253. R. Cercola, K. O. Uleanya and C. E. H. Dessent, *Mol. Phys.*, 2019, **118**, e1679402.
254. P.S. Spencer and H.H. Schaumburg, *Environ. Health Perspect.* 1975, **11**, 129–133.

References

255. C.E.H. Dessent, C.G. Bailey and M.A. Johnson, *J. Chem. Phys.* 1996, **105**, 10416–10423.
256. Ø.S. Pedersen, S.C. Byskov, F. Turecek, B.S. Nielsen, *J. Phys. Chem. A* 2014, **118**, 4256–4265.
257. M. Berdakin, G. Féraud, C. Dedonder-Lardeux, C. Jouvet, G.A. Pino, *Phys. Chem. Chem. Phys.* 2014, **16**, 10643–10650.
258. E.R. Molina, D. Ortiz, J.Y. Salpin, R. Spezia, 2015, **50**, 1340–1351.
259. B. Lucas, M. Barat, J.A. Fayeton, C. Jouvet, P. Çarçabal, G. Grégoire, *Chem. Phys.* 2008, **347**, 324–330.
260. C.E.H. Dessent, J. Kim, M.A. Johnson, *Faraday Discuss.* 2000, **115**, 395–406.
261. E. Matthews, R. Cercola, G. Mensa-Bonsu, D.M. Neumark, C.E.H. Dessent, *J. Chem. Phys.* 2018, **148**, 084304.
262. A. Sen, E.M. Matthews, G.-L. Hou, X.-B. Wang, C.E.H. Dessent, *J. Chem. Phys.*, 2015, **143**, 184307.
263. N. Igarashi-Yamamoto, A. Tajiri, M. Hatano, S. Shibuya and T. Ueda, *Biochimica et Biophysica Acta (BBA) - Nucleic Acids and Protein Synthesis*, 1981, **656**, 1–15.
264. S. M. Pimblott and J. A. LaVerne, *Radiat. Phys. Chem.*, 2007, **76**, 1244–1247.
265. L. Sanche, *Radiat. Phys. Chem.*, 1989, **34**, 15.
266. B. Boudaiffa, P. Cloutier, D. Hunting, M. A. Huels and L. Sanche, *Science*, 2000, **287**, 1658–1660.
267. J. K. Wolken and F. Turecek, *J. Phys. Chem. A*, 2001, **105**, 8352–8360.
268. S. G. Ray, S. S. Daube and R. Naaman, *Proc. Natl. Acad. Sci. U. S. A.*, 2005, **102**, 15–19.
269. H. Abdoul-Carime, S. Gohlke and E. Illenberger, *Phys. Rev. Lett.*, 2004, **92**, 168103.
270. J. Simons, *Acc. Chem. Res.*, 2006, **39**, 772–779.
271. J. D. Gu, J. Leszczynski and H. F. Schaefer, *Chem. Rev.*, 2012, **112**, 5603–5640.
272. H. Y. Chen, P. Y. Yang, H. F. Chen, C. L. Kao and L. W. Liao, *J. Phys. Chem. B*, 2014, **118**, 11137–11144.
273. X. Pan and L. Sanche, *Chem. Phys. Lett.*, 2006, **421**, 404–408.

References

274. G. Z. Zhu, L. F. Cheung, Y. Liu, C. H. Qan and L. S. Wang, *J. Phys. Chem. Lett.*, 2019, **10**, 4339–4344.
275. Y. Dong, Y. Gao, W. Liu, T. Gao, Y. Zheng and L. Sanche, *J. Phys. Chem. Lett.*, 2019, **10**, 2985–2990.
276. S. Denifl, S. Ptasinska, G. Hanel, B. Gstir, M. Probst, P. Scheier and T. D. Mark, *J. Chem. Phys.*, 2004, **120**, 6557–6565.
277. J. Ameixa, E. ArthurBaidoo, R. Meißner, S. Makurat, W. Kozak, K. Butowska, F. Ferreira da Silva, J. Rak and S. Denifl, *J. Chem. Phys.*, 2018, **149**, 164307.
278. J. K. Wolken and F. Turecek, *J. Am. Chem. Soc.*, 2001, **123**, 5804–5805.
279. J. H. Hendricks, S. A. Lyapustina, H. L. de Clercq, J. T. Snodgrass and K. H. Bowen, *J. Chem. Phys.*, 1996, **104**, 7788–7791.
280. M. Haranczyk and M. Gutowski, *J. Am. Chem. Soc.*, 2005, **127**, 699–706.
281. M. A. Fennimore and S. Matsika, *J. Phys. Chem. A*, 2018, **122**, 4048–4057.
282. M. A. Yandell, S. B. King and D. M. Neumark, *J. Am. Chem. Soc.*, 2013, **135**, 2128–2131.
283. S. B. King, M. A. Yandell and D. M. Neumark, *Faraday Discuss.*, 2013, **163**, 59–72.
284. S. B. King, M. A. Yandell, A. B. Stephansen and D. M. Neumark, *J. Chem. Phys.*, 2014, **141**, 224310.
285. S. B. King, A. B. Stephansen, Y. Yokoi, M. A. Yandell, A. Kunin, T. Takayanagi and D. M. Neumark, *J. Chem. Phys.*, 2015, **143**, 024313.
286. W. Li, K. Alice, E. Matthews, N. Yoshikawa, C. E. H. Dessent and D. M. Neumark, *J. Chem. Phys.*, 2016, **145**, 044319.
287. A. Kunin and D. M. Neumark, *Phys. Chem. Chem. Phys.*, 2019, **21**, 7239–7255.
288. J. Kopyra, K. K. Kopyra, H. Abdoul-Carime and D. Branowska, *J. Chem. Phys.*, 2018, **148**, 234301.
289. S. Taras-Goslinska and J. Bobrowski, *Molecules*, 2019, **24**, 4402.
290. X. Li, J. Chen and K. H. Bowen, *J. Chem. Phys.*, 2011, **134**, 074304.
291. O. Dolgounitcheva, V. G. Zakrzewski and J. V. Ortiz, *J. Chem. Phys.*, 2011, **134**, 074305.
292. W. R. Garrett, *J. Chem. Phys.*, 1982, **77**, 3666–3673.
293. O. H. Crawford and W. R. Garrett, *J. Chem. Phys.*, 1977, **66**, 4968–4970.

References

294. O. H. Crawford, *Mol. Phys.*, 1971, **20**, 585–591.
295. W. C. Schneider and I. F. Halverstadt, *J. Am. Chem. Soc.*, 1948, **70**, 2626–2631.
296. S. Arslançan, L. Martí'nez-Ferna'ndez and I. Corral, *Molecules*, 2017, **22**, 998.
297. We note that at higher mass resolution, the masses are $I = 126.90522$ and $(2\text{-TU-H})^-$ or $(4\text{-TU-H})^- = 126.99735$. These masses can be distinguished in the Orbitrap Fusion Tribrid mass spectrometer available in our research group. Photofragmentation is not possible in this mass spectrometer, but higher-collisional energy dissociation (HCD) was performed on the clusters. We observed both I^- and $(\text{TU-H})^-$ as fragments in these experiments (Section 4.6.2, Figure 4.18) for both $I\text{-}2\text{-TU}$ and $I\text{-}4\text{-TU}$ with an intensity ratio of 90% to 10%, respectively. This shows that the electronic ground states of the $I\text{-}2\text{-TU}$ and $I\text{-}4\text{-TU}$ clusters do fragment with production of both I^- and $(\text{TU-H})^-$.
298. A. J. A. Harvey, N. Yoshikawa, J. G. Wang and C. E. H. Dessent, *J. Chem. Phys.*, 2015, **143**, 101103.
299. A. Henley and H. H. Fielding, *Int. Rev. Phys. Chem.*, 2019, **38**, 1–34.
300. C. S. Anstoter, J. N. Bull and J. R. R. Verlet, *Int. Rev. Phys. Chem.*, 2016, **35**, 509–538.
301. F. Mbaiwa, D. Dao, N. Holtgrewe, J. Lasinski and R. Mabbs, *J. Chem. Phys.*, 2012, **136**, 114303.
302. C. E. Crespo Hernandez, B. Cohen, P. M. Hare and B. Kohler, *Chem. Rev.*, 2004, **104**, 1977–2020.
303. A. Sen and C. E. H. Dessent, *J. Phys. Chem. Lett.*, 2014, **5**, 3281–3285.
304. A. Sen and C. E. H. Dessent, *J. Chem. Phys.*, 2014, **141**, 241101.
305. C. Desfrancois, H. Abdoul-Carime, N. Khelifa and J. P. Schermann, *Phys. Rev. Lett.*, 1994, **73**, 2436–2439.
306. S. Daly, M. Pornini, F. Rosu and V. Gabelica, *Faraday Discuss.*, 2019, **217**, 361–382.
307. M. Ahmed, et al., *Faraday Discuss.*, 2019, **217**, 138–171.
308. A. Les and L. Adamowicz, *J. Am. Chem. Soc.*, 1990, **112**, 4, 1504–1509.
309. C. Walsh, *Acc. Chem. Res.* 1980, **13**, 148–155.
310. M. Insinska-Rak, D. Prukata, A. Golczak, E. Fornal and M. Sikorski, *Journal of Photochem. Photobiol., A: Chemistry* 403, 2020, 1128373

References

311. K.S. Conrad, C.C Manahan and B.R Crane, *Nat. Chem. Biol.*, 2014, **10**, 801–809.
312. A. Losi, *Photochem. Photobiol.* 2007, **83**, 1283–1300.
313. M. Kondo, J. Nappa, K.L. Ronayne, A.L. Stelling, P.J. Tonge and S.R. Meech, *J. Phys. Chem. B* 2006, **110**, 20107
314. A.J. Penzkofer, *Photochem. Photobiol. A Chem.*, 2016, **314**, 114–124.
315. A.Tyagi, and A., J. Penzkofer, *Photochem. Photobiol. A Chem.*, 2010, **215**, 108–117. 20110
316. J. R. Dainty, N. R. Bullock, D. J. Hart, A. T. Hewson, R. Turner, P. M. Finglas and H. J. Powers, *Am. J. Clin. Nutr.*, 2007, **85**, 1557–156
317. J.N. Bull, E. Carrascosa, L. Giacomozzi, E.J. Bieske and M.H. Stockett, *Phys. Chem. Chem. Phys.*, 2018, **20**, 19672
318. B.D Etz, J.M. DuClos and S.J Vyas S, *Phys. Chem. A* 2020, 124, **21**, 4193–4201
319. R. Miura, *Chem. Rec.* 2001, **1**, 183– 194
320. V. Piano, B.A Palfey, A. Mattevi, *Biochem. Sci.* 2017, **42**, 457– 469
321. L.M Antill and J.R Woodward, *J. Phys. Chem. Lett.* 2018, 9, 2691–2696.
322. L. Zanetti-Polzi, M. Aschi, A. Amadei and I. Daidone, *J. Phys. Chem. Lett.* 2017, **8**, 3321–3327.
323. W. Holzer, J. Shirdel, P. Zirak, A. Penzkofer, P. Hegemann, R. Deutzmann, and E. Hochmuth, *Chem. Phys.*, 2005, **308**, 69–78.
324. J. Berg, J. Tymoczko and L. Stryer, *Biochemistry*, 5th edn, 2002.
325. K. S. Conrad, C. C. Manahan and B. R. Crane, *Nat. Chem. Biol.*, 2014, **10**, 801–809.
326. Y. E. Bruggeman, A. Honegger, H. Kreuwel, A. J. W. G. Visser, C. Laane, A. Schots and R. Hilhorst, *Eur. J. Biochem.*, 1997, **249**, 393–400
327. M. T. Stankovich, CRC Press, Boca Raton, 1991, vol. 1, pp. 401–425.
328. M.A. Sheraz, S. Hafeez Kazi , S. Ahmed, Z. Anwar and I. Ahmad, *Beilstein J. Org. Chem.* 2014, **10**, 1999–2012
329. J. Iqbal, A. Husain. and A. Gupta, *Chem.Pharm. Bull. (Tokyo)*, 2006, **54**, 519–521.
330. L. Zanetti-Polzi, M. Aschi, I. Daidone, and A. Amadei, *Chem. Phys. Lett.* 2017, **669**, 119–124.

References

331. X.P. Chang, X.Y. Xie, S.Y. Lin and G.J. Cui, *Phys. Chem. A*, 2016, **120**, 6129–6136.
332. S. Salzmann and C.M. Marian, *Chem. Phys. Lett.* 2008, **463**, 400–404.
333. S. Salzmann, J. Tatchen, and C.M. Marian, *J. Photochem. Photobiol. A Chem.*, 2008, **198**, 221–231.
334. S. Salzmann and C.M. Marian, *Photochem. Photobiol. Sci.*, 2009, **8**, 1655–1666.
335. P.S. Song, E.C. Smith and D.E. Metzler, *J. Am. Chem. Soc.*, 1965, **87**, 4181–4184.
336. W.M. Moore and C. Baylor, *J. Am. Chem. Soc.*, 1969, **91**, 7170–7179.
337. I. Ahmad, Q. Fasihullah and F.H. Vaid, *J. of Photochem. Photobiol. A: Chemistry*, 2020, **403**, 1128373
338. M. H. Stockett, *Phys. Chem. Chem. Phys.*, 2017, **19**, 25829–25833.
339. A. Sheldrick, D. Müller, A. Günther, P. Nietoa and O. Dopfer, *Phys. Chem. Chem. Phys.*, 2018, **20**, 7407–7414.
340. T. Zhang, K. Papson, R. Ochran and D. P. Ridge, *J. Phys. Chem. A*, 2013, **117**, 11136–11141.
341. A. Günther, P. Nieto, D. Müller, A. Sheldrick, D. Gerlich and O. Dopfer, *J. Mol. Spectrosc.*, 2017, **332**, 8–15.
342. J. Langer, A. Günther, S. Seidenbecher, G. Berden, J. Oomens and O. Dopfer, *Chem. Phys. Chem.*, 2014, **15**, 2550–2562.
343. M. H. Stockett, M. Boesen, J. Houmøller and S. B. Nielsen, *Angew. Chem., Int. Ed.*, 2017, **56**, 3490–3495.
344. C. E. H. Dessent, C. G. Bailey, and M. A. Johnson, *J. Chem. Phys.*, 1996, **105**, 10416.
345. F. Mbaiwa, M. Van Duzor, J. Wei, and R. Mabbs, *J. Phys. Chem. A*, 2010, **114**, 1539.
346. *Journal Of Mathematical Analysis and Applications*, 1969, **26**, 163-169.
347. B. Bellina, J. M. Brown, J. Ujma, P. Murray, K. Giles, M. Morris, I. Compagnon and P.E. Barran, *Analyst*. 2014, **139**, 6348–6351.
348. L. Giacomozzi, C. Kjær, J. Langeland Knudsen, L. H. Andersen, S. Brøndsted Nielsen, and M. H. Stockett, *J. Chem. Phys.*, 2018, **148**, 214309.
349. M.A. Yandell, S.B. King, and Neumark, D. M., *J. Chem. Phys.* 2014, **140**, 184317.
350. A. Treibs, *Liebigs, Ann. Chem.*, 1935, **520**, 144–150.

References

351. A. Treibs, *Angew. Chem.*, 1936, **49**, 682-686.
352. H. Dunning and N.A. Rabon, *Indust. Eng. Chem.*, 1956, **48**, 5, 951-955.
353. A. B. P. Lever, *Advan. Inorg. Chem. Radiochem.*, 1965, 7, 27
354. J. E. Falk, "Porphyrins and Metalloporphyrins," Elsevier Publishing Co., Amsterdam, 1964.
355. R. Giovannetti, in *Macro To Nano Spectroscopy*, ed. J. Uddin, InTech, <https://www.intechopen.com/books/macro-to-nano-spectroscopy/the-use-of-spectrophotometry-uv-vis-for-the-study-of-porphyrins>, Vol 1, Ch. 6, pp. 87-108.
356. C.B Nielsen, J. S Forster, P.R Ogilby, and S. B Nielsen, *J. Phys. Chem. A*, 2005, **109**, 3875-3879.
357. L. Bajema, M. Gouterman, and C. B. Rose, *J. Mol. Spectrosc.*, 1971, **39**, 421.
358. A. M. Schaffer, M. Gouterman, and E. R. Davidson, *Theor. Chim. Acta*, 1973, **30**, 9.
359. T.-H. Huang and J. H. Sharp, *Chem. Phys.*, 1982, **65**, 205
360. T.-H. Huang, K. E. Rleckhoff, and E. M. Voigt, *J. Phys. Chem.*, 1981, **85**, 3322.
361. N. E. Khatib, B. Boudjema, and M. Maitro, *Can. J. Chem.*, 1988, **66**, 2313.
362. B. J. Prince, B. E. Williamson, and R. J. Reeves, *J. Lumin.*, 2001, **93**, 293.
363. L.D. Bushnell, and H. F. Haas, *J. Bacteriol.*, 1941, **41**, 653-673.
364. J.G. Speight, *The chemistry and technology of petroleum*, 1991, Marcel Dekker, New York, N.Y. 1
365. J.P. Dickie and T.F. Yen, *J. Anal. Chem.*, 1967, **39**, 1847-1852.
366. D. Manna, R. Lo and P. Hobza, *Dalton Trans.*, 2020, **49**, 164-170
367. P.F. Schwab, M.D. Levin, and J. Michi, *Chem. Rev.*, 1999, **99**, 1863-1934
368. M.C. Durrant, *Dalton Trans.*, 2014, **43**, 9754-9765
369. D. Kuter, K. Chibale and T. J. Egan, *J. Inorg. Biochem.*, 2011, **105**, 684-692
370. U. Even and J. Jortner, *The Journal of Physical Chemistry*, 1983, **87**, 28-29.
371. J.A. Wyer, A.V. Jørgensen, A.V. Pedersen, and S.B. Nielsen, *Chem. Phys. Chem.*, 2013, **14**, 4109 - 4113
372. L. E. Leverman, A. Wanat, J. Oszejca, G. Stochel, P. C. Ford, R. van Eldik, *J. Am. Chem. Soc.*, 2001, **123**, 285.
373. J.A. Wyer, and S.B. Nielsen, *Angew. Chem. Int. Ed.*, 2012, **51**, 10256.
374. J. A. Wyer and S.B. Nielsen, *J. Chem. Phys.*, 2010, **133**, 084306.

References

375. M. K. Lykkegaard, A. Ehlerding, P. Hvelplund, U. Kadhane, M.-B. S. Kirkerterp, S. B. Nielsen, S. Panja, J. A. Wyer, H. Zettergren, *J. Am. Chem. Soc.*, 2008, **130**, 11856.
376. A. Sarmah and P. Hobza, *Mater. Adv.*, 2020, **1**, 1895-1908
377. Y. Liu, W. Xu, J. Zhang, W. Fuller, C. E. Schulz and J. Li, *J. Am. Chem. Soc.*, 2017, **139**, 5023–5026
378. B. D. L. Torre, M. Švec, P. Hapala, J. Redondo, O. Krejčí, R. Lo, D. Manna, A. Sarmah, D. Nachtigallová, J. Tuček, P. Błoński, M. Otyepka, R. Zbořil, P. Hobza and P. Jelínek, *Nat. Commun.*, 2018, **9**, 2831
379. M.A.H. Amad, N.B. Cech, G.S. Jackson, C.G. Enke, *J. Mass Spectrom.*, **2000**, 784–789.
380. S. Tang, A. Babai, A.V. Mudring, *Angew. Chem. Int. Ed.*, 2008, **47**, 7631–7634.
381. J. Pape, K. L. Vikse, E. Janusson, N. Taylor and J. S. McIndoe, *Int. J. of Mass Spectro.*, 2014, **373**, 66–71.
382. S. R. Stoyanov, C. X Yin, M.R Gray, J. M Stryker, S. Gusarov and A. Kovalenko, *J. Phys. Chem.*, 2010, **114**, 2180–2188
383. W. E. Boxford and C. E. H. Dessent, *Phys. Chem. Chem. Phys.*, 2006, **8**, 5151-5165.
384. T. F. M. Luxford, E. M. Milner, N. Yoshikawa, C. Bullivant and C. E. H. Dessent, *Chem. Phys. Lett.*, 2013, **577**, 1-5.
385. M. T. Rodgers and P. B. Armentrout, *Mass Spectrom. Rev.*, 2000, **19**, 215-247.
386. R. M. Burke, W. E. Boxford and C. E. H. Dessent, *J. Chem. Phys.*, 2006, **125**, 021105
387. M. C. Durrant, *Inorg. Chem. Commun.*, 2001, **4**, 60–62.
388. R. Gilson and M. C. Durrant, *Dalton Trans.*, 2009, **46**, 10223–10230
389. M. C. Durrant, *Chem. Eur. J.*, 2007, **13**, 3406–3413
390. S. C. Davies, M. C. Durrant, D. L. Hughes, R. L. Richards and J. R. Sanders, *J. Chem. Soc., Dalton Trans.*, 2000, **24**, 4694–4701.
391. M. Swart, *J. Chem. Theor. Comput.*, 2008, **4**, 2057–2066.
392. M. Swart, *Int. J. Quantum Chem.*, 2013, **113**, 2–7
393. S. P. de Visser, M. G. Quesne, B. Martin, P. Comba and U. Ryde, *Chem. Commun.*, 2014, **50**, 262–282.

References

394. S. Shankar, M. Peters, K. Steinborn, B. Krahwinke, F. D. Sönnichsen, D. Grote, W. Sander, T. Lohmiller, O. Rüdiger and R. Herges, *Nat. Commun.*, 2018, **9**, 4750.
395. A.C. Reed and F.A. Guiset, *J. Am. Chem. Soc.*, 1996, **118**, 3281–3282.
396. G. E. Toney, L. W. TerHaar, J. E. Savrin, A. Gold, W. E. Hatfield, and R. Sangaiah, *Inorg. Chem.*, 1984, **23**, 2561-2563.
397. F. A. Walker, M.-W. Lo, and M. T. Ree, *J. Am. Chem. Soc.*, 1976, **98**, 5552–5560
398. D. Sahoo, M.G. Quesne, S.P de Visser and S.P Rath, *Angew. Int. Ed.*, 2005, **54**, 4796–4800.
399. R. S. Hosmane and J. F. Liebman, *Struct. Chem.* 2009, **20**, 693–697
400. R. Bonnett, P. Brewer, K. Noro, and T. Noro, *Tetrahedron*, 1978, **34**, 379-385.
401. Y. O. Su, R.S. Czernuszewicz, L.A. Miller and T. G. Spiro, *J. Am. Chem. Soc.* 1988, **110**, 4150-4157.
402. M. Kasha, H.R. Rawls and M. A. El-Bayoumi, *Pure Appl. Chem.*, 1965, **11**, 371-392
403. F. Paulat and N. Lehnert, *Inorganic Chemistry*, 2008, 47, **11**, 4963-4976.
404. N. Sprutta, M. Swiderska and L. Latos-Grazynski, *J. Am. Chem. Soc.*, 2005, **127**, 13108–13109.
405. T. Gozetz, L. Huynh and D. K Bohme, *International Journal of Mass Spectrometry*, 2009, **279**, 113–118
406. M. K. Lykkegaard, H. Zettergren, M.-B. S. Kirketerp, A. Ehlerding, J. A. Wyer, U. Kadhane, S. B. Nielsen, *J. Phys. Chem. A*, 2009, **113**, 1440-1444.
407. O. P. Charkin, N. M. Klimenko, D. O. Charkin, H. C. Chang and S. H. Lin, *J. Phys. Chem. A*, 2007, **111**, 9207-9217
408. S. Nonose, S. Iwaoka, K. Mori, Y. Shibata, K. Fuke, *Eur. Phys. J. D* 2005, **34**, 315-319
409. O. P. Charkin, N. M. Klimenko, P. T. Nguyen, D. O. Charkin, A. M. Mebel, S. H. Lin, Y. S. Wang, S. C. Wei, H. C. Chang, *Chem. Phys. Lett.*, 2005, **415**, 362-369
410. G. J. Van Berkel, S. A. McLuckey and G. L. Glish, *Anal. Chem.*, 1991, **63**, 1089-1098

References

411. F. Filsinger, D. S. Ahn, G. Meijer and G. von Helden, *Phys. Chem. Chem. Phys.*, 2012, **14**, 13370-13377.
412. E. Besic, *J. Mol. Struct.*, 2009, **917**, 71-75
413. J.R.R. Verlet, C.S. Anstoter, J.N. Bull and J.P. Rogers, *J. Phys. Chem. A*, 2020, 124, **18**, 3507-3519

